UNIVERSITY OF SOUTHAMPTON

The synthesis and characterisation of pyrochlore frameworks

A thesis submitted for the Degree of Doctor of Philosophy

by

Charles Francis Simon

SCHOOL OF CHEMISTRY

FACULTY OF SCIENCE, ENGINEERING AND MATHEMATICS

September, 2010

UNIVERSITY OF SOUTHAMPTON

ABSTRACT

FACULTY OF SCIENCE, ENGINEERING AND MATHEMATICS

SCHOOL OF CHEMISTRY

Doctor of Philosophy

The synthesis and characterisation of pyrochlore frameworks

By Charles Francis Simon

Structural studies have been undertaken on a wide range of pyrochlore phases, with a focus on garnering a better understanding of the factors determining the formation and behavior of these materials. Extensive structural characterisation has been undertaken primarily using powder X-ray and powder neutron diffraction techniques to explore the subtle structural changes that occur as a result of changes in composition on the two interlocking networks that make up the pyrochlore structure.

Particular attention has been paid to hydrated *beta*-pyrochlore materials, using high resolution TOF and constant wavelength PND to accurately determine the location and orientation of the water molecules within the structure. The location of these molecules has been shown to be directly correlated to the overall lattice dimensions of the pyrochlore framework, with the subsequent molecular orientation and internal bond angles changing to provide an optimum stabilization effect on the *A*-site cation.

Investigation into the effects of hydration upon the superconducting *beta*-pyrochlore series $A Os_2O_6.nH_2O$ (where A = K, Rb and Cs) has also been investigated; with a correlation between the structural changes, the degree of hydration and the onset of the superconducting state being discussed.

Also presented is work seeking to determine the scope and effects of ion-exchange on the A_2O' network of the pyrochlore framework, with several new phases synthesised and other known phases extensively characterized along with a discussion regarding the limits of what may be included in the pyrochlore framework.

TABLE OF CONTENTS

DECLARATION OF AUTHORSHIP

I, Charles Francis Simon, declare the thesis entitled

The synthesis and characterisation of pyrochlore frameworks

and the work presented in the thesis are both my own, and have been generated by me as a result of my own original research. I confirm that:

- this work was done wholly or mainly while in candidature for a research degree at this University;
- where any part of this thesis has previously submitted for a degree or any other qualification at this University or any other institution, this has clearly been stated;
- where I have consulted the published work of others, this is clearly attributed;
- where I have quoted from the work of others, the source is always given. With the exception of such quotations, this thesis is entirely my own work;
- I have acknowledged all main sources of help;
- where the thesis is based on the work done by myself jointly with others, I have made it clear exactly what was done by others and what I have contributed myself;
- parts of this work have been published as

Galati, R.; Simon, C.; Henry, P. F.; Weller, M. T., Phys. Rev. B, 2008, 77.

Galati, R.; Simon, C.; Knee, C. S.; Henry, P. F.; Rainford, B. D.; Weller, M. T., Chemistry of Materials, 2008, 20, 1652-1659.

Signed:

Date:

ACKNOWLEDGEMENTS

My initial thanks must go to Professor Mark Weller for his support and academic guidance throughout this project which have been greatly appreciated.

Thanks of course must go to the Weller group both past and present with special mentions to; Rosa Galati for getting me excited about pyrochlores in the first place and Drs Jenny Armstrong and Valeska Ting for providing useful advice and proof reading elements of this work.

Peter Hickey also deserves a particular mention for providing a sounding board for ideas, teaching me not just how to use a whole variety of instruments but how they work as well and for partaking in the endless cricket based discussions that seemed to inevitably ensue over a couple of beers.

Finally I'd like to thank Sarah for her love and support throughout, her understanding when I disappeared to France for a week at a time and staying with me as an eternal student.

Chapter One

INTRODUCTION

1.1 Complex metal oxides

Complex metal oxides adopt many structures and are extensively studied due to their wide ranging chemical and physical properties. Applications of such materials cover a spectrum of areas; common uses include in solid state devices as capacitors[1], superconducting magnets[2] and semiconductors[3], but also in more diverse fields such as in ion conductors[4], ion exchange phases[5] and ferroelectric devices[6]. A large volume of research is also undertaken into these materials for a much simpler purpose, that they are often highly coloured and can be used as pigments[7]. The majority of phases discussed in this work are pure metal oxides, along with their hydrates; the remainder adopt structures most commonly seen in metal oxide type systems, but with differing or mixed cations present within the framework.

The properties of most metal oxide phases centre on the multi dimensional units that make up the primary structural network of the material[8]. These are generally constructed from metal-oxygen polyhedra, with varying degrees of coordination, with further atoms then being coordinated into this framework to provide structural stability and charge balancing as required. The linked polyhedra produce a long range structure which allows cooperative electronic effects to occur, leading to materials with applications as superconductors, semiconductors, conductors, and in ferroelectronic and piezoelectronic devices[3,9-12]. The regular nature of these structures, that accompanies long range ordering, also allows their local structure to be readily studied using a variety of diffraction techniques leading to a strong understanding of the link between the structure of a material and its properties.

In many of these structure types the materials can adopt highly diverse compositions with a wide variety of elemental ratios forming that particular phase type under the correct synthetic conditions. In addition mixed stoichiometry is also common with a single crystallographic site being occupied by multiple atom types. This feature leads to a virtually infinite variety of potential compositions within the metal-oxide family of materials. The control of these compositions has been proven to be of great importance and it is this feature more than any other that has led to the wide variety of applications and a enormous body of research, as altering the composition has allowed materials to be tailored to produce precisely the desired properties.

A limited number of fluoride materials are also studied in this work; in general similar structures are formed with the fluorine being used as the structural anion as opposed to oxygen. This is possible as fluorine and oxygen are both 'hard' anions with similar ionic radii and bonding requirements, they are thus often interchangeable. Materials found in the natural environment are commonly seen with both oxygen and fluorine present in the structure[13,14], this ability to adopt multiple anions further increases the potential compositions and properties of the materials as well as allowing further control over the oxidation state of the cations present within the materials leading to some degree of selectivity in properties. An example of this is seen in the work of Ravez[15], where the ratio of oxygen to fluorine present was shown to effect the temperature at which ferroelectric behaviour was induced in a range of materials adopting both the perovskite and tungsten bronze type frameworks.

1.1.1 Pyrochlore phases

A large number of known complex metal oxides adopt a structure similar to that of the mineral pyrochlore, $(Ca,Na)_2Nb_2O_6F$, the structure of which was first described by Gaertner in 1930[16]. The mineral is located in several sites around the world and provides the main source of mined niobium, it is found as small octahedral crystals normally suspended in other mineral deposits. Since this time a wide variety of compounds of the general formula $A_2B_2O_7$ (where *A* and *B* are metals) have been discovered synthetically. The ability to adopt a large range of atoms on different crystallographic sites leads to a wide range of properties being observed including metal-insulator transitions[17], magnetic frustration[18], magnetoresistance[19], superconductivity[20], ferroelectrics[21], ionic conductivity[22] and catalysis[23]. Figure 1.1 shows the wide range of elements that have been incorporated into the pyrochlore framework.

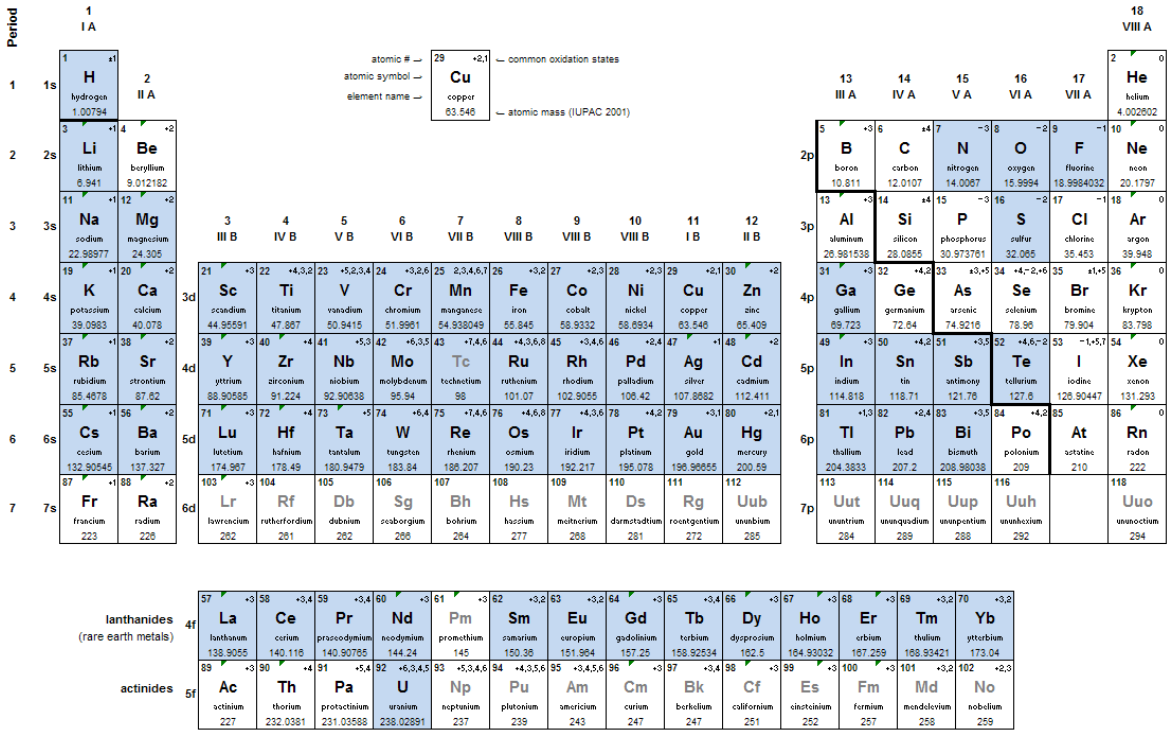

Figure 1.1 - This figure shows the wide range of elements that have conclusively been shown to be accepted into the pyrochlore structure at the time of printing (those highlighted in blue are present within the literature).

The pyrochlore structure displays cubic symmetry (space group No. 227, $Fd\bar{3}m$) with a general stoichiometry of $A_2B_2X_7$, where generally *A* is a large low valence cation and *B* is a small more highly charged cation capable of octahedral coordination. The *X* site is most commonly occupied by O^{2-}, although other anions have also been reported (e.g. S^{2-} [24], F^{-} [25] and N^{3-} [26]). The structure type is often written as $A_2B_2X_6X'$ which better represents the local structure of the lattice and can be described as two weakly interacting interpenetrating sub-lattices, a cuprite like A_2X' lattice and a B_2O_6 framework built up of corner sharing BO_6 octahedra, as shown in Figure 1.2.

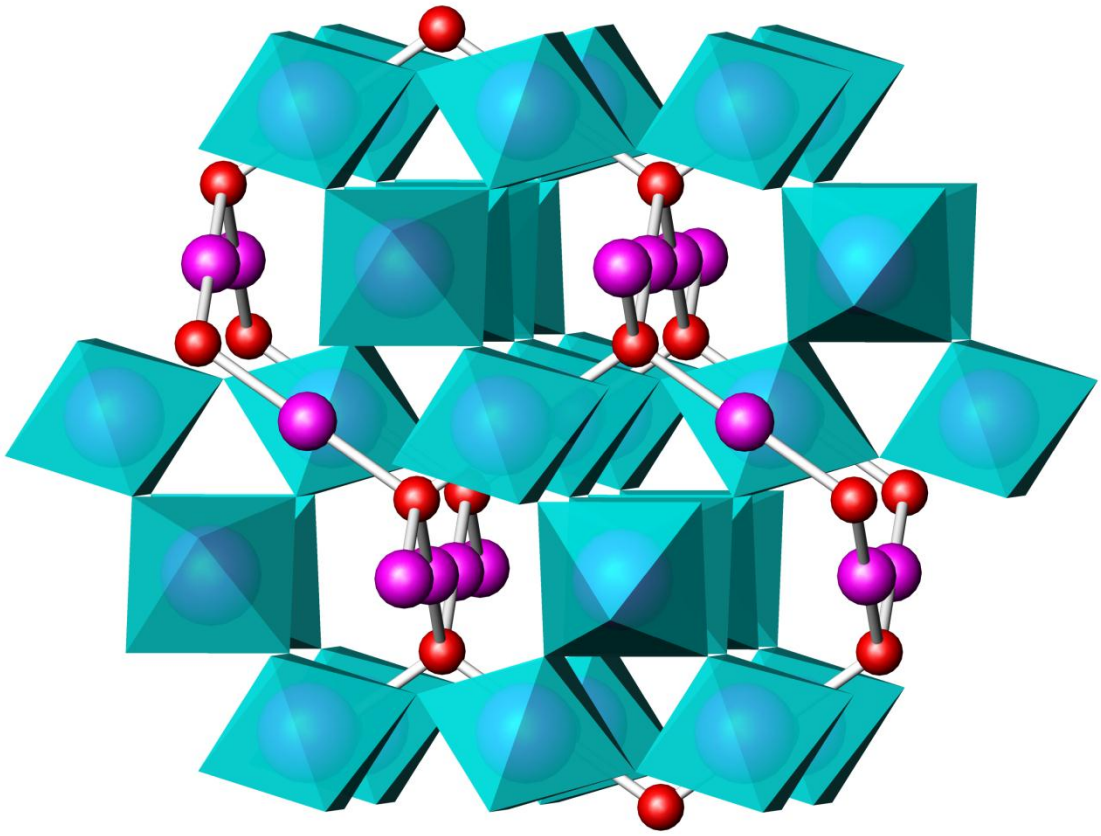

Figure 1.2 – The typical structural makeup of a $A_2B_2X_7$ pyrochlore showing the two interlinked structures of blue BO_6 octahedra and A_2O' frameworks (oxygens shown as red and A site cations in purple).

The cubic space group used in the structural determination of pyrochlores provides two possible crystallographic origins, both of which are commonly used in the literature to describe the structure. The first and most common setting places the crystallographic origin at $\bar{3}m$. This locates the smaller *B*-type cation at a 16*c* Wyckoff position (0,0,0) and the *X* type anion occupies the 48*f* site (x,⅛,⅛) forming an octahedral coordination, 4 + 2, around each *B* cation. The A_2X' network is then

described with the *A*-type cation on a 16*d* site (½,½,½) with a compressed AX_8 scalenohedral coordination environment and the *X*' on the 8*b* site (⅜,⅜,⅜) at the centre of the cavities formed within the BO_6 framework in a 4-fold coordination site. The crystallographic model used allows for only one variable positional parameter that of the *x* coordinate for the *X* atom and is summarised in Table 1.1. If $x > 0.3125$ the octahedra that these atoms makeup are compressed in the [111] direction and if $x < 0.3125$ the octahedra are elongated along the same vector.

Table 1.1 – Crystallographic positions of $A_2B_2X_6X'$ for origin choice 1

Origin choice 1 with the origin centred on the $\bar{3}m$ position					
Atom	Site	*x*	*y*	*z*	Occupancy
A	16*d*	0.5	0.5	0.5	1
B	16*c*	0	0	0	1
X	48*f*	*x*	0.125	0.125	1
X'	8*b*	0.375	0.375	0.375	1

The second available origin choice places it at $\bar{4}3m$ which is displaced by (-⅛,-⅛-,⅛) from the $\bar{3}$m centre. All of the atoms therefore retain the same multiplicity and Wyckoff positions with just the relative coordinates of each site changing, these positions are shown in Table 1.2.

Table 1.2 - Crystallographic positions of $A_2B_2X_6X'$ for origin choice 2

Origin choice 2 with the origin centred on the $\bar{4}3m$ position					
Atom	Site	*x*	*y*	*z*	Occupancy
A	16*d*	0.625	0.625	0.625	1
B	16*c*	0.125	0.125	0.125	1
X	48*f*	*x*	0	0	1
X'	8*b*	0.5	0.5	0.5	1

For ease of use and comparison all values in the remainder of this work have been altered to agree with origin choice 1 regardless of which origin was chosen in the original work, this is however by far the most common choice presented in the majority of the studied literature.

As well the ideal *alpha*-pyrochlore structure presented above defect structures of the series $A_{2-x}B_2X_6X'_{1-y}$ commonly exist with the end member of this series producing the *beta*-pyrochlore, with the general formula AB_2X_6. The *beta*-pyrochlore, shown graphically in Figure 1.3, maintains the same B_2X_6 network as the *alpha*-pyrochlore, but with half of the *A*-type cations and the *X*' anion being lost, thus destroying the A_2X' network. This leaves a single *A*-type cation per formula unit which shifts to the now unoccupied 8*b* (0.375, 0.375, 0.375) site. This site can often therefore accommodate larger *A* site cations than are typically seen in *alpha*-pyrochlore phases. The resulting crystallographic positions are summarised in Table 1.3.

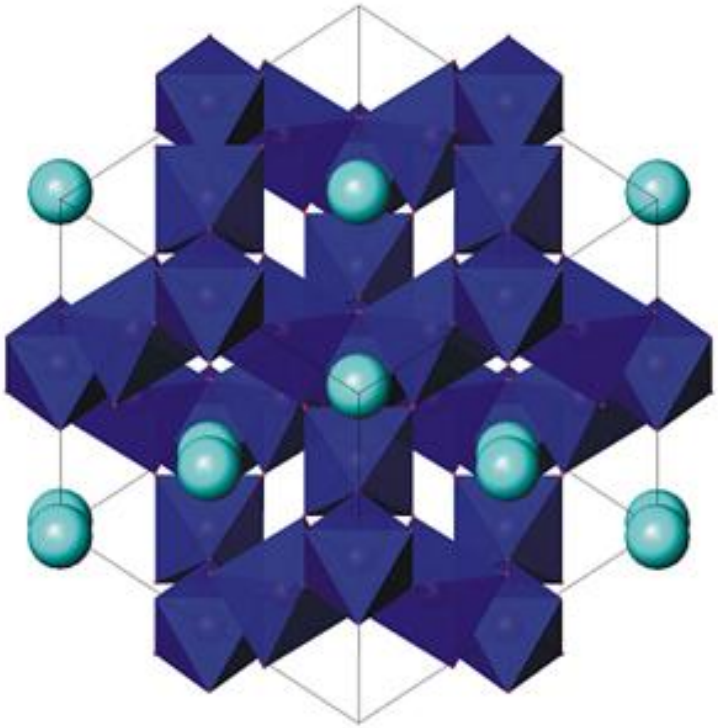

Figure 1.3 – An example of the standard beta-pyrochlore structure, general formula AB_2O_6, with A-type cations on the large 9-fold, 8b site previously occupied by the oxygen atoms in the pyrochlore phases.

Table 1.3 – The standard crystallographic positions for the beta-pyrochlore structure, AB_2X_6 using origin choice 1.

Atom	Site	*x*	*y*	*z*	Occupancy
A	8*b*	0.375	0.375	0.375	1
B	16*c*	0	0	0	1
X	48*f*	*x*	0.125	0.125	1

Other commonly seen defects in this structure type include systematic losses of oxygen from the A_2O' network such as in K_2GeTeO_6[27] without the accompanying cation loss and partial oxygen loss from the BO_6 network such as in $Pb_2Ir_2O_{6.5}$[28].

1.1.2 Structurally related phases

When studying the pyrochlore structure it is important to also look at related structure types. The simplest structural deviations lead, as described in Section 1.1.1 to retention of the pyrochlore structure with the displacement of cations within a similar overall framework. The pyrochlore structure itself can be described as an ordered superstructure with a lattice constant that is twice that of a fluorite type structure, with the general formula M_4O_8 (space group = $Fm\bar{3}m$ (225)). The fluorite structure type, Figure 1.4, has a face centred cubic arrangement of the cations with the anions occupying all tetrahedral interstices. The formation of the pyrochlore superstructure from this involves the ordering of the large *A*-type cations into a string of polyhedra along the (110) plane. The *B*-type cations in turn order in an analogous set of (110) rows, which can be viewed as alternating with the rows of *A*-type cations. It is this ordering that leads to the doubling of the unit cell dimensions and the resulting changes in symmetry.

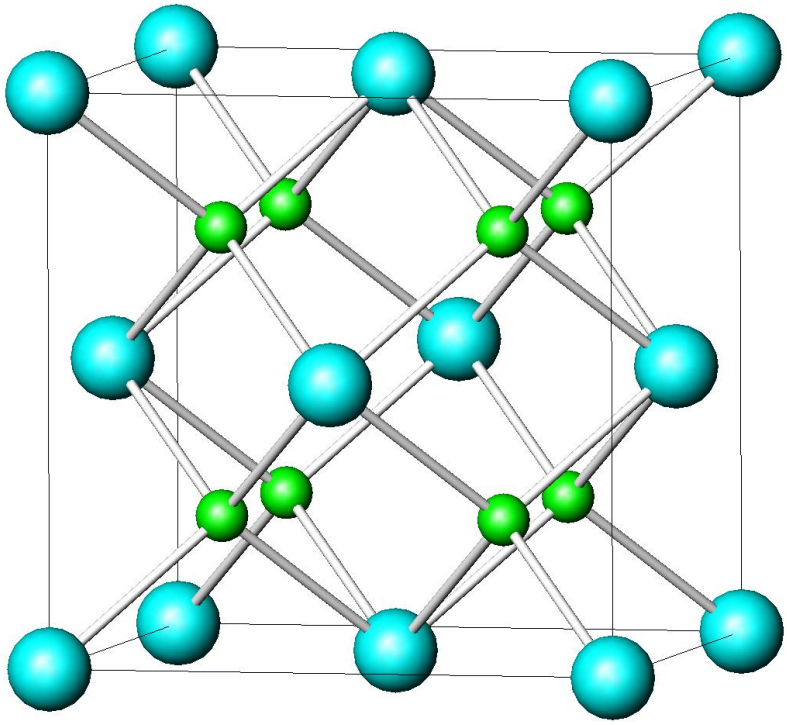

Figure 1.4 – The crystallographic structure of the mineral fluorite, CaF_2, calcium (blue) and fluorine (green) ions are shown on their appropriate sites.

The weberite crystal structure (space group = *Imma* (74)), Figure 1.5, is a further derivation of the fluorite type structure. It displays a typical stoichiometry of $A_2B_2X_7$, identical to that of the *alpha* pyrochlore. The structure itself is composed of a cationic sublattice similar to that of fluorite; a face centred cubic arrangement, whilst distortions in the anionic lattice lead to a different coordination environment for the *B*-type cations. The arrangement of the BX_6 framework leads in turn to two separately refineable *A*-type cation sites, one with a square pyramidal type coordination environment and the other within a bi-hexagonal pyramid type arrangement.

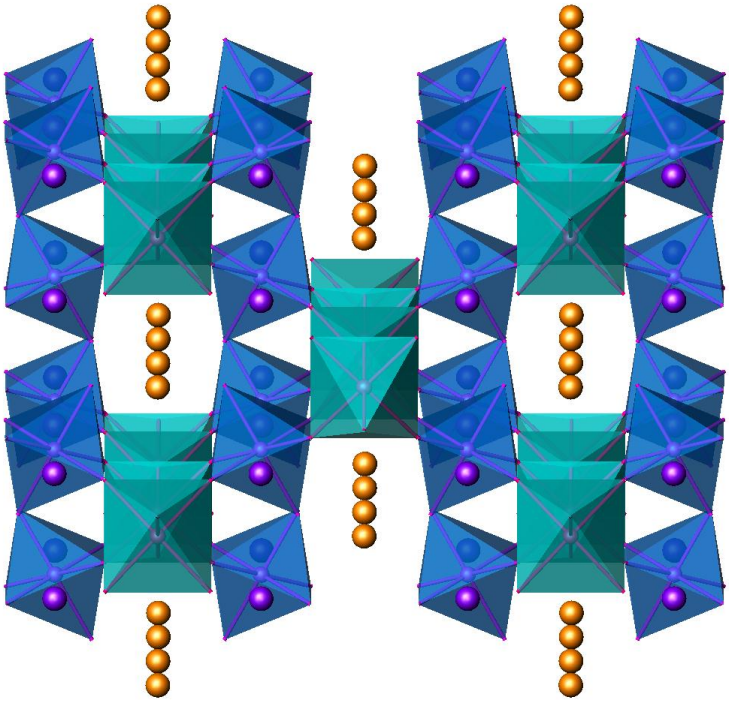

Figure 1.5 – The crystal structure of the naturally occurring mineral weberite, Na_2MgAlF_7. Light green polyhedra are that of MgF_6, and dark blue AlF_6. Sodium atoms are shown in both orange and purple depicting the two different crystallographic sites occupied within the structure.

1.1.3 Pyrochlores – Properties and applications

As previously discussed the pyrochlore structure is capable of accommodating a huge variety of elements and elemental compositions, with mixed occupancies and unusual stoichiometries commonly seen. A review of the pyrochlore system describing the wealth of materials adopting this structure and their properties was published by Subramanian and co-workers in 1983[29], further work by many researchers worldwide has expanded the range of known materials with several hundred phase compositions now well documented. The pyrochlore family of materials are predominantly cubic and ionic in nature, lending themselves to ionic substitution on all three available sites, *A*, *B* and *X*, providing that charge neutrality and ionic radius criteria are satisfied. The crystal structure also allows for vacancies on the *A* and *X* sites to occur, further enhancing the range of materials available. Pyrochlores have been shown to exhibit a wide range of physical properties arising from the variety of elements, and oxidation states, which can be accommodated. More recent attention in pyrochlore chemistry has focused particularly on the ferroelectric, magnetic and electronic properties of members of this family that contain transition elements on the *B*-site, primarily due to their potential applications.

The presence of this wide range of available electronic states has led to the identification of pyrochlores that cover the spectrum of electrical natures; from the highly insulating $Gd_2Ti_2O_7$[30], through semiconducting $CaNdNb_2O_7$[31] to the metallic behaviour of $Sm_2Mo_2O_7$[32]. Superconductivity has also been observed in pyrochlore phases, initially in the *alpha*-type phase $Cd_2Re_2O_7$[33]and more recently in the *beta*-series AOs_2O_6 (A = K, Rb and Cs)[34-36].

Magnetic properties are also prevalent in this class of materials. Within the pyrochlore framework there are three structural possibilities that give rise to a variety of magnetic properties; either the *A*-site or *B*-site are occupied by magnetic ions or both sites are occupied thus. The spatial arrangement of these sites leads to two independent networks of corner sharing polyhedra; with different metallic species potentially present on each one. It is relatively common for magnetic species to be hosted on both positions, the 16*d* and 16*c* sites, as in the material $Tb_2Ru_2O_7$. Whilst this material nominally contains two independent networks of magnetic nuclei, with

the Ru^{4+} and Tb^{3+} sublattices ordering at 110 and 3.5 K [37], the internal field of the Ru^{4+} network polarizes the Tb sublattice leading it to display a significant moment at 7 K.

Pyrochlores with magnetic ions on only the *A*-site have also attracted considerable attention in recent years, in particular the $A_2Ti_2O_7$ phases with lanthanides occupying the *A*-site[38] due to some unusual properties that arise from the resulting magnetic frustration and their potential applications in multiferroic devices[39]. The degree of distortion inherent to the pyrochlore framework, whilst still retaining cubic symmetry, leads to a 16*d* , *A*-site, that is coordinated to eight oxygen ions, six on 48*f* and two on 8*b* sites. In materials such as $Gd_2Ti_2O_7$ this leads to a puckered ring type conformation with two shorter and six longer Gd-O bond distances of 2.21 and 2.55Å respectively, unusual as they are amongst the shortest observed in any gadolinium/oxygen compound, with significant levels of structural distortion[30]. This ability to structurally distort whilst retaining the highly symmetric cubic system is key; utilizing both the long range magnetic phenomena and allowing the adaption of materials for application by altering the stoichiometric makeup.

Several phases, notably the ruthenates, $Ln_2Ru_2O_7$, have been investigated due to the magnetic frustration displayed by their structures[40-42].

Magnetoresistance has been observed in several phases, most notably in $Tl_2Mn_2O_7$ which displays colossal magnetoresistance (CMR)[43] of particular interest both as it was the first non-perovskite phase recorded as displaying this property and due to the process of magnetoresistance observed which differed from the conventional mechanism postulated at the time of its discovery[19]. These effects are of particular technological interest as they can be exploited for the sensitive detection of magnetic fields in magnetic memory devices, thus being used in hard drive reader heads. Whilst varying degrees of magnetoresistance have been observed in several pyrochlore phases, for instance in $A_2Mo_2O_7$ (*A* = Gd and Tb)[44] and $Lu_2V_2O_7$[45] the chemistry in this field, as with other metal oxides, is dominated by manganese containing materials. A number of these compounds have been identified and while substitution may be undertaken on both the *A* and *B*-sites the retention of manganese on the *B*-site is most commonly observed *i.e.* $Tl_2Mn_{2-x}Ru_xO_7$[46] and $Tl_{2-x}In_xMn_2O_7$[47].

Particular focus has been paid to the series $A_2B_2O_7$ (A = Dy or Ho and B = Ti or Sn) which have been shown to behave as spin-ices[48-50]. This term is used to describe materials which, by their atomic structure, allow non-zero residual entropy. These geometrically frustrated magnetic systems have been extensively studied to better understand this behaviour[51], with ongoing research continuing to identify new materials and increase the understanding of their origins[52]. Similar behaviour has previously been observed in fluoride analogues, for instance $CsNiCrF_6$, where low temperature powder neutron diffraction studies have shown a high degree of antiferromagnetic frustration resulting in a continuously disordered ground state. This results in a strong correlation between nearest-neighbour spins, but with no significant longer correlations, showing the material to be behaving as a spin-liquid[53].

Certain families of pyrochlores have been amongst the main areas investigated in recent years, with the ruthenates for example being widely studied due to both their technological importance, as electrode materials[54], catalysts[55] and components in thick film resistors[56], along with their unusual electronic properties[57,58]. The electronic properties are of interest since the ruthenium 4*d* electrons are on the borderline between localised and itinerant behaviour. For example the bismuth ruthenate, $Bi_2Ru_2O_7$ and the lead ruthenate $Pb_2Ru_2O_{6.5}$[57] are metallic Pauli paramagnets displaying a nearly temperature independent resistivity whereas the rare earth ruthenates $Ln_2Ru_2O_7$ (Ln = Pr-Lu) are all semiconducting with a spontaneous ruthenium atomic moment. Gradual changes in materials such as $Bi_{2-x}Y_xRu_2O_7$ where the end members are a metal and an insulator have been used to show how structural changes can be tailored to meet the desired applications[59]. $Tl_2Ru_2O_{7-y}$ is one example of a phase that displays a metallic-semiconductor transition, occurring at ~120K, with the exact temperature being dependent upon on the amount of oxygen vacancies controlled by the synthetic conditions employed[60].

Pyrochlores have also been of particular interest due to their wide range of applications arising from their varied properties. Some degree of control of these properties can often be exhibited, or at least strongly influenced, by parameters such the choice of cations, polarisabilty of these ions, electronic configuration and in certain applications the method of synthesis (*e.g.* control of particle size for catalytic activity or optical properties). Several pyrochlore materials have found uses in solid

state devices notably as high permittivity ceramics, thermistors, thick film resistors and switching elements.

Pyrochlores have long been used as a component of ceramic waste forms; primarily in the immobilisation of actinides, particularly plutonium, with Synroc[61] ('Synthetic rock') having been widely used commercially since the early 1970's. Wide ranging studies of a variety of metal oxide material types has identified the pyrochlore structure as amongst the most resistant to radiation induced amphorisation. Work in the last decade has looked more specifically at using pure pyrochlore materials as hosts for these radioactive nuclei, as opposed to the composites previously used. Primarily this interest has focused on titanate based pyrochlores due to their chemical stability[62-65], however this has shifted in recent years as these materials often undergo radiation induced transitions from the crystalline to aperiodic state due to radiation damage caused by the alpha decay of the hosted actinides. Ion beam irradiation experiments on zirconate pyrochlores have identified these materials as also undergoing a transition but rather than becoming amorphous remaining crystalline as a defect fluorite structure[66-68] significantly reducing the risk of leeching. In addition to this chemical stability coupled with desirable decay behaviour these pyrochlore structures have the added features of being acid stable[69] and as a natural product are known to be stable over a geological timeframe[70].

Other uses in the area of nuclear fuels have included the possibility of using zirconate pyrochlores in the production of inert matrix fuels, materials that do not include 'fertile' nuclides (^{238}U becomes ^{239}Pu by neutron capture and subsequent β-decay reactions) allowing the natural decay of fissile actinides to be safely utilized for further power production[67], a technique already being employed at ~40 nuclear reactors in Europe.

Several pyrochlores have been identified as potentially useful materials for the production of fuel cells. The ruthenium pyrochlores $A_2Ru_2O_7$ (A = Pb and Bi) have been suggested as cathode materials for solid oxide fuel cells. These materials display low cathodic over potential even at high operating temperatures, ~800 °C, high metallic electrical conductivity and no reaction with the yttria-stabilised zirconia often used in cells of this type[71]. Ongoing research into these phases has shown that the insertion of further A-type cations on to the ruthenium site, leading to

$A_2A_xRu_{2-x}O_7$, can significantly improve the level of observed oxygen reduction[72] and has led to testing of these materials for use in both liquid and gas fed fuel cells[73]. Other materials such as $Y_2Zr_{2-y}Ti_yO_7$ are being investigated as their highly disordered structures allow high levels of oxygen ion conduction[74], with mixed conducting electrodes such as this believed to better catalyze the redox reactions at the gas solid interface[75].

Within the last decade pyrochlores have also been studied in terms of thermal conduction, specifically in respect for their potential uses in turbines[76], as high-temperature catalyst supports[77] and in other applications where low-thermal-conductivity ceramics may be utilised[78]. Many processes can have their efficiencies significantly improved by elevating the temperature at which they occur, to increase the maximum operating temperature of high temperature alloys they may be coated in a ceramic layer several hundred microns thick protecting them from intense heat. At present the material of choice for such applications, known as thermal barrier coatings, is yttria-stabilized zirconia (typically $(Y_2O_3)_{0.08}(ZrO_2)_{0.92}$) which has a thermal conductivity of ~ 2-3 W mK^{-1} [79], several oxides and particularly some pyrochlore materials have emerged as leading candidates for a new generation of these ceramics. $Gd_2Zr_2O_7$ has been successfully grown as a barrier coating on a Ni-based superalloy using the well established bond coating method[80] and is one of several zironcates to be experimentally investigated for this application[81,82]. Current research in this field has focused on the effects of doping with a variety of lanthanides onto the *A*-site and with this series of materials having been identified by the NASA Ultra Efficient Engine Technology Project as likely to be heavily utilized in the near future[83].

Two lead based pyrochlores, $Pb_2Ru_2O_7$ and $Pb_2Ir_2O_7$, are amongst the materials that have been used in alkali zinc-air fuels cells (ZAFCs), one of the few successful commercial fuel cells[84]. Pyrochlores have shown potential applicability in this field as they can be tuned to provide an active surface and are self supporting, removing the issue of carbon-support oxidation associated with many other candidate materials[85]. Certain members of the ceria-zirconia family of phases have also been studied as promising oxygen storage materials for automotive catalysts[86].

The series $Ln_2Zr_2O_7$ (*Ln* = Sm, Eu and Gd) has been identified as a potential combustion catalyst for methane in gas-turbine power generation, lowering both the temperature of combustion and suppressing the formation of NO_x therefore increasing the efficiency of the process[87]. Once again the high level of thermal stability coupled with high thermal shock resistance of these materials lends itself to applications such as this, where small changes in the process can lead to significant commercial gains. The samarium form of this material has been identified as a leading candidate as a selective sol-gel synthetic route has enabled a stable material with an unusually high surface area to be synthesised increasing the level of activity achieved[88].

Bi_2NbInO_7 has been investigated due to its potential as a photo catalyst, displaying a considerably higher level of activity than the well known titanium dioxide photo catalyst[89]. Substitution of some of the indium present for a small quantity of iron has also been shown to further increase the level of activity with the energy band for all materials being sufficiently low for UV light[90]. Several other pyrochlore phases including $Ca_2Ta_2O_7$[91] and the distorted pyrochlore series Bi_2MTaO_7 (*M* = In, Ga and Fe)[92] have also been shown to have high levels of photocatalytic activity when the reaction conditions are tuned appropriately, with a co-catalyst of Pt (0.2% wt) being required for the highest level of H_2 production for the latter.

The properties and applications of pyrochlore materials are broadly captured within this section and paint a picture of a class of materials that are already widely used and have the potential for application in many fields. Whilst several significant areas where pyrochlores have been investigated are discussed here this is far from an comprehensive review as in virtually any area where solid state materials may find an application pyrochlores prove to be a candidate material.

1.2 Transition metals

The transition metals are classified as metals with partially filled *d* orbitals and are normally defined as including all elements in rows 4-6 and Groups 3-12, although those in Group 12, cadmium, mercury and zinc are often disputed as they exist with full valence electron shells, in the d^{10} state, in their metallic states. The maximum valence state available to each of these metals varies depending upon their position in the series, in general rising as we go across this series then falling again towards Group 12, as shown in Tables 1.4, 1.5 and 1.6.

Table 1.4 – This table shows the oxidation states formed in first row transition metal complexes. Those greyed out are less common and generally less energetically favourable.

	Sc	Ti	V	Cr	Mn	Fe	Co	Ni	Cu	Zn
d^0	III	IV	V	VI	VII					
d^1		III	IV	V	VI					
d^2		II	III	IV	V	VI				
d^3			II	III	IV	V				
d^4				II	III	IV				
d^5					II	III	IV			
d^6						II	III	IV		
d^7							II	III		
d^8								II	III	
d^9									II	
d^{10}									I	II

Table 1.5– This table shows the oxidation states formed in second row transition metal complexes. Those greyed out are less common and generally less energetically favourable.

	Y	Zr	Nb	Mo	Tc	Ru	Rh	Pd	Ag	Cd
d^0	III	IV	V	VI	VII	VIII				
d^1		III	IV	V	VI	VII				
d^2		II	III	IV	V	VI				
d^3			II	III	IV	V	VI			
d^4				II		IV	V			
d^5						III	IV			
d^6						II	III	IV		
d^7							II			
d^8							I	II	III	
d^9									II	II
d^{10}									I	

Table 1.6– This table shows the oxidation states formed in third row transition metal complexes. Those greyed out are less common and generally less energetically favourable.

	Lu	Hf	Ta	W	Re	Os	Ir	Pt	Au	Hg
d^0	III	IV	V	VI	VII	VIII				
d^1		III	IV	V	VI	VII				
d^2			III	IV	V	VI				
d^3			II	III	IV	V	VI			
d^4				II	III	IV	V			
d^5					II	III	IV			
d^6						II	III	IV		
d^7							II			
d^8							I	II	III	
d^9										
d^{10}									I	II

As can be seen the majority of transition metal elements can form more than one oxidation state, with some being far more commonly observed than others. The relative stabilities of each oxidation state vary widely as do the reasons for these variations. In general available oxidation states begin to rise as the row is crossed as more *d*-shell electrons are available to be removed, then decrease again as the outer electrons become more tightly bound. Several effects affect the relative stabilities of each oxidation state, primarily arising from the increasing shielding power of the extra nuclear electrons, the change in ionization potentials linked to this as more electrons are removed and the effective nuclear charge increasing along with atomic number. In general as we go down the three rows of transition metals the contribution from *d*-shell electrons is greater providing more shielding and a small increase in the amount of oxidation states available.

The ability of these elements to form a variety of oxidation states, coupled with their widely varying ionic radii, enables them to display a wide range of geometries *e.g.* octahedral, tetrahedral, square planar and square pyramidal depending upon the steric requirements and charge of the opposing anions. Thus, variety also leads to a high degree of adaptability for possible applications as systems may be tailored to requirement.

1.3 Structural considerations

1.3.1 Octahedral building units

The common feature in *alpha* and *beta*-pyrochlores is the retention of the BX_6 network in both structure types. The overall cubic symmetry of the pyrochlore structure allows for a limited distortion of these octahedra, occurring through a change in the *x* position of the anions on the BX_6 network. In order to retain the framework and overall cubic symmetry the bond lengths remain the same for all six of the metal anion bonds during any distortion. The distortion therefore occurs through a change in bonding angles within the polyhedra, away from the ideal 90° *X-B-X* angle. This in turn provides a small change to the size of the cavities available to the A_2X' network and in part leads to the ability of these materials to incorporate a wide range of cations.

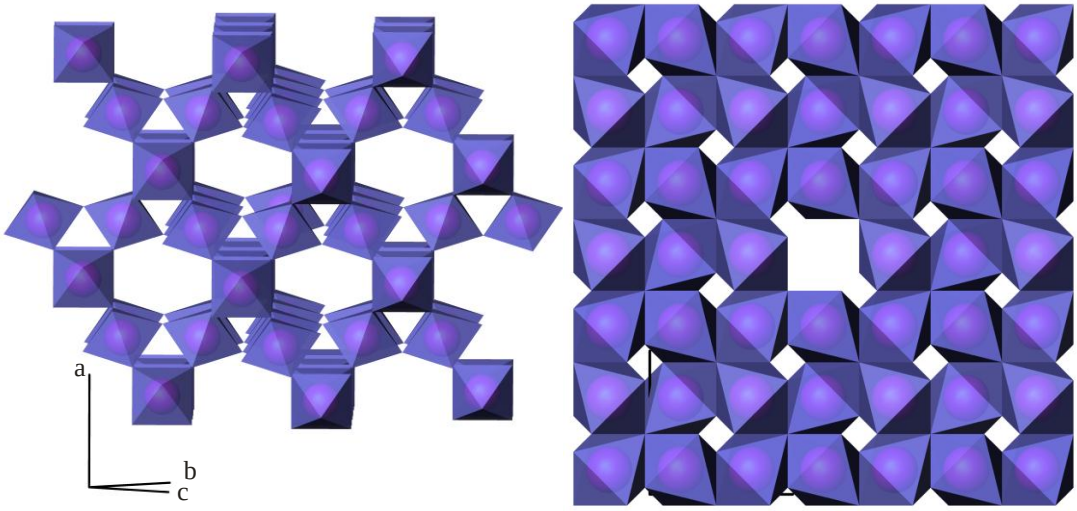

Figure 1.6 – Schematic of the BX_6 network. The left hand image is off axis looking in the [011] direction through the channels and the right hand image down the a-axis.

1.3.2 Jahn-Teller effects

There are two primary types of Jahn-Teller effects; the first of these arises from incomplete shells of degenerate electron orbitals, this includes both first order Jahn-Teller and pseudo Jahn-Teller effects. The second type arises from the interactions of filled and empty molecular orbitals that are close to one another in energy and are generally referred to as second order Jahn-Teller effects[93]. The contribution of these two types of effects vary significantly but in general terms those which are first order result in small, dynamic geometric distortions only, whereas second order effects can potentially produce significantly larger levels of structural distortion.

The *beta*-pyrochlores throughout this work are typically comprised of a BO_6 network with the metal centres in a d^0 electron configuration, thus first order effects have minimal bearing on this work. However, second order effects may be used to explain an anomaly seen throughout this work, that is that certain heavy elements are regularly seen to have larger than expected thermal motion. This effect is particularly notable in several of the niobium containing phases and is explained by the shifting of the heavy metal away from the centre of its polyhedra, however as this effect is different in every individual polyhedron there is no observable ordering and thus the density is spread across a range of sites and appears as an increase in thermal motion on the metal atoms. In reality the atoms are likely to be fixed onto a site closer to one of the surrounding cations; however, the techniques in this work coupled with the normally random occupation by either of the two potential *B*-site cations seen in *beta*-pyrochlores means we are unable to conclusively show this.

1.4 Alkali metals

The alkali metals are composed of the Group 1 elements, these elements are highly reactive metals with increasing reactivity down the group but retaining a closer similarity between the elements of this group than any other group in the periodic table. Whilst generally referred to as metals the Group 1 elements differ from the transition metals in several ways, specifically they have low densities and low enthalpies of melting and vaporization. In general they also show very weak metallic bonding as only one electron is available from each atom. The atomic radii of the alkali metals are considerably larger than their ionic radii due to the atoms containing only one electron in an *s* level which is comparably far from the nucleus in a new quantum shell. When it is then removed to form the ion the remaining electrons are much more closely bound to the nucleus, this coupled with the increased effective nuclear charge attracts the electrons to the nucleus and significantly decreases the size of the ion.

Table 1.7 – Information on the characteristics of the alkali metals used in this work.

	Atomic Number	Relative Atomic Mass	Melting Point/K	Density/kg m^{-3}	Atomic Radius/nm	Ionic Radius/nm
Lithium	3	6.94	453.7	534	0.152	0.068
Sodium	11	22.99	371.0	971	0.185	0.098
Potassium	19	39.10	336.8	862	0.227	0.133
Rubidium	37	85.47	312.2	1532	0.247	0.148
Caesium	55	132.91	301.6	1873	0.265	0.167

All the common compounds containing alkali metals form around the M^+ ion, although other unusual materials can form and are used in this work such as the alkali metal superoxide KO_2. The dominance of the +1 oxidation state is due to the first ionisation energy of these elements being low as the outermost electron is well shielded from the attraction of the nucleus by filled inner electron levels and so is relatively easy to remove and the second ionisation energy much higher due to being

much more difficult to remove as it is part of a full level and is also closer to the nucleus which now displays a higher effective charge.

Hydroxides of these metals form readily in air and are highly stable, however a wide range of other compounds are formed and are utilised here such as KF and KH. Care must therefore always be taken to ensure these materials are not exposed to air or water as they will hydrolyse and/or oxidise rapidly in air.

1.5 Superconductivity

In normal metals and alloys a linear decrease in resistivity with decreasing temperature is observed, theoretically tending towards zero resistance at 0 K for a pure metal. Electrical resistance of this sort arises from the interactions between lattice vibrations and the conduction of electrons as they pass through a structure. As the temperature decreases so to do the lattice vibrations, leading in turn to a weakening of the interactions with the conduction electrons and lower resistance.

In 1911 Onnes[94] showed that mercury underwent an abrupt transition to a state with an immeasurably small resistance below 4.2 K, clearly not displaying typical behaviour. Onnes described this as a superconducting state and the temperature at which the transition took place as the critical temperature, T_c. In materials that enter this superconducting state the electrons are believed to move through the lattice in a concerted motion with the lattice vibrations, resulting in no electron scattering and therefore zero resistance.

The superconducting transition is often very sharp in highly pure, crystalline samples with a width as low as 10^{-3} K, with the highest elemental T_c being seen in niobium at 9.2 K[95]. Significant amounts of research have been undertaken to look for alloys with higher T_cs than this and in 1972 Nb_3Ge was shown to have a T_c of 23 K, the first significant increase observed[96]. A further fourteen years passed without a higher transition being observed and much speculation with theoretical backing was proposed suggesting the highest T_c observed was close to the theoretical maximum.

Superconducting materials may be divided into two categories generally referred to as Type 1 and Type 2. Type 1 superconductors are generally metals and metalloids that show some degree of conductivity at room temperature, normally requiring extremely low temperatures to reduce molecular vibrations to a level where they no longer impede electron flow through the structure. This superconductivity is explained by the generally accepted BCS (Bardeen, Cooper and Schreiffer) theory[97,98] which suggests that electrons form 'Cooper pairs' enabling them to more readily overcome molecular obstacles facilitating the extremely low energy movement through the lattice, although the mechanism of the formation of these pairs remains unknown.

Typically Type 1 superconductors exhibit a very sharp transition to the superconducting state and are then diamagnetic, displaying a complete repulsion to applied magnetic fields. A large amount of metals show this property at very low temperatures including lead, lanthanum and tantalum.

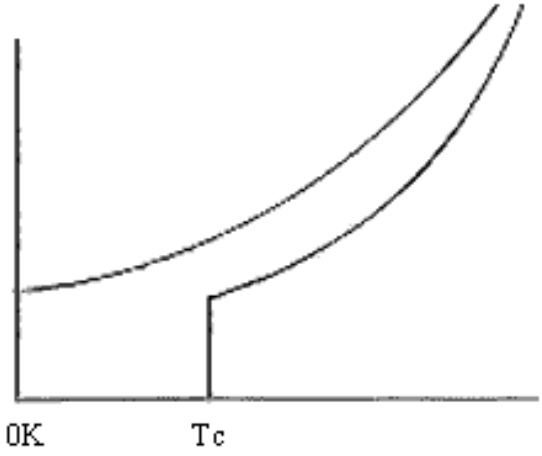

Figure 1.7 – A graph of temperature vs resistance. The upper line shows the classic behaviour of a non-superconducting metal, the lower line shows the rapid onset of superconduction normally observed in Type 1 superconductors.

In contrast the majority of Type 2 superconductors are compounds or alloys, the exceptions being vanadium, technetium and niobium which all display this type of superconductivity. Type 2 superconductors have been observed over a much larger range of temperatures, with temperatures as high as 371 K claimed in single crystals[99]. More commonly seen are the high temperature cuprates in which superconduction is observed in bulk samples above liquid nitrogen temperatures, examples of this are $Tl_2Ba_2CuO_{6+x}$[100] and $YBa_2Cu_3O_{6+x}$[101]. The mechanism of superconduction in these materials is very poorly understood, but there is general consensus that it is related to the planar layering within the structures. Unlike Type 1 superconductors exposure to a magnetic field allows some penetration into its surface leading to interesting magnetic fields around this boundary. The majority of known metal oxide superconductors are cuprates. Because of this superconductivity discovered in copper-less pyrochlore phases such as $Cd_2Re_2O_7$[102] and KOs_2O_6[36] have been of particular interest especially as they are non-planar in nature, unusually amongst the materials being studied.

1.6 Scope of this work

The principle aims of this work were based around furthering the range of known defect pyrochlores and improving our understanding of those already known. Synthetic routes utilized have been broad with both solid state methods and other more unusual routes undertaken to produce materials in the solid state. In general oxide pyrochlores were the focus of this study as they are most abundant, however materials with fluorine both as the sole anion and in mixed occupation with oxygen were also looked at, both for comparison with the behaviour of the oxides and as examples of how the range of materials can be expanded by anion substitution.

The primary experimental technique used in this work was that of powder diffraction, with the routine use of powder X-ray diffraction for phase identification and structural characterisation. Powder neutron diffraction was used for more advanced studies of materials where the technique proved advantageous or lower temperature studies, difficult to achieve with X-ray diffraction, were required. Other techniques including thermal gravimetric analysis, vibrating sample magnometry and infrared spectroscopy were also used where they could contribute important information to allow better understanding of the structure and properties of the materials studied.

1.7 References

(1) Liu, A. S.; Jones, R.; Liao, L.; Samara-Rubio, D.; Rubin, D.; Cohen, O.; Nicolaescu, R.; Paniccia, M. *Nature* **2004**, *427*, 615.

(2) Anderson, P. W. *Science* **1987**, *235*, 1196.

(3) Hoffmann, M. R.; Martin, S. T.; Choi, W. Y.; Bahnemann, D. W. *Chem. Rev.* **1995**, *95*, 69.

(4) Kharton, V. V.; Kovalevsky, A. V.; Viskup, A. P.; Shaula, A. L.; Figueiredo, F. M.; Naumovich, E. N.; Marques, F. M. B. *Solid State Ionics* **2003**, *160*, 247.

(5) Babel, S.; Kurniawan, T. A. *J. of Haz. Mat.* **2003**, *97*, 219.

(6) Junquera, J.; Ghosez, P. *Nature* **2003**, *422*, 506.

(7) Adams, R. *Focus on Pigments* **2007**, *2007*, 1.

(8) Schuth, F. *Chem. Mat.* **2001**, *13*, 3184.

(9) Sheng, Z. Z.; Hermann, A. M. *Nature* **1988**, *332*, 138.

(10) Kawazoe, H.; Yasukawa, M.; Hyodo, H.; Kurita, M.; Yanagi, H.; Hosono, H. *Nature* **1997**, *389*, 939.

(11) Goodenough, J. B. *Rep. Prog. Phys.* **2004**, *67*, 1915.

(12) Kim, S. H.; Lee, J. S.; Choi, H. C.; Lee, Y. H. *IEEE Elec. Dev. Lett.* **1999**, *20*, 113.

(13) Grice, J. D.; Gault, R. A.; Rowe, R.; Johnsen, O. *Can. Min.* **2006**, *44*, 1137.

(14) Aia, M. A.; Mooney, R. W.; Hoffman, C. W. W. *J. of the Elec. Soc.* **1963**, *110*, 1048.

(15) Ravez, J. *Comptes Rendus Acad. Sci. Ser. II C* **1999**, *2*, 415.

(16) Von Gaertner, H. *Min.Geol. Palaeontol.* **1930**, 1.

(17) Matsuhira, K.; Wakeshima, M.; Nakanishi, R.; Yamada, T.; Nakamura, A.; Kawano, W.; Takagi, S.; Hinatsu, Y. *J. of the Phys. Soc. of Japan* **2007**, *76*.

(18) Greedan, J. E.; Reimers, J. N.; Stager, C. V.; Penny, S. L. *Phys. Rev. B* **1991**, *43*, 5682.

(19) Subramanian, M. A.; Toby, B. H.; Ramirez, A. P.; Marshall, W. J.; Sleight, A. W.; Kwei, G. H. *Science* **1996**, *273*, 81.

(20) Yamaura, J. I.; Yonezawa, S.; Muraoka, Y.; Hiroi, Z. *J. of Solid State Chem.* **2006**, *179*, 336.

(21) Kolpakova, N. N.; Sinii, I. G.; Polomska, M.; Margraph, R. *Fizika Tverdogo Tela* **1982**, *24*, 1729.

(22) Tuller, H. L.; Moon, P. K. *Mater. Sci. Eng. B-Solid State Mater. Adv. Technol.* **1988**, *1*, 171.

(23) Mallat, T.; Baiker, A. *Chem.Rev.***2004**, *104*, 3037.

(24) Kawabata, S.; Yasui, Y.; Kobayashi, Y.; Sato, M. *J. of the Phys. Soc. of Japan* **2007**, *76*, 5.

(25) Grzechnik, A.; Posse, J. M.; Morgenroth, W.; Friese, K. *J. of Solid State Chem.* **2007**, *180*, 1998.

(26) Martinez-Lope, M. J.; Casais, M. T.; Alonso, J. A. *Z.Naturforsch.(B)* **2006**, *61*, 164.

(27) Amarilla, M.; Veiga, M. L.; Pico, C.; Gaitan, M.; Jerez, A. *Inorganic Chem.* **1989**, *28*, 1701.

(28) Kennedy, B. J. *J. of Solid State Chem.* **1996**, *123*, 14.

(29) Subramanian, M. A.; Aravamudan, G.; Rao, G. V. S. *Progress in Solid State Chemistry* **1983**, *15*, 55.

(30) Raju, N. P.; Dion, M.; Gingras, M. J. P.; Mason, T. E.; Greedan, J. E. *Phys. Rev. B* **1999**, *59*, 14489.

(31) Istomin, S. Y.; Dyachenko, O. G.; Antipov, E. V.; Svensson, G. *Mater. Res. Bull.* **1997**, *32*, 421.

(32) Taguchi, Y.; Tokura, Y. *Phys. Rev. B* **1999**, *60*, 10280.

(33) Sakai, H.; Yoshimura, K.; Ohno, H.; Kato, H.; Kambe, S.; Walstedt, R. E.; Matsuda, T. D.; Haga, Y. *J. of Physics-Condensed Matter* **2001**, *13*, L785.

(34) Yonezawa, S.; Muraoka, Y.; Matsushita, Y.; Hiroi, Z. *J. of the Phys. Soc. of Japan* **2004**, *73*, 819.

(35) Yonezawa, S.; Muraoka, Y.; Hiroi, Z. *J. of the Phys. Soc. of Japan* **2004**, *73*, 1655.

(36) Hiroi, Z.; Yonezawa, S.; Muraoka, Y. *J. of the Phys. Soc. of Japan* **2004**, *73*, 1651.

(37) Chang, L. J.; Prager, M.; Persson, J.; Walter, J.; Jansen, E.; Chen, Y. Y.; Gardner, J. S. *J. of Physics-Condensed Matter*, *22*, 5.

(38) Bramwell, S. T.; Field, M. N.; Harris, M. J.; Parkin, I. P. *J. of Physics-Condensed Matter* **2000**, *12*, 483.

(39) Dong, X. W.; Wang, K. F.; Luo, S. J.; Wan, J. G.; Liu, J. M. *J. Appl. Phys.* **2009**, *106*, 4.

(40) Dunsiger, S. R.; Kiefl, R. F.; Chow, K. H.; Gaulin, B. D.; Gingras, M. J. P.; Greedan, J. E.; Keren, A.; Kojima, K.; Luke, G. M.; MacFarlane, W. A.; Raju, N. P.; Sonier, J. E.; Uemura, Y. J.; Wu, W. D. *Phys. Rev. B* **1996**, *54*, 9019.

(41) Taira, N.; Wakeshima, M.; Hinatsu, Y. *J. of Physics-Con. Matter* **1999**, *11*, 6983.

(42) Taira, N.; Wakeshima, M.; Hinatsu, Y. *J. of Solid State Chem.* **1999**, *144*, 216.

(43) Shimakawa, Y.; Kubo, Y.; Manako, T. *Nature* **1996**, *379*, 53.

(44) Troyanchuk, I. O.; Kasper, N. V.; Khalyavin, D. D.; Szymczak, H.; Nabialek, A. *Phys. Status Solidi A-Appl. Res.* **1998**, *167*, 151.

(45) Zhou, H. D.; Choi, E. S.; Souza, J. A.; Lu, J.; Xin, Y.; Lumata, L. L.; Conner, B. S.; Balicas, L.; Brooks, J. S.; Neumeier, J. J.; Wiebe, C. R. *Phys. Rev. B, Condens, Matter Mater. Phys.* **2008**, *77*, 020411.

(46) Martinez, B.; Senis, R.; Fontcuberta, J.; Obradors, X.; Cheikh-Rouhou, W.; Strobel, P.; Bougerol-Chaillout, C.; Pernet, M. *Phys. Rev. Lett.* **1999**, *83*, 2022.

(47) Cheong, S. W.; Hwang, H. Y.; Batlogg, B.; Rupp, L. W. *Solid State Commun.* **1996**, *98*, 163.

(48) Harris, M. J.; Bramwell, S. T.; McMorrow, D. F.; Zeiske, T.; Godfrey, K. W. *Phys. Rev. Lett.* **1997**, *79*, 2554.

(49) Bramwell, S. T.; Gingras, M. J. P. *Science* **2001**, *294*, 1495.

(50) Ramirez, A. P.; Hayashi, A.; Cava, R. J.; Siddharthan, R.; Shastry, B. S. *Nature* **1999**, *399*, 333.

(51) Greedan, J. E. *J. Mater. Chem.* **2001**, *11*, 37.

(52) Morris, D. J. P.; Tennant, D. A.; Grigera, S. A.; Klemke, B.; Castelnovo, C.; Moessner, R.; Czternasty, C.; Meissner, M.; Rule, K. C.; Hoffmann, J. U.; Kiefer, K.; Gerischer, S.; Slobinsky, D.; Perry, R. S. *Science* **2009**, *326*, 411.

(53) Harris, M. J.; Zinkin, M. P.; Tun, Z.; Wanklyn, B. M.; Swainson, I. P. *Phys. Rev. Lett.* **1994**, *73*, 189.

(54) Esposito, V.; Traversa, E.; Wachsman, E. D. *J. of the Electrochemical Society* **2005**, *152*, A2300.

(55) Felthouse, T. R.; Fraundorf, P. B.; Friedman, R. M.; Schosser, C. L. *J. Catal.* **1991**, *127*, 421.

(56) Carcia, P. F.; Ferretti, A.; Suna, A. *J. Appl. Phys.* **1982**, *53*, 5282.

(57) Hsu, W. Y.; Kasowski, R. V.; Miller, T.; Chiang, T. C. *Appl. Phys. Lett.* **1988**, *52*, 792.

(58) Cox, P. A.; Goodenough, J. B.; Tavener, P. J.; Telles, D.; Egdell, R. G. *J. of Solid State Chem.* **1986**, *62*, 360.

(59) Kanno, R.; Takeda, Y.; Yamamoto, T.; Kawamoto, Y.; Yamamoto, O. *J. of Solid State Chem.* **1993**, *102*, 106.

(60) Takeda, T.; Nagata, M.; Kobayashi, H.; Kanno, R.; Kawamoto, Y.; Takano, M. *J. of Solid State Chem.* **1998**, *140*, 182.

(61) Ringwood, A. E.; Kesson, S. E.; Ware, N. G.; Hibberson, W.; Major, A. *Nature* **1979**, *278*, 219.

(62) Moller, T.; Clearfield, A.; Harjula, R. *Micro. and Meso. Mat.* **2002**, *54*, 187.

(63) Chen, J.; Lian, J.; Wang, L. M.; Ewing, R. C.; Boatner, L. A. *Appl. Phys. Lett.* **2001**, *79*, 1989.

(64) Fortner, J. A.; Kropf, A. J.; Finch, R. J.; Bakel, A. J.; Hash, M. C.; Chamberlain, D. B. *J. of Nuc. Mat.* **2002**, *304*, 56.

(65) Strachan, D. M.; Scheele, R. D.; Buck, E. C.; Icenhower, J. P.; Kozelisky, A. E.; Sell, R. L.; Elovich, R. J.; Buchmiller, W. C. *J. of Nuc. Mat.* **2005**, *345*, 109.

(66) Boccaccini, A. R.; Atiq, S.; Grimes, R. W. *Advanced Eng. Mat.* **2003**, *5*, 501.

(67) Lutique, S.; Staicu, D.; Konings, R. J. M.; Rondinella, V. V.; Somers, J.; Wiss, T. *J. of Nuc.Mats.* **2003**, *319*, 59.

(68) Wang, S. X.; Begg, B. D.; Wang, L. M.; Ewing, R. C.; Weber, W. J.; Kutty, K. V. G. *J. of Mat. Research* **1999**, *14*, 4470.

(69) Begg, B. D.; Hess, N. J.; Weber, W. J.; Devanathan, R.; Icenhower, J. P.; Thevuthasan, S.; McGrail, B. P. *J. of Nuc. Mats.* **2001**, *288*, 208.

(70) Ewing, R. C. *Canadian Mineralogist* **2001**, *39*, 697.

(71) Takeda, T.; Kanno, R.; Kawamoto, Y.; Takeda, Y.; Yamamoto, O. *J. of the Electrochemical Soc.* **2000**, *147*, 1730.

(72) Zhong, Z. M. *Electrochem. Solid State Lett.* **2006**, *9*, A215.

(73) Zen, J. M.; Manoharan, R.; Goodenough, J. B. *J. Appl. Electrochem.* **1992**, *22*, 140.

(74) Wuensch, B. J.; Eberman, K. W.; Heremans, C.; Ku, E. M.; Onnerud, P.; Yeo, E. M. E.; Haile, S. M.; Stalick, J. K.; Jorgensen, J. D. *Solid State Ionics* **2000**, *129*, 111.

(75) Tuller, H. L. *Solid State Ionics* **1992**, *52*, 135.

(76) Schelling, P. K.; Phillpot, S. R.; Grimes, R. W. *Philos. Mag. Lett.* **2004**, *84*, 127.

(77) Zwinkels, M. F. M.; Druesne, S.; Menon, P. G.; Bjornbom, E.; Jaras, S. G. *Ind. Eng. Chem. Res.* **1998**, *37*, 391.

(78) Wu, J.; Wei, X. Z.; Padture, N. P.; Klemens, P. G.; Gell, M.; Garcia, E.; Miranzo, P.; Osendi, M. I. *J. Am. Ceram. Soc.* **2002**, *85*, 3031.

(79) Bisson, J. F.; Fournier, D.; Poulain, M.; Lavigne, O.; Mevrel, R. *J. Am. Ceram. Soc.* **2000**, *83*, 1993.

(80) Maloney, M. J.; U.S., Ed. 2001; Vol. 6177200.

(81) Zhou, H. M.; Yi, D. Q.; Yu, Z. M.; Xiao, L. R. *Journal of Alloys and Compounds* **2007**, *438*, 217.

(82) Xia, D. L.; Liu, M. D.; Zeng, Y.; Li, C. R. *Mater. Sci. Eng. B-Solid State Mater. Adv. Technol.* **2001**, *87*, 160.

(83) Choi, S. R.; Bansal, N. P.; Zhu, D. M. In *Advances in Ceramic Coatings and Ceramic-Metal Systems*; Zhu, D., Plucknett, K., Eds.; Amer Ceramic Soc: Westerville, 2005; Vol. 26, p 11.

(84) Neburchilov, V.; Wang, H. J.; Martin, J. J.; Qu, W. *J. Power Sources*, *195*, 1271.

(85) Goodenough, J. B.; Manoharan, R.; Paranthaman, M. *J. of the American Chem. Soc.* **1990**, *112*, 2076.

(86) Sugiura, M. *Catal. Surv. Asia* **2003**, *7*, 77.

(87) Sohn, J. M.; Kim, M. R.; Woo, S. I. *Catal. Today* **2003**, *83*, 289.

(88) Sohn, J. M.; Woo, S. I. *Catal. Lett.* **2002**, *79*, 45.

(89) Tang, X. D.; Ye, H. Q.; Ma, C. X.; Liu, H. *Prog. Chem.* **2009**, *21*, 2100.

(90) Zou, Z. G.; Ye, J. H.; Arakawa, H. *J. Mol. Catal. A-Chem.* **2001**, *168*, 289.

(91) Ikeda, S.; Fubuki, M.; Takahara, Y. K.; Matsumura, M. *Appl. Catalysis a-General* **2006**, *300*, 186.

(92) Wang, J. H.; Zou, Z. G.; Ye, J. H. *J. of Phys. and Chem. of Solids* **2005**, *66*, 349.

(93) Pearson, R. G. *Proc. Natl. Acad. Sci. U. S. A.* **1975**, *72*, 2104.

(94) Onnes, H. K. *Leiden. Comm.* **1911**, *124C.*

(95) Xue, J.; Zhou, Q.; Suzuki, H.; Misawa, S. *J. Low Temp. Phys.* **2000**, *121*, 127.

(96) Cadieu, F. J.; Weaver, J. S. *Bull. of the American Phys. Soc.* **1973**, *18*, 704.

(97) Bardeen, J.; Cooper, L. N.; Schrieffer, J. R. *Physical Review* **1957**, *106*, 162.

(98) Bardeen, J.; Cooper, L. N.; Schrieffer, J. R. *Phys. Rev.* **1957**, *108*, 1175.

(99) Shabetnik, V. D.; Butuzov, S. Y.; Plaksii, V. I. *Pisma Zhurnal Tek. Fiz.* **1995**, *21*, 67.

(100) Iijima, S.; Ichihashi, T.; Shimakawa, Y.; Manako, T.; Kubo, Y. *Jpn. J. Appl. Phys. Part 2 - Lett.* **1988**, *27*, L1061.

(101) Wu, M. K.; Ashburn, J. R.; Torng, C. J.; Hor, P. H.; Meng, R. L.; Gao, L.; Huang, Z. J.; Wang, Y. Q.; Chu, C. W. *Phys. Rev. Lett.* **1987**, *58*, 908.

(102) Hanawa, M.; Muraoka, Y.; Tayama, T.; Sakakibara, T.; Yamaura, J.; Hiroi, Z. *Phys. Rev. Lett.* **2001**, *8718*.

Chapter Two

EXPERIMENTAL TECHNIQUES

2.1 Introduction

The work carried out in this thesis centred on the synthesis of materials in the solid state and a range of appropriate synthetic techniques were used to produce polycrystalline phases. Initial phase identification was carried out using in-house powder X-ray diffraction (PXRD) equipment with further data collection being carried out once suitable pure phase samples had been synthesised. Assignment of the relative contributions of phase components allowed structural characterisation to be carried out on a routine basis using these data. Where it was deemed beneficial and when possible powder neutron diffraction (PND) techniques were employed, the primary advantage of this being the ability to better locate lighter elements that would otherwise be obscured by heavier ones when studied with PXRD.

Other techniques were used to a lesser degree when deemed beneficial. Thermogravimetric analysis (TGA) was carried out on the hydrated phases being studied to ascertain exact water content and the resultant information used in refinements in conjunction with the diffraction data. Selected samples, primarily the superconducting osmate phases, were studied using a vibrating sample magnetometer (VSM) to provide magnetic data and to determine the point at which a phase became superconducting. On a select few phases infra red spectra were collected to confirm the presence or lack thereof of water within a particular phase. This chapter provides a summary of the synthetic and characterisation techniques used over the course of this work and their application to polycrystalline materials.

2.2 Synthetic methods

Reactions in the solid state normally have very high activation energies. As it is important that both thermodynamic and kinetic properties are taken into account, reasonably high temperatures are often necessary in order to achieve a reasonable rate of reaction. With polycrystalline materials the rate of reaction is also governed by the ion diffusion within the component lattices. Heating of the sample leads directly to an increase in the rate of diffusion but must be controlled and an appropriate degree of heating used to allow for the stability of both the decomposition products of the starting phases and the target material. When planning an experimental route it is therefore imperative to find a balance between the temperature and rate of reaction.

In this work several synthetic techniques were used to provide the appropriate conditions and achieve this balance.

2.2.1 Direct high temperature method

The initial components, usually oxides or carbonates, were ground thoroughly using agate pestles and mortars. Often a volatile organic solvent such as acetone was used to form a slurry and encourage thorough mixing. This grinding reduces the particle size of the starting materials, increasing their surface area which in turn provides a larger area for interfacial contact. The surface interactions can be further increased by pressing samples into pellets under high pressure. Dies of various sizes are used depending upon the size of the initial sample, appropriate pressures are then applied using a hydraulic press. Samples would then be sintered in a furnace using alumina crucibles to avoid contamination and phase identification undertaken using PXRD. Where required, samples were fired multiple times and were further ground and re-pelletised between each firing.

2.2.2 Citrate gel precursor route

In the synthesis of many phases the direct method, whilst producing the desired phase, does not enable pure samples to be produced or requires excessive reaction times to do so. To reduce the reaction timescale the citrate gel precursor route can be adopted as an alternative synthetic route. Precursors for this method can be generated by preparations or co-precipitation of metal ions using precipitating agents such as hydroxides, oxalates, carbonates or citrate ions.

The primary advantage of such methods is that they allow near molecular mixing of the precursors and provide a reactive environment during the subsequent heating cycles and their decomposition. This improvement in precursor mixing lowers the level of ion diffusion required to produce the target phase and thus can result in a reduction of both the reaction temperature and time required. When deciding whether such a route is viable the solubility of the starting materials must be assessed. The solubility must be high and the starting materials must be selected so that they do not react with one another in solution to form stable, undesirable by-products.

In this work the citrate gel precursor route was used to immobilise ions from relevant nitrated solutions to form an amalgam. For this method citric acid, ethylene glycol and a mixed solution of the nitrated starting materials in the desired stoichiometries were used. The citric acid was dissolved in ethylene glycol and water forming a viscous solution when heated and stirred. The solution of nitrates is then added and the resulting mixture boiled down until a gel formed. The gel was then further heated to form a resin which in turn was ground in a pestle and mortar before being fully decomposed at higher temperatures (~500°C). The final powder was then reground and pelletised before annealing at the temperature required to reach the target phase.

2.2.3 Controlled environment furnace reactions

A large proportion of the phases synthesised in this work required the control of the atmospheric environment to help determine the final stoichiometry, prevent contamination (most notably in this work for the production of pure, oxygen free fluoride phases) or ensure the desired oxidation state is retained. The simplest method of controlling the atmosphere is to anneal the sample under a flow of an appropriate gas, in this work generally oxygen or nitrogen. The antimonate compounds, presented in Chapter Three, for instance were synthesised under oxygen to ensure that the 5+ oxidation state of the starting materials was retained.

A further method used for the control of the environment is to seal the reactants in a silica tube under vacuum. This technique is particularly important when synthesising materials from volatile starting materials such as the osmate compounds discussed in Chapter Six. When using this technique it was vital that the starting materials are free from water or carbonates, as the presence of either can lead to a potentially dangerous pressure build up. When extremely high temperatures were required, up to ~1400°C, a small amount of argon is allowed to flow into the tube retaining the low pressure but stabilising the shape of the tube at higher temperatures where they are liable to soften and collapse.

2.2.4 Ion exchange reactions

Many target phases cannot be reached by high temperature routes, either due to kinetic instability of these phases or the very high stability of starting materials relative to the target phase. Ion exchange routes provide an alternative which is particularly effective in porous and semi porous materials and has been used widely in both industrial and academic environments[1,2].

There are several routes available in ion exchange; most commonly seen is the aqueous route. Where the ion exchanging phase is sensitive to hydration, such as in KOs_2O_6 where the partially hydrated phase has been shown to have different properties to its dry analogue[3], or the material being used as the ion source is insoluble in water, other solvents may be used. When solution based ion exchange proves ineffective or is undesirable a similar process may be carried out at higher temperatures. The main factor to be considered is the melting point of the ion source, leading to two conditions; either direct ion exchange between two intimately mixed solids or high temperature liquid ion exchange with the ion source acting as its own solvent. When considering which of these two routes is most appropriate several other factors must also be discussed; the relative stability of the ion exchanging phase, the possible decomposition point of the ion-source, the behaviour of the ion being removed and the probable material this will form on cooling.

All of these routes are based upon the principle of maintaining a high concentration gradient, ensuring that when an ion is lost from the starting phase it is likely to be replaced by the desired ion. This gradient can be maintained in several ways, commonly by regular substitution of the ion source to ensure a minimal amount of removed ion is present but also by trapping these ions. For instance crown ethers can be used to selectively trap alkali metal ions.

2.3 Powder diffraction

2.3.1 Diffraction theory

X-rays were first discovered in 1895 by Willhelm Röntgen. At roughly the same time the idea that crystalline solids are made of atoms arranged in regular repeating patterns, now known as lattices, first emerged. It was soon recognised that the wavelength of X-rays were of the same order of magnitude as the inter-atomic spacings (~10^{-10}m) of crystalline solids and that this property would lead to the diffraction of X-rays from these materials. X-ray diffraction (XRD) patterns were first collected in 1912 by Friedrich and Knipping[4], who recorded an interference pattern on photographic film. Since that time XRD has become an invaluable tool for the study of crystalline solids.

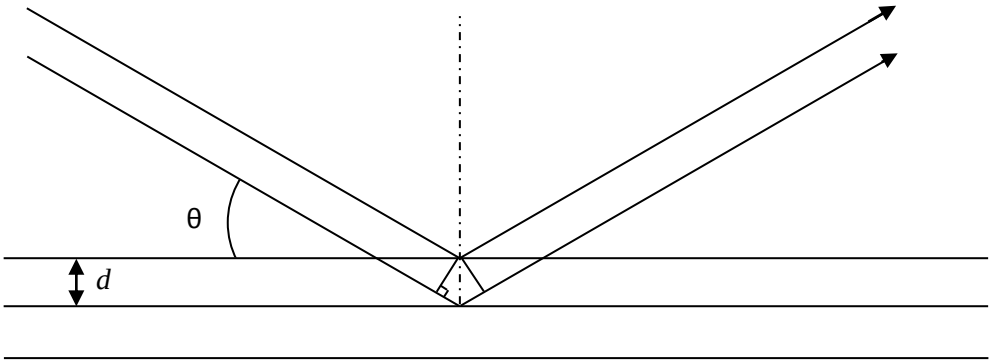

Figure 2.1. Schematic representing diffraction of X-rays from parallel planes of scattering centres.

Electromagnetic radiation, of which X-rays are a form, interacts with compounds by being scattered from its original vector. This can occur in two ways; if the energy remains unchanged the scattering is deemed to be elastic in nature whereas if the energy alters, thus changing frequency, the scattering is inelastic. Diffraction, both neutron and X-ray, are forms of elastic scattering. For a material to be studied in this way it must meet certain criteria: the compound must be crystalline in nature *i.e.* have repeating lattice spacings, the wavelength of the incident radiation must be of a similar order of magnitude to the lattice spacing under to study and the resulting scattering must be elastic and coherent in nature.

Diffraction may be explained by the application of Bragg's Law[5]. A crystal can be imagined as consisting of planes of atoms, which in turn can scatter X-rays. A typical example of this form of diffraction is shown in Figure 2.1 where two parallel X-ray beams with an angle of incidence θ and wavelength, λ, are diffracted by parallel planes of atoms separated by the distance, *d*.

To achieve constructive interference the path difference between the two waves must be an integral number of wavelengths, leading to the Bragg equation[6] and characteristic reflections for each possible value of *d*.;

$$n\lambda = 2d\sin\theta \ (n = 1,2,3.....)$$

The angle of incidence, θ, is referred to as the Bragg angle. When the beams are scattered from numerous planes, at any angle other than the Bragg angle, they destructively interfere with each other. This arises as the diffracted waves are out of phase with one another and therefore altogether cancel each other out. The interplanar separations can be calculated by measuring the positions of the diffraction maxima from the recorded pattern; the crystal structure can then be derived from these values by the identification of the planes involved.

The planes of the lattice are defined by their Miller indices, *h k l*, these represent the inverse values for positions where the planes intercept the *a*, *b* and *c* axes of the unit cell. The crystal should display diffraction from each of the lattice planes of the structure; however this often does not occur due to systematic absences arising in certain crystal systems and the presence of reflection planes reducing the intensity of maxima to a level where they cannot be observed.

The crystal system of the phase can be derived from the values of *d* that arise allowing identification of the Bravais lattice type (Table 2.1.1).

Table 2.1– Equations for d-spacings in the different crystal systems

Crystal System	Expression for d_{hkl}
Cubic	$\frac{1}{d_{hkl}^2} = \frac{h^2 + k^2 + l^2}{a^2}$
Tetragonal	$\frac{1}{d_{hkl}^2} = \frac{h^2 + k^2}{a^2} + \frac{l^2}{c^2}$
Orthorhombic	$\frac{1}{d_{hkl}^2} = \frac{h^2}{a^2} + \frac{k^2}{b^2} + \frac{l^2}{c^2}$
Hexagonal	$\frac{1}{d_{hkl}^2} = \frac{4}{3}\left(\frac{h^2 + hk + k^2}{a^2}\right) + \frac{l^2}{c^2}$
Monoclinic	$\frac{1}{d_{hkl}^2} = \frac{1}{\sin^2\beta}\left(\frac{h^2}{a^2} + \frac{k^2 \sin^2\beta}{b^2} + \frac{l^2}{c^2} - \frac{2hl\cos\beta}{ac}\right)$
Triclinic	$\frac{1}{d_{hkl}^2} = \frac{1}{V^2}[h^2b^2c^2\sin^2\alpha + k^2a^2c^2\sin^2\beta + l^2a^2b^2\sin^2\gamma + 2hkabc^2(cos\alpha cos\beta - cos\gamma) + 2kla^2bc(cos\beta cos\gamma - cos\alpha) + 2hlab^2c(cos\alpha cos\gamma - cos\beta)]$ where $V = abc(1 - cos^2\alpha - cos^2\beta - cos^2\gamma + 2cos\alpha cos\beta cos\gamma)^{\frac{1}{2}}$

2.3.2 X-ray radiation

X-rays are a type of electromagnetic radiation, the term normally being applied to wavelengths between 10 and 0.01 nanometres. Commonly this type of radiation is generated in the laboratory by bombarding a metal target with high energy electrons generated *in situ*. These electrons deccelerate as they enter the metal generating radiation across a continuous broad range of wavelengths. This is generally referred to as *Bremsstrahlung*[7] radiation. As well as the *Bremsstrahlung* radiation a series of sharp high intensity peaks are also observed within the same range of wavelengths. These peaks are generated by collisions of the incoming electrons with electrons in the core orbitals of the metal which generate high energy photons in the X-ray region. This is caused by an electron in a higher energy shell decaying to the vacant energy level generated by the collision, resulting in an excess of energy which is lost by the emittance of an X-ray photon. These X-rays are therefore of characteristic energies for each metal relating to the relative energies of the electron shells.

Each peak is assigned a symbol relating to the energy level that the ejected electron was lost from and the energy level that the decaying electron originates from. All powder X-ray diffraction data in this work was collected using copper $K_{\alpha 1}$ radiation arising from differing energy states in the *p* electrons. In the copper target used, vacant 1*s* orbitals are generated, the symbol K is used to denote the filling of vacant orbitals with the principle quantum number 1 *i.e.* 1*s*. In a copper target this can occur by the decay of electrons from either the 2*p* or 3*p* shells, thus the X-rays generated by L electrons decaying to the K shell, $2p \rightarrow 1s$, are called K_{α}, whilst those generated by the decay of M electrons to K, $3p \rightarrow 1s$, are termed K_{β}.

2.3.3 Powder X-ray diffraction

Since the realisation that the similarity between X-ray wavelength and interatomic separation led to diffraction and that collection of this data provided important structural information, PXRD has progressed to become a routine characterisation method. Early work, initially carried out by Laue[4], used a very simple system where a broad band of X-rays were passed through a single crystal and the resulting reflections collected using photographic films. The technique has since developed greatly and has been adapted to allow precise data to be collected on polycrystalline products, the common outcome of solid state reactions. This is of particular importance as it is often not possible to isolate single crystals of many phases. A strong understanding of the contributions of each atom type to the overall pattern allows three dimensional information to be calculated from two dimensional data sets. PXRD is a particularly useful technique as it is non-destructive, has simple sample preparation requirements and can be carried out as required in the laboratory.

2.4 PXRD Instrumentation

2.4.1 Siemens D5000 diffractometer

The majority of powder X-ray data was collected in-house on a Siemens D5000 diffractometer. This instrument uses the copper $K_{\alpha 1}$ radiation emissions at λ=1.5406 Å with a germanium single crystal used as the primary monochromator to filter out unwanted wavelengths, primarily the $K_{\alpha 2}$ band. The beam then passes through aperture slits (2 mm wide in a standard setup) to collimate the beam on the centre of the sample plate. The diffracted beam is then further collimated before hitting a standard scintillation detector.

Samples are ground thoroughly before analysis to reduce preferred orientation of the crystallites and to ensure as many crystal faces as possible are available for diffraction. The samples are then placed on an aluminium disc with a recess in the centre and flattened using a glass slide. The sample is then placed on the diffractometer as shown in Figure 2.2.

Throughout data collection the incident beam, sample and detector are retained in a Bragg Brentano geometry in which the incident beam and take off angle are fixed at a $\theta/2\theta$ relationship by rotation of the sample plate at half the rate of the detector across the entire angular range being studied.

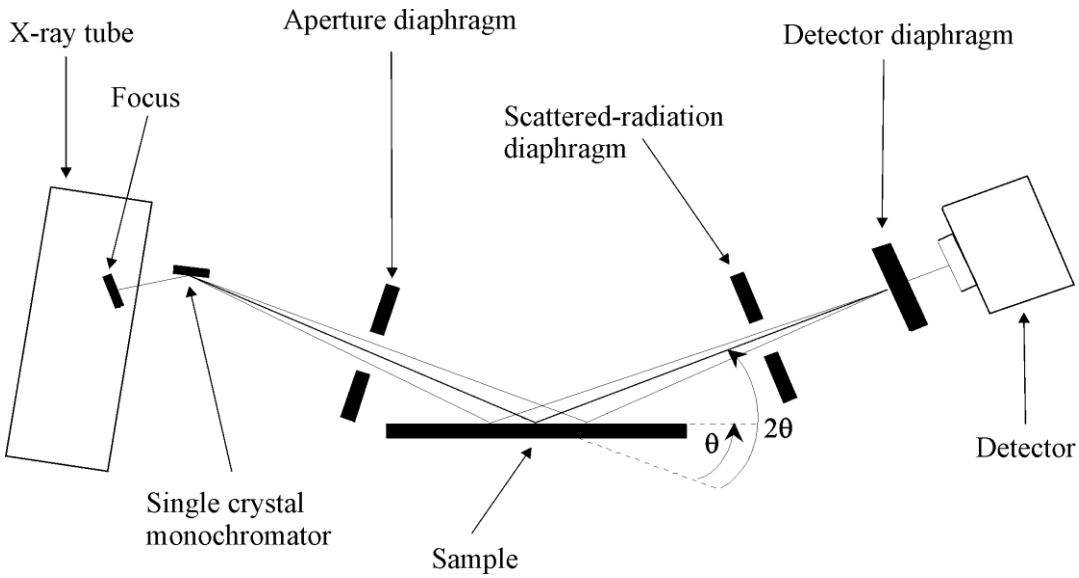

Figure 2.2 - A schematic of the Siemens D5000 diffractometer used for routine phase identification.

2.4.2 Bruker D8 powder diffractometer

Although the majority of data was collected on the Siemens D5000 a significant proportion was also collected on a second in-house diffractometer, a Bruker D8 Advance. This instrument was generally utilised when conditions other than the standard flat plate setup were required.

The instrument follows a θ - 2θ setup using monochromated copper $K_{\alpha 1}$ radiation as used on the Siemens D5000, but has different sample environments and detectors available. The Bruker D8 can be set up with three detector options that are easily interchanged; these are a standard point detector as on the Siemens D5000, a Position Sensitive Detector (PSD) and an energy sensitive SOL-EX™ detector.

The PSD allows simultaneous data collection over a 7-8° 2θ range greatly reducing the time required for a data set to be completed. This detector is comprised of an anode and a cathode separated by a work gas. An intense electric field is then applied at the anode. The diffracted X-rays ionise the argon detector gas with the electrons produced having sufficient energy to further ionise other argon atoms. This triggers a series of fast ionisations which in turn lead to an induced charge being carried to the cathode at a point perpendicular to the direction of the ionisations. The instrument is then able to determine the point of impact on the cathode and hence the initial point of ionisation. The detector itself is split into channels, each of which separately measures points of impact. These channels are then calibrated to known 2θ positions using a reference sample of α-quartz, allowing accurate peak intensities and positions to be collected over a wide 2θ range simultaneously. The primary disadvantage of this detector is a loss of resolution leading to peak broadening in the diffraction pattern.

The SOL-EX™ detector is primarily used to study materials containing first row transition metals such as cobalt or nickel. The copper radiation generated by the D5000 can interact with these transition metals leading to fluorescence, in turn resulting in a very high, noisy background which can obscure smaller peaks. The SOL-EX™ selects only the pure elastic scattering where the X-rays retain the same energy level, and therefore wavelength, thus removing the fluorescence from the powder pattern. The detector consists of a Si/Li semiconductor detector and a multi-spectrum analyser. This form of detector allows the direct conversion of X-rays to

an electrical signal which in turn is sent to the analyser. The analyser allows an energy window to be defined and only X-rays that lie within this window are then counted.

As well as supporting a standard sample stage the D8 diffractometer can also be fitted with a Paar HTK-1200 furnace stage, a water cooled sample chamber that can be ramped at any desired rate from room temperature to 1200°C. The sample is mounted on an alumina holder which is then inserted inside the sealable sample chamber. When the instrument is operating both the incident and diffracted X-ray beams pass through Kapton (a type of polyamide highly resistant to radiation damage) windows on either side of the sample mounting with data then being collected on any of the three detectors discussed earlier. The sealed chamber also allows some control over the sample environment as it can be placed under vacuum or have gas flowed through, further increasing the range of conditions available.

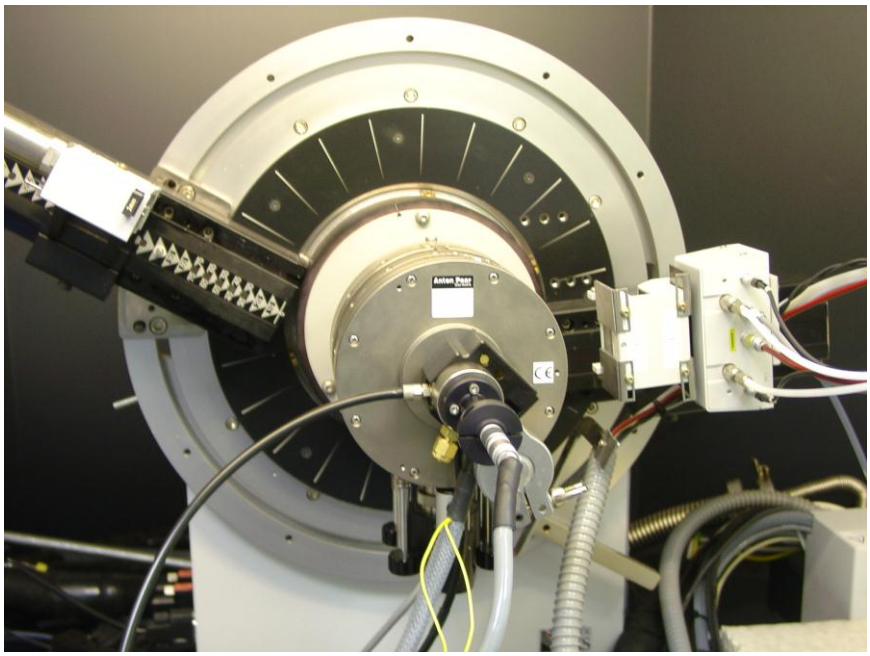

Figure 2.3 – The Bruker D8 setup with the HTK1200 furnace stage and position sensitive detector

2.4.3 Analysis of PXRD data

Typically routine data collections were carried between 10 and 60° 2θ with a step size of 0.02° 2θ and a total scan time of between 30 minutes and 1 hour. These PXRD patterns were assessed for phase purity through comparison with known materials using Bruker's EVA evaluation software coupled with the JCPDS Powder Diffraction File[8] allowing for direct identification of both the target phases and any impurities present.

Where structural data for comparison was not available lattice constants were calculated using the CELL computer software which uses an iterative least squares procedure to minimise the expression, *M:*

$$M = \sum_{n} W_n \, (\sin^2 \theta_n^{obs} - \sin^2 \theta_n^{calc})^2$$

where W_n is a weighting factor that lends greater statistical significance to the peaks at higher 2θ values.

The atomic positional parameters of the ideal pyrochlore presented in Chapter One were then used to provide a starting model for the lattice, usually proving sufficiently close to the final refined structure to be an acceptable starting point. Data for the final refinements were typically collected over a longer period and larger 2θ range, typically 16 hours between 10 and 110° 2θ to provide the suitable statistics for further data analysis.

2.4.4 Intensity calculations

The theory presented here allows the full calculation of a simulated diffraction pattern from an initial structural model *i.e.* cell parameters, atomic positions and symmetry elements. This is an essential element in any form of structural modelling where a full understanding of how the reflections are generated and where the various contributions arise from is required.

For any regular arrangement of atoms the structure factor, *F*, can be shown to be equal to the sum over all the atoms of a combination of the scattering amplitudes, *f*, and the phases, δ, of each atom leading, to the expression[9];

$$F = \sum_{j=1}^{N} f_j \, exp[i\delta_j]$$

In any unit cell the total phase shift of an atom, *j*, at a point from the origin (x_j, y_j, z_j) is the sum of the phase shift in each direction. The structure factor for each unit cell therefore can be expanded to give;

$$F_{hkl} = \sum_{j=1}^{N} f_j \, exp[2\pi i(hx_j + ky_j + lz_j)]$$

where *h*, *k* and *l* are the Miller indices that define the plane from which the reflection originates. For very small crystals the intensity of the scattered beam can be shown to be proportional to the square of the structure factor:

$$I_{hkl} = kL^2|F_{hkl}|^2$$

where *k* is the scaling constant and *L* is the Lorentz factor. The Lorentz factor is a geometric function of the method of data collection and thus the instrument used[9].

In real crystals several other factors can also be shown to affect the observed scattering intensities. Imperfections in a crystal, commonly taking the form of defects or substitutional disorder may cause local structural irregularities. Time dependent vibrations (*i.e.* thermal motion) of the atoms about their mean positions lead to the atoms being displaced from the idealised in-plane *hkl* position. This causes disruption to the in-phase scattering behaviour of their combined scattering. The correction to a structure factor reflected by a plane, *hkl*, takes the form[10]:

$$T_{hkl} = exp\left[-B_{hkl}\frac{sin^2\theta}{\lambda^2}\right]$$

where T_{hkl} represents the thermal motion correction and B is equal to $8\pi^2U$, where U is the root mean square thermal displacement, so that in turn the structure factor for a unit cell becomes:

$$F_{hkl} = \sum_{j=1}^{N} f_j n_j \, exp\left[-B_j\frac{sin^2\theta_j}{\lambda^2}\right] exp[2\pi i(hx_j + ky_j + lz_j)]$$

where n_j is the occupation factor of the j^{th} atom, equal to unity in a structure free from vacancies. This formula assumes that all thermal displacements are equal in directions whereas a more rigorous analysis describes the anisotropy of thermal motion in the form of a ellipsoid, yielding a more rigorous definition of T_{hkl}:

$$T_{hkl} = exp\left[-\frac{1}{4}\begin{pmatrix} B_{11}h^2a^{*2} + B_{22}k^2b^{*2} + B_{33}l^2c^{*2} \\ +2B_{12}hka^*b^* + 2B_{23}klb^*c^* + 2B_{13}hla^*c^* \end{pmatrix}\right]$$

There are a number of other expressions for T_{hkl} but the form given here is used to describe the anisotropic temperature factors presented in this work.

The final factor seen to affect the overall peak intensity is the multiplicity of an *hkl* reflection. In a given crystal system, for any particular *hkl* reflection, there are a number of equivalent planes diffracting at the same angle to give an enhanced intensity.

The theories summarised above allow the calculation of a simulated diffraction pattern from an initial structural model by incorporating cell parameters, atomic positions and the various symmetry elements. Section 2.6 provides a more precise description of the application of this theory in the analysis of diffraction data using the Rietveld method[11]. The basic theory, although developed for X-ray crystallography, may be applied to other types of radiation that are diffracted from a crystal lattice.

2.5 Powder Neutron Diffraction

2.5.1 Constant wavelength theory and the benefits of neutrons

In 1936 it was first recognised that neutron motion could be described in terms of waves and that they therefore could be used in diffraction experiments[12]. Neutrons are scattered predominately by the nucleus of the target molecules, which due to their small size in comparison to the neutron wavelength eliminates the scattering power drop off at higher angles that is observed in X-ray diffraction.

The theory and instrumentation setup involved are fundamentally similar to those used in PXRD as discussed in Sections 2.3 and 2.4

In contrast to X-rays, neutron scattering is not dependent upon ionic radii but instead relies upon potential scattering and resonant scattering, the values of which vary erratically often giving atoms next to each other vastly different scattering factors. This leads to atoms having vastly different neutron scattering abilities compared to X-ray diffraction which can in turn enable the accurate determination of lighter elements in the presence of heavier ones the contribution of which would dominate any PXRD data. In this work it is of particular relevance when looking at oxygen and the lighter alkali metals being studied as they prove hard to accurately locate using PXRD alone. Another benefit arising from this variation in scattering length is the ability to differentiate ordering on shared sites of elements near to one another in the periodic table, this is particularly notable for materials such as $KTaWO_6$ discussed in Chapters Three and Four, where the tantalum and tungsten are refined onto a shared site. X-ray data will always show the site to be randomly occupied as their similar electron density does not allow differentiation between the ion types, however the two metals have significantly different neutron scattering lengths[13], thus any ordering on this site would be observable in neutron powder data.

Once data had been collected Rietveld refinements were then carried out using the same software as used for X-ray data[10].

2.5.2 Instrumentation – Constant wavelength PND

All instruments used for constant wavelength PND were situated at the Institut Laue-Langevin, Grenoble, France. These neutrons are produced by a reactor generating in the region of 1.5×10^{15} neutrons per second per cm^2, with a thermal power of 58.3 MW when operating under normal conditions using a uranium source.

For all the data presented in this work the samples were loaded into vanadium cans and then mounted vertically in the required sample environments for data collection.

2.5.3 High intensity two-axis diffractometer D20

This instrument is situated within the reactor hall at the ILL providing an extremely high flux due to the proximity of the reactor. The instrument uses a large array position sensitive detector containing 1536 individual cells each covering 0.1° 2θ giving continuous coverage over 153.6° of 2θ. Each cell is filled with a mix of ^3He and CF_4 to provide a work gas for excitations to be picked up by the chromium anodes and cathode. The setup of the cells allow for very high count rates and a high level of efficiency.

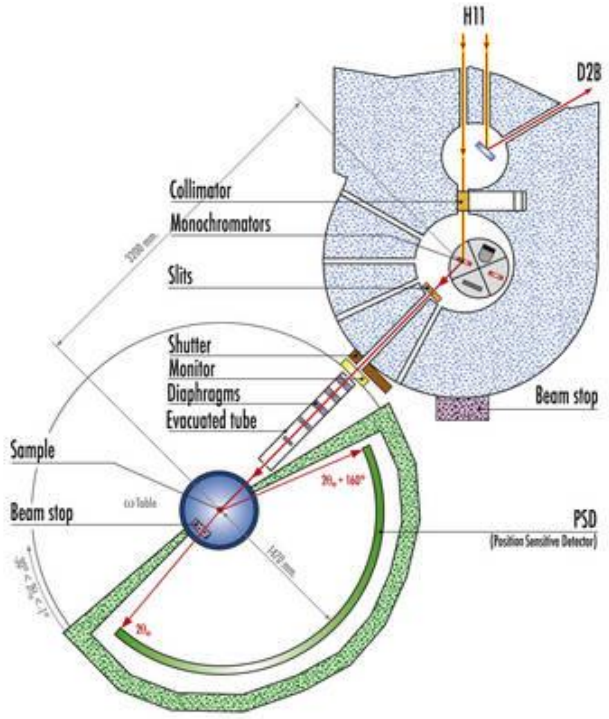

Figure 2.4 – Schematic of the setup of the High intensity two-axis diffractometer D20[14]

The instrument has several different takeoff angles and monochromators available providing a range of neutron wavelengths with the user being able to rapidly switch between these options to best adapt the diffraction conditions to suit the sample being studied. Collection times are typically short. For cubic systems times of less than 5 minutes are often sufficient, whilst for variable temperature runs data may be collected continuously as the temperature is ramped with data summed over the desired time period, greatly reducing the overall collection times when compared to other instruments.

2.5.4 High resolution two-axis diffractometer Super D2B

As for D20, Super D2B is situated inside the reactor hall of ILL and in fact shares the same guide tube as D20, so also has an extremely high available flux. The instrument is characterized by an unusually high takeoff angle of 135° providing an extremely high level of beam collimation, in turn leading to a high potential resolution. The instrument's 64 detectors cover a similar angular range to that of D20 but are separated by 2.5° 2θ from one another; data collection is therefore carried out stepwise over 100 steps of 0.025° 2θ typically taking about 30 minutes for a complete scan and being repeated as required.

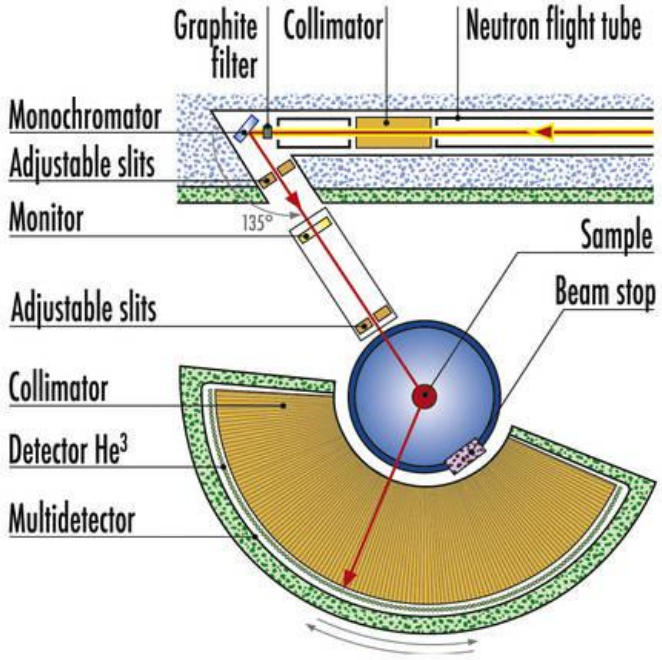

Figure 2.5 – Schematic of the setup of the high resolution two-axis diffractometer Super D2B[15]

Multiple wavelengths are also available on D2B by the computer controlled rotation of a single crystal germanium monochromator providing neutrons between 1.051 Å and 3.152 Å with the instrument flux optimized for 1.594 Å from the [335] plane.

D2B is a very high-resolution powder diffractometer designed to achieve the highest possible resolution, limited only by powder particle size, or to operate with a resolution similar to that available on D1A (discussed below) but with a far greater neutron beam intensity.

2.5.5 High resolution two axis diffractometer D1A

Unlike the two other ILL instruments discussed in this section D1A is situated outside of the main reactor hall, the primary advantage this provides is extremely high beam collimation with shorter wavelengths eliminated by the guide tube coupled with a high take off angle of 122° leading to high resolution at large scattering angles, up to 160° 2θ. The instrument provides excellent results with the Rietveld method owing to its near perfect Gaussian peak shape across the 2θ range 30° to 150° 2θ leading in turn to refinements with a significant number of varying structural parameters being feasible. Data is once again collected stepwise by 25 detectors typically with a step size of 0.05° 2θ, however due to the distance from the reactor beam intensity is considerably lower than for either of the other two instruments discussed, leading to typical data collection times of several hours.

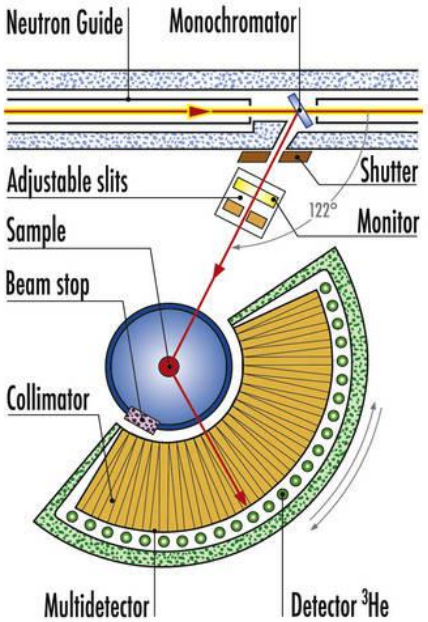

Figure 2.6 – Schematic of the setup of the high resolution two axis diffractometer D1A[16].

2.5.6 Time of flight powder neutron diffraction (TOF PND)

All TOF PND data was collected at the ISIS facility situated at the Rutherford Appleton Laboratory (RAL), Oxfordshire. The facility is a spallation neutron source which provides pulses of a range of neutrons covering the entire neutron spectrum. Fixed angle detectors are used allowing the separation of neutrons according to their time of flight and thus, over a fixed distance, their wavelength. This differs from constant wavelength experiments where the variables of the Bragg equation *d* and θ are at a fixed λ. For TOF experiments λ and *d* are the variables at fixed θ.

The relationship between time of flight and *d*-spacing is linear and can be derived from the combination of de Broglie's relationship and Bragg's law:

$$\lambda = \frac{h}{P_n} = \frac{h}{m_n v_n} = 2dsin\theta$$

where p_n, m_n and v_n are the momentum, mass and velocity of the neutron respectively, h is Planck's constant with d and sinθ being defined according to Bragg's law. Consideration of the two neutron flight paths involved, moderator to sample, L_1, and sample to detector, L_2, along with their corresponding flight times, t_1 and t_2, gives:

$$\frac{h}{m_n}.\left[\frac{t_1}{L_1} + \frac{t_2}{L_2}\right] = 2dsin\theta$$

Hence with an overall flight path, L, and time of flight, t, such that:

$$L = L_1 + L_2, t = t_1 + t_2$$

leads to:

$$t = 2dL\left(\frac{m_n}{h}\right)sin\theta$$

$$\therefore t \; \alpha \; d$$

Therefore for an instrument such as POLARIS where the overall flight path is 12 m, a 1 Å d-spacing reflection will be detected in the backscattering bank at a time of flight of ≈5000 μs.

2.5.7 POLARIS

POLARIS is a high intensity, medium resolution, time of flight powder neutron diffraction instrument. The high flux on POLARIS combined with a large detector solid angle provides a high count rate, along with relatively short data collection times. POLARIS receives a white beam of neutrons from the ambient temperature water moderator, with the sample 12.0 m from this moderator. The incident and transmitted neutron flux are constantly monitored to ensure a consistent applied flux can be used for each sample when required. The instrument uses 434 ^{3}He gas ZnS scintillation detectors arranged into four separate banks, at average angles of 14°, 35°, 90° and 145° relative to the incident beam. POLARIS is particularly suited for measuring extremely short *d*-spacings, as low as 0.3 Å being achievable, due to the epithermal neutrons available at a spallation source. This in turn provides a very wide *Q* range providing invaluable data to refinements particularly in relation to site occupancies and temperature factors, both factors of importance to this work.

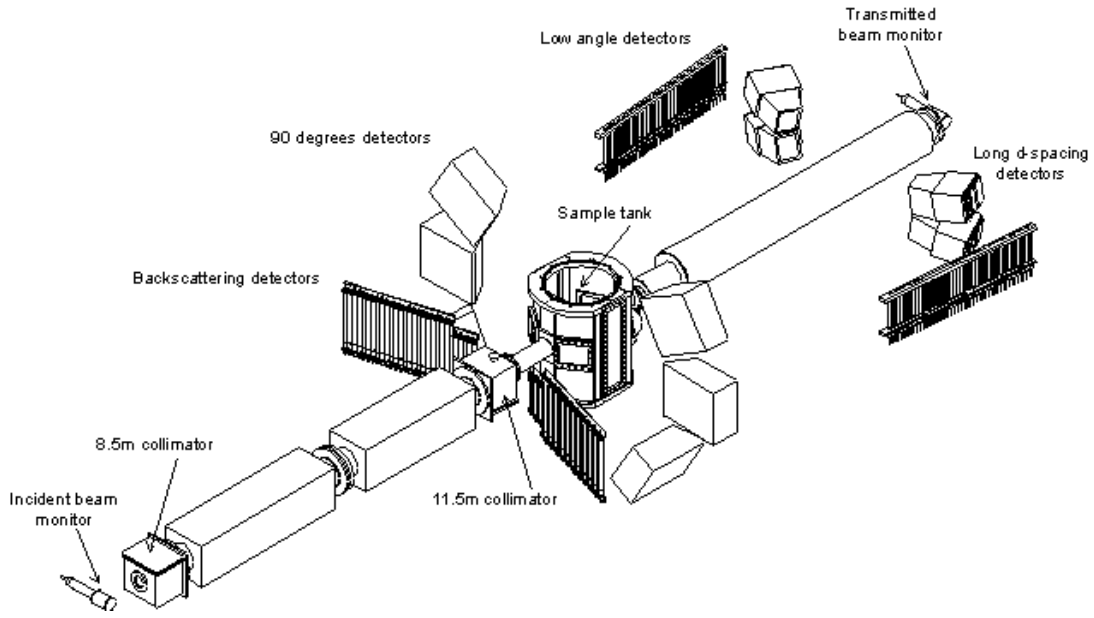

Figure 2.7 – Schematic of the POLARIS diffractometer[17].

2.5.8 Environmental control

A variety of environmental control systems are available at both the ILL (Grenoble, France) and ISIS (Oxfordshire, UK), as supplied by their respective sample environment teams. The primary use of these systems, within the scope of this work, was to access a wide range of temperatures. Three main systems were utilised; cryostats, cryofurnaces and furnaces. Each of these systems provides a different range of accessible temperatures generally in the region of 1.4 K to 300 K, 5 K to 500 K and 300 K to 1800 K respectively. In each case a vacuum is maintained within the apparatus throughout and a feedback loop is used to control the temperature as required, either at a fixed temperature or through a constant ramp with data being collected in either of these conditions depending upon the experiment being undertaken and the instrument being used.

2.6 Data handling

Although data is extracted in different ways for constant wavelength and TOF measurements a single technique can be used for interpretation of both types of data. In this work the Rietveld method is used throughout. Unlike single crystal data, where individual *hkl* reflections can be identified and intensities assigned this is not possible for a polycrystalline sample. Instead diffraction rings are observed from the randomly orientated crystals and a slice is taken through these rings to produce what is commonly referred to as diffraction pattern. Due to the nature of the techniques structure factor information often proves hard to determine as overlapping peaks are often observed thus restricting the amount of information that can be extracted.

2.6.1 The Rietveld Method

In 1967, H.M. Rietveld developed the idea that a least squares method could be used to fit an entire diffraction pattern[11,18]. Rietveld's theory centres on the realisation that although many of the individual reflections may overlap they could still be modelled using simple peak shape parameters to determine the total intensity and peak shape contribution of each overlapping reflection. Initially this method was only used for relatively simple crystal systems but with the advent of computers far more complex systems could be modelled with relative ease. The aim of the technique is to

minimise the difference between the observed data and the reflections generated from a simulated diffraction pattern.

The Rietveld method is one of structural refinement rather than structural determination and therefore is reliant upon a good starting model to be successful. Typically once diffraction data has been recorded scale factors and background parameters are introduced both of which are derived from coefficients of normal or orthogonal polynomials, providing a linear problem and thus rapid convergence regardless of the starting values used. Lattice parameters and zero point error are then refined to allow accurate positioning of the Bragg reflections over the recorded reflections of the powder pattern. Once these parameters have been refined peak shape parameters may also be introduced to improve the fit, typically these are modelled using a variety of Gaussian and Lorentzian functions, background coefficients may also be added at this point to account for asymmetry. Atom positions may then be varied to allow further improvement in the determination of peak shape and intensity. Finally thermal motion of the atoms is calculated by the variation of the isotropic temperature factors and peak shape is further refined. Additional background coefficients may also be added to account for asymmetry of the peak shape or observed sample broadening and where a high quality of data is available it may also be feasible to calculate anisotropic temperature factors at this point.

The quantity minimised at each stage of this least squares process is the function M which is calculated as shown below

$$M = \sum_i w_i \left(y_i^{obs} - y_i^{calc}\right)^2$$

w_i is a weighting factor given by $1/y_i^{obs}$, y_i^{obs} being the observed intensity for each data point i (this corresponding to 2θ values for constant wavelength and time for TOF) and y_i^{calc} is the calculated step intensity.

For powder X-ray diffraction data the calculated peak intensities, y_i^{calc}, are determined from the structural model by summing the calculated contributions from its neighbouring Bragg reflections (k) plus the background contribution as given in the formula:

$$y_i^{calc} = s\sum_k L_k\,|F_k|^2 \emptyset(2\theta_i - 2\theta_k)P_k A + y_{bi}$$

where s is the scale factor, L_k the Lorentz, polarisation and multiplicity factors, $\emptyset$ the reflection profile function, F_k the structure factor for the k^{th} Bragg reflection, P_k the preferred orientation function, A the absorption factor and y_{bi} the background intensity at the i^{th} step.

In an idealised system crystal orientation is entirely random, in turn leading to all reflections being equally likely. In real systems however this is not always the case. Preferred orientation is the tendency of crystallites, generally due to their morphology, to order in a particular way, leading to systematic distortions in the reflection intensities. This can be corrected for by the expression:

$$P_k = \{G_2 + (1 - G_2)exp[-G_1\alpha_k^2]\}$$

where G_1 and G_2 are refineable parameters and α_k is the angle between the presumed cylindrical symmetry axis and the preferred orientation axial direction.

Background functions are normally modelled using one of several available polynomial terms, most commonly a cosine Fourier series, to best match the background intensity of the recorded data.

The measured profile of a single diffraction peak depends upon several factors including; sample shape, crystallinity and the neutron spectral distribution. To model these peak shapes a pseudo-Voigt function is used, which provides a rough approximation for the Gaussian and Lorentzian components of the peaks. The overall contribution to a peak of integrated intensity I_k to the total counts y_i^{calc} at a point $2\theta_i$ is given by the expression:

$$y_{ik}^{calc} = \sum y_{ik} = \sum_k \alpha j_k L_k S_k^2 . \left[\frac{2\sqrt{In2}}{H_k\sqrt{\pi}}\right] exp\left[-4In2\left(\frac{2\theta_i - 2\theta_k}{H_k}\right)^2\right]$$

where α is a scaling factor, $S_k = F_k^2 + J_k^2$, the nuclear and magnetic contributions to the reflection, j_k is the reflection multiplicity (the number of degenerate equivalents), L_k the Lorentz correction, $2\theta_k$ the Bragg peak position and H_k is the full width half height of a Gaussian peak.

The sum for y_i^{calc} given here is for all reflections contributing to point *i* on the diffraction pattern. The formula given here applies strictly to PND data only with corrections being required for TOF PND and PXRD. The underlying principles however remain the same for all three methodologies.

The half width, H_k, of a Gaussian peak varies in relation to the scattering angle which can be modelled by the expression:

$$H_k^2 = Utan^2\theta_k + Vtan\theta_k + W$$

where *U, V* and *W* are refinement parameters and θ_k is the scattering angle. This formula also takes account of the peak broadening resulting from the particle size effect, which is turn can be extrapolated from the data to give an average particle size.

At low scattering angles peaks begin to show asymmetric characteristics due to finite slit width and sample heights, this results in a shift of the peak maxima to a lower than expected angle. The integrated peak area will however remain unchanged; a semi-empirical correction factor may therefore be applied to model this effect:

$$k' = 1 - sP\frac{(2\theta_l - 2\theta_k)^2}{tan\theta_k}$$

Where *P* is the asymmetry parameter and *s* = +1, 0 or -1 when $(2\theta_l - 2\theta_k)$ is positive, zero or negative respectively.

By the consideration of these factors and the adoption of them when required, to allow for the various crystal systems, theoretical diffraction patterns may be calculated for any crystalline material. Refinement of the various parameters allows full structural determination to be undertaken and theoretically any structural deviations to be modelled.

2.6.2 Criteria of fit

In refinements of this type a number of values are used to quantitatively determine the degree of agreement between the observed and calculated data. These criteria of fit are known as reliability factors or R-factors and are defined as $R_{profile}$, $R_{expected}$ and $R_{weighted\ profile}$. They are expressed as:

$$R_{profile} = R_p = 100\left[\frac{\sum_i \left|y_i^{obs} - y_i^{calc}\right|}{\sum_i y_i^{obs}}\right]$$

and

$$R_{expected} = R_{exp} = 100\left[\frac{(N - P + C)}{\sum_i \omega_i \left(y_i^{obs}\right)^2}\right]^{1/2}$$

where N is the number of observations, P is the number of refineable parameters and C the number of constraints. Thus it can be seen that R_{exp} is derived purely from statistical considerations of the refinement.

Of the three criteria of fit mentioned the final value, $R_{weighted\ profie}$, is the most meaningful as the residual that is being minimised is the numerator. Therefore it is the factor that best reflects the progress of a refinement and is given by:

$$R_{wp} = 100\left[\frac{\sum_i w_i\left(y_i^{obs} - y_i^{calc}\right)^2}{\sum_i w_i\left(y_i^{obs}\right)^2}\right]^{1/2}$$

The final criterion routinely used is the chi-squared parameter, defined as:

$$\chi^2 = \left[\frac{1}{N - P + C}\right]^2 \sum_i w_i \left|y_i^{obs} - y_i^{calc}\right|^2 = \left[\frac{R_{wp}}{R_{exp}}\right]^2$$

which is normally minimised during the course of a refinement. For a good fit the R_{wp} should therefore approach the R_{exp} leading to an 'ideal' value of 1 for chi-squared.

As well as using statistical measures of fit the goodness of fit can be estimated visually by examining a plot of the difference line as extracted from the observed and calculated intensities. The plot should be flat as possible, with noise levels being acceptable once they reach the level of experimental error.

All analysis of diffraction data was carried out using the Generalised Structural Analysis Suite (GSAS) of Von Dreele and Larson[10,19] , which is built around the Rietveld method discussed here and aims to minimise the difference between the observed and calculated profiles as described in this section. For the majority of refinements this was coupled with the graphical interface EXPGUI[15] of Toby to allow for more rapid refinements.

2.6.3 Neutron diffraction data handling

PND data provide several advantages over X-ray data. Primarily this arises from the difference in interactions that cause scattering. For PND the scattering length is related to the size and structure of the nucleus as opposed to the number of electrons present. Neutron diffraction experiments are therefore not affected by a form factor as PXRD experiments are and thus there is no drop off of peak intensity arising from increased scattering angles. This allows the collection and interpretation of data over a much wider angular range, yielding considerably more information at higher angles along with more refineable reflections. Preferred orientation effects are also significantly reduced as a result of the sample mounting, samples being placed in cylindrical vanadium cans as opposed to the flat plate setup used in PXRD where the sample must lie flush and is therefore mechanically flattened to achieve this.

TOF data in particular requires handling in a different manner. The TOF data is initially converted to *d*-spacing values before a *d*-spacing dependent absorption correction is applied. The peak shape for data of this type is also more complex often requiring Gaussian, Lorentzian and exponential expressions as opposed to the mainly Gaussian expression used to fit single wavelength neutron data.

2.7 Vibrating Sample Magnometry (VSM)

Magnetic and superconductivity data was collected on a Oxford Instruments 3001 Vibrating Sample Magnometer (VSM) with a 12 T superconducting magnet. The material under investigation was mounted on the end of a carbon fibre rod using Teflon tape and inserted into an Oxford Instruments CF1200 continuous flow Helium Cryostat with the bottom of the cryostat lying inside the NbSn superconducting magnet. The sample is vibrated at a constant frequency of 66 Hz with a magnitude of approximately 1.5 mm. Two pickup coils, placed above and below the sample, experience a change of the magnetic flux due to the motion of the sample and an electro magnetic field (EMF) is therefore induced in the two pickup coils. The induced EMF, which is also proportional to the magnetic susceptibility of the sample, passes through a two-stage amplification process and is monitored by the VSM electronics before being recorded on a computer. The sample temperature is measured by a AuFe/Chromel thermocouple in direct contact with a copper heat exchanger situated below the sample. Although a field of up to 12 T was available for measurements a much smaller field, routinely 0.1 T , was deemed appropriate for most of the materials studied.

The collected data reveals the presence of any magnetic behaviour in the material *e.g.* paramagnetism, ferromagnetism, superconductivity or antiferromagnetism.

In this work magnetic data was primarily used to determine the superconducting transition temperatures of materials, T_c.

2.8 Thermogravimetric analysis

Throughout this work samples have been studied using a Polymer Laboratories PL-STA 1500 simultaneous thermal analysis system. This instrument allows concurrent thermogravimetric analysis (TGA) and differential thermal analysis (DTA).

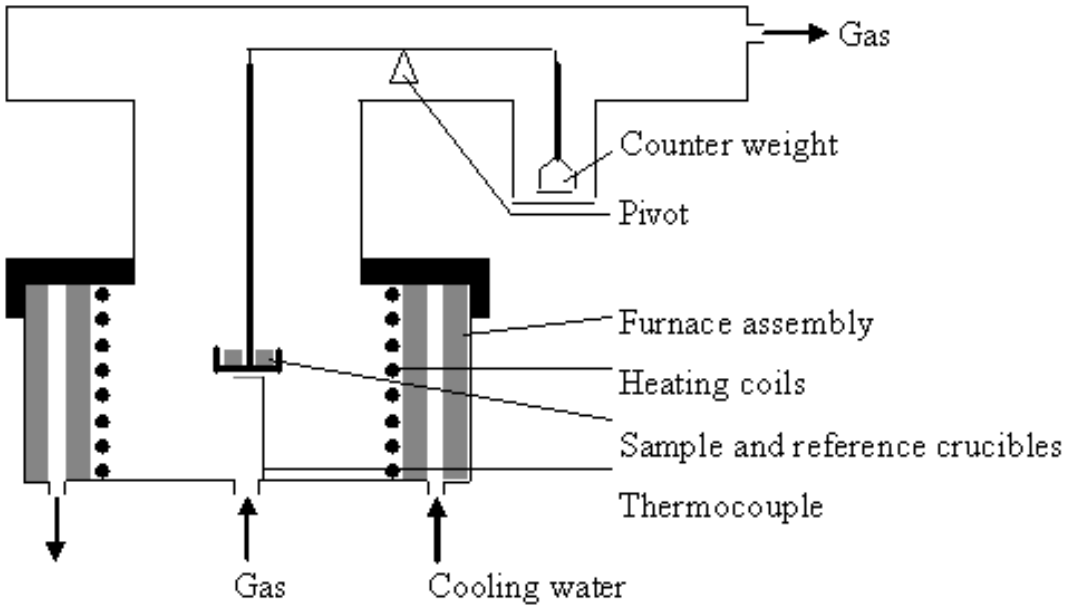

Figure 2.8 – A schematic of the PL-STA 1500 apparatus as used in this work.

TGA is a theoretically simple technique where the mass of the sample is recorded as a function of temperature or time. The sample is heated at a set heating rate, between 1 to 50 °C per minute, under a controlled atmosphere and the mass loss recorded. The collected data can then be interpreted, in this work it has typically been used to study water content within the pyrochlore framework and oxygen content by reduction of the sample to the component metals under a hydrogen atmosphere.

DTA centres on the comparative temperature changes between the sample being studied and a reference sample, typically alumina, both of which should be of approximately the same mass. The temperature change for the two materials should be identical until a thermal event occurs, as the alumina undergoes no changes across the studied temperature range and thus acts as a fixed baseline. Examples of thermal events can include; melting, dehydration, structural changes and the loss of component groups. The DTA plot, temperature vs. relative energy change, can show

the nature of these events, if the sample temperature increases faster than that of the reference the event is exothermic and if the rate is slower it is endothermic in nature. Data is often also collected whilst the samples are left to cool, this can be used to show if changes, particularly structural changes, are reversible.

For a typical data collection 15-20 mg of sample is heated from room temperature to 1000°C at 10°C per minute under dry air with data points collected every 2 seconds. The data was then saved at the end of the collection and exported for further analysis.

2.9 Infra-red spectroscopy

Bonds in solids typically vibrate at frequencies of around 10^{12} to 10^{13} Hz. The adsorption of infra-red radiation at the appropriate frequencies can then excite these vibrational modes to higher energy levels. Infra-red spectra display plots of absorption intensity as a function of frequency. The frequency of the incident radiation is therefore varied and the amount of radiation after interaction with the sample recorded. The resulting spectrum is composed of a variety of peaks each of which represents a particular vibrational mode, these peaks can then be compared to other known samples to allow us to assign their origins.

The IR spectra used in this work were collected on a Perkin-Elmer Spectrum One Fourier-Transform Infra-red Spectrometer (FT-IR) using powdered samples in reflection mode.

2.10 Electron Microscopy

Electron microscopy is a powerful analytical technique with a variety of uses, most notably electron diffraction and imaging. In this work scanning electron microscopy was used to a limited extent for imaging and the study of morphology and energy dispersive X-ray spectroscopy (EDX) was used to study the composition of samples.

Electrons are generated from thermionic emission and then accelerated through a potential to create a monochromatic beam of electrons. The wavelength can be controlled by altering the voltage as given in the equation below.

$$\lambda = \left[\frac{1.5}{(V + 10^{-6}V^2)}\right]^{1/2}$$

where λ is the wavelength in nm and V is the potential difference.

These electrons may then interact with a surface, doing so either elastically, where the scattered electrons retain the same energy as the incident electrons, or inelastically, where the energy of the scattered electron is changed. Inelastic scattering can yield different types of interaction products: X-rays, backscattered electrons, secondary electrons and Auger electrons. The secondary electrons

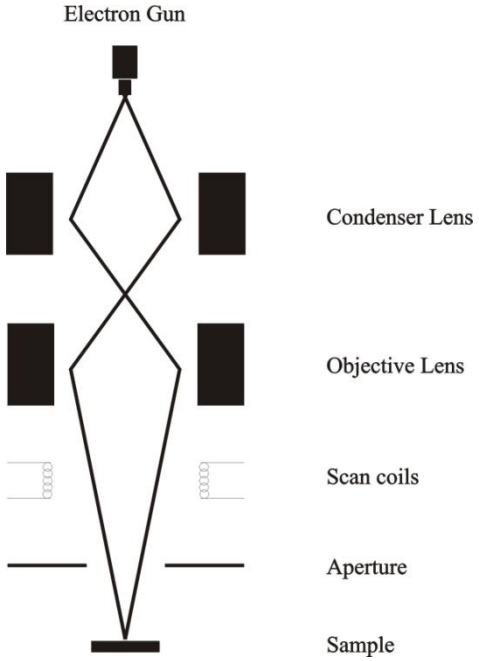

Figure 2.9 Schematic of the JEOL JSM 5910 Scanning Electron Microscope

escaping from the sample typically have energies below 50 eV, depending upon the setup of the specific instrument and can be used for imaging. Backscattered electrons retain a large amount of the incident energy and can also be used for imaging or in electron diffraction.

Auger electrons and X-rays are generated when an inner shell electron is ejected by the primary beam leaving the sample in an excited state, it will then relax back to a ground state by dropping an outer shell electron to the core level, with the ejection of either an Auger electron or an X-ray photon accompanying this process. Both sets of emissions are characteristic for each atom type and can therefore be used to study the elemental composition by energy dispersive X-ray spectroscopy (EDX) or Auger electron spectroscopy (AES).

All experiments in this work were carried out on a JEOL JSM 5910 Scanning Electron Microscope, fitted with an Oxford Instruments Inca Energy 300 Energy-Dispersive X-ray Spectrometry analysis system. Samples were mounted on aluminium stubs using carbon tape before being coated with a further thin layer of carbon, ~5-10nm, and placed under vacuum within the SEM chamber. The electron beam is then focused onto the sample by a series of electromagnetic lenses and scanned across the sample with a detector counting the secondary electrons generated as this occurs. From this an image can be built up which is then utilised to locate a suitable sample for EDX analysis. Initially the EDX detector is calibrated using a cobalt sample to ensure accurate energy levels are recorded, a measurement is then run on the desired sample and a spectrum generated with a computer then being used to interpret the data. It is then possible to assign each line on the spectrum to an element and by observing the relative intensities calculate the percentage of each element present in the sample.

When interpreting this data care must however be taken as there are limitations intrinsic to the technique. Elements lighter than sodium are normally impossible to detect with a standard setup and other light elements may not give accurate quantities, particularly when heavy elements are also present. The energy resolution of the detector is also poor leading to broad peaks which may overlap causing the contributions to be ill defined.

2.11 References

(1) Ewing, R. C.; Weber, W. J.; Lian, J. *Journal of Applied Physics* **2004**, *95*, 5949.

(2) Ringwood, A. E.; Kesson, S. E.; Ware, N. G.; Hibberson, W.; Major, A. *Nature* **1979**, *278*, 219.

(3) Galati, R.; Simon, C.; Knee, C. S.; Henry, P. F.; Rainford, B. D.; Weller, M. T. *Chem. Mat.* **2008**, *20*, 1652.

(4) Friedrich, W.; Knipping, P.; von Laue, M. *Sitz. Bayer. Akad. Wiss.* **1912**, 303.

(5) Woolfson, M. M. *An Introduction to X-ray crystallography*; Cambridge University Press, 1970.

(6) Bragg, W. L. *Proc. Camb. Phil. Soc.* **1913**, *17*, 43.

(7) Young, H. D.; Freedman, R. A. *University Physics*; 9 ed.; Addison Wesley (USA), 1996.

(8) *International Centre for Diffraction Data*, 12 Campus Boulevard, Newton Square, Pennsylvania 19073-3273, USA: 1995.

(9) Buerger, M. J. *Contemporary Crystallography*; McGraw-Hill, 1970.

(10) Larson, A. C.; Von Dreele, R. B. 1990.

(11) Rietveld, H. M. *Acta Cryst.* **1967**, *22*, 151.

(12) Mitchell, D. P.; Powers, P. N. *Phys. Rev.* **1936**, *50*, 486.

(13) Sears, V. F. *Neutron News* **1992**, *3*, 26

(14) http://www.ill.eu/html/instruments-support/instruments-groups/instruments/d20/.

(15) http://www.ill.eu/html/instruments-support/instruments-groups/instruments/d2b/.

(16) http://www.ill.eu/html/instruments-support/instruments-groups/instruments/d1b/.

(17) *ISIS, Oxford, POLARIS User guide*.

(18) Rietveld, H. M. *J. Appl. Cryst.* **1969**, *2*, 65.

(19) Toby, B. H. *Journal of applied crystallography* **2001**, *34*, 210.

Chapter Three

BETA-PYROCHLORES

3.1 Introduction

The nature of the interlocking lattices that make up the extended pyrochlore structure enable the material to adopt a wide variety of structures that can incorporate defects and mixed site occupations. Defect pyrochlores generally accept absences in one of the two available networks, the most commonly seen is the *beta*-pyrochlore, AB_2O_6, which can be viewed as having the *A*-type cation displaced on to the 8*b* site previously occupied by the O' of the A_2O' network. A wide ranging synthetic study of these oxide/fluoride *beta*-pyrochlores was carried out by Darriet *et al.*[1] who synthesised a variety of these materials where the *A*-site was occupied by an alkali metal or thallium and the *B*-site by a Group 5 or 6 transition metal. The majority of the materials studied in this paper also displayed mixed occupancy on the *B*-site, for example $CsNbWO_6$[2], which allows for charge balance over the structure. None of the *beta*-pyrochlores presented in the literature have, to date, displayed decreased symmetry relating to ordering on the *B*-site so it is generally accepted that the site is randomly occupied throughout the structure.

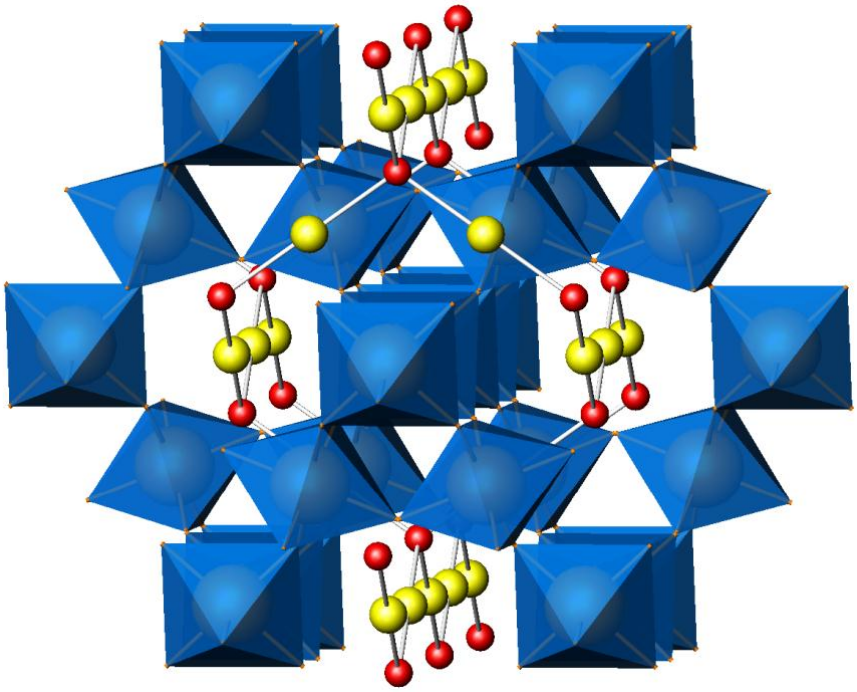

Figure 3.1.1 – A schematic of the alpha-pyrochlore framework, showing the 16d (yellow) and 8b (red) sites. In the beta-pyrochlore the cation shifts from the 16d to the 8b site with the loss of all the anions (red) on the A_2O' network.

The materials presented in this chapter characteristically display compositional variance on the sites occupied by the A_2O' network in *alpha*-pyrochlores while retaining ideal BO_6 networks. The varying occupancies and stoichiometries incorporated into this framework identify some interesting structural phenomena to be investigated, ideally allowing more general conclusions to be drawn regarding what can and cannot be incorporated into this network and further, some information regarding the limitations on the size of atoms that can be accommodated on the sites available within this network.

Primary sources[1,3-5] for all the phases discussed in this chapter place the *A*-site cations solely onto the 8*b* site and we discuss evidence that this may not be the case for the entire range of these phases.

A wide variety of neutral molecules and cations can be used to stabilise the B_2O_6 network, for example H_2O and NH_4^+ can replace or be incorporated in addition to the *A*-site cation already present providing an increased degree of stability. Examples of this include NH_4NbWO_6[6] and $NaW_2O_6.nH_2O$[7]. For several of these phases the loss of these molecules leads to a simultaneous structural collapse implying they have a significant stabilising effect; others, however, are stable both with and without their incorporation.

Whilst not utilised for as wide a variety of applications as their *alpha* analogues several key properties have been studied in *beta*-pyrochlore phases. Interesting electronic properties are relatively unusual; generally this can be explained by the majority of *beta* phases possessing *B*-site cations that are present in d^0 configurations thus diminishing the possibility of magnetic ordering. Properties that are more commonly seen arise from the behaviour of the *A*-site cations and include ion exchange[8,9], fast ion conduction[10-12] and superconduction[13-15].

Ion exchange pyrochlores are relatively well known and are used both commercially for heavy metal disposal and as a synthetic route to materials that would otherwise be inaccessible by more conventional routes, such as $LiNbWO_6.H_2O$[16]. Fast ion conduction has been observed in several materials, principally as proton conduction in materials such as $(H_3O^+)SbTeO_6$[10] and $HTaWO_6.H_2O$[17] but also as a relatively common feature in oxygen-deficient and *alpha* pyrochlore systems[18-21] **.** At the time

of writing, superconduction has only been observed in the series AOs_2O_6 (where *A* = K, Rb and Cs), phases which differ in electronic configuration to the majority of pyrochlores due to the osmium being present at an average oxidation state of +5.5 leading to mixed states between atom centres. All three osmate phases, more extensively discussed in Chapter Six, have been studied due to the unusual nature of the superconduction occurring, leading to a large volume of available data for these materials[22-24]. The interest in these materials, beyond the superconduction itself, has been due to the localised displacement of the alkali metal ions away from an 8*b* site at the centre of the cavities formed by the B_2O_6 network. It is believed that this behaviour contributes in some way to the non-conventional superconduction observed in these materials[22,24]. This 'rattling' occurs as the site is too large for the cation which thus occupies a site closer to the framework to improve the available level of bond valence. As these multiple, 32*e*, crystallographic sites are close to one another the cation 'rattles' between these sites but never settles to a single observable position, when viewed at the timescales of the characterisation techniques used to study materials of this type (*e.g.* PXRD, PND *etc*). The cation is thus normally observed as occupying the 8*b* site at the centre of these four nearby 32*e* sites, but displays a substantially larger degree of thermal motion than the surrounding framework thus spreading the associated density across the available sites as well as the pathways between them.

This chapter summarises a large volume of general characterisation of a range of alkali metal *beta*-pyrochlore phases and particularly focuses upon the behaviour of the cations within this framework. This work was undertaken to provide a strong background of the variability of this behaviour and to allow us to better understand the 'ideal' *beta*-pyrochlore structure for comparison to more unusual compositions as discussed in later chapters of this work.

3.2 The *beta*-pyrochlore series $ABB'O_6$ where *A* = K, Rb or Cs, *B* = Ta, Nb or Sb *B*' = Mo, W or Te

Attempts were made to synthesise a wide range of *beta*-pyrochlores containing a mixture of 5+/6+ cations on the *B*-site so as to better understand the factors affecting the lattice size and cation incorporation. The principle aim behind this, as well as providing a comprehensive study of these materials, was to identify potential new compositions for later synthesis and routes for the synthesis of materials in 'bulk' quantities for the measurement of properties. Although the majority of materials presented here have previously been studied[25] we have also looked at optimization of synthetic routes so that ideally we can observe trends in the environmental conditions required for formation and thus the relative stability of the synthetic products.

3.2.1 Synthetic routes

Initially all syntheses was attempted by a conventional high temperature route in air, following a variety of synthetic procedures as presented in the literature[25-29]. If these routes did not prove viable or provided significant impurities, the method was further refined to produce samples of a suitable quantity and purity for study. Primarily this was attempted either via a citrate method, by controlling the surrounding atmosphere (*e.g.* oxidising/reducing) or simply by variations in temperature and duration of annealing. For several of the phases the alkali metal source was also varied, as the choice of starting material was shown to have a significant effect upon the purity of the final product. Final synthetic routes used for each of the materials are presented in Table 3.2.1. In each case on the first heating the materials were left as powders to allow the volatile components to escape. If a second heating was required the samples were pelletised into 13 mm pellets under pressure. Particular care was taken when using alkali metal carbonates as starting materials as both rubidium and caesium carbonate are highly hygroscopic; these materials were therefore stored and weighed under a nitrogen atmosphere to retain the desired stoichiometries.

Of the phases attained only those containing molybdenum or antimony proved more complex to synthesise as the relatively low stability of MoO_3 and Sb_2O_5 were an issue. When carried out in air the reactions involving molybdenum often formed

phases of two general, undesired, stoichiometries, *i.e.* B_2MoO_6[30] and ABO_5. Later attempts at synthesis were carried out under flowing oxygen to encourage the formation and retention of the higher oxidation states available to the transition metals being used and in several cases this proved to be successful. In some cases, for the molybdenum materials, the desired phases were present *e.g.* in $CsSbMoO_6$, however impurity phases were also present in significant quantities, whereas for the majority of the materials where synthesis proved unsuccessful the phase was not present at any time. $RbSbTeO_6$ also proved particularly difficult to synthesise, instead forming the previously uncharacterised hydroscopic tetragonal phase $Rb_{22}Te_{32}O_{107}$, identified from the structurally analogous tungsten phase[31]. Attempts to separate the target phase from its impurities proved unsuccessful.

From a brief study of the successful reaction pathways we can conclude that as expected there is a strong correlation between the stability of the starting materials and the reaction conditions required to achieve the desired products. Whilst some materials appear to readily form the desired pyrochlore phase as both the thermodynamic and kinetic products, notably the majority of the niobium containing compounds, others showed a higher dependency upon the reaction pathways. Of particular note were the tantalum-containing materials which, whilst forming the pyrochlore phase as the kinetic product, tended towards more structurally complex metal oxides, such as $Ta_{22}W_4O_{67}$[32], if the reaction time was not firmly controlled. PXRD data on several of the compounds after the intermediate stages of heating showed the formation of an alkali metal/transition metal oxide complex along with the retention of the remaining metal oxide starting material. Thus, for the majority of these materials a further stage of heating coupled with pelletisation was required to ensure a single phase product was achieved, a technique typically utilised in metal oxide synthesis.

Table 3.2.1- Synthetic conditions used to produce the targeted beta-pyrochlores.

Target phase	Starting materials	Conditions	
		Temp/°C + Gas	Duration/hrs
$CsTaMoO_6$	$Cs_2CO_3 + Ta_2O_5 + MoO_3$	400	24
		600	24
$KTaWO_6$	Citrate Gel	300	8
	$KNO_3 + Ta_2O_5 + WO_3$	600	48
$RbTaWO_6$	$Cs_2CO_3 + Ta_2O_5 + WO_3$	400	24
		700	48
$CsTaWO_6$	$Cs_2CO_3 + Ta_2O_5 + WO_3$	400	24
		700	48
$KTaTeO_6$	Citrate Gel	300	8
	$KNO_3 + Ta_2O_5 + Te(OH)_6$	600	48
$RbTaTeO_6$	$RbNO_3 + Ta_2O_5 + Te(OH)_6$	400	24
		700	48
$CsTaTeO_6$	$CsNO_3 + Ta_2O_5 + Te(OH)_6$	400	24
		700	48
$CsNbMoO_6$	$Cs_2CO_3 + Nb_2O_5 + MoO_3$	500	24
		600	24
$KNbWO_6$	Sol Gel	400	16
	$KNO_3 + Nb_2O_5 + WO_3$	700	24
$RbNbWO_6$	$RbNO_3 + Nb_2O_5 + WO_3$	400	24
		700	48
$CsNbWO_6$	$CsNO_3 + Nb_2O_5 + WO_3$	400	24
		700	48
$KNbTeO_6$	$KNO_3 + Nb_2O_5 + Te(OH)_6$	450	20
		700	20
$RbNbTeO_6$	$RbNO_3 + Nb_2O_5 + Te(OH)_6$	450	20
		700	20
$CsNbTeO_6$	$CsNO_3 + Nb_2O_5 + Te(OH)_6$	450	20
		700	20
$KSbTeO_6$	$K_2CO_3 + Sb_2O_5 + Te(OH)_6$	800 under O_2	48
$CsSbTeO_6$	$Cs_2CO_3 + Sb_2O_5 + Te(OH)_6$	800 under O_2	48

3.3 Initial structural characterisation

Phase identification was initially carried out using 1 hr scans on a Siemens D5000 diffractometer over a 2θ range of 10 to 60°. All phases were indexed with a cubic unit cell with undesired phases identified using Bruker's PXRD data analysis suite EVA coupled with the JCPDS crystallographic database. Where data was not available in the literature for comparative purposes patterns were calculated based upon the structure of similar pyrochlores being studied. Once initial phase identification was completed further characterisation was then carried out using a wider range of techniques including the collection of higher quality PXRD data.

3.3.1 Initial PXRD structural refinement of the series $ABB'O_6$ where *A* = K, Rb or Cs, *B* = Ta, Nb or Sb and *B*' = Mo, W or Te

Data in the 2θ range 10 to 110° were collected for the sixteen samples of the series on the Siemens D5000 over a period of 16 hrs using a step size of 0.02°. A variety of starting models were used from the literature, using whichever was best applicable to each individual phase[1,5,27]. To confirm the validity of the starting model rapid refinements were undertaken with the global parameters varied before the lattice parameter was also included. The one refineable atomic fractional coordinate, that of the *x* of the oxygen atoms, was initially fixed to $x = 0.3125$ at this stage. The *B/B'* occupancies were fixed at 1:1 for all refinements. All phases were shown to be cubic and refined well in the space group $Fd\bar{3}m$ using von Dreele and Larson's GSAS refinement suite[33] coupled with Toby's user interface EXPGUI[34]. Each observed reflection was assignable using this model and this was therefore used as the standard cubic model for *beta*-pyrochlores in all subsequent refinements.

Once it had been established that the correct model was available for each phase more thorough refinements were undertaken proceeding with the variation of the global parameters: background and peak profile coefficients. Isotropic temperature factors were then introduced for each atom followed by the variation of the one refinable coordinate (that of the *x* position of the oxygen atoms). Final refinements resulted in reasonable degrees of fit between the calculated structure and observed data for all phases.

Table 3.3.1 – Initial starting model used for the refinement of the series $ABB'O_6$ where A = K, Rb or Cs and B = Ta, Nb and Sb B' = Mo, W and Te

Atom	Site	*x*	*y*	*z*	U_{iso}
Alkali Metal	8*b*	0.375	0.375	0.375	0.025
B/B'	16*c*	0	0	0	0.025
O	48*f*	0.3125	0.125	0.125	0.025

Table 3.3.2 – Refined lattice constants for the series $ABB'O_6$ where A = K, Rb or Cs and B = Ta, Nb and Sb B' = Mo, W and Te. Estimated standard deviations (ESDs) are given in parenthesis.

Product	Lattice parameter/Å		
	K	Rb	Cs
ANbWO$_6$	10.4747(2)	10.38835(17)	10.3840(3)
ANbTeO$_6$	10.2257(3)	10.23822(3)	10.277(4)
ANbMoO$_6$	-	-	10.4387(3)
ATaTeO$_6$	10.2423(9)	10.27201(1)	10.28222(15)
ATaWO$_6$	10.49859(16)	10.34351(19)	10.36062(11)
ATaMoO$_6$	-	-	10.3866(7)
ASbTeO$_6$	10.0890(5)	-	10.1908(2)

3.4 Preliminary data examination

Inspection of the ionic radii and the averaged ionic radii of the *B*-site cations (presented in Table 3.4.1), for the series studied, would lead us to expect a predictable trend in lattice constants. Allowing for these variations in ionic radii and assuming similar contributions from the *A*-site cations to each phase we would expect the lattice parameters to be similar for ANbWO$_6$ and ATaWO$_6$ and between ANbTeO$_6$ and ATaTeO$_6$. In general this is the observed trend and can be seen in Figure 3.4.1, which clearly shows a general increase in cell parameter with increasing *B*-site cation size. The clear outlier from this series is CsTaMoO$_6$ (which shows a considerably larger than expected cell volume) and to a lesser extent CsNbMoO$_6$. It is possible that this slight increase in cell volume may be partially explained by a pseudo Jahn-Teller effect that has been previously observed in both molybdenum and niobium-containing materials whereby the polyhedra distort[35,36]. If no ordering is observed in these distortions it is expected that they will lead to an overall increase in lattice parameter and this is therefore a possible origin of what is observed here. In the case of these materials this behaviour is observed with a greater degree of distortion within the polyhedra than in the other caesium-containing phases.

Table 3.4.1 – Ionic radii and average ionic radii for the series presented in Figure 3.4.1, radii are taken from Shannon[37].

Atom	Ionic radius/Å
Nb	0.64
W	0.60
Te	0.56
Ta	0.64
Sb	0.60
Mo	0.59

Atoms	Average radius/Å
Nb/W	0.62
Nb/Te	0.60
Ta/Te	0.60
Ta/W	0.62
Nb/Mo	0.62
Ta/Mo	0.58
Sb/Te	0.58

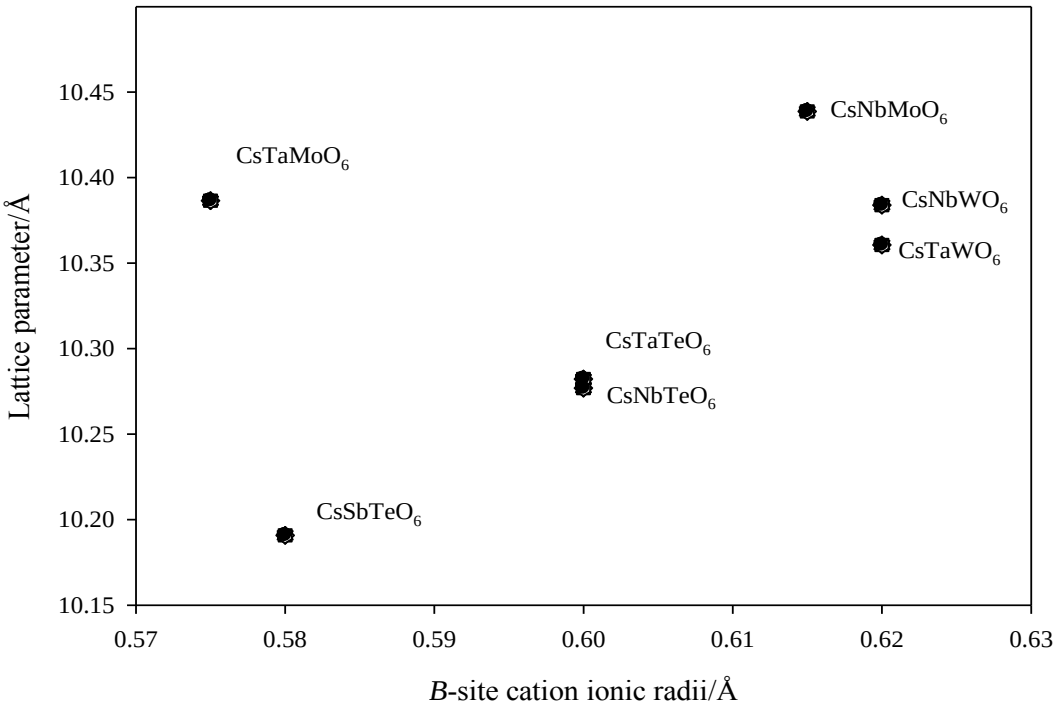

Figure 3.4.1 – A plot of the average ionic radii of the B-site cations in the series $CsBB'O_6$ against lattice parameter.

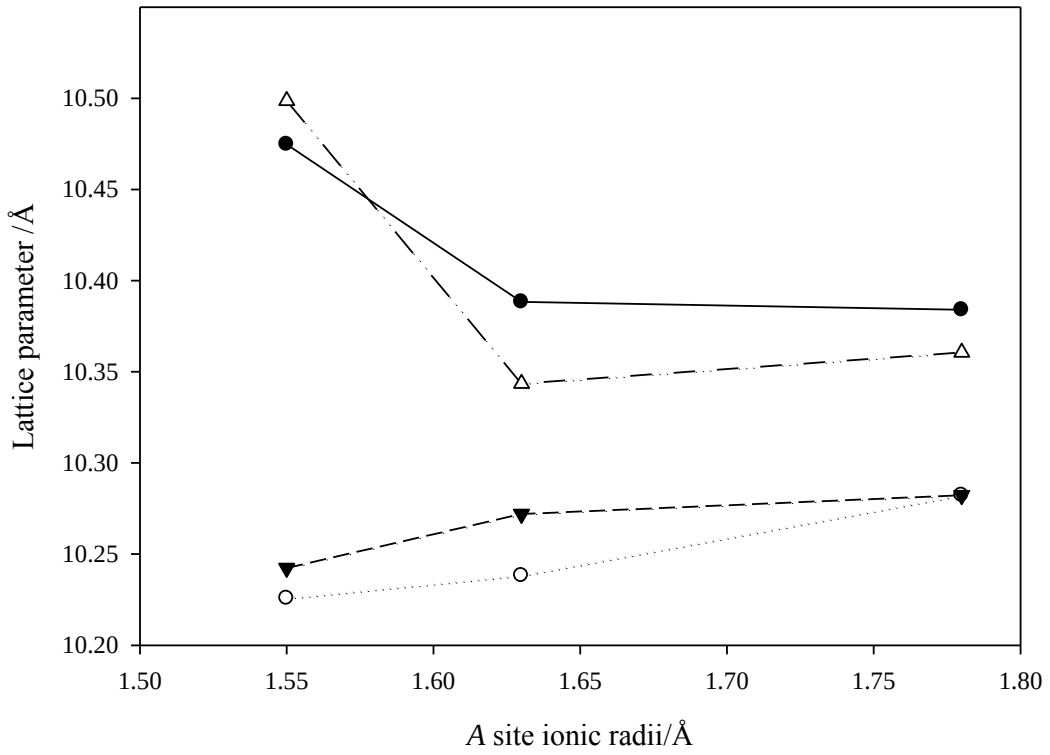

Figure 3.4.2 – Refined lattice parameter against the ionic radius of the A-site cation for the series of materials studied. ($ANbWO_6$ (●), $ANbTeO_6$ (○), $ATaTeO_6$ (▼) and $ATaWO_6$ (Δ) where A is K, Rb and Cs).

Further inspection of the refined data shows little evidence of a strong correlation between the size of the largest *B*-site species and the overall lattice parameter, with the average ionic radii appearing to provide the dominant effect. The refined average metal-oxygen bond length in materials such as $CsNbMoO_6$, at 1.9679(7) Å, is shorter than those we would expect to see in a pure Mo/O environment, the smaller of the two cations present, where we would typically expect bonds of ~1.99 Å[38]. It would appear that the dominant force here is the size of the *A*-site cation relative to the BO_6 octahedra with a significant level of distortion of the octahedra being observed to allow incorporation of these cations, including a compression of the metal/oxygen bonds when compared to similar bonds in other metal oxide frameworks.

Inspection of the refined lattice parameters of the four completed series, $ANbWO_6$, $ANbTeO_6$, $ATaTeO_6$ and $ATaWO_6$ (where A = K, Rb and Cs), Figure 3.4.2, shows an unexpected trend in the lattice parameters. The series $ANbTeO_6$ and $ATaTeO_6$ show an increase in lattice parameter directly correlating to the increase in ionic radius of the A-site ion. In contrast, for $ANbWO_6$ and $ATaWO_6$ this is not observed, with minimal change in lattice parameter for the two rubidium-containing phases and a significant increase when potassium is incorporated. The discrepancies in lattice parameter in both $KNbWO_6$ and $KTaWO_6$ can be explained by the incorporation of water into the structure as previously described by various authors[1,26], although other studies have failed to note this effect[39]. Whilst other work in this area showed no reference to hydration in the other materials presented here it was easily shown that several of the other phases studied hydrate readily in air using both thermogravimetric data and infrared (IR) spectroscopy.

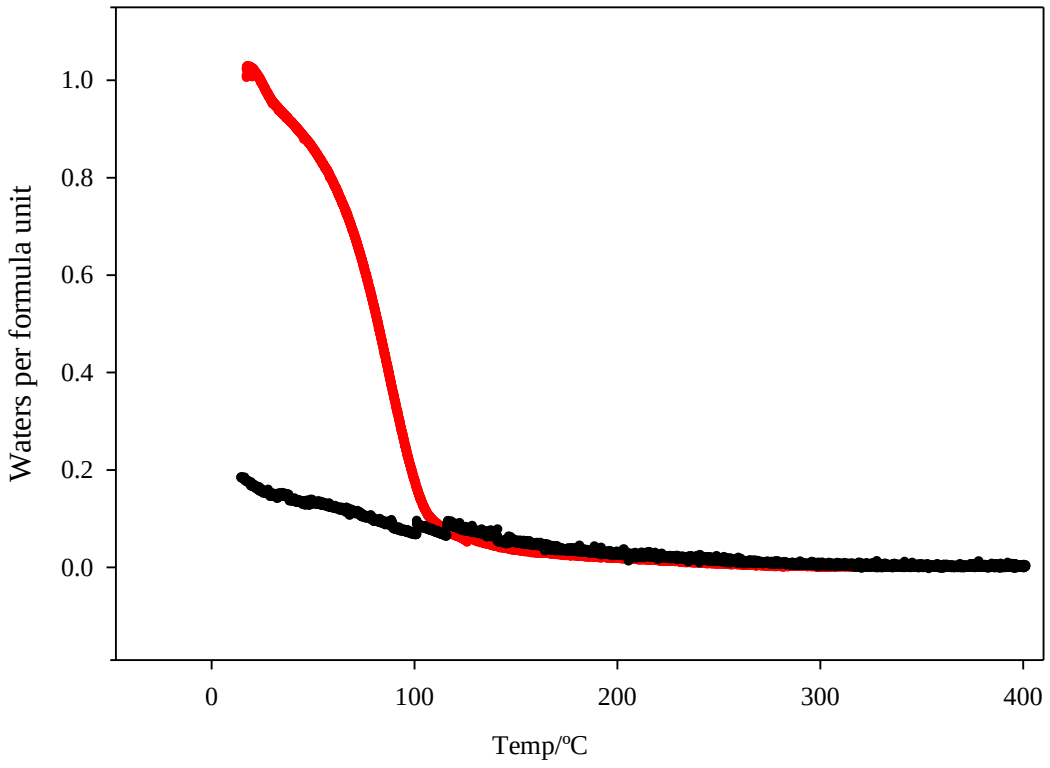

Figure 3.4.3 – Calculated water content for $RbNbWO_6.nH_2O$ (black) and $KNbWO_6.nH_2O$ (red) from TGA data.

Figure 3.4.4 shows IR spectra collected for the series ANbWO$_6$ (A = K,Rb and Cs) indicating an increased contribution from intercalated water to the spectra as A-site cation size is increased, observed in the broad stretch ~3600 cm^{-1}.

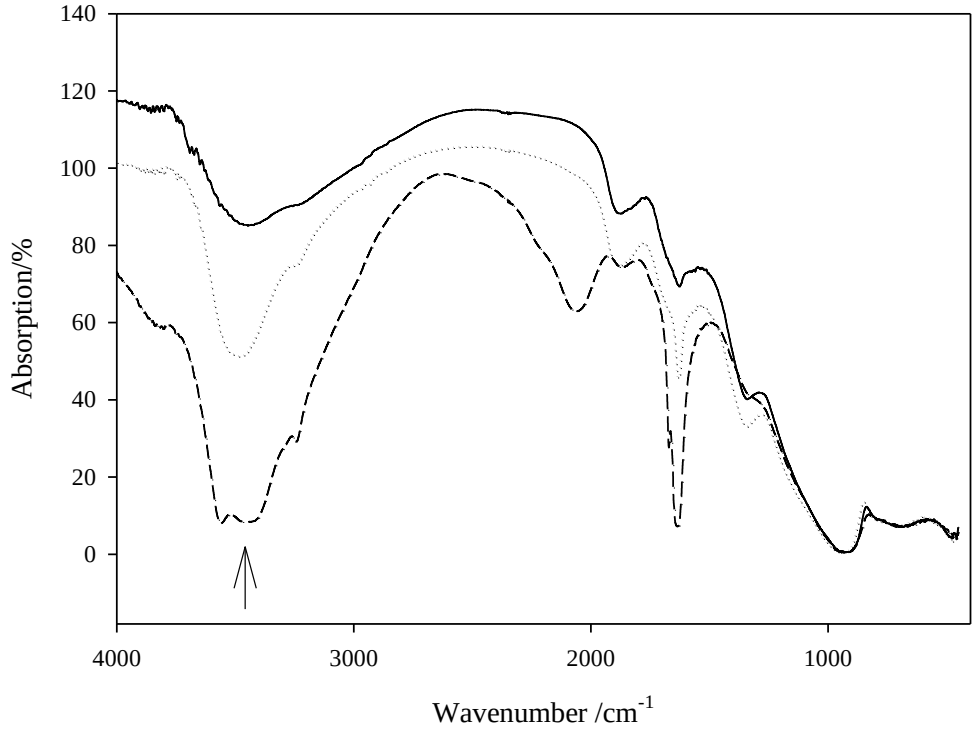

Figure 3.4.4 – Infrared spectra of KNbWO$_6$(---), RbNbWO$_6$(….) and CsNbWO$_6$(-). Data was collected using a reflection setup such that all absorptions could be assigned to the sample.

Typically waters of crystallisation, as observed in solid state spectra, display a broad band between 3600 and 3100 cm^{-1} (indicated the arrow in Figure 3.4.4) and a weaker band between 1640 and 1615 cm^{-1}, both of which are observed in these spectra[40]. A small contribution from water is observed in all phases and this is attributed to surface water. To establish this relationship clearly, samples which were considered 'dry' (*i.e.* without intercalated water), were dried at 200°C for 24 hours to remove surface water. Further IR spectra were collected, with the broad peak attributed to water significantly reduced.

The RbNbWO$_6$ phase appears to show a small contribution from water in the IR spectrum and this is further confirmed by TGA data which shows a small mass loss between room temperature and 400°C which equates to approximately 1/6 of a water molecule per formula unit. This incorporation of water may go some way to explaining the slightly larger than expected lattice parameter observed in this phase.

Study of several of the hydrated *beta*-pyrochlore phases are presented later in this work. The remainder of this chapter deals exclusively with the dehydrated phases. To ensure total dehydration, the initial preparation methods presented in Section 3.2.1 were undertaken followed by heating under a nitrogen atmosphere for 8 hours at 400°C before recollecting PXRD data under the conditions used earlier in this chapter. Once dried, samples were handled exclusively under nitrogen as rapid rehydration otherwise occurred.

3.4.1 Final PXRD structural refinements for the series $ABB'O_6$ where *A* = K, Rb or Cs and *B* = Ta, Nb or Sb *B*' = Mo, W or Te

Refinements for the dried materials were repeated as described in Section 3.3.1, providing significantly improved fits to the data for the phases that had previously included intercalated water. Calculated fit parameters are presented in Table 3.4.2 along with examples of graphical fits in Figures 3.4.4 and 3.4.5 of phases displaying amongst the best and worst statistical fits. It can be clearly seen in Table 3.4.2 that the degree of fit, shown as the fit parameters, varies significantly between data sets, whilst the graphical fit remains similar throughout. A significant contributing factor to this is the relative contribution of the background to the data sets; those with backgrounds that are lower in proportion to the intensity of the reflections provide significantly improved levels of fit. Separate refined data presented later in this work, collected on a variety of PND instruments, along with literature sources do however provide an excellent level of agreement to the refined PXRD data.

Table 3.4.2 – Refined final fit parameters from PXRD data for the series $ABB'O_6$ where A = K, Rb or Cs and B = Ta, Nb and Sb B' = Mo, W and Te.

Phase	χ^2	R_{wp}(%)	R_p(%)
$CsTaMoO_6$	1.153	36.65	25.98
$RbTaWO_6$	3.601	18.09	13.72
$KTaWO_6$	5.362	23.63	18.11
$CsTaWO_6$	3.457	4.47	3.21
$RbTaTeO_6$	2.251	5.94	4.56
$KTaTeO_6$	0.9990	35.80	25.68
$CsTaTeO_6$	1.678	5.61	4.17
$CsNbMoO_6$	2.146	5.17	4.03
$RbNbWO_6$	8.462	11.01	7.57
$KNbWO_6$	0.5717	42.45	35.17
$CsNbWO_6$	2.373	5.41	3.89
$RbNbTeO_6$	1.209	33.46	22.61
$KNbTeO_6$	1.081	32.86	21.82
$CsNbTeO_6$	1.146	34.99	24.44
$KSbTeO_6$	1.168	29.68	19.84
$CsSbTeO_6$	1.677	19.63	13.53

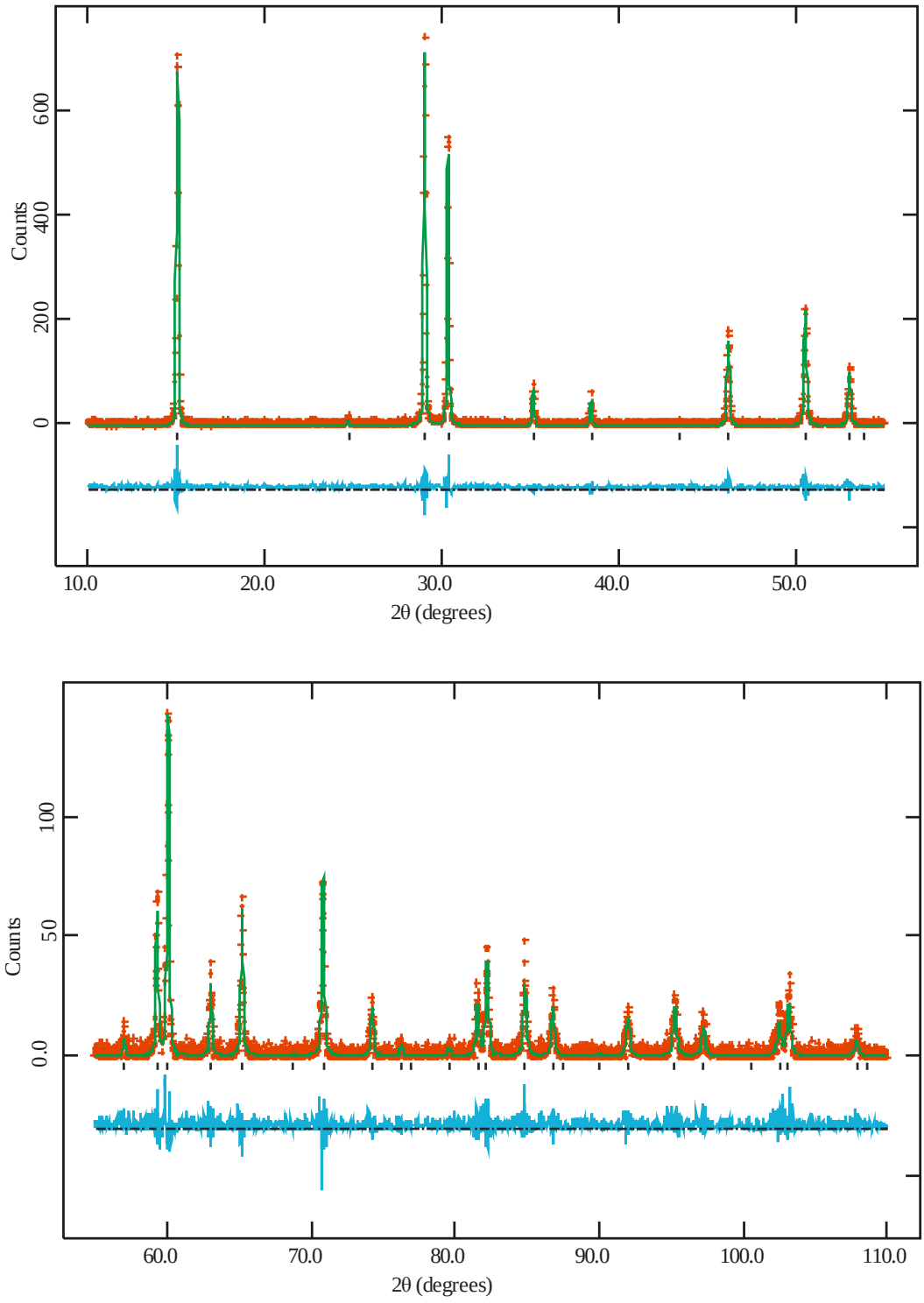

Figure 3.4.4 – Profile fit to PXRD data for $KNbTeO_6$. Experimental data points are shown as red crosses, upper continuous green line the calculated profile and the lower continuous blue line the difference. Allowed reflections are indicated by tick marks.

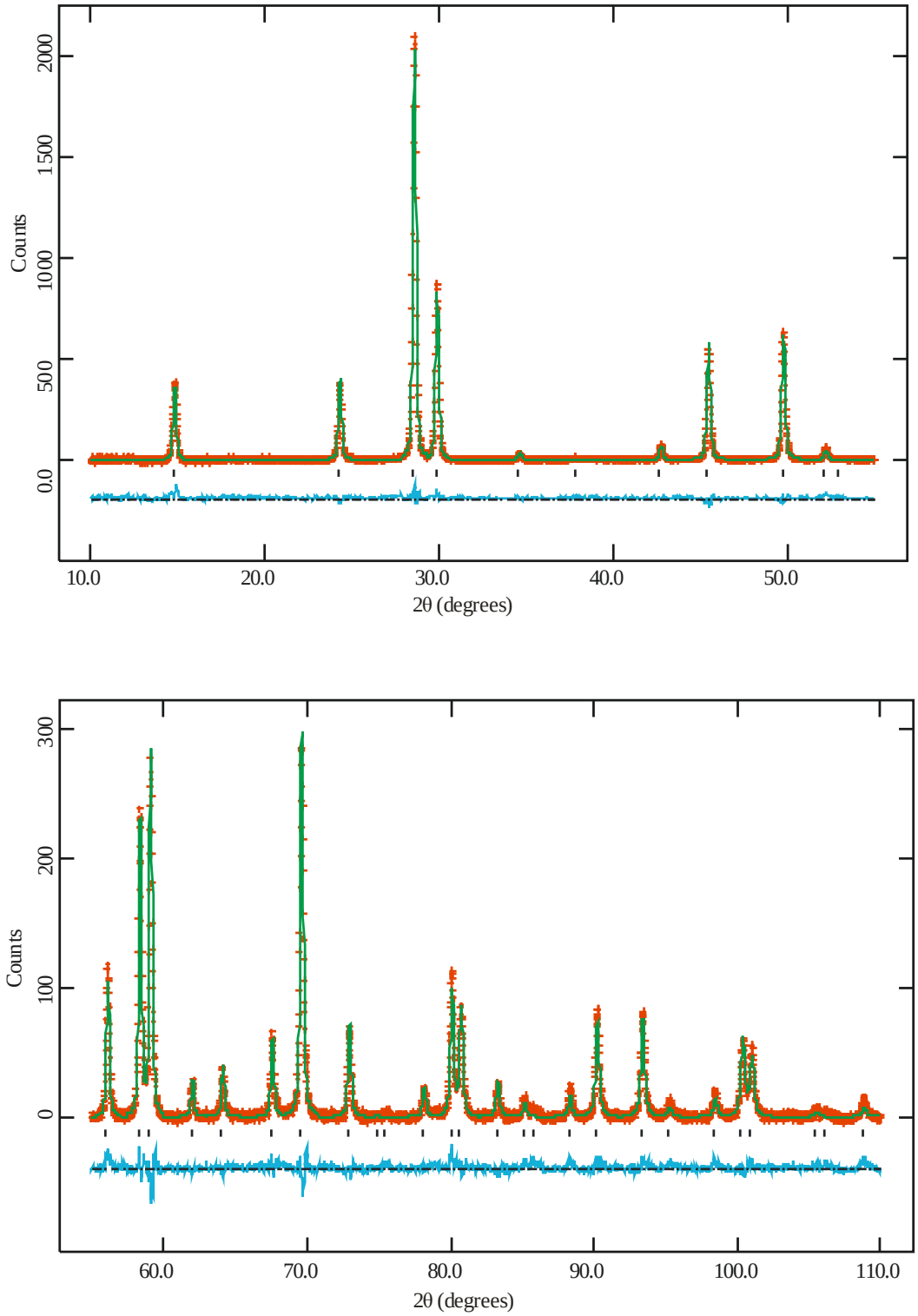

Figure 3.4.5 – Profile fit to PXRD data for $CsNbWO_6$. Experimental data points are shown as red crosses, upper continuous green line the calculated profile and the lower continuous blue line the difference. Allowed reflections are indicated by tick marks.

3.4.2 Discussion

Lattice parameters for the investigated phases were calculated and are presented in Table 3.4.3. The expected trends of these dehydrated phases are, in general, predictable showing an extremely strong correlation between the cation sizes and lattice constants. For the phases previously presented as hydrated materials the expected lattice contractions, as the *A*-site cations are reduced in size, were now observed, Figure 3.4.6. The decay is smooth and proportional to the reduction in cation size, with the exception of $KNbTeO_6$ and to some degree $KSbTeO_6$ (although the identification of any trend associated with this phase is speculative as the rubidium analogue was not synthesised successfully) where a smaller than expected reduction is observed. Both of these phases are smaller than the other series under investigation and it is thus expected that this behaviour is purely a result of better coordination of the potassium atoms being provided by this degree of contraction.

Table 3.4.3 – Refined lattice constants for the series $ABB'O_6$ where A = K, Rb or Cs and B = Ta, Nb and Sb B' = Mo, W and Te. ESD's are given in parenthesis.

Product	Lattice parameter/Å		
	K	Rb	Cs
ANbWO$_6$	10.3566(2)	10.3677(7)	10.3840(3)
ANbTeO$_6$	10.2257(3)	10.23822(3)	10.277(4)
ANbMoO$_6$	-	-	10.4387(3)
ATaTeO$_6$	10.2423(9)	10.27201(1)	10.28222(15)
ATaWO$_6$	10.3194(11)	10.34351(19)	10.36062(11)
ATaMoO$_6$	-	-	10.3866(7)
ASbTeO$_6$	10.0890(5)	-	10.1908(2)

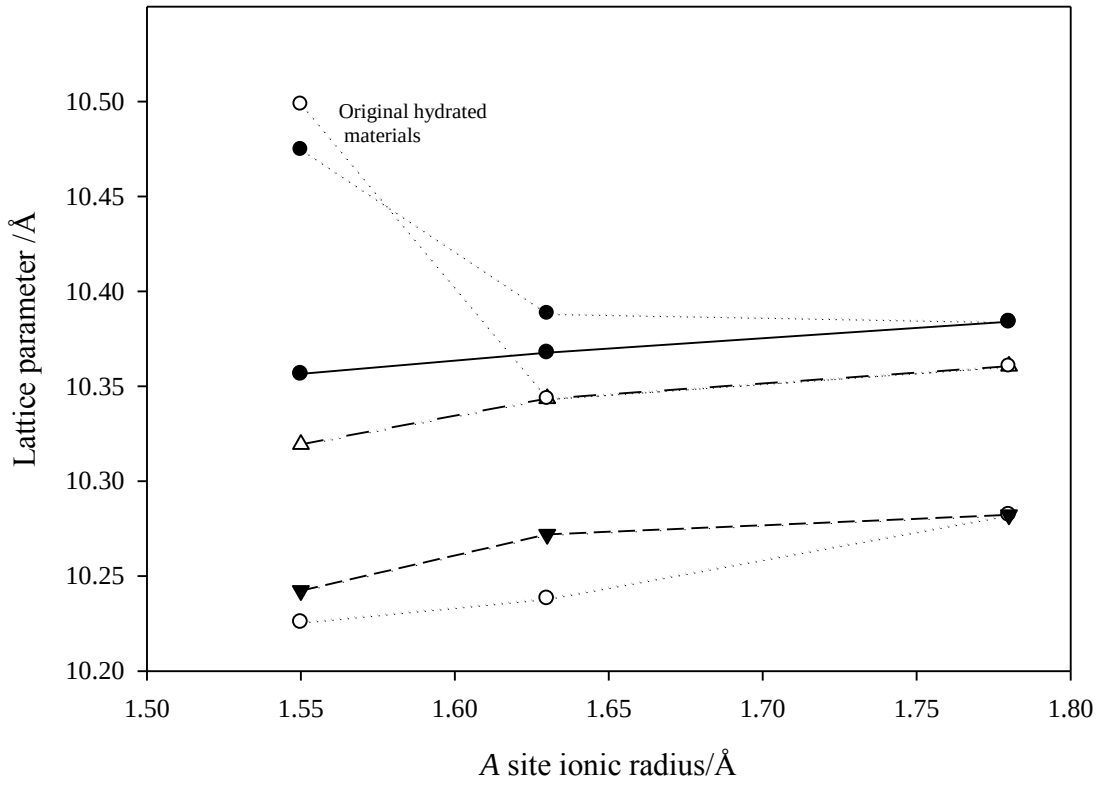

Figure 3.4.6 – Refined lattice parameter against the ionic radius of the A cation for the series of materials studied. ($ANbWO_6$ (●), $ANbTeO_6$ (○), $ATaTeO_6$ (▼) and $ATaWO_6$ (Δ) where A is K, Rb and Cs) after dehydration.

Further inspection of the data shows a strong correlation between the increasing thermal motion of the *A*-site cations and the decreasing ion size, regardless of the composition of the surrounding framework. The degree of displacement this represents appears to reach a threshold where the atom moves from the 8*b* site in the centre of the cavity with a high degree of thermal motion to an independently refineable 32*e* site with a more reasonable level of motion. Only two phases fall into this second category, $KNbWO_6$ and $KTaWO_6$, both of which possess the largest average ionic radius, 0.62 Å in a six fold site, for the *B*-site cations and are thus expected to provide the largest internal cavities of any of the materials studied. Both of these phases were therefore refined with displaced potassium ion positions. Further discussion and details of the refinements for these phases are presented in Chapter Four. In general the behaviour of these cations is excluded from this discussion as the coordination is significantly different and they effectively adopt a different local structure type.

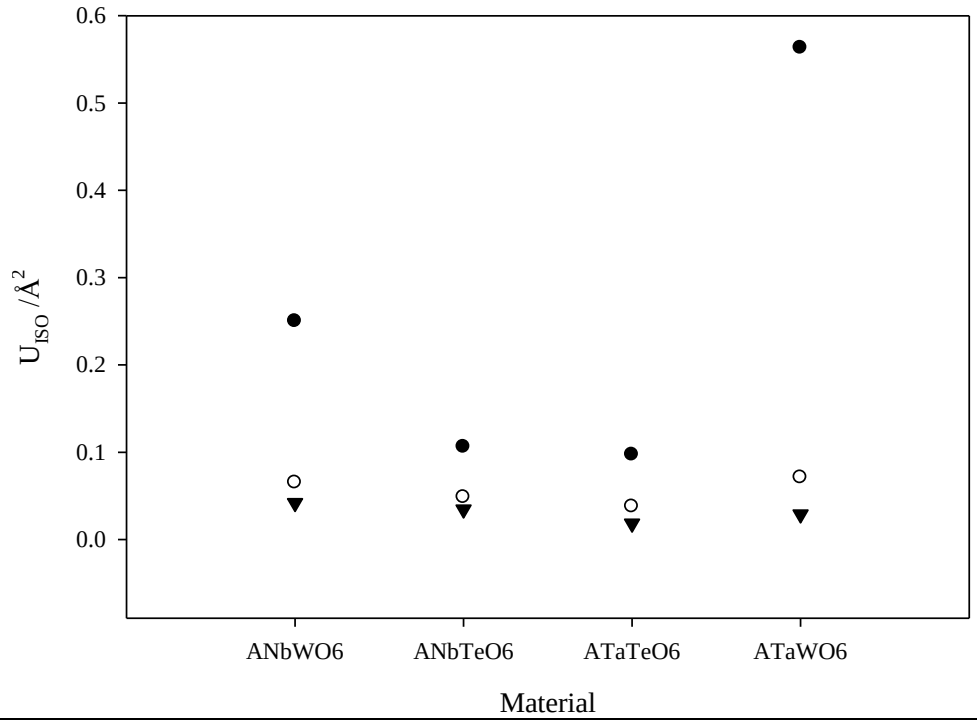

Figure 3.4.7 – A plot of the refined isotropic thermal parameters for the series ABB'O_6 where the A-cation is represented by K(●), Rb(○) and Cs(▼) for the four completed series

The thermal motion of the alkali metals shown in Figure 3.4.7 displays a very simple and clear trend, with the alkali metal ion size increasing as it becomes more tightly bound within the framework leading to lower degrees of thermal motion. The exact degree of thermal motion however appears to be only loosely linked to the overall lattice size; whilst on average the greater the lattice parameter the higher the U_{ISO}, the link is not direct. So while the two largest of the potassium containing phases, $KNbWO_6$ and $KTaWO_6$, display the highest degrees of thermal motion for the potassium cations present they do so in a manner that we would not expect with the smaller $KTaWO_6$ having a far more significant degree of thermal motion than the $KNbWO_6$ with its larger internal spacings. This can possibly be explained by more complex movements of the potassium ions within the cavities, such as has been shown in the smaller KOs_2O_6 (a = ~10.1 Å) where the potassium ions are displaced from the 8*b* site and can be localised to other sites surrounding this at extremely low temperature with the overall density thus appearing to be 'smeared' across the cavity[41].

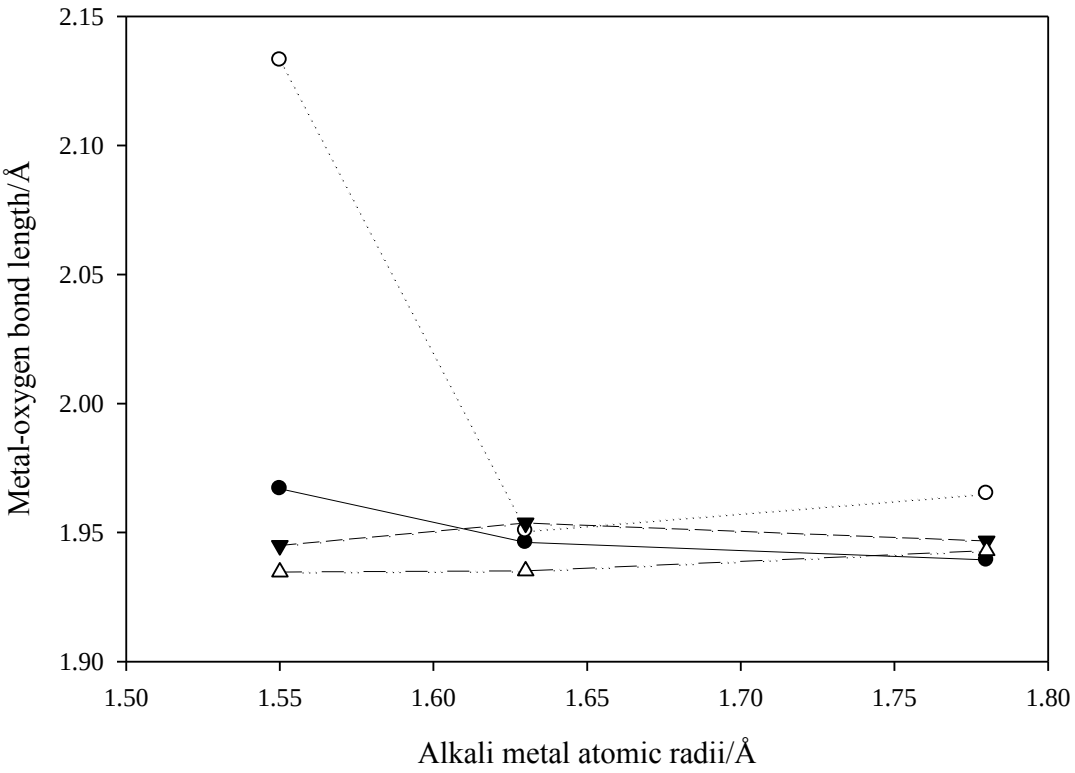

Figure 3.4.8 – Plot of the relationship between alkali metal ion size and the average metal-oxygen bond lengths for the series; $ANbWO_6$ (●), $ATaWO_6$ (○), $ATaTeO_6$ (▼) and $ANbTeO_6$ (Δ).

The total volume of the polyhedra, determined through the bond lengths and internal bond angles, are relatively consistent for most phases, independent of the alkali metal cation size (Figure 3.4.8). The exception appears to be the two phases capable of hydrating, $KNbWO_6$ and $KTaWO_6$, both of which, once dehydrated, display metal-oxygen bond lengths in excess of what would be expected by inspection of the other phases being studied here. Whilst this phenomenon is worth noting here it will be investigated more thoroughly in Chapter Four, where the use of PND allows more accurate determination of the oxygen atom positions. What this behaviour does imply however is that the cation species has some effect upon the volume of these polyhedra and that when it is no longer tightly bound, as in $KNbWO_6$ and $KTaWO_6$, these polyhedra will expand. This behaviour is typical of such structure types and is to be predicted with the metal-oxygen bond lengths displayed in these materials being shorter than normally seen in an octahedrally-coordinated environment for these elements.

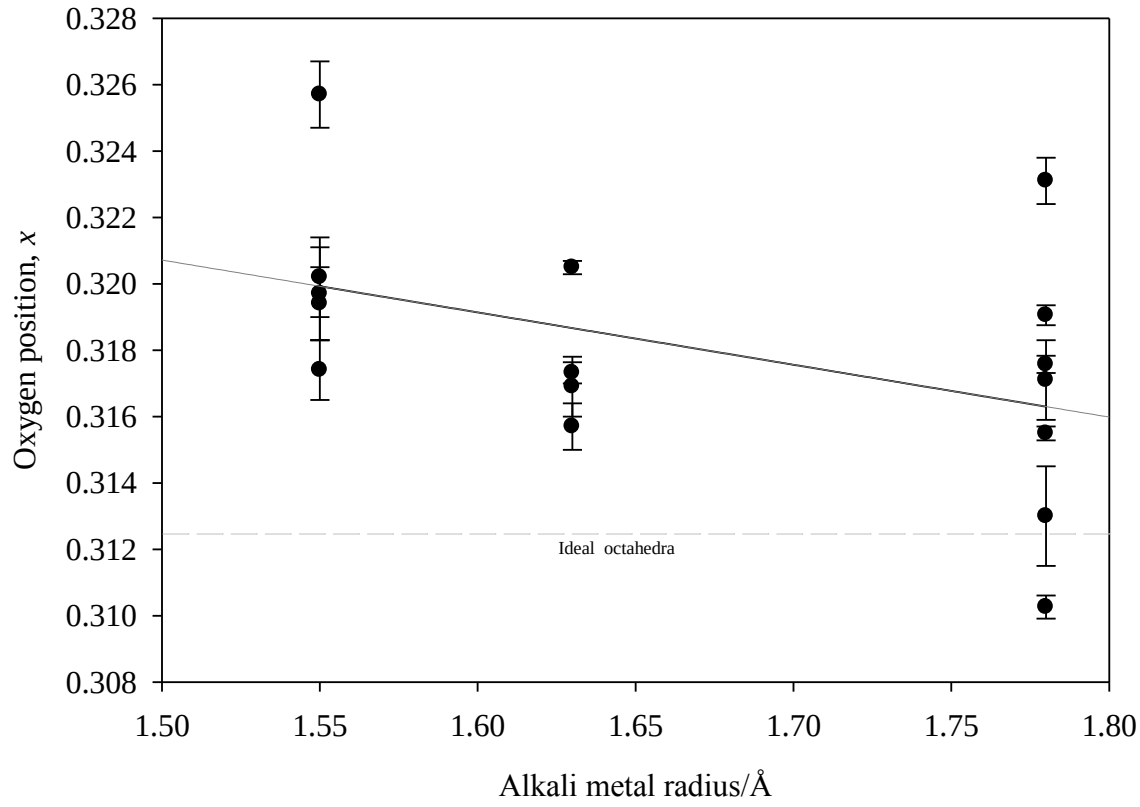

Figure 3.4.9 – A plot of the one refineable co-ordinate 'x' for the oxygen positions in the series $ABB'O_6$ discussed in this chapter against the ionic radii of the A-site cations. Values used are; K - 1.55Å, Rb – 1.63Å and Cs – 1.78Å[37]

Although weak, there is a loose trend in alkali metal ion size to oxygen position that is independent of the lattice parameter of the original compound. Figure 3.4.9 further shows this trend to greater levels of distortion within the BO_6 octahedra with respect to reducing ion size. It is expected that this behaviour arises, at least in part, to allow better coordination of the alkali metal species thus stabilising both the framework and the *A*-site cations. As the cation size is reduced a smaller coordination environment is required and as previously stated the change in the shape of these octahedra allows this to occur.

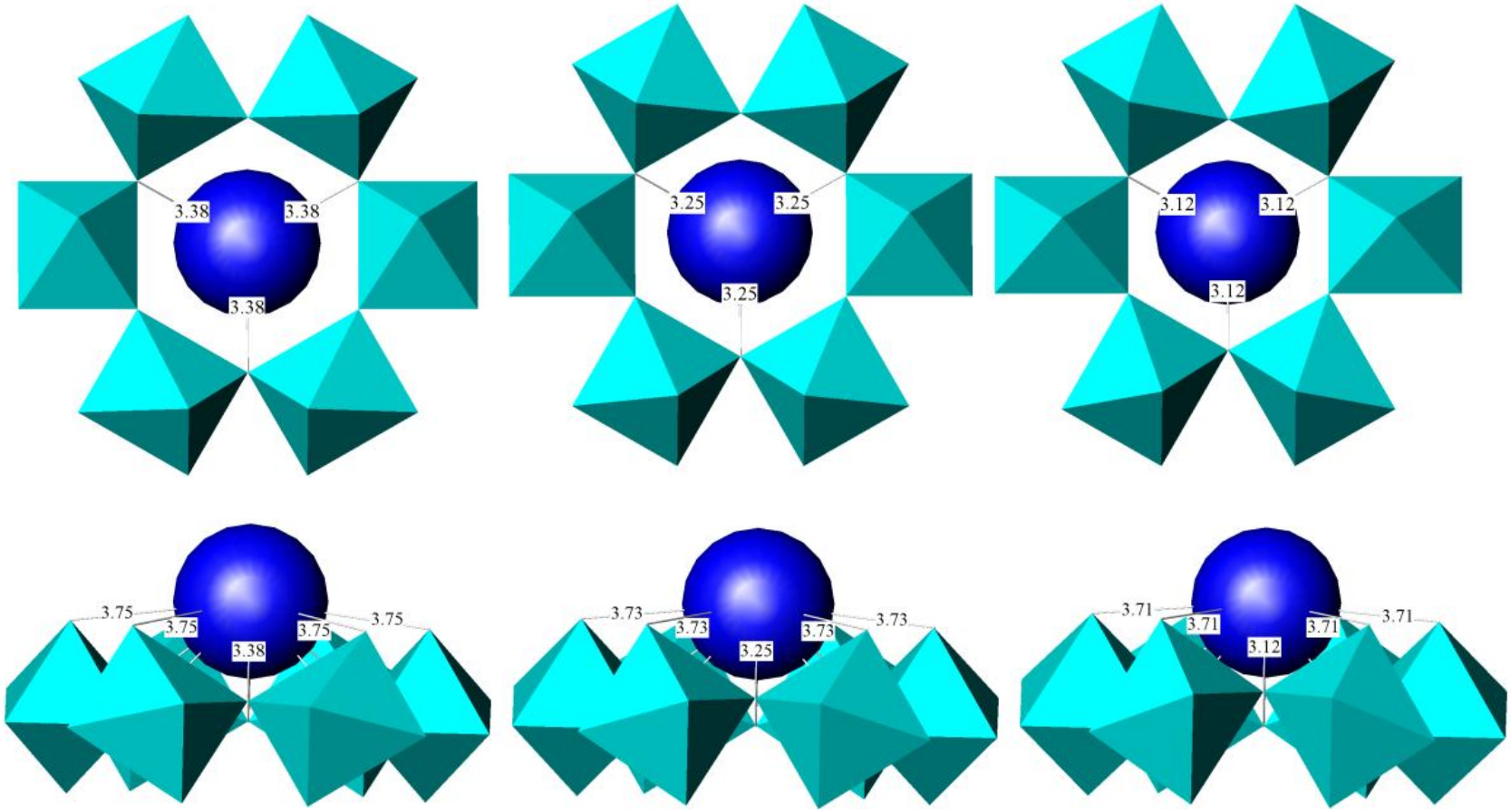

Figure 3.4.10 – Graphics showing the effect of altering the x position of the oxygen upon the coordination of the 8b A-site cations. From left to right x = 0.3000, 0.3125 and 0.3250. The bond length values presented here are representative of the general effect upon phases of this type. Upper images look down the [110] direction and the lower pictures are perpendicular to this.

In the case of the majority of the *beta*-pyrochlore series studied here the variable positional parameter for the oxygen atoms, that of the *x* coordinate, is equal to or greater than 0.3125 meaning that in each case the MO_6 polyhedra these atoms make up are compressed in the [111] direction. Figure 3.4.10 shows the effect that this has upon the coordination of the *A*-site cation. It can clearly be seen that this compression leads to shorter oxygen-alkali metal distances, thus the smaller the cation occupying this site the greater the value of *x* that is required to provide an ideal coordination environment.

The one exception seen in the general trend is observed in $CsNbWO_6$ where the opposing distortion is seen, with the octahedra elongating in the [111] direction. This behaviour is not predicted as the lattice parameter and other refined data on this phase follows the expected trends for the *beta*-pyrochlore series. As this material also displays some interesting electronic properties further work was carried out and is discussed in Section 3.7.

Finally, inspection of the general trends in thermal motion of the atoms within these frameworks shows no strong correlations with respect to cation size. It is reasonable to expect a higher degree of thermal motion for the oxygen atoms as the alkali metal ions decrease in size due to the ions being more loosely coordinated; this is not however observed (Table 3.4.4). For the interpretation of the majority of this oxygen data we must be aware that the e.s.d. are more significant due to the poor resolution of oxygen position that arises from the use of PXRD when heavier elements are also present in the sample. This may go some way to explain why the expected link between these two features is not observed.

As part of this work attempts were also undertaken to synthesise pyrochlores of similar composition as those presented here but incorporating first row transition metals on to the *B*-sites. Fluoride analogues with only first row transition metals on these *B*-sites are relatively well known with the majority of compositions forming for species that are in the d^0 state[39,42]. The oxides, however, are sparse with only one composition previously identified, $ATi_{0.5}B'O_6$[43]. Several naturally occurring phases also contain first row transition metals but once again the *B*-site occupancy is low with second and third row metals dominating[44-46]. This difference between the formation of the fluoride and oxide phases is somewhat surprising as both have

extremely similar ionic radii, of 1.285 Å and 1.35 Å respectively but can be partially explained by the preference of many first row transition elements to lower oxidation states than their second and third row counterparts. A suitable example of this is the series $CsTaB'O_6$ where *B'* = Cr, Mo and W, both the molybdenum and tungsten compounds form readily adopting the +6 oxidation state. However chromium, which can also be reduced to a +6 oxidation state, forms a variety of phases including Cs_2CrO_4[47] and Ta_2CrO_6[48], which whilst having chromium present in the desired oxidation state appear to be both the thermodynamic and kinetic products of this reaction type with the pyrochlore phases not forming.

Table 3.4.4 – Refined positional parameters for the x coordinate of the oxygens in the series $ABB'O_6$ where A = K, Rb or Cs and B = Ta, Nb and Sb B' = Mo, W and Te, along with their associated thermal motion. E.s.d's are given in parenthesis.

Phase	*x coordinate of O*	U_{ISO}
$CsTaMoO_6$	0.3130(15)	3.1(8)
$RbTaWO_6$	0.3157(7)	1.7(3)
$KTaWO_6$	0.3202(12)	5.2(6)
$CsTaWO_6$	0.3191(3)	1.82(16)
$RbTaTeO_6$	0.3205(2)	1.09(10)
$KTaTeO_6$	0.3197(14)	1.1(6)
$CsTaTeO_6$	0.3176(3)	0.67(13)
$CsNbMoO_6$	0.3155(2)	0.54(10)
$RbNbWO_6$	0.3309(13)	5.1(7)
$KNbWO_6$	0.3194(11)	3.6(5)
$CsNbWO_6$	0.3103(4)	1.97(17)
$RbNbTeO_6$	0.3169(9)	2.83(6)
$KNbTeO_6$	0.3174(9)	3.04(7)
$CsNbTeO_6$	0.3171(12)	3.9(7)
$KSbTeO_6$	0.3257(10)	1.2(4)
$CsSbTeO_6$	0.3231(7)	0.9(4)

3.5 Neutron diffraction experiments on the series ANbTeO$_6$ where A = K, Rb or Cs

This work was carried out alongside that of Miss R. Galati who as part of the same research project has carried out detailed structural analysis of the series AOs$_2$O$_6$ (A = Cs, Rb or K)[41,49]. These materials have been heavily studied in recent years as they are a form of non-cuprate superconductor, undergoing superconducting transitions at 3.6, 6.3 and 9.6 K respectively for Cs, Rb and K[50-52]. These materials are of particular interest as superconductivity has been partially attributed to the 'rattling' motion of the alkali metal[13,22], observable through an abnormally large thermal motion of these ions. Rattling is an effect by which the atom moves rapidly between multiple sites and is therefore observed as having its assigned density 'smeared' across these sites. As previously discussed, the stability of the B_2O$_6$ network can allow the retention of a similar sized framework across a series; thus, this 'rattling' behaviour becomes more significant as the alkali metal ion becomes smaller. The series ANbTeO$_6$ (A = K, Rb and Cs) was studied to provide the basis for a structural comparison to AOs$_2$O$_6$[53] in a material that is structurally similar but is non-superconducting. Specifically ANbTeO$_6$ was chosen as it is relatively simple to produce in bulk quantities as a single phase and provided the closest lattice parameter to AOs$_2$O$_6$ for a series that could be synthesised for all three analogues (difference in lattice constants of ~0.1 Å). It was therefore expected that the behaviour of the alkali metal cations, the speculated origin of superconductivity in AOs$_2$O$_6$[54], would be similar in each phase, and thus a more in-depth study was undertaken.

3.5.1 Sample preparation

Large scale samples of ANbTeO$_6$ were produced using a variation on the methods employed by Darriet *et al*[1] who previously synthesised the potassium and rubidium-containing phases. Each material was prepared in multiple ~1 g batches as larger samples contained significant quantities of impurities. Stoichiometric quantities of ANO_3 (A = K, Rb and Cs, all Aldrich, 99, 99.7 and 99.99% respectively), Nb_2O_5 (Aldrich, 99.9%) and $Te(OH)_6$ (Aldrich, 97.5-102.5% metal basis) were weighed and initially ground together, followed by sintering at 450°C for 16 hrs to remove the volatile components. The samples were then reground and pelletised before a further heating at 700°C also for 16 hrs. Phase purity of each sample was checked using PXRD data and matched the data presented in Section 3.4 well. Individual samples were then combined, ground, pelletised and annealed a final time for 4 hrs at 700°C. Inspection of the resulting material by PXRD showed the sample to be phase pure and produced a sample of ~5 g suitable for PND.

3.5.2 Variable temperature structural studies of ANbTeO$_6$ where A = K, Rb or Cs using PND data

Data were collected on the D20 high intensity powder neutron diffraction instrument at the ILL, Grenoble at a wavelength of 1.8768 Å over an angular range of 12 to 153.6° 2θ. Samples were mounted in 8 mm vanadium cans housed within a cryofurnace. Initially a 20 minute data set was collected on each sample at 2 K so that an initial starting model could be refined. Further data were then collected continuously over a 3 hour temperature ramp from 2-500 K for each sample. Data were then summed over every 5 K temperature rise to improve statistics, mirroring the data collection method used for the osmate analogues.

Initially the three data sets, collected at 2 K, were fitted to the standard cubic *beta*-pyrochlore model[3] with the two *B*-site cations sharing a site, with the refinement of global parameters proceeding smoothly. A small amount of vanadium was also visible in the data which can be attributed to the sample can and beam windows of the cryofurnace. This was therefore included in the refinement (using the model of Seybolt and Sumsion[55]) as a second phase with cell constant and phase fraction being allowed to vary, with the initial peak shape parameter proving a sufficient

match to the data quality. The model used provided an extremely close fit to the data with no evidence for ordering of the niobium and tellurium present. Further inspection of the data showed abnormally large isotropic thermal parameters on the alkali metals as seen in the related osmate phases[50,56], particularly notable in the potassium-containing phase.

As for the osmium phases several other models were tested on $KNbTeO_6$ for completeness. The structural model developed by Schuck *et al.*[57] from single crystal data was investigated, this model suggests a lowering of symmetry to $F\bar{4}3m$ which would result in multiple weak reflections not allowed within the higher symmetry $Fd\bar{3}m$ model. Careful observation of the data shows no intensity in these areas and Le Bail extractions carried out in $F\bar{4}3m$, varying just the profile and lattice parameters, showed no significant improvement in the extracted fit profiles. Data was studied over the entire temperature range as work by Hiroi *et al.*[23] suggested a temperature-dependent phase transition was occurring in KOs_2O_6 at T_p= 7.5K, independent of the superconducting transition. No evidence was observed for any change in symmetry over the temperature range studied, there were however indications that a model incorporating a localised displacement of the potassium ions, as postulated by Hiroi *et al.*, provided an improvement in extracted fit parameters.

A model was therefore tested with the potassium cations displaced to a 32*e* (*x*,*x*,*x*) site initially close to the 8*b* (0.375,0.375,0.375) position at the centre of the large channels. This model provided a significant improvement to the overall fit of the data and was therefore used as an initial starting model for the potassium phase at 2K. Similar processes were undertaken for the rubidium and caesium phases but were rapidly discarded as profile fit parameters proved to be inferior for the models with a shifted alkali metal ion position over one incorporating increased thermal motion. The final refined crystallographic data for the three initial data collections at 2 K are presented in Tables 3.5.1, 3.5.2 and 3.5.3 along with extracted profile fits in Figures 3.5.1, 3.5.2 and 3.5.3.

Table 3.5.1 – Refined atomic parameters for a 2K PND data set of $CsNbTeO_6$. E.S.D's are given in parentheses.

Atom	Site	*x*	*y*	*z*	Occupancy	U_{iso}
Cs	8*b*	0.375	0.375	0.375	1	0.6(2)
Nb	16*d*	0	0	0	0.5	0.50(12)
Te	16*d*	0	0	0	0.5	0.50(12)
O	48*f*	0.3166(3)	0.125	0.125	1	1.04(8)

Space group $Fd\bar{3}m$. Cell parameters: $a = b = c = 10.2875(7)$ Å

Final fit parameters: $\chi^2 = 13.46$, $R_{wp} = 6.20\%$, $R_p = 2.70\%$

Table 3.5.2 – Refined atomic parameters for a 2K PND data set of $RbNbTeO_6$. E.S.D's are given in parentheses.

Atom	Site	*x*	*y*	*z*	Occupancy	U_{iso}
Rb	8*b*	0.375	0.375	0.375	1	1.45(10)
Nb	16*d*	0	0	0	0.5	0.76(7)
Te	16*d*	0	0	0	0.5	0.76(7)
O	48*f*	0.31743(15)	0.125	0.125	1	1.25(5)

Space group $Fd\bar{3}m$. Cell parameters: $a = b = c = 10.2459(4)$ Å

Final fit parameters: $\chi^2 = 9.059$, $R_{wp} = 6.98\%$, $R_p = 3.68\%$

Table 3.5.3 – Refined atomic parameters for a 2K PND data set of $KNbTeO_6$. E.S.D's are given in parentheses.

Atom	Site	*x*	*y*	*z*	Occupancy	U_{iso}
K	32*e*	0.3947(6)	0.3947(6)	0.3947(6)	0.25	1.04(5)
Nb	16*d*	0	0	0	0.5	0.72(8)
Te	16*d*	0	0	0	0.5	0.72(8)
O	48*f*	0.31736(18)	0.125	0.125	1	1.10(5)

Space group $Fd\bar{3}m$. Cell parameters: $a = b = c = 10.23973(14)$ Å

Final fit parameters: $\chi^2 = 2.987$, $R_{wp} = 8.42\%$, $R_p = 5.15\%$

Using this model as a starting point the remaining data sets were refined using the SEQGSAS module included in the GSAS program[33]. For each refinement the background, lattice parameter, thermal parameters and peak profile parameters were allowed to vary with the sequential refinements running smoothly to completion in each case.

Whilst the models for both the rubidium and caesium phases proved stable and consistent across the entire temperature range studied the potassium model failed to do so. Between 70 and 80 K the position of the potassium ions, situated on a 32*e* site, became indistinguishable from the 8*b* site with $x \approx 0.375$. For all refinements above this temperature the standard *beta*-pyrochlore was therefore once again used and provided a slight improvement of fit above 70 K.

Table 3.5.4 – Refined atomic parameters for a 100K PND data set of $KNbTeO_6$. E.S.D's are given in parentheses.

Atom	Site	*x*	*y*	*z*	Occupancy	U_{iso}
K	8*b*	0.375	0.375	0.375	1	7.0(4)
Nb	16*d*	0	0	0	0.5	0.73(8)
Te	16*d*	0	0	0	0.5	0.73(8)
O	48*f*	0.31735(19)	0.125	0.125	1	1.14(7)

Space group $Fd\bar{3}m$. Cell parameters: $a = b = c = 10.24043(15)$ Å

Final fit parameters: $\chi^2 = 3.070$, $R_{wp} = 8.50\%$, $R_p = 5.25\%$

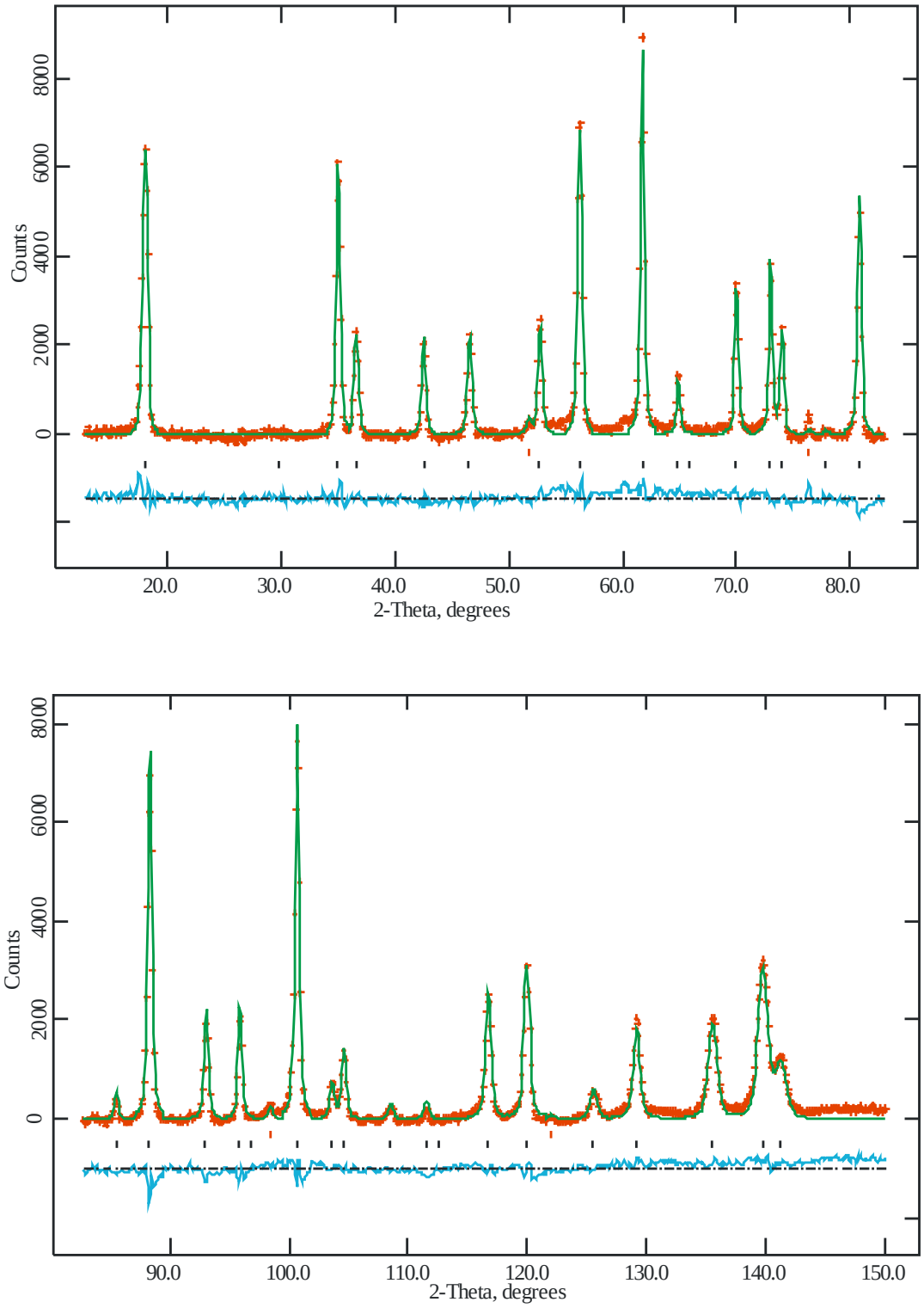

Figure 3.5.1 – Profile fit for a 2K PND data set of $CsNbTeO_6$. Experimental data points are shown as crosses, upper continuous line the calculated profile and the lower continuous line the difference. Allowed reflection positions are indicated by tick marks, red for vanadium and black for $CsNbTeO_6$

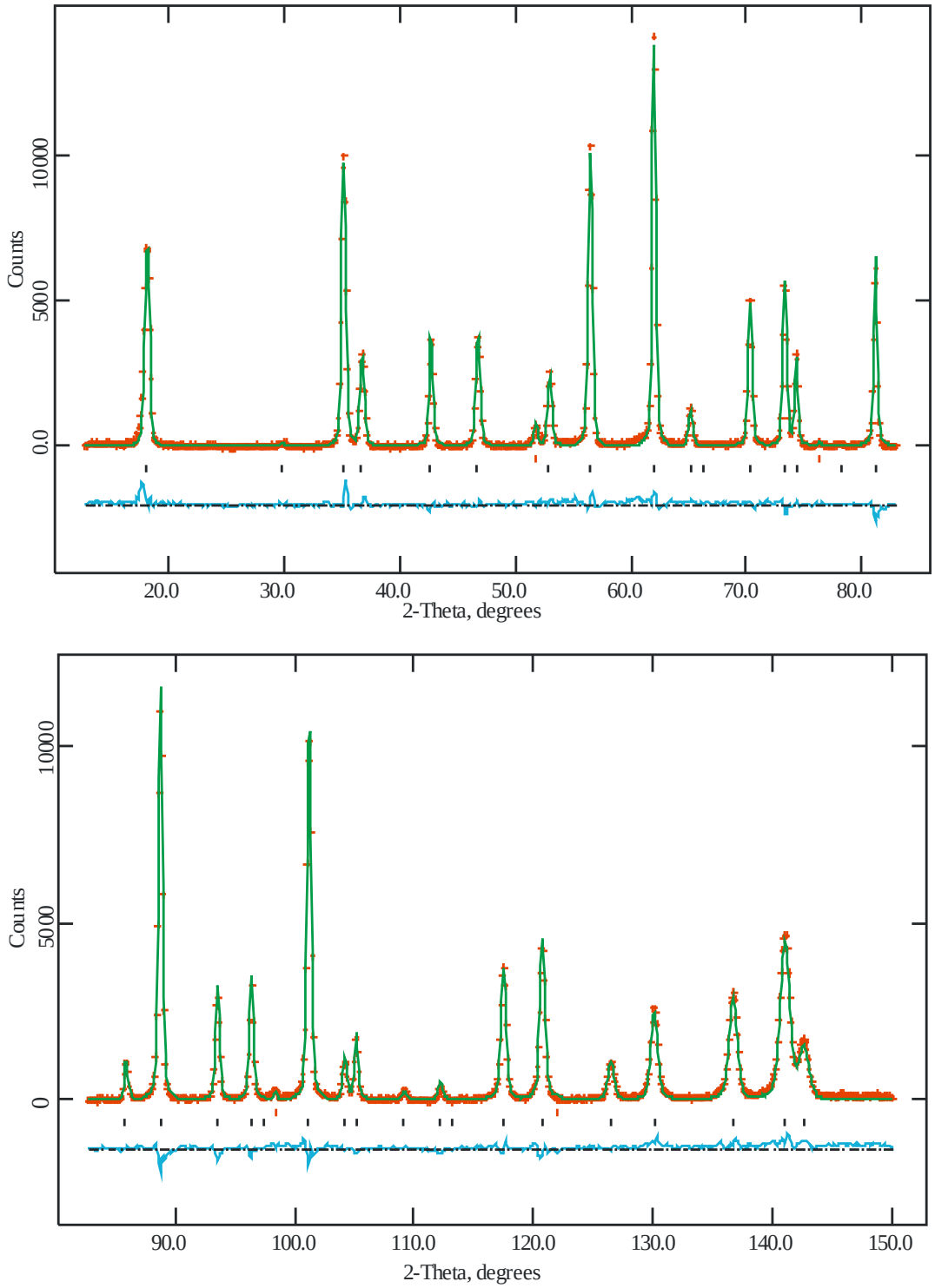

Figure 3.5.2 – Profile fit for a 2K PND data set of $RbNbTeO_6$. Experimental data points are shown as crosses, upper continuous line the calculated profile and the lower continuous line the difference. Allowed reflection positions are indicated by tick marks red for vanadium and black for $RbNbTeO_6$

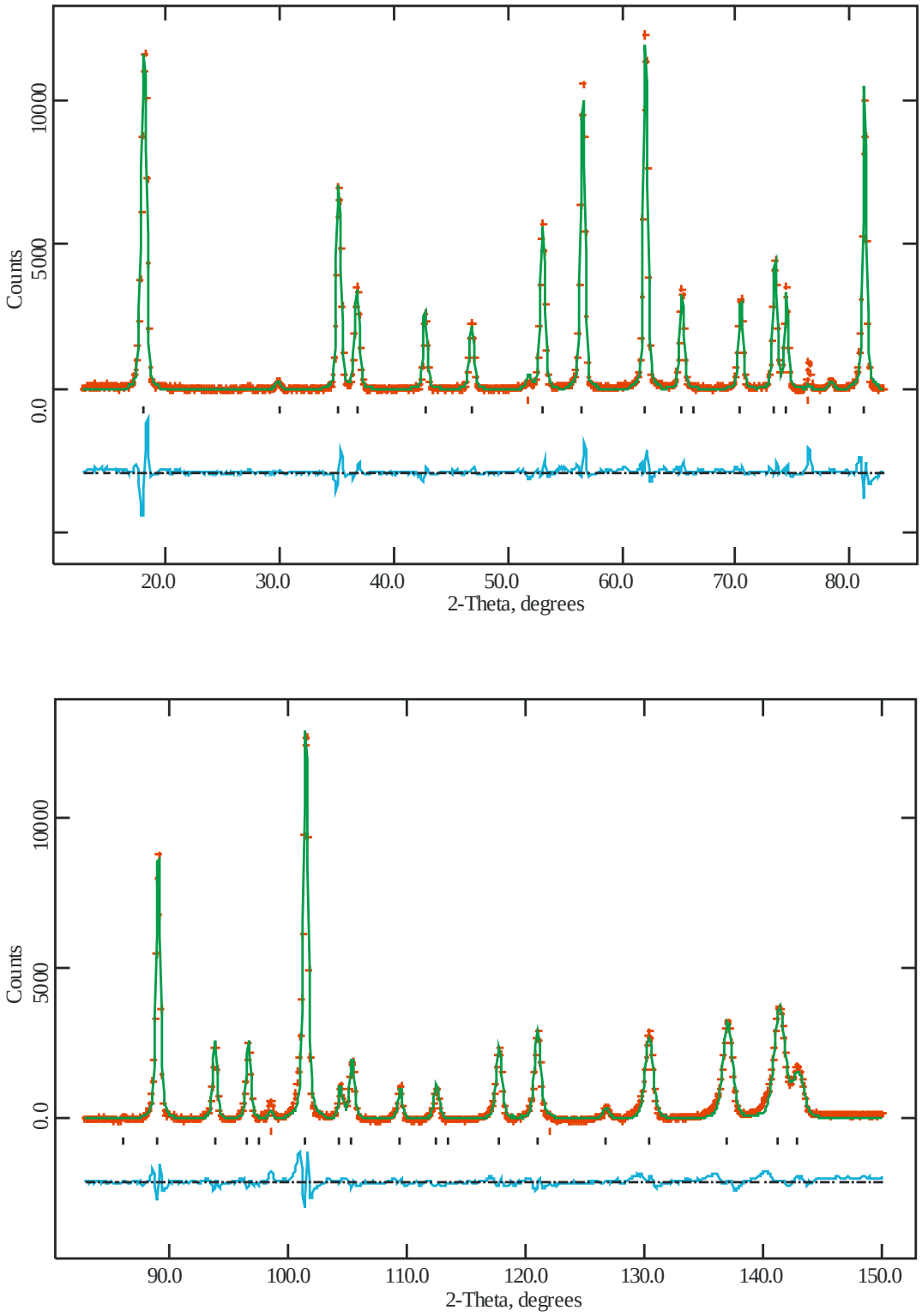

Figure 3.5.3 – Profile fit for a 2K PND data set of $KNbTeO_6$. Experimental data points are shown as crosses, upper continuous line the calculated profile and the lower continuous line the difference. Allowed reflection positions are indicated by tick marks red for vanadium and black for $KNbTeO_6$

3.5.3 Discussion

The application and analysis of high resolution powder neutron data has allowed us to precisely view the structural behaviour of the series ANbTeO$_6$ with respect to temperature. Calculated lattice parameters for the series were observed as generally increasing across the range of temperatures as expected, Figure 3.5.4. Extracted lattice parameters at 2 K were 10.238 Å, 10.247 Å and 10.286 Å for the K, Rb and caesium containing phases respectively, showing the expected increase in lattice constant with the increasing size of alkali metal. This increase in lattice constant however is not directly proportional to the increasing ion size, suggesting that they are differently affecting the overall B_2O_6 lattice structure. Over the entire temperature range studied the materials where A= Rb and Cs display conventional thermal expansion in these lattice constants with no suggestion of structural change as may be associated with the alkali metal moving from a general to a fixed position within the framework. The behaviour of KNbTeO$_6$ however is significantly different, with anomalous variation being found below 70 K. This behaviour can also be observed in the average thermal expansion coefficients of the materials between 10 and 500 K which are 4.20 x 10^{-6} K^{-1} (Cs), 4.06 x 10^{-6} K^{-1} (Rb) and 3.15 x 10^{-6} K^{-1} (K), clearly implying some unusual behaviour is occurring in the potassium phase.

Careful examination of the lattice parameters below 70 K shows that between 70 and 40 K the lattice parameter is almost invariant, before rapidly contracting between 35 and 15 K then once again levelling off or possibly showing a slight expansion on cooling below 10 K, as can be seen in Figure 3.5.5. This behaviour is very similar to what has also been observed in KOs$_2$O$_6$[41] and appears to be associated with the freezing-out of the potassium ion displacement at these low temperatures. At 2 K this displacement is significant with x = 0.3947(6), equating to a shift of ~0.35 Å from the 8*b* site.

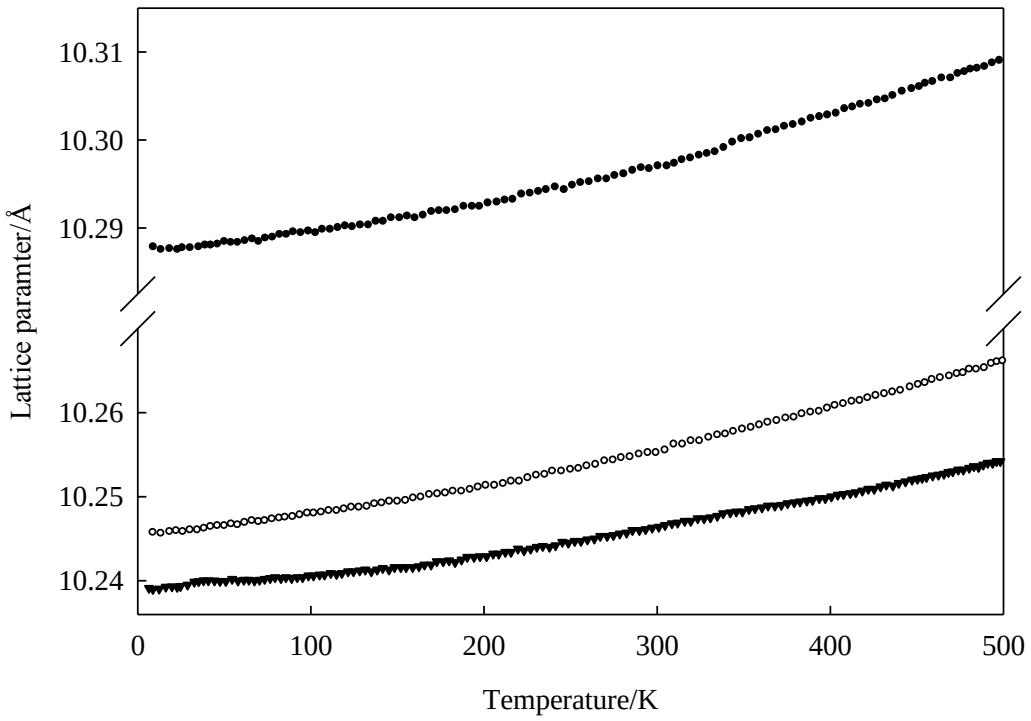

Figure 3.5.4 – Extracted lattice parameters for the series $ANbTeO_6$ (A = Cs(●), Rb(○) and K(▼)) from the refinement of variable temperature PND data. Calculated errors are within the points.

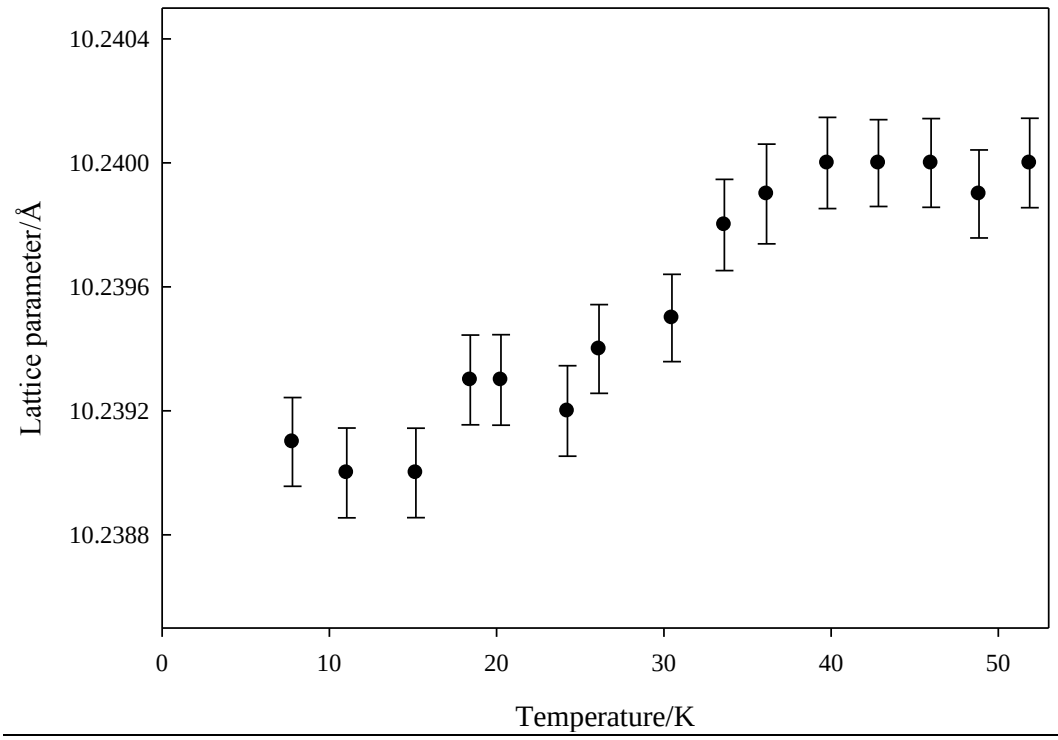

Figure 3.5.5 –Low temperature lattice parameters, along with associated errors, for $KNbTeO_6$.

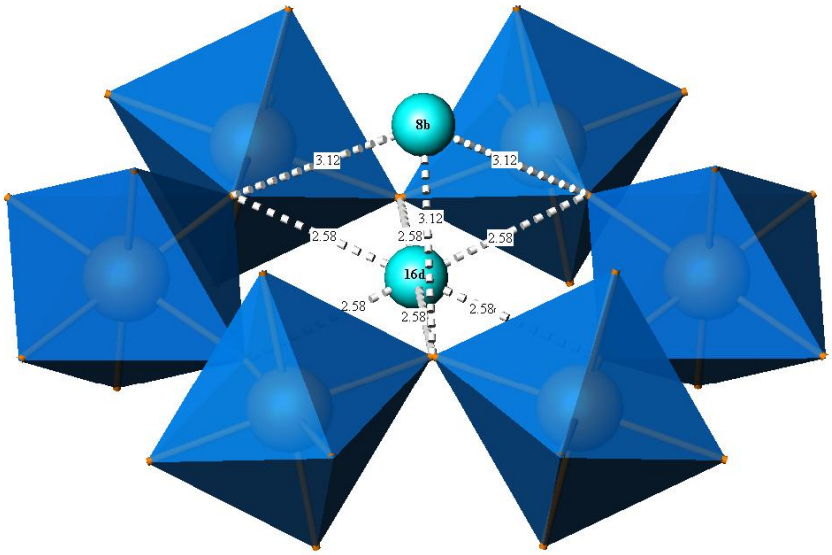

Figure 3.5.6 – Schematic of $KTeNbO_6$ showing the coordination environments achievable for the potassium ions (turquoise) on the 8b and 16d sites within the cavities. The available 32e sites lie between these two sites with a variety of coordination environments possible.

Figure 3.5.6 shows the range of possible sites that can potentially be occupied by the potassium ions in this model and the variation in coordination environment that any atomic shift allows. The initial model for $KTeNbO_6$ places the potassium ions on a 32*e* site between the 8*b* and 16*d* sites shown. At higher temperature the average ion position appears to move towards the 8*b* site as the thermal energy and associated thermal motion they gain requires a more complete coordination environment.

The constant and approximately linear increase in lattice parameters also indicates no loss of water as the materials are heated, ruling out the possibility that the large thermal motion of the potassium ions can be explained by displacement away from the modelled 8*b* site by inclusion of water within the framework. This was confirmed by TGA which showed no significant mass loss as the materials were heated.

In this analysis of the polycrystalline material the trapping of the cation appears to occur randomly leaving the $Fd\bar{3}m$ description with statistically disordered potassium ions as the best model. The distance between the metal centres of the octahedra, from which the size of the channels within these frameworks are derived, remain reasonably constant throughout the series whilst the alkali metal ion increases in size (for K, Rb and Cs the size of the cations being 1.55 Å, 1.63 Å and 1.78 Å respectively), leading to an effect referred to as 'rattling'. As previously discussed,

this process as described by Kunes and Pickett[22] for materials of this type, suggests a movement of the alkali metal ions away from the idealised 8*b* site in the centre of the tetrahedral cavities towards four off-centre 32*e* positions closer to the 16*d* sites (the additional site occupied by the *A*-type cation in a conventional *alpha*-pyrochlore). The term "rattling" arises from observations that the alkali metals ions undergo local vibrations between these four available 32*e* sites, leading to an observable average of an 8*b* position at the centre of these sites with a large degree of thermal motion attributed to the ion. Figures 3.5.7, 3.5.8 and 3.5.9 show the thermal motion of each atom with respect to temperature for the three phases $CsNbTeO_6$, $RbNbTeO_6$ and $KNbTeO_6$. These graphs show the thermal motion of each alkali metal increasing, as expected, with rising temperature. The thermal motion gained for each atom however is not equal and provides more evidence for the level of coordination achieved by each cation in their respective networks. Figure 3.5.9 is included to show that for each phase the Nb/TeO_6 networks display comparable thermal stability to one another regardless of their host cations. Thermal motions associated with the octahedra are as expected, with similar vibrational energies on the metal and bonded oxygen. In each case the oxygen atoms have a slightly higher degree of thermal motion, as would be expected for a lighter element.

It is of interest to note that whilst at low temperatures the caesium and rubidium cations display similar degrees of thermal motion as the supporting framework at low temperature this convergence of thermal motion for the entire structure never occurs in the potassium-containing phase. This behaviour supports the idea that the potassium instead settles onto a fixed crystallographic position and in this way improves the overall stability of the framework.

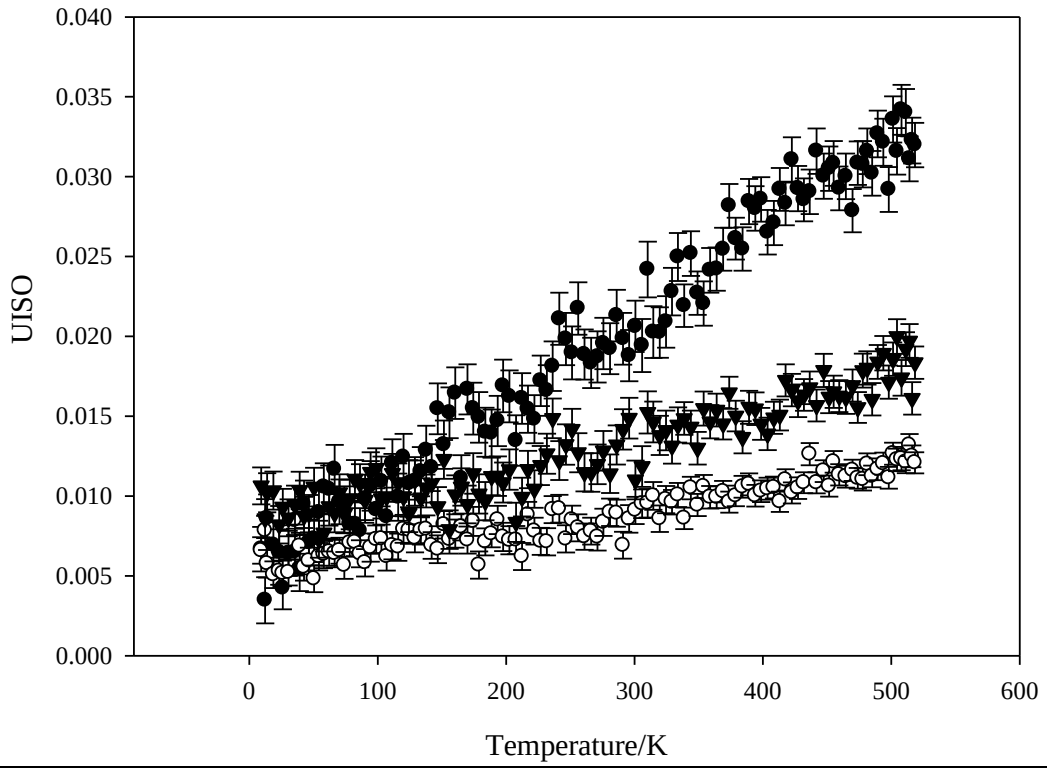

Figure 3.5.7 – Refined isotropic temperature factors for the atoms comprising $CsNbTeO_6$ where Cs (●), Nb/Te (○) and O(▼) with associated calculated errors.

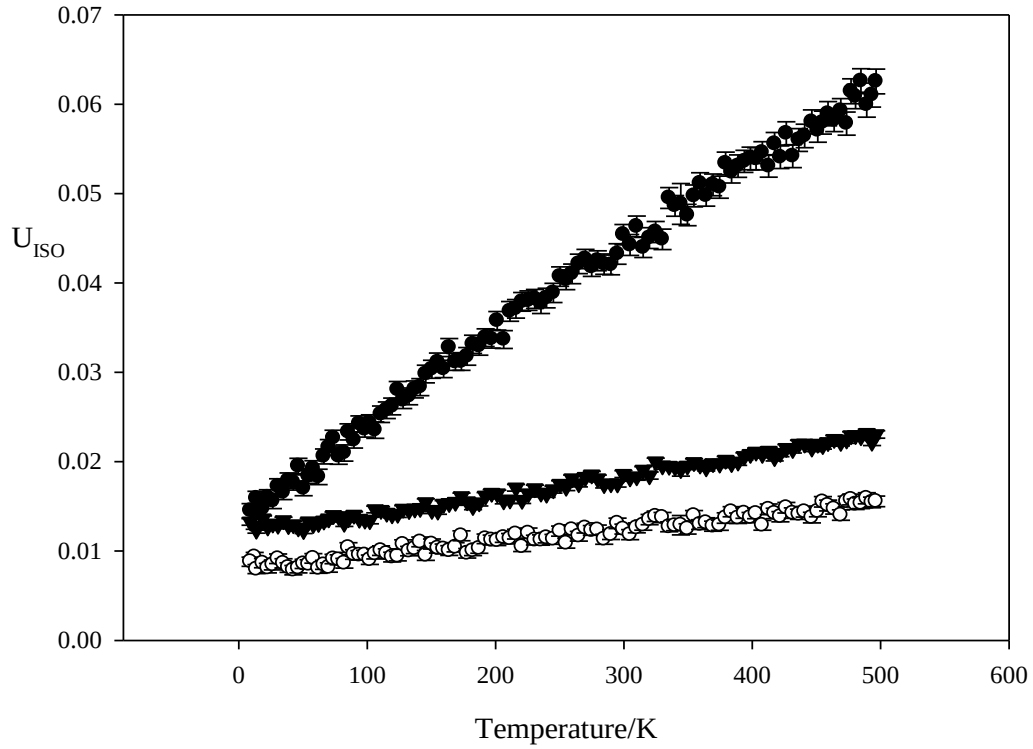

Figure 3.5.8 – Refined isotropic temperature factors for the atoms comprising $RbNbTeO_6$ where Rb (●), Nb/Te (○) and O (▼) with associated calculated errors.

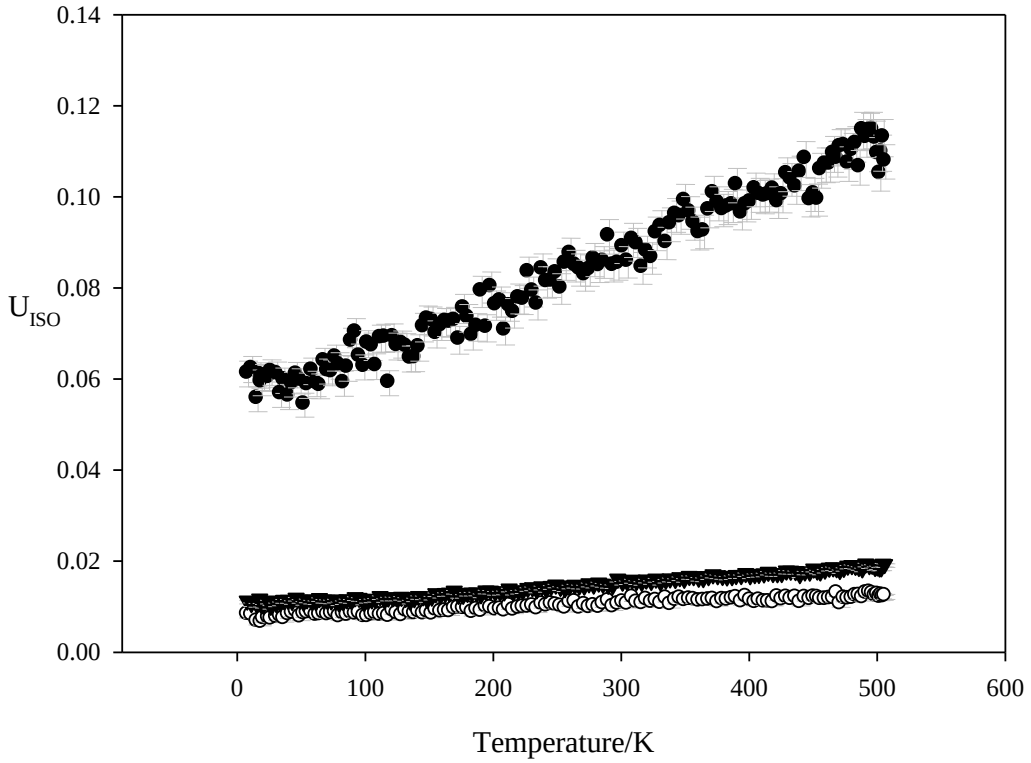

Figure 3.5.9 – Refined isotropic temperature factors for the atoms comprising $KNbTeO_6$ where K (●), Nb/Te (○) and O (▼) with associated calculated errors.

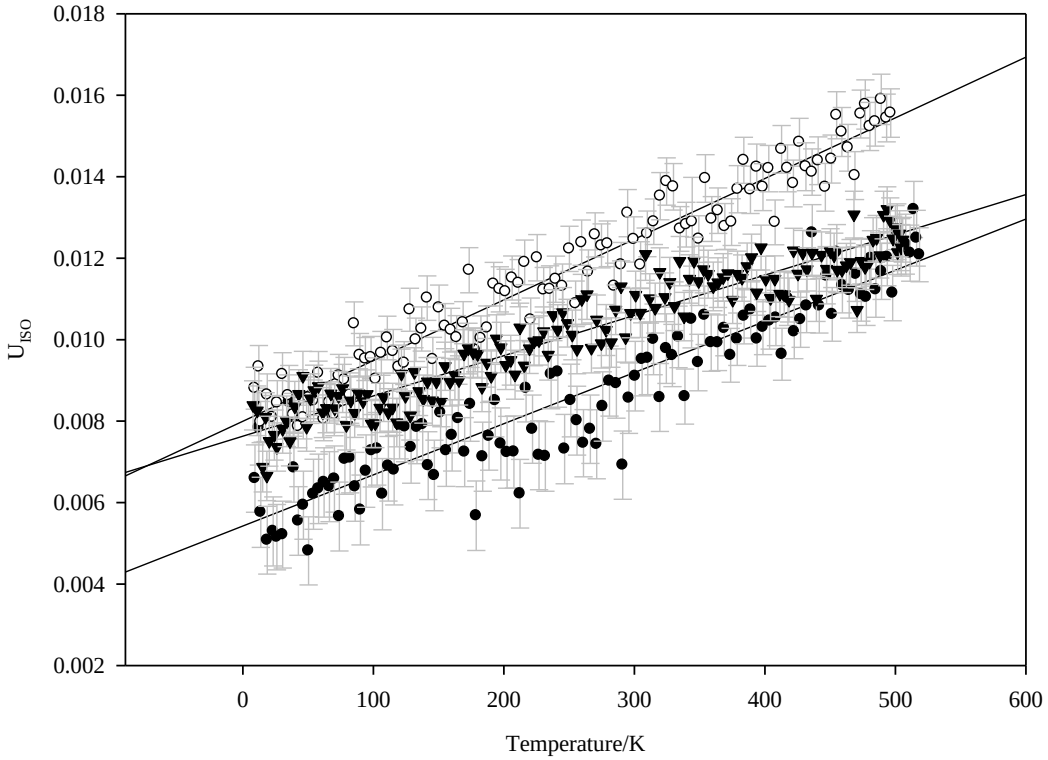

Figure 3.5.10 – Refined isotropic thermal parameters for Nb/Te atoms in $KNbTeO_6$ (▼), $RbNbTeO_6$ (○) and $CsNbTeO_6$ (●) along with associated errors and calculated trend lines.

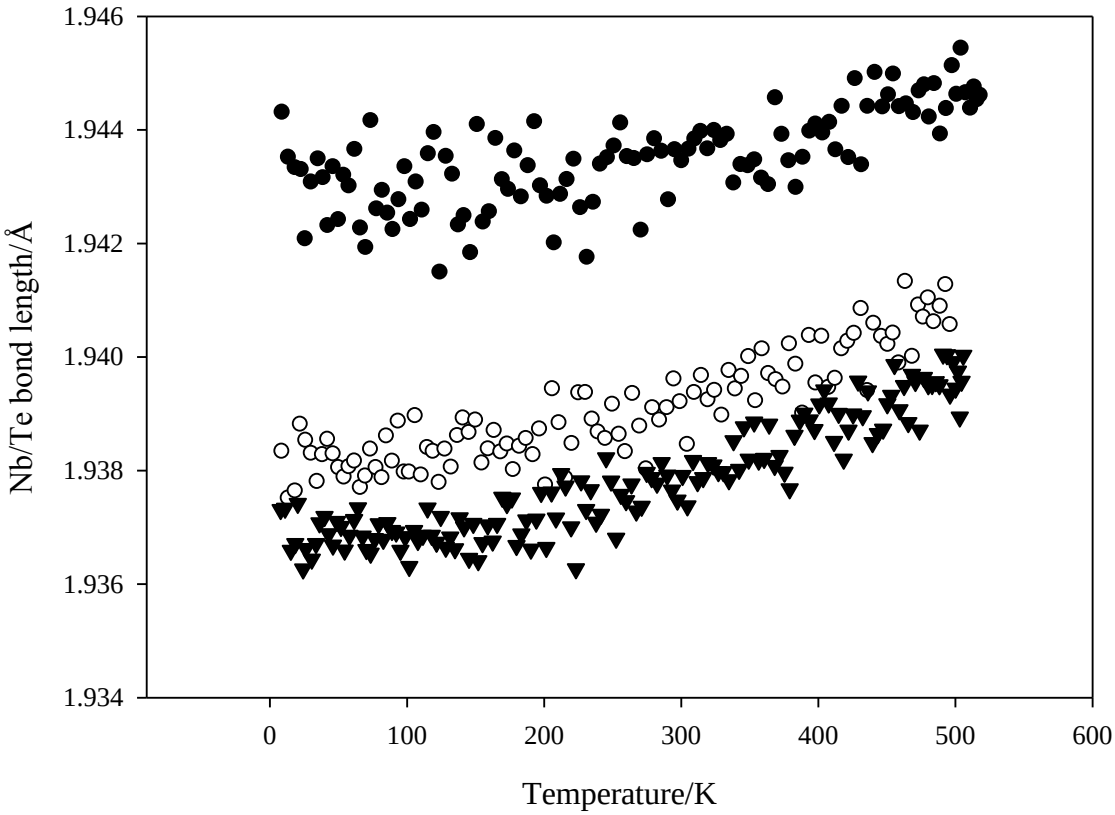

Figure 3.5.11 – Refined Nb/Te-O bond lengths for $KNbTeO_6$ (▼), $RbNbTeO_6$ (○) and $CsNbTeO_6$ (●).

A plot of the calculated oxygen-transition metal bond lengths, Figure 3.5.11, shows the effects of increasing thermal energy on the BO_6 framework. What we observe is normal thermal expansion for a material of this sort with only a small lengthening of the oxygen bond length. To a large degree this can be explained by the stability of the BO_6 network which retains its structure and expands only slightly with the increasing size of the *A* cation. The similarity in bond lengths and lattice parameters for the rubidium and potassium samples can be explained by the ions being smaller than the cavities they inhabit; therefore the size of these ions and their increasing thermal motion with temperature has little effect upon the overall size of the unit cell. However in $CsNbTeO_6$ the caesium ion is effectively filling all the available space within the cavity and therefore an increased cavity size allows for overall relaxation of the framework. This is created by increasing the size of the BO_6 octahedra in turn causing an elongation of the metal/oxygen bond length, and increase in unit cell size.

A further change arising from the changes in effective alkali metal ion sizes is the level of distortion of the polyhedral units comprising the B_2O_6 framework. Whilst rarely a marked effect in these octahedra it is often a strong indicator of how readily the *A*-site cation is being accommodated and may suggest the level of strain within the material.

Figure 3.5.12 shows the angles within the polyhedra as calculated from the longer 2 K data collections. In each case all six Nb/Te-O bond lengths are identical with the only distortions arising from a change in the internal bond angles. Whilst the rubidium and potassium phases appear identical the level of distortion observed in the caesium compound is marginally less. This is in good agreement with what we have seen in the remainder of the data with the smaller rubidium and potassium cations encouraging structural changes to allow for better overall coordination. Inspection of the same octahedral angles, but at 500 K, shows very little change with the octahedra of the potassium phase retaining the same geometry and the rubidium and caesium phases relaxing slightly, by ~0.2°, implying the temperature has marginal effect upon this distortion and that the majority of this effect arises purely from alkali metal ion size.

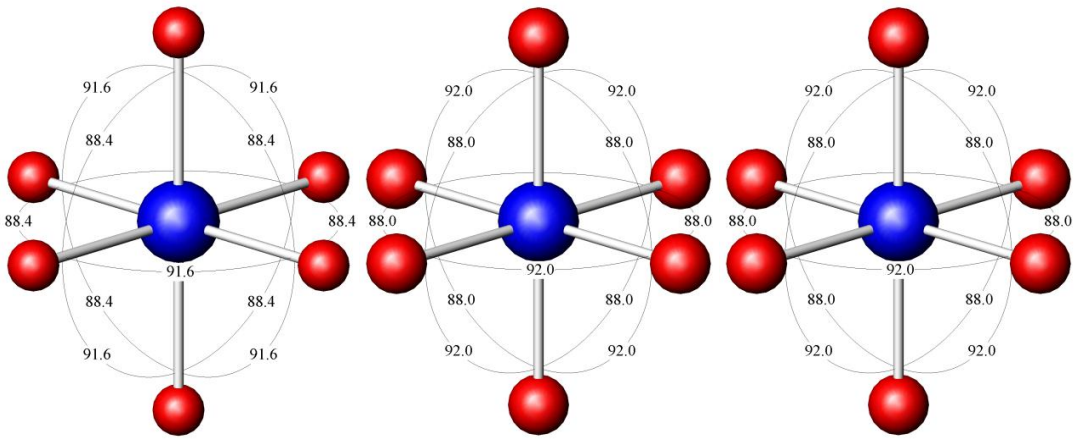

Figure 3.5.12 – Refined angles for the Nb/Te-O bonds from 2 K data sets, from left to right they represent the octahedra of $CsNbTeO_6$, $RbNbTeO_6$ and $KNbTeO_6$.

A significant part of the rationale behind this work was to provide direct comparison between the behaviour of the series AOs_2O_6 and $ANbTeO_6$ (where A = Cs, Rb and K). Of particular interest to us were the similarities between the low temperature behaviours of KOs_2O_6 and $KNbTeO_6$ both of which displayed a localisation of the potassium ions on to a fixed site away from the 8*b* site. Figures 3.5.13 and 3.5.14, below, show the coordination environment of the potassium ions in $KNbTeO_6$ with the potassium shifting significantly closer to the oxygen atoms of the B_2O_6 network at low temperatures allowing for better coordination of the potassium ions and

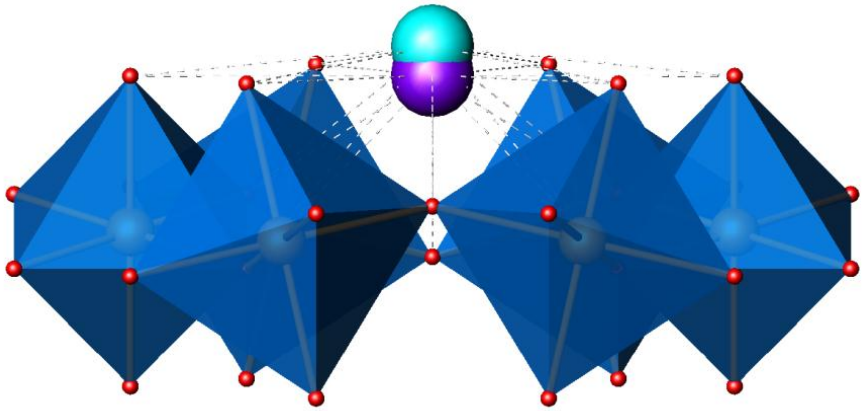

Figure 3.5.13 – Schematic showing the two proposed coordination environments in $KNbTeO_6$. Purple is the theorised position at 2 K and turquoise the position above 70 K. Polyhedra represent the Nb/Te-O octahedral units.

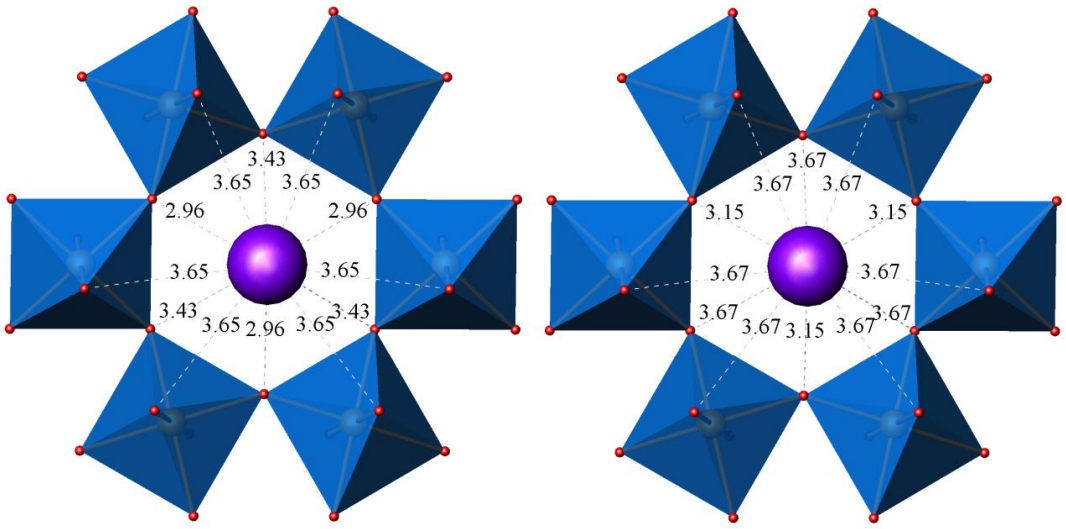

Figure 3.5.14 – The left hand image shows the coordination environment at 2 K of the potassium ions (purple). The right hand image shows the coordination if the potassium ions remained on the 8b site. K-O bond lengths are given in Å and the polyhedra represent the Nb/Te-O octahedral units.

therefore lowering the overall free energy of the structure. This behaviour is further evidenced by the non-Grüneisen-type contraction we observe in the lattice parameter with respect to temperature, where we initially see the lattice parameter stabilising then further contracting. This trend can be explained through consideration of what is occurring within the pyrochlore channels. The movement of the potassium ions away from the central 12-coordinate 8*b* site towards the 6-fold 16*d* site inhibits the contraction of the framework. A contraction in overall lattice parameter also leads to a reduction in the size of the 16*d* site, with the movement of the potassium ions towards this site becoming significantly less favourable. Figure 3.5.13 shows the change in coordination environment associated with this movement and it can be seen that a significant improvement is achieved.

Overall the behaviour between the two phases is predictable with similar trends followed by all compounds; in each case a reduction in alkali metal ion size leads to an increased thermal motion on these ions. Lattice behaviour is also isotypic in corresponding phases with typical Grüneisen behaviour seen in both rubidium and caesium containing materials. Finally KOs_2O_6 and $KNbTeO_6$ show a similar trend in behaviour with the potassium ions settling onto refineable positions away from the 8*b* site. As would be predicted this occurs at a higher temperature and to a more significant degree in $KNbTeO_6$, the larger of the two phases, where at 2 K the cations have shifted by ~0.35 Å as opposed to 0.23 Å in KOs_2O_6.

It is also worth noting that more recent work carried out within the research group[49], discussed in more detail later in this work, implies that KOs_2O_6 can incorporate limited amounts of water into its framework, in the region of 0.05 waters per unit cell and that this can have significant effects upon the materials' behaviour and lattice parameter. This behaviour was not however observed in the potassium phase studied here even with a fractionally larger lattice volume being displayed by $KNbTeO_6$. Recorded TGA data showed no mass loss associated with a dehydration event and no rapid lattice parameter shift is observed above room temperature as had been seen in other hydrated phases upon water loss[58].

Whilst $Fd\bar{3}m$ remains the best model for this polycrystalline sample of $KNbTeO_6$ it is also worth noting that in single crystal samples such displacements of the potassium ions could occur in a more concerted manner in portions of the crystal leading to domains of lower symmetry. If such domains were large enough then single crystal diffraction studies may show extra reflections consistent with the lower symmetry of the ordered regions.

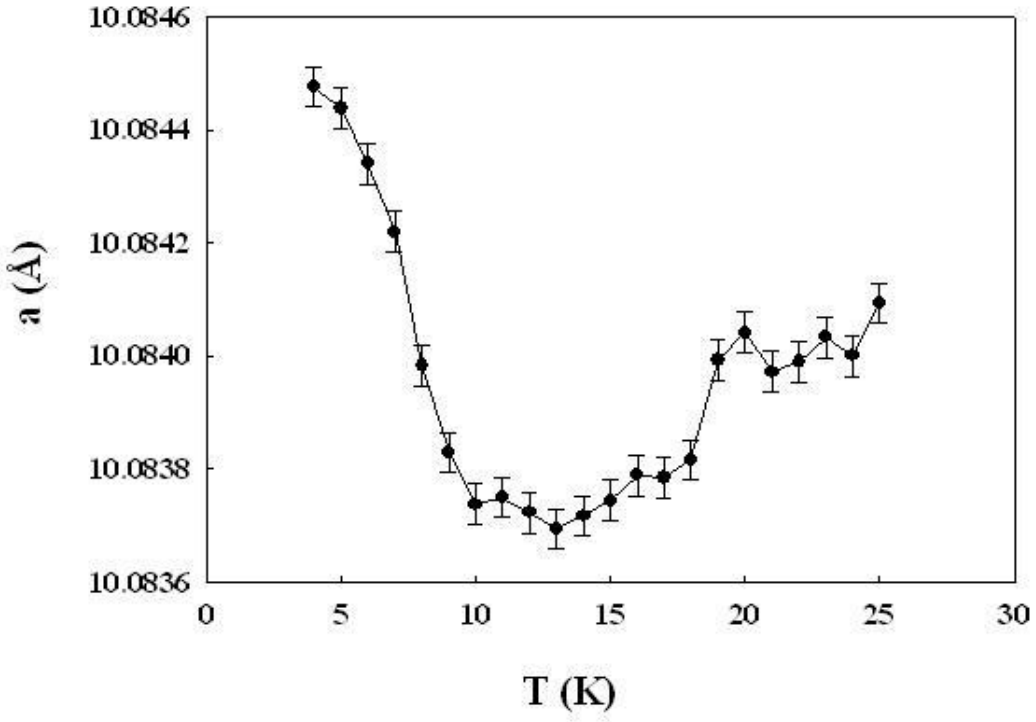

Figure 3.5.15 – Refined lattice parameters for KOs_2O_6 from low temperature data collected on the D2B instrument at the ILL. Data was collected and refined by Miss R. Galati

Finally there is the indication that negative thermal expansion may be occurring in $KNbTeO_6$ as observed in KOs_2O_6 at low temperature. Very similar behaviour has been observed in other materials where delocalisation of an atom from split and partially occupied sites occurs as a function of temperature. In Ba_6Ge_{25} the structure at low temperatures has been modelled with the barium atom split over two sites whose separation markedly varies with respect to temperature, while at room temperature a fully ordered model may be used. The transition between these two models occurs between 200 and 250 K and is associated with negative thermal expansion of the material. It is also of interest that this structural change is

associated with a significant drop in the electrical conductivity of this material[59]. To fully clarify this structural behaviour further low temperature work would be required. It may also be of interest to look at the low temperature electrical conductivity of $KNbTeO_6$ to see if the structural change here also leads to a change in resistance as seen elsewhere[60].

3.6 Variable temperature studies of $CsNbWO_6$

As part of the further study to better characterise the series $ABB'O_6$ a thorough literature search was undertaken to establish any unexplained behaviour within these materials that could be attributed to changes in the overall structure. Dielectric measurements undertaken by Kar and Choudhary[2] reported small anomalies in the behaviour of $CsNbWO_6$ and $CsTaWO_6$ at 183 ± 2 and 328 ± 2 K respectively. It was also noted from refined PXRD data in Section 3.4.3 that $CsNbWO_6$ displayed a variable oxygen positional parameter where $x < 0.3125$, the only *beta* pyrochlore studied to do so, suggesting an elongation of the octahedral building units along the [111] direction.

3.6.1 PND data collection

A single phase sample of $CsNbWO_6$ was prepared by a conventional high temperature route, with the exact preparatory method described previously in Section 3.2.1. To reduce data collection times larger quantities of sample were prepared. This was undertaken by the amalgamation of several phase pure samples of ~1 g which were ground together, pelletised and annealed for 8 hours at 700°C. This method produced a monophasic sample, as confirmed by PXRD, of suitable size for further data collection.

Powder neutron diffraction data were collected on the D1A instrument at the ILL, Grenoble between 12 and 157.9° 2θ with a collection time of ~4 hours per data set. Measurements were undertaken at four temperatures: 2, 160, 200 and 300 K. Each data set was independently refined using the GSAS[33,34] refinement suite using the model originally presented by Babel *et al*[4] which suggests that $CsNbWO_6$ adopts the typical *beta*-pyrochlore structure type.

3.6.2 Structural refinement

Final analysis was carried out on data collected between 14 and 150° 2θ as this region covered all the observed reflections within the data sets whilst excluding several instrument-derived peaks. All refinements proceeded smoothly with initial variation of background coefficients, lattice parameter and zero point displacement. Once these proved stable, a pseudo-Voigt peak shape function was also introduced. Finally atom parameters and thermal factors were introduced to the refinement. All

parameters varied refined smoothly and stably across the entire temperature range studied. As with all pyrochlores where multiple atoms randomly occupy the same site niobium and tungsten were constrained for all their variable parameters.

Table 3.6.1 – Refined atomic parameters for a room temperature PND data set of $CsNbWO_6$. E.S.D's are given in parentheses.

Atom	Site	*x*	*y*	*z*	Occupancy	U_{iso}
Cs	8*b*	0.375	0.375	0.375	1	2.31(15)
Nb	16*d*	0	0	0	0.5	1.96(11)
W	16*d*	0	0	0	0.5	1.96(11)
O	48*f*	0.31208(17)	0.125	0.125	1	1.50(6)

Space group $Fd\bar{3}m$. Cell parameters: $a = b = c = 10.3989(6)$ Å

Final fit parameters: $\chi^2 = 5.052$, $R_{wp} = 6.23\%$, $R_p = 4.80\%$

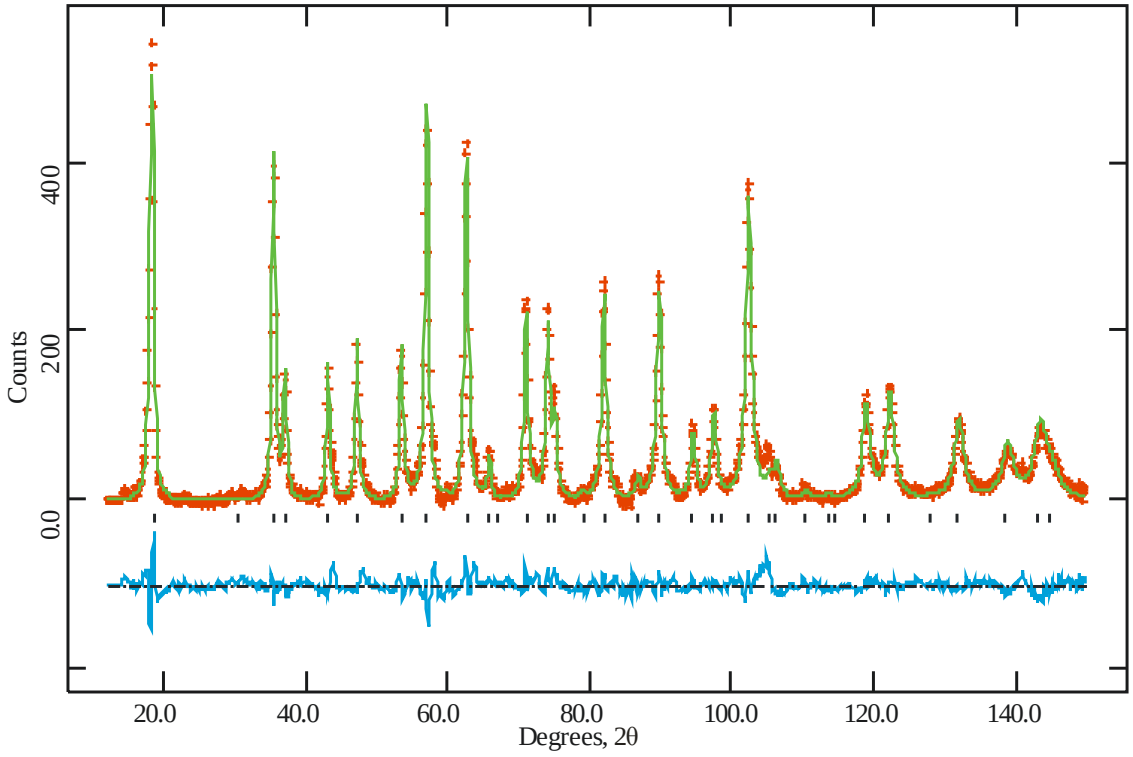

Figure 3.6.1 – PND refinement profile for $CsNbWO_6$ at room temperature. Crosses indicate observed data, the continuous green line the calculated profile and the lower blue line the difference. Tick marks indicate allowed reflection positions.

All four data sets fitted well with similar levels of fit throughout. Examination of the peak shape provides no evidence of splitting that would be associated with a possible structural change leading to a lowering in symmetry, nor were any new peaks observed in the data that would forbid the use of the $Fd\bar{3}m$ spacegroup. Lattice parameters, shown in Figure 3.6.2, show a slow, constant contraction of unit cell with decreasing temperature in line with other materials of this type. However careful study of the structural changes occurring along with this contraction implies that something different is occurring.

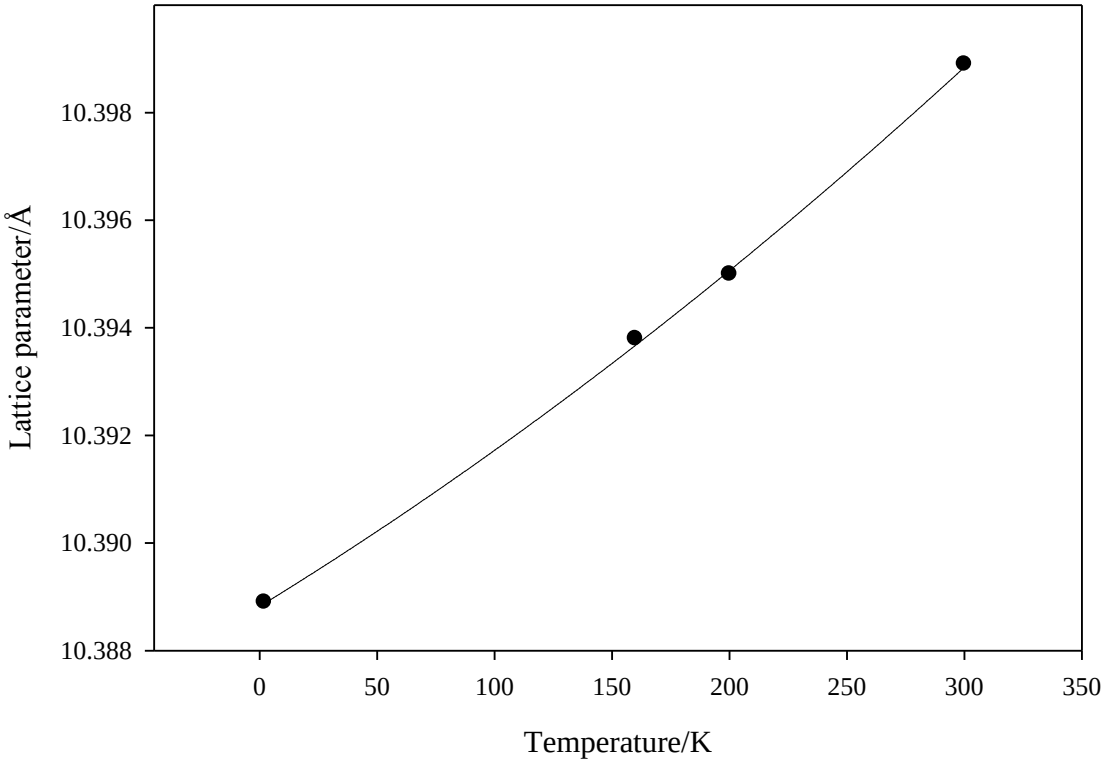

Figure 3.6.2 – A plot of refined lattice parameters vs temperature from PND data for $CsNbWO_6$.

As discussed earlier in this chapter the main driving force in lattice contraction for *beta*-pyrochlores appears to be through a shortening of the metal-oxygen bond length leading in turn to smaller polyhedra which in turn determine the overall unit cell size. Commonly the reduction in thermal motion, associated with the lowering in temperature, also leads to a change in the polyhedra to more 'perfect' shapes with bond angles nearer to 90° throughout; although in materials of this type the distortion is rarely substantial. In this material the behaviour appears to be somewhat different. Figure 3.6.3 shows that while the polyhedra tend towards the 'perfect' coordination

at low temperature, when x = 0.3125 the O-M-O bonds are at 90°, this is not accompanied by the expected contraction in bond lengths, which appear to remain relatively constant across the temperature range studied. In turn study of the various degrees of thermal motion exhibited by the atoms present shows that, as expected the Nb/W and O drop off at a consistent rate with respect to temperature. The caesium's thermal motion however drops much more rapidly than either of the other two sites, this may suggest that the effect upon its surrounding environment may also change as the caesium settles to what is effectively a more localised position at low temperature. This behaviour appears to be fairly typical with similar changes observed in the thermal motion, with respect to temperature, for the $CsNbTeO_6$ phase discussed in Section 3.5.

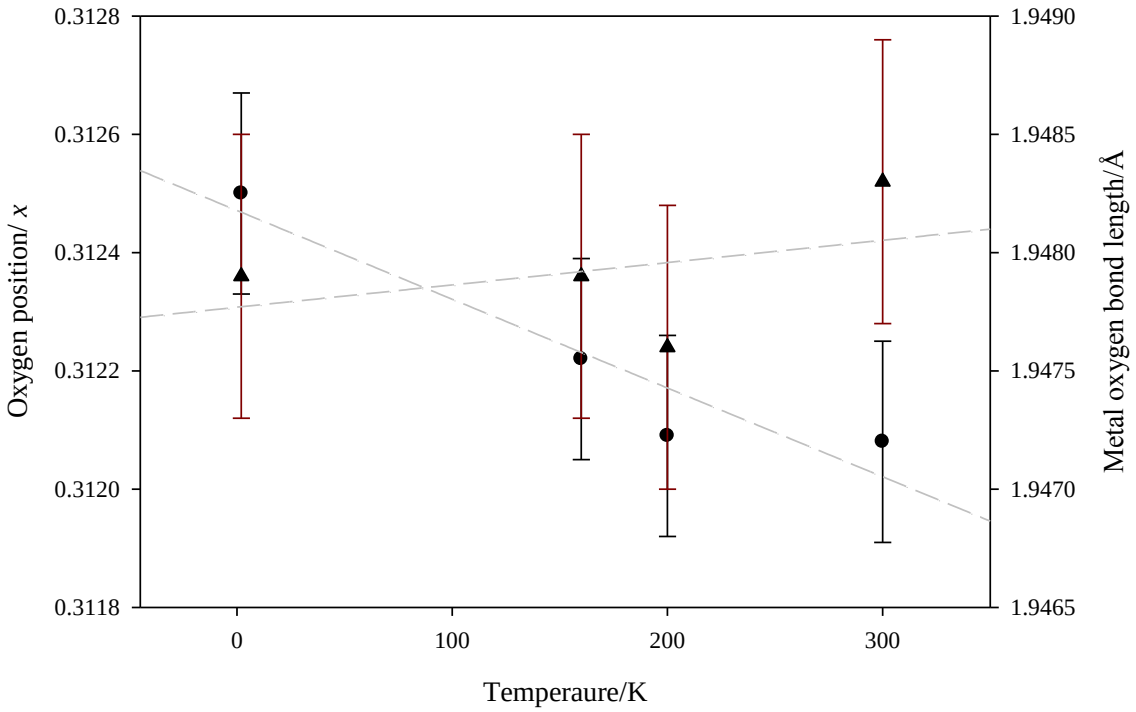

Figure 3.6.3 – Refined oxygen positions (●) and metal oxygen bond lengths (▲) from PND data for $CsNbWO_6$ along with calculated error bars.

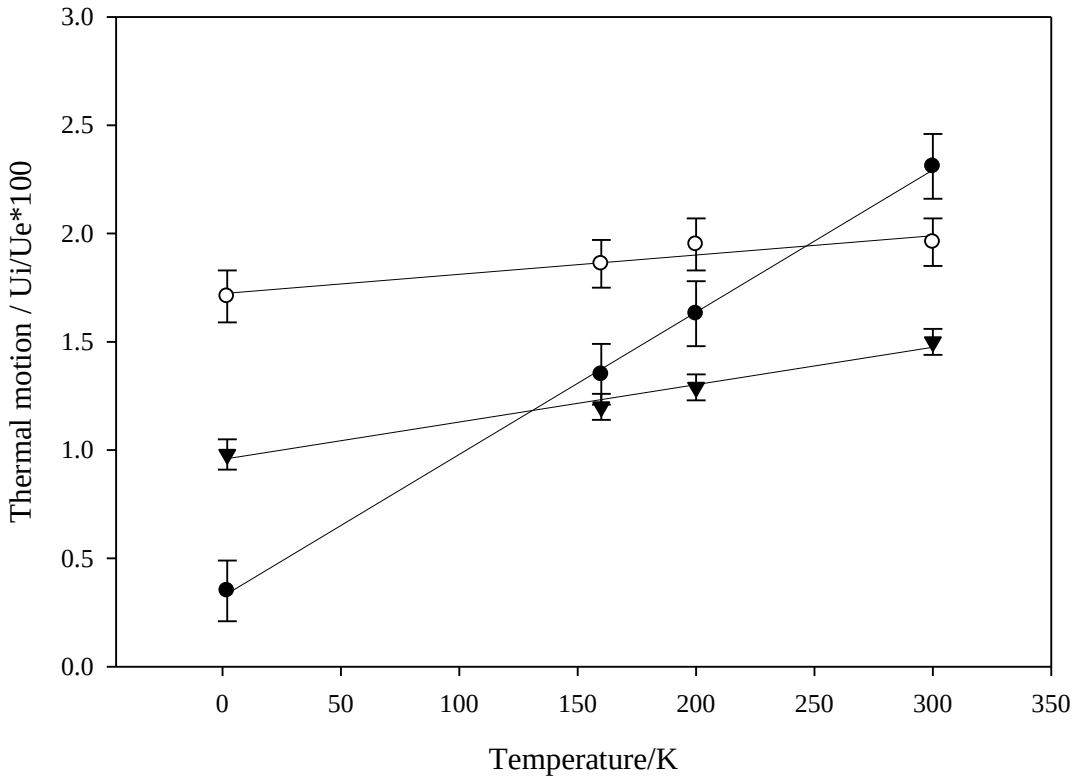

Figure 3.6.4 – Refined displacement parameter for Cs (●), Nb/W (○) and O (▼) in $CsNbWO_6$, along with associated calculated errors.

3.7 Synthesis and characterisation of $CsTa_2O_{6-x}$

This material was synthesised as part of a wider attempt to synthesise new rhenium containing *beta*-pyrochlores, a family of materials that have not yet been successfully characterised. Whilst it was initially hoped that a rhenium-containing phase had been produced the conditions, coupled with the choice of starting materials (the reaction being carried out at 400°C, only 20°C below the decomposition temperature of ReO_3, the rhenium source used), ensured there was a high probability that this would not be the case. It was quickly shown using EDX compositional analysis that no rhenium had been incorporated into the phase. However, any pyrochlore-type phase with only tantalum occupying the *B*-cation site must be oxygen deficient to achieve the desired stoichiometry. As no pure Cs/Ta/O pyrochlores have previously been presented in the literature and there was the possibility of oxygen deficiency present in the B_2O_6 network further study was undertaken.

3.7.1 Synthetic route

As previously mentioned the phase was synthesised in an unconventional manner; further attempts at direct synthesis proved ineffectual with no pyrochlore phase forming. Thus, materials with the stoichiometry required for $CsReTaO_6$ were used. The sample was synthesised from Cs_2CO_3 (Fluka, 99%), ReO_3 (Aldrich) and Ta_2O_5 (Aldrich, 99%) which were ground together under nitrogen to avoid the rapid hydration of Cs_2CO_3. The ground sample was then pelletised and annealed for 16 hours under flowing oxygen at 400°C. Analysis of PXRD data showed a single phase sample with all the reflections being readily assigned to the cubic pyrochlore system. Calculations of dummy histograms for both the *alpha* and *beta*-pyrochlore phases with the respective general formulae $Cs_2Ta_2O_7$ and $CsTa_2O_6$ showed a closer match to the *beta* structure type which was thus used as a starting model from this point.

3.7.2 Compositional analysis

EDX measurements were initially undertaken to establish the presence or lack thereof of rhenium. The scan showed no rhenium to be present, with only caesium, tantalum and oxygen within the sample. The relative ratios of caesium to tantalum correspond well to those what would be expected in a *beta*-pyrochlore phase at approximately 1:2.

Table 3.7.1 – Calculated compositional analysis from EDX data

Element	Weight %	Atomic %
O	4.64	33.52
Cs	24.18	21.03
Ta	71.18	45.45
Re	0.00	0.00
Total	100	

TGA analysis carried out alongside this showed no mass loss (such as would be expected if the structure also incorporated water molecules), with structural collapse occurring at ~570 °C.

3.7.3 PXRD analysis of $CsTa_2O_{6-x}$

Data were collected over the 2θ range 10 to 110° with a step size of 0.02° over a period of 48 hours on a Siemens D5000 diffractometer. Refinements were then carried out using the GSAS rietveld refinement suite of von Dreele and Larson[33,34]. The crystallinity of the sample proved to be extremely poor with a very low degree of scattering. A starting model assuming a standard *beta*-pyrochlore arrangement was initially used which accounted for all observed reflections.

The refinement proceeded smoothly with initial variation of the background parameters and peak profile coefficients coupled with the lattice constants and zero point. Isotropic temperature factors were then introduced for each atom followed by the refinement of the one variable coordinate, that of the *x* position of the oxygen atoms. The variation of these parameters led to the expected improvement in the least-squares fit. Once a satisfactory model had been established variation of the occupancies of each site were undertaken independently of one another. The occupation of both the tantalum and caesium sites proved stable with occupations remaining within 1-2% of the starting values. The oxygen site, in contrast, varied sufficiently for the change to appear meaningful with a loss of ~10% electron density on the 48*f* site. This behaviour has previously been observed in both *alpha* and *beta* pyrochlores[61,62] and was thus seen as reasonable to include within the model. The final model used is presented in Table 3.7.1. This model gives a charge balanced formula that (within errors) results in a stoichiometry of $CsTa_2O_{5.5}$ which is therefore used as the composition in subsequent discussions.

Table 3.7.1 – Refined atomic parameters for a PXRD room temperature data set of $Cs_xTa_2O_6$ with associated E.S.D.

Atom	Site	*x*	*y*	*z*	Occupancy	U_{iso}
Cs	8*b*	0.375	0.375	0.375	1	5.56(17)
Ta	16*d*	0	0	0	1	2.43(8)
O	48*f*	0.3179(13)	0.125	0.125	1	0.89(3)

Space group $Fd\bar{3}m$. Cell parameters: $a = b = c$ =10.4983(5) Å

Final fit parameters: χ^2 = 1.498, R_{wp} = 25.38%, R_p = 18.69%

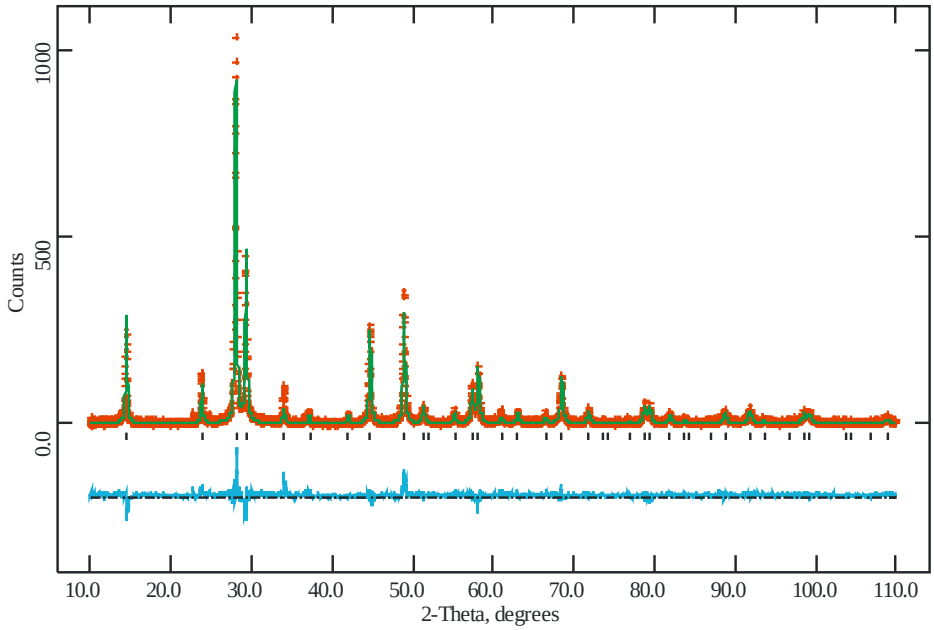

Figure 3.7.2- Profile fit for a room temperature PXRD data set of $CsTa_2O_{5.5}$. Experimental data points are shown as red crosses, upper continuous line the calculated profile and the lower continuous line the difference. Allowed reflection positions are indicated by tick marks.

3.7.4 Discussion

Overall the collected data provided a good level of agreement with the calculated powder pattern. Inspection of the final model used, Table 3.7.1, shows behaviour as expected in a *beta*-pyrochlore with the oxygen variable positional parameter, *x*, being >0.3125 indicating a compression of the TaO_6 polyhedra. The thermal displacement parameters of the various atoms vary significantly, the tantalum and caesium ions display reasonable levels of motion, with the caesium being slightly higher than would strictly be expected at room temperature. In contrast the oxygen atoms display a very low degree of thermal motion, it is expected that to some degree this is a result of the quality of the data which seems reasonably poor due to a low degree of sample crystallinity, coupled with the oxygen deficiency on this site increasing the complexity of the problem being studied.

The tantalum-oxygen bond lengths, at 2.008(5) Å, are marginally shorter than those of octahedrally coordinated tantalum atoms seen in similar studies[63,64], which are typically closer to 2.1 Å. This is an expected trend as the degree of oxygen deficiency requires an increased bond valance contribution to each tantalum centre which can be readily provided by a contraction of these bonds. The octahedra these

bonds make up are somewhat more distorted than is typical of materials of this type displaying an internal O-Ta-O bond angle of 94.2°. This can be explained by distortions arising from the significant oxygen deficiency displayed in this material; a relaxation of the surrounding bonds can reasonably be expected when one of the interlocking metal-oxygen-metal bonds does not form due to a lack of oxygen. As no ordering of these deficiencies is observed this would be characterised by a change in the average bond angle, it is possible that with higher quality data the structure would be better modelled by the introduction of a second oxygen site allowing for separate areas of electron density arising from locally 'ideal' octahedra and those where the effective coordination is that of a square based pyramid with a local TaO_5 unit.

The extracted lattice parameters seem reasonable for this material: comparison to similar materials, presented in Tables 3.7.2-3, show a lattice parameter in between these two previously presented phases. As expected, the change in *B*-site cation from $CsTaWO_6$ to $CsTa_2O_{5.5}$ leads to a significant increase in lattice parameter, from 10.361 Å to 10.498 Å in line with the increase in average *B*-site ionic radius that this corresponds to. The framework $H_2Ta_2O_6$, a pyrochlore-type material with the *A*-site cations occupying atypical sites very close to the oxygen atoms of the framework

Table 3.7.2 – Refined atomic parameters for a room temperature data set for $CsTaWO_6$

Atom	Site	*x*	*y*	*z*	Occupancy	U_{iso}
Cs	8*b*	0.375	0.375	0.375	1	2.93(3)
Ta	16*c*	0	0	0	0.5	1.774(15)
W	16*c*	0	0	0	0.5	1.774(15)
O	*48*f	0.3191(3)	0.125	0.125	1	1.82(16)

Space group $Fd\bar{3}m$. Cell parameters: $a = b = c = 10.3606(3)$ Å

Table 3.7.3 – Extracted atomic parameters for a room temperature data set of $H_2Ta_2O_6$ as presented by Groult et al[17]

Atom	Site	*x*	*y*	*z*	Occupancy	U_{iso}
H	48*f*	0.402	0.125	0.125	0.3333˙	5.4
Ta	16*c*	0	0	0	1	1.82
O	48*f*	0.3109	0.125	0.125	1	1.06

Space group $Fd\bar{3}m$. Cell parameters: $a = b = c = 10.6032(6)$ Å

can be considered as a fully relaxed material with the polyhedra in something close to their ideal coordination environments. With oxygen deficiency present in the $CsTa_2O_{5.5}$ phase, however, we would expect a contraction in lattice parameter regardless of the *A*-site cation effects, arising from the previously mentioned contraction of tantalum-oxygen bond lengths. It is also possible that the inclusion of caesium ions leads to a higher degree of distortion in the octahedra to allow better coordination of these ions. This is typified by the change in the *x* coordinate of the oxygen atoms observed in $CsTaWO_6$ and $H_2Ta_2O_6$, where an increase in this value is seen when the larger caesium cation is incorporated onto the *A*-site, matching the behaviour seen in $CsTa_2O_{5.5}$.

The degree of electron density available is significantly increased by this tilting motion producing a 12-coordinate environment with six 3.17 Å and six 3.75 Å Cs-O distances, whereas un-tilted octahedra in the same model would lead to distances of 3.28 Å and 3.78 Å respectively. This reduction of Cs-O distance brings the average distances much closer to those predicted by theoretical considerations which lead to an ideal average bond length of ~3.25 Å in these coordination environments. It is also interesting to note that this coordination is almost identical to those seen in $CsTaWO_6$ where the coordination is produced by bonds of 3.17313(3) Å and 3.70914(3) Å. It is also not dissimilar to those of $CsTaTeO_6$ at 3.159(3) Å and 3.6826(4) Å.

3.8 Conclusions

3.8.1 PXRD and synthetic studies of the *beta*-pyrochlore series $ABB'O_6$ where *A* = K, Rb or Cs, *B* = Ta, Nb or Sb and *B*' = Mo, W or Te

In general it can be seen that *A*-site cation size plays an important role in determining the overall unit cell dimensions in *beta*-pyrochlores and that one of two environments are normally observed; either the cation is trapped into a smaller than ideal site and thus acts to force the unit cell to be larger than would be the case if the polyhedra relaxed to their idealised positions (where the oxygen atom occupies (0.3125, 0, 0)) or that the cation displaces to a 32*e* site allowing the framework to relax. We have also seen that whilst unit cell size is affected by several factors the primary determining factor is the ionic radius of the *B*-site cation with the radius of the larger of the two atoms sharing this site providing the dominant contribution.

The oxide materials presented here show a limited dependency upon the relative sizes of the two *B*-site cations as a formation determining factor. This can be seen in terms of which series will form completely and which are only stable when an *A*-site cation that can be tightly coordinated, typified by a lower degree of thermal motion, is present. In terms of these materials this has generally been for caesium which tends to provide a more ideally sized cation for the larger *B*-site cations. This type of behaviour is entirely typical of many metal oxide structure types, where the relative size of various atoms within the framework determines the structure type that forms. This argument can be used to explain why both ATaWO$_6$ and ANbWO$_6$ form for the complete series with both transition metals being similar in size to one other in each case. For other phases such as ANbMoO$_6$ and ATaMoO$_6$ the cation size appears to be marginally more significant and only the caesium phases will form.

3.8.2 Variable temperature PND studies of the series *A*$NbTeO_6$ where *A* = K, Rb or Cs

In general it was shown that the behaviour of the lattice framework, with respect to temperature, was determined by the size of the *A*-site cation being incorporated. This was seen most clearly in both the measured lattice parameters, increasing as the cation size increased, and the average level of thermal motion of the framework atoms which decreased as the cation size was increased. Whilst the changes in lattice parameter in general displayed conventional thermal contraction as the temperature was reduced some anomalies were observed at very low temperatures for $KNbTeO_6$. This behaviour appears to be similar to that observed in KOs_2O_6 where at these temperatures the potassium ions are localised onto 32*e* sites reducing the overall thermal motion of the system but resulting in a small increase in lattice parameter. This displacement of the potassium ions proved refineable below ~100 K, a higher temperature than observed in the osmate material. This behaviour is logical as the lattice parameter of $KNbTeO_6$ is greater than in KOs_2O_6 so the potassium ions would be expected to settle onto a site at a higher temperature, as the degree of thermal motion on these atoms is greater.

3.8.3 Variable temperature PND studies of $CsNbWO_6$

Interpretation of the data presented in this study leads us to the conclusion that no major structural changes are occurring that may lead directly to the dielectric anomaly previously observed. It does however seem feasible that a localized effect, with the caesium settling to a more defined structural site, occurs with the reduction in temperature. The localization of this site in turn reduces the need for the polyhedral framework to distort to better coordinate the alkali metal, with these polyhedra then able to relax to a coordination that is ideal within experimental limits.

To enable us to better understand if this shift is marked, with respect to temperature, and therefore more likely to be linked to other observed effects, more data points would be required.

3.8.4 PXRD studies of $CsTa_2O_{5.5}$

This material displays characteristics typical of many oxygen deficient materials with higher levels of distortion within the polyhedral building blocks of the framework and a shortening of the metal-oxygen bonds that compose these polyhedra. Comparison with other similar phases, notably $CsTaWO_6$ and $CsTaTeO_6$, showed that all three materials display coordination environments that are extremely similar to one another, in terms of caesium-oxygen bond lengths, for the *A*-site cations, yet display significant differences in lattice parameter ($CsTaWO_6$ at 10.3606(3) Å , $CsTa_2O_{5.5}$ at 10.4975(5) Å and $CsTaTeO_6$ at 10.28222(15) Å). This behaviour suggests that the coordination of the *A*-site cations, and notably providing sufficient bond valence to these cations, has a significant effect in determining the overall lattice parameter and in turn the size and shape of the octahedra composing the B_2O_{6-x} network.

3.8.5 General conclusions on *beta*-pyrochlores

In general we can observe subtle structural changes in the B_2O_6 network that allow for better coordination of the *A*-type cations. This adaption of the cavity size is achieved in one of two ways; either by a change in the total lattice dimensions derived from a combination of *B*-cation size and metal-oxygen bond length or from smaller distortions in the shape of the BO_6 polyhedra themselves.

Throughout this work, where shared occupancy was displayed on the *B*-site, the relative *B*:*B*' ratios were retained at precisely 1:1 which in turn supports the assumption that the overall stoichiometry is retained as $ABB'O_6$. It is however worth stating that whilst this is an assumption these values were initially refined where possible, but were fixed for the final refinements as no improvement in fit was achieved by compositional variation on this site. In several of the true *beta*-pyrochlore phases, as opposed to the more general defect pyrochlore phases, the oxygen proportion varied if allowed to freely refine, by up to ~5% when studied by PXRD, this variation being observed as both positive and negative levels of occupation. These sites were therefore assumed to be fully occupied and the variation assumed to arise from the weakness of PXRD to accurately determine the position and electron density of light elements when in the presence of heavy ones. When the transition metal occupations were refined this was done so with a constraint so that any increase in one metal led directly to a decrease in the other, typically a very small variation was observed ~1-2% with a slightly larger variation being seen in some phases where the electron density of the two metals sharing the sites were particularly similar to one another. In each case these variations were well within the experimental error and thus the ideal stoichiometry was retained, leading to the conclusion that fully oxidised metal centres are highly preferable in these materials.

3.9 References

(1) Darriet, B.; Rat, M.; Galy, J.; Hagenmuller, P. *Mat. Res. Bull.* **1971**, *6*, 1305-1316.

(2) Kar, T.; Choudhary, R. N. P. *Mat. Sci. and Eng. B-Sol. St. Mat. for Advanced Tech.* **2002**, *90*, 224-233.

(3) Subramanian, M. A.; Aravamudan, G.; Rao, G. V. S. *Progress in Sol. St. Chem.* **1983**, *15*, 55-143.

(4) Babel, D.; Pausewang, G.; Viebahn, W. *Zeitschrift fuer Naturforschung, Teil B. Anorganische Chemie, Organische Chemie* **1967**, *22*, 1219-1220.

(5) Ory, G.; Fourquet, J. L.; Jacoboni, C.; Miranday, J. P.; de Pape, R. *Comptes Rendus Hebdomadaires des Seances de l'Academie des Sciences, Serie C, Sciences Chimiques* **1971**, *273*, 747-750.

(6) Perottoni, C. A.; Haines, J.; da Jornada, J. A. H. *J. of Sol. St. Chem.* **1998**, *141*, 537-545.

(7) Thorogood, G. J.; Kennedy, B. J.; Luca, V. *Physica B: Condensed Matter* **2006**, *385-386*, 91-93.

(8) Man, P. P.; Theveneau, H.; Papon, P. *Sol. St. Ionics* **1983**, *9-10*, 73-76.

(9) Moller, T.; Clearfield, A.; Harjula, R. *Micro. and Meso. Mat.* **2002**, *54*, 187-199.

(10) Alonso, J. A.; Turrillas, X. *Dalton Transactions* **2005**, *2005*, 865-867.

(11) Luca, V.; Griffith, C. S.; Chronis, H.; Widjaja, J.; Li, H. J.; Scales, N. In *27th Symposium on Scientific Basis for Nuclear Waste Management*; Oversby, V. M., Werme, L. O., Eds.; Materials Research Society: Kalmar, SWEDEN, 2003, p 309-314.

(12) Irvine, J. T. S.; Feighery, A. J.; Fagg, D. P.; Garcia-Martin, S. In *12th International Conference on Solid State Ionics*; Elsevier Science Bv: Halkidiki, Greece, 1999, p 879-885.

(13) Yamaura, J. I.; Yonezawa, S.; Muraoka, Y.; Hiroi, Z. *J. of Sol. St. Chem.* **2006**, *179*, 336-340.

(14) Yonezawa, S.; Muraoka, Y.; Matsushita, Y.; Hiroi, Z. *J. of the Phys. Soc. of Japan* **2004**, *73*, 819-821.

(15) Sasai, K.; Hirota, K.; Nagao, Y.; Yonezawa, S.; Hiroi, Z. *J. of the Phys. Soc. of Japan* **2007**, *76*, 5.

(16) Goodenough, J. B.; Hong, H. Y. P.; Kafalas, J. A. *Mat. Res. Bull.* **1976**, *11*, 203-220.

(17) Groult, D.; Pannetier, J.; Raveau, B. *J. of Sol. St. Chem.* **1982**, *41*, 277-285.

(18) Podkorytov, A. L.; Kudakaeva, S. R.; Sokolova, E. V.; Shtin, S. A.; Ashikhmin, D. N. *Russian J. of Inorg. Chem.* **2006**, *51*, 46-50.

(19) Takamura, H.; Kakuta, H.; Kamegawa, A.; Okada, M.; Tuller, H. L. In *Solid State Ionics-2004. Symposium*; Knauth, P., Masquelier, C., Traversa, E., Wachsman, E. D., Eds.; Materials Research Society: Boston, MA, USA, 2005, p 63-67.

(20) Shlyakhtina, A. V.; Savvin, S. N.; Levchenko, A. V.; Boguslavskii, M. V.; Shcherbakova, L. G. In *16th International Conference on Solid State Ionics*; Elsevier Science Bv: Shanghai, PEOPLES R CHINA, 2007, p 985-990.

(21) Wiggers, H.; Simon, U.; Schon, G. *Solid State Ionics* **1998**, *107*, 111-116.

(22) Kunes, J.; Pickett, W. E. *Physica B-Cond. Matter* **2006**, *378-80*, 898-899.

(23) Hiroi, Z.; Yonezawa, S.; Yamaura, J. In *International Conference on Highly Frustrated Magnetism*; Iop Publishing Ltd: Osaka, JAPAN, 2006.

(24) Hiroi, Z.; Yonezawa, S.; Nagao, Y.; Yamaura, J. *Phys. Rev. B* **2007**, *76*, 19.

(25) Darriet, B.; Rat, M.; Galy, J.; Hagenmul.P *Mat. Res. Bull.* **1971**, *6*, 1305-&.

(26) Barnes, P. W.; Woodward, P. M.; Lee, Y.; Vogt, T.; Hriljac, J. A. *J. of the American Chem. Soc.* **2003**, *125*, 4572-4579.

(27) Michel, C.; Groult, D.; Raveau, B. *Mat. Res. Bull.* **1973**, *8*, 201-210.

(28) Michel, C.; Groult, D.; Deschanvres, A.; Raveau, B. *J. of Inorg. and Nuclear Chem.* **1975**, *37*, 251-255.

(29) Garciamartin, S.; Jerez, A.; Pico, C.; Veiga, M. L. *J. of Mat. Sci. Letters* **1990**, *9*, 1174-1175.

(30) Laarif, A.; Theobald, F. R.; Vivier, H.; Hewat, A. W. *Zeitschrift fuer Kristallographie* **1984**, *167*, 117-124.

(31) Okada, K.; Marumo, F.; Iwai, S. I. 1977; Vol. 33, p 3345-3349.

(32) Holcombe, C. E.; Smith, D. D. *Journal of the American Ceramic Society* **1978**, *61*, 163-169.

(33) Larson, A. C.; von Dreele, R. B. *Los Alamos National Laboratory, Los Alamos* 1990.

(34) Toby, B. H. *J. of appl. Cryst.* **2001**, *34*, 210-213.

(35) Hughbanks, T.; Hoffmann, R. *J. of the American Chem. Soc.* **1983**, *105*, 3528-3537.

(36) Abell, G. C. *Phys. Rev. B* **1979**, *20*, 4773-4788.

(37) Shannon, R. D. *Acta Crystallographica Section A* **1976**, *32*, 751-767.

(38) Andersson, G.; Magneli, A. *Acta Chemica Scandinavica* **1950**, *4*, 793-794.

(39) Babel, D.; Pausewang, G.; Viebahn, W. *Zeitschrift fuer Naturforschung, Teil B. Anorganische Chemie, Organische Chemie* **1967**, *22*, 1219-1220.

(40) Williams, D.; Fleming, I. *Spectroscopic methods in organic chemistry*; Fifth ed. The McGraw-Hill Companies, 1995.

(41) Galati, R.; Simon, C.; Henry, P. F.; Weller, M. T. *Phys. Rev. B* **2008**, *77*.

(42) Fleischer, T.; Hoppe, R. *J. of Fluorine Chem.* **1982**, *19*, 529-552.

(43) Castro, A.; Rasines, I.; Turrillas, X. M. *J. of Sol. St. Chem.* **1989**, *80*, 227-234.

(44) Bonazzi, P.; Bindi, L.; Zoppi, M.; Capitani, G. C.; Olmi, F. *American Mineralogist* **2006**, *91*, 794-801.

(45) Ercit, T. S.; Hawthorne, F. C.; Cerny, P. *Canadian Mineralogist* **1994**, *32*, 415-420.

(46) Perrault, G. *Canadian Mineralogist* **1968**, *9*, 383-402.

(47) Miller, J. J. *Zeitschrift fuer Kristallographie, Kristallgeometrie, Kristallphysik, Kristallchemie* **1938**, *99*, 32-37.

(48) Massard, P.; Bernier, J. C.; Michel, A. *Annales de Chimie* **1971**, *1971*, 41-52.

(49) Galati, R.; Simon, C.; Knee, C. S.; Henry, P. F.; Rainford, B. D.; Weller, M. T. *Chem. of Mat.* **2008**, *20*, 1652-1659.

(50) Galati, R.; Hughes, R.; Knee, C.; Henry, P. F.; Weller, M. T. *J. Mat. Chem.* **2007**, *17*, 160-163.

(51) Hiroi, Z.; Yonezawa, S.; Muraoka, Y. *J. of the Phys. Soc. of Japan* **2004**, *73*, 1651-1654.

(52) Yonezawa, S.; Muraoka, Y.; Hiroi, Z. *J. of the Phys. Soc. of Japan* **2004**, *73*, 1655-1656.

(53) Galati, R.; Simon, C.; Henry, P. F.; Weller, M. T. *Phys. Rev. B* **2008**, *77*, 104523-104529

(54) Nagao, Y.; Yamaura, J. I.; Ogusu, H.; Okamoto, Y.; Hiroi, Z. *J. of the Phys. Soc. of Japan* **2009**, *78*, 21.

(55) Seybolt, A. U.; Sumsion, H. T. *J. of Metals* **1953**, *5*, 292-299.

(56) Schuck, G.; Kazakov, S. M.; Rogacki, K.; Zhigadlo, N. D.; Karpinski, J. *Phys. Rev. B* **2006**, *73*, 144506-1-144506-9.

(57) Schuck, G.; Kazakov, S. M.; Rogacki, K.; Zhigadlo, N. D.; Karpinski, J. *Phys. Rev. B* **2006**, *73*, 9.

(58) Pannetier, J. *Sol. St. Comms.* **1980**, *34*, 405-408.

(59) Schmidt, M.; Radaelli, P. G.; Gutmann, M. J.; Billinge, S. J. L.; Hur, N.; Cheong, S. W. *J. of Phys. -Condensed Matter* **2004**, *16*, 7287-7302.

(60) Hanawa, M.; Muraoka, Y.; Tayama, T.; Sakakibara, T.; Yamaura, J.; Hiroi, Z. *Phys. Rev. Letters* **2001**, *8718.*

(61) West, D. V.; McQueen, T. M.; Huang, Q.; Cava, R. J. *J. of Sol. St. Chem.* **2008**, *181*, 1753-1758.

(62) Cascales, C.; Alonso, J. A.; Rasines, I. *J. of Mat. Sc.Letters* **1986**, *5*, 675-677.

(63) Shannon, J.; Katz, L. *Acta Crystallographica Section B* **1970**, *26*, 102-105.

(64) Mitchell, R. H.; Liferovich, R. P. *J. of Sol. St. Chem.* **2004**, *177*, 4420-4427.

Chapter Four

HYDRATED BETA PYROCHLORES

4.1 Introduction

The nature of the *beta*-pyrochlore structure, with large cavities centred on the 8*b* site coupled with the rigidity of the BO_6 framework can lead to a mismatch between the size of the ion occupying this site and the space available to it. This in turn can further allow the absorption of water into the pores of the BO_6 framework. This has been observed in several materials, notably in $KNbWO_6.H_2O$ and $KTaWO_6.H_2O$[1,2].

The first hydrated pyrochlores were identified by Babel *et al* (1967) [1] in a wide ranging synthetic study of *beta*-pyrochlore type phases. Although the phases synthesised, $KNiCrF_6.H_2O$, $KCoCrF_6.H_2O$, $KNiVF_6.H_2O$ and $KNbWO_6.H_2O$, were identified as being hydrated little characterisation was attempted with only lattice parameters being extracted for $KCoCrF_6.H_2O$ and $KNiVF_6.H_2O$, and a simple framework assigned to the remaining phases allowing the calculation of the one variable; the oxygen atom *x* position within this structure. The level of hydration was not identified in any of these phases; rather it was acknowledged that water was present in some amount within the structure. Babel *et al* went on to explain the absorption of water into the structure by the movement of the potassium ion from the 8*b* site to one of the adjacent 16*d* sites; this was then envisaged as allowing the water molecules to sit on the now empty 8*b* site.

A more in depth study was carried out by Darriet *et al* [2] in 1971 looking at a range of both hydrated and non-hydrated oxide *beta*-pyrochlores, with the general formula $AB_2O_6.xH_2O$ (*A* = K, Rb, Cs and Tl, *B* = Nb, W, Ta and Te). Of these phases $KNbWO_6.H_2O$ was once again shown to be hydrated as previously identified by Babel, with $KTaWO_6.H_2O$ also being shown to form. Thermogravimetric studies were also carried out on these two materials confirming, in both cases, a single molecule of water per formula unit. The TGA data also showed similar thermal stabilities for these two phases with the water starting to be lost at ~60°C and ~80°C for $KNbWO_6.H_2O$ and $KTaWO_6.H_2O$ respectively. Refinements were carried out using the model proposed by Babel, although the opposing model, with the oxygen atoms of the waters on the 16*d* site and potassium ions on the 8*b* site was studied but provided a marginally worse fit than the starting model.

The next and largest, in terms of pore size, hydrated pyrochlore to be identified was $KTa_2O_5F.H_2O$ (a = ~10.61 Å)[3]. Whereas the previous materials discussed were produced by conventional solid state routes this material was synthesised by an ion exchange method from $RbTa_2O_5F$ in molten KNO_3 to give KTa_2O_5F which readily absorbed water from the air to give the hydrated product. Studies by thermogravimetric analysis (TGA) showed a broad, fully reversible, loss of water between 50 and 200°C with approximately one water molecule per KTa_2O_5F unit. Analysis of the PXRD data on this phase showed electron density of both the 16*d* and 8*b* sites in an approximate ratio of 2.5:1 corresponding well to those expected for potassium and oxygen respectively, thus it was once again concluded that the Babel model provided the best fit to the available data. It was also noted for the first time that this relates well to what we would expect to observe, with the oxygen cations having a preference for the coordination environment provided by the 8*b* site over that available on the 16*d* site and that this model does display an unusually short potassium-oxygen separation of 2.29 Å between the 8*b* and 16*d* sites.

The last of the early series of works carried out on hydrated pyrochlores was that of Michel *et al* where the researchers synthesised and studied several novel phases of varying stoichiometry, with the general formula; $ABWO_6.H_2O$ (*A* = Li, Na and Ag, *B* = Nb, Ta and Sb)[4-8]. These phases were produced by a combined solid state/ ion exchange route, with the *A*-site cation and water content confirmed by elemental analysis and TGA studies. All the phases synthesised were studied by PXRD and although unit cells were calculated little structural work was carried out with the water and *A*-site cations being placed on the same sites as those used by Babel *et al*.

The first neutron diffraction study of materials of this sort was published by Groult *et al*[9] in 1982 and looked at the series of defect pyrochlores $TaWO_{5.5}$, $HTaWO_6$, $H_2Ta_2O_6$ and $HTaWO_6.H_2O$ (with deuterated phases being used for neutron work). By a combination of conventional refinement, Fourier techniques and electrostatic potential calculations the individual nuclei in $DTaWO_6.D_2O$ were located onto a partially occupied 48*f* (x = 0.418(4), y,z = 0.125) site and the oxygen atoms of the water to a 32*e* site near to the 8*b* site. Low temperature study (4 K) of the phase indicated a lowering of the symmetry and it was assumed that this was caused by ordering of the water within the framework.

Little further work was published on hydrated phases for the following ten years and the next significant publication was a study on $K_{3/2}Cr_{1/2}Te_{3/2}O_6.0.5H_2O$ by Isasi *et al*[10] in 1994. The material was produced by conventional solid state methods and studied by a wide range of techniques including, PXRD, TGA and DSC measurements. The X-ray diffraction data led to an assignment of the water and potassium onto the 32*e* (*x*,*x*,*x*) position, a displacement from the 8*b* site (0.375, 0.375, 0.375) in the [111] direction, in the case of this material to a position where *x* = 0.392(1). The potassium and water were then assigned occupancies of 3/8 and 1/8, respectively. This puts the potassium ions and hence the oxygen of the water on a site with 3+3+3 anions surrounding it. The partial occupation of these 32*e* sites and the tetrahedral positions they inhabit around the 8*b* site was also shown to lead to ionic conductivity within this phase, much of the further work on materials of this type centred around and was driven by the study of this property[11-13].

Around this time a significant body of work began to be published on phases with the general formula H*BB*'O_6.*n*H_2O due to the potential of many of these materials in the field of proton conduction. Amongst these were studies by Binesh *et al*[14,15] on $HNbWO_6$.*x*H_2O, a material that had been previously identified[16]. These works used solid state NMR, more particularly Magic Angle Spinning (MAS) to closely observe the environment in which the protons were present. $(H_3O)SbTeO_6$ has also been looked at due to the high proton conduction previously observed in Sb_2O_5.*n*H_2O and $HSbO_3$.*n*H_2O[17] and the potential use of such materials in fuel cells. High quality powder neutron diffraction and PXRD data were collected on the material and combined. Rietveld refinements were then carried out using the $SbTeO_6$ framework as a starting point and difference Fourier maps calculated. From this the oxygen atoms were once again assigned to a 32*e* (*x* = 0.493) position, however in this case the 32*e* position was closer to the 16*d* than the 8*b* position. The quality of the neutron data also allowed the assignment of areas of negative nuclear density from the difference Fourier plot, leading to an unambiguous location of the hydrogen atoms on to a 96*g* site (*x*,*x*,*z*, *x* = 0.4007, *z* = 0.5024).

Chowdhry *et al*[18] studied $HSbO_3.1.15H_2O$, a material adopting a defect pyrochlore structure, by pulsed ^1H NMR and reported the presence of H_3O^+ with a rapid exchange mechanism of all the protons within the sample. This differs from other

studies on $HTaWO_6.H_2O$ (including deuterated samples[19]) which show H^+ and H_2O present as separate species[20] on 16*d* and 8*b* sites, respectively. The protons of the water were also located on 96*g* sites close to the 8*b* position. Yet another model proposed for this structure type was that of Dickens and Weller[21] who studied $(D_2O)_{0.38}D_2Ta_2O_6$ by low temperature powder neutron diffraction. They proposed a similar structure as used for $HTaWO_6.H_2O$ above however, initial refinements carried out, using high resolution neutron diffraction data, placed the deuterium atoms on a 32*e* position (*x*,*x*,*x*, $x = 0.3125$). Attempts to place the deuterium on a 96*g* site as used in several other studies showed a slight reduction of fit so the previous model was retained. They also noted that this reduction in fit could be due to a peak shape that was not purely Gaussian in nature, a common feature in ion exchange compounds/zeolites and therefore may not be a true reflection of deuterium peak position.

High pressure studies on $HNbWO_6.H_2O$ and $KNbWO_6.H_2O$ were carried out by Barnes *et al*[22]. Whereas ambient pressure studies by X-ray diffraction on $KNbWO_6.H_2O$ had placed the potassium ion once again on a 32*e* site, in this study *x* was shown to be ~0.49, placing the potassium atoms much nearer to the 16*d* sites, centring the potassium atoms near to a position equidistant from six lattice oxygens arranged in a manner similar to the chair configuration of cyclohexane. The oxygen atoms of the water molecules were then assigned to another set of 32*e* sites close to the 8*b* sites with $x = 0.4143$. In contrast the $HNbWO_6.H_2O$ phase only displays occupation of one of these 32*e* sites with the proton and water molecule forming a H_3O^+ ion that sits near to the 8*b* site ($x = 0.349(7)$). The application of high pressures to these phases has little effect upon the structure with a small compression of the BO_6 lattice leading to a movement of the H_2O/H_3O^+ molecules towards the 8*b* site due to the reduced space within the channels. Another interesting material studied in this paper was $RbNbWO_6$ which was shown to adopt the ideal *beta*-pyrochlore structure, with the rubidium atoms on the 8*b* site. When placed under high pressure (>3GPa) the water molecules were forced into the structure and occupied the same site as seen in the other materials studied here (32*e*, $x = 0.42$) with the rubidium ions shifting to a site near to the 16*d* site. Interestingly this led to a increase in lattice parameter with application of pressure, counter intuitive to what we would normally expect in most materials.

Finally recent work carried out within the group[23] has shown that KOs_2O_6 exhibits partial hydration, with approximately 0.1 water molecules per formula unit. The incorporation of water into the phase has been shown to lead to an increase in the temperature at which this material undergoes a transition to the superconducting state. This is of particular interest as this material is one of very few hydrated pyrochlores that displays a water occupancy of less than one in ambient conditions and the only one in which the degree of hydration has been shown to effect the physical properties.

Overall a wide range of structural derivations have been used to describe the makeup of hydrated pyrochlores. In all models the B_2O_6 framework has been retained, although the level of distortion of the octahedra that compose this framework has altered (shown by varying values of *x* for the 48*f* site, *x*,0.125,0.125). Work in this chapter focuses on better characterising known materials, both in their hydrated and to a lesser extent, their dehydrated forms. High resolution powder neutron diffraction has been used to locate the water molecules and extraction of hydrogen positions allowed the assignment of the orientation of these molecules with respect to their surrounding frameworks.

Two other types of hydrated pyrochlores are known to exist, with general stoichiometries of $A^{II}(B^{V}WO_6)_2.nH_2O$ (known for *A* = Ca, Sr and Ba, *B* = Nb and Ta) [24] and $A^{II}B_2O_6.H_2O$ (known for *A* = Cd and Pb, *B* = Nb and Ta)[25]. The study of the series $A^{II}(B^{V}WO_6)_2.nH_2O$ (*A* = Ca, Sr and Ba, *B* = Nb and Ta) placed the water on a 8*b* site but made no attempt to locate the A^{II} ions within the framework as only powder X-ray data was available which was deemed of insufficient quality at the time due to the available refinement tools. Groult *et al* [25] provided the only other examples of divalent *A*-site ions within the literature, with the more conventional structure type $A^{II}B_2O_6.H_2O$ (*A* = Cd, Pb B = Nb, Ta). These phases, synthesised by ion exchange routes from $H_2(H_2O)M_2O_6$[26], were assigned to the simplest accepted model for this structure type with the 8*b* and 16*d* sites occupied. The study did look at the possibility of the water being displaced from this site but could find no evidence for it with the PXRD data available. Some of these materials and other phases of similar composition are discussed in more detail in Chapter Five.

4.2 PXRD Studies of $KTaWO_6.nH_2O$

A large volume of research has been carried out as part of this work looking into the structural features of $KTaWO_6.nH_2O$. This was primarily undertaken as the phase can readily be synthesised in substantial quantities and rapidly hydrates allowing for data to be collected on both the hydrated and dehydrated analogues. Of particular interest are the structural changes that occur as the water is lost, in particular the position of the potassium ions but also the effects this shift has upon the B_2O_6 network. We also expect to observe a 'rattling' of the potassium ions as seen in similar phases[27] as the water molecules are lost and more space becomes available within the framework.

A limited amount of work has been carried out on this phase, notably by Mari *et al*[28] where the researchers characterised a phase including an unknown quantity of water. This material is of further interest as a large variety of materials have been synthesised through ion exchange using this as a starting material[4,24,29].

4.2.1 Synthetic route

Samples of $KTaWO_6.nH_2O$ were synthesised via a sol gel route. Initially stoichiometric quantities of ethylene glycol and citric acid were dissolved in warm water. Separately KNO_3 (Sigma Aldrich, 99%), Ta_2O_5 (Sigma Aldrich, 99%) and WO_3 (Alfa Aesar, 99.7%) were dissolved in concentrated nitric acid. The resulting solutions were then mixed together and stirred for several minutes before the mixture was heated and allowed to boil down until a gel like solid formed (NB: Care should be taken at this stage as noxious gases are given off upon heating). The resulting gel was then fired at 300 °C for 4 hours, reground and then fired again for 16 hours at 600 °C. Phase composition was confirmed by short PXRD data collections, ~20 minutes over 10 to 70° 2θ. This product was shown to contain small amount of an impurity phase either $Ta_{22}W_4O_{67}$[30] or $(Ta_2O_5)_{15}(WO_3)_2$[31] both orthorhombic phases, indistinguishable from one another in the quantities present. A further cycle of heating at 600 °C was therefore undertaken, this resulted in a similar amount of impurity a further phase being present, ~1-2 % by mass, but of the structurally simpler phase Ta_2O_5[32].

4.2.2 Initial structural characterisation

Initial structural models were refined from room temperature data sets were collected on a Siemens D5000 diffractometer using data over a 2θ range of 10 to 110 ° and a step size of 0.02 °. The data set were collected continuously over a period of 16 hours, with all subsequent refinements undertaken using the GSAS structural refinement suite [33,34].

Thermogravimetric data were collected for the phase using a Polymer Laboratories PL-STA 1500. From the data collected, water content was calculated on the assumption that once a stable mass had been reached, at ~120 °C, the resulting product was $KTaWO_6$, with the retention of the pyrochlore structure being confirmed by PXRD. The final calculated water loss with respect to temperature is plotted in Figure 4.2.1 and results in a value of 1.01 water molecule per formula unit. A slight excess of mass loss may be assigned to the loss of surface bound water, thus a value of 1 water molecule, the theoretical maximum assuming full potassium occupancy, per formula unit was assigned and used in all subsequent analysis.

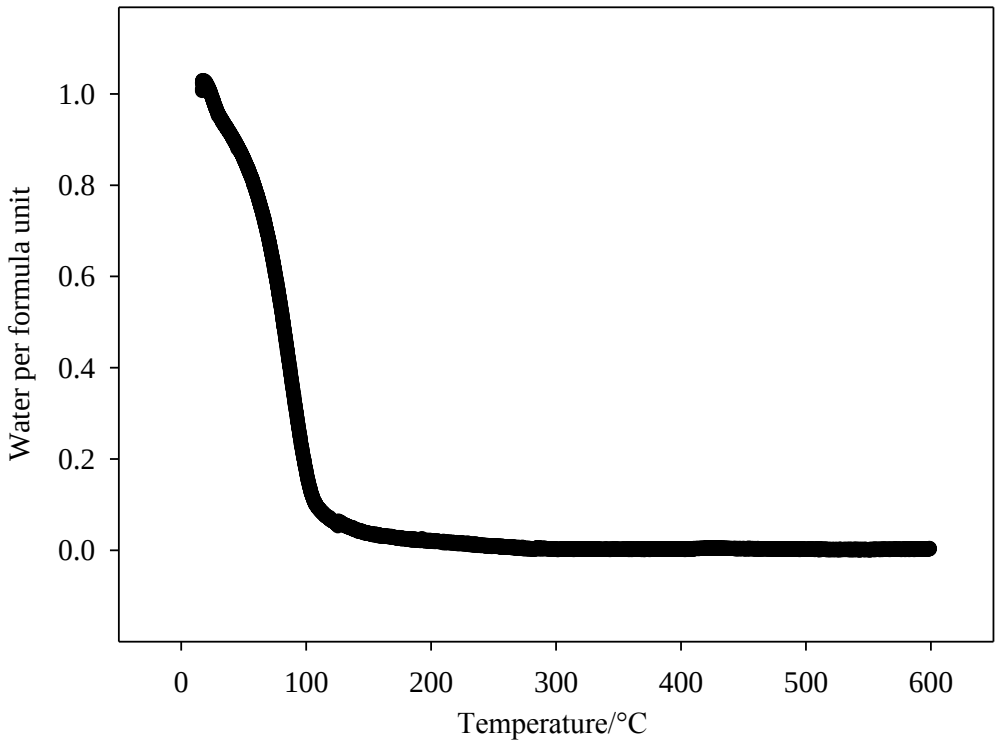

Figure 4.2.1 - Water content per formula unit calculated from TGA data for the fully hydrated samples of $KTaWO_6.nH_2O$.

4.2.3 Structural analysis

Initial refinements provided reasonable fits to the data, clearly confirming the adoption of the pyrochlore phase and occupation of a species in the cavities of the structure, seen through significant electron density present in calculated Fourier density maps. Within the central cavities the model appeared to be far from ideal with occupation of the sites failing to refine stably and considerably larger than expected thermal parameters arising for the potassium ions and oxygen atoms of the water molecules. Therefore, further models were studied to provide a better fit to data.

Subsequently the hydrated material was refined in two models; using the model presented by Mari *et al*[28], with the potassium atoms and water molecules each occupying half of the available 16*d* sites (0.5,0.5,0.5), and in the model used in studies of $KNbWO_6.nH_2O$ by Barnes *et al*[22] where the potassium ions sit on the 16*d* site and the oxygen anions of the water molecules on the 8*b* site. Of these the second model provided a significantly better fit to the data, refining to R_{wp}'s for the two models of 18.31% and 8.45% respectively. As the model presented by Mari *et al* allows for no electron density within the larger cavities of the framework the model is easily dismissed as calculated Fourier density plots clearly show this not to be the case.

This initial starting model provided higher than excepted thermal parameters for the oxygen atom of the water molecule. It seemed likely that this is due to 'smearing' of the oxygen atoms electron density on to the four nearby 32*e* sites. Therefore, a further variable was introduced to the refinement allowing this oxygen position to refine onto a 32e site rather than the initial 8*b* position, with the site occupation being adjusted from 1 to 0.25 accordingly to maintain the same overall stoichiometry. This change provided a significant drop in the thermal motion of these atoms and a small increase in level of overall fit. Due to this drop in the thermal motion of the oxygen atoms the model using the 32*e* site was selected for further analysis.

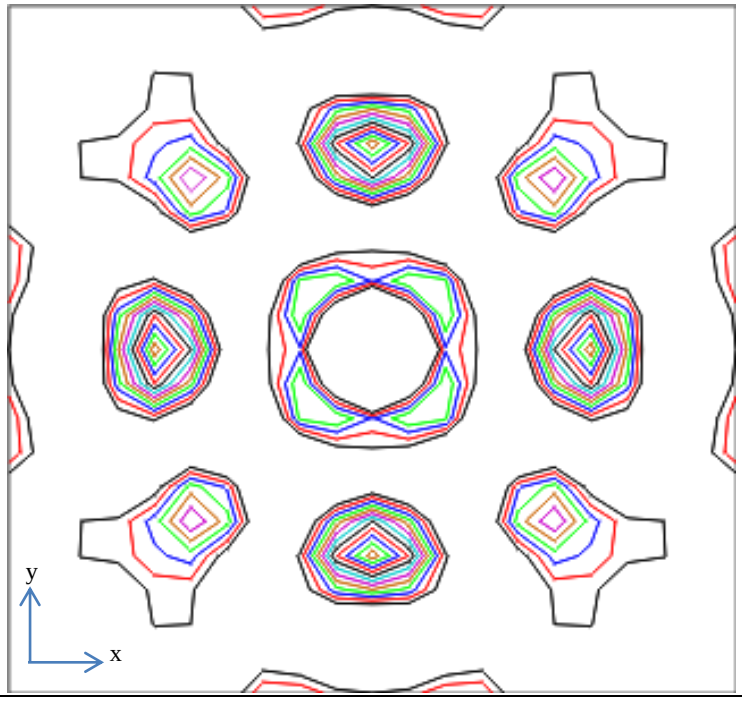

Figure 4.2.2 – A Fourier map showing the calculated electron density surrounding an unoccupied 8b position in $KTaWO_6$. The figure is centred on 0.375,0.375,0.375 looking out 3 Å in each direction along the x-axis clearly showing that there is no significant density on the 8b site itself but considerable amounts in surrounding positions.

The final variable studied relates to the position of the *A*-site cation, with the potassium ions occupying either a fixed 16*d* site or a variable 32*e* site. Both options provided similar levels of fit, however, allowing the potassium position to vary, whilst leading to a stable atomic position, provided negative thermal parameters suggesting a less than satisfactory model. Therefore, the final model used for the hydrated phase placed the potassium ions on the 16*d* site (0.5,0.5,0.5) and the oxygen atoms of the water molecules on a 32*e* site (*x*,*x*,*x*) where $x = 0.4156(7)$. Attempts were made to locate the hydrogen atoms present in the structure but were discarded as they provided no improvement to the fit on the data available.

Table 4.2.1 – Final refined atomic parameters for a room temperature PXRD data set of $KTaWO_6.H_2O$. E.S.D's are given in parentheses.

Atom	Site	*x*	*y*	*z*	Occupancy	U_{iso}
K	16*d*	0.5	0.5	0.5	0.5	3.44(10)
Ta	16*c*	0	0	0	0.5	2.438(15)
W	16*c*	0	0	0	0.5	2.438(15)
O	48*f*	0.3154(3)	0.125	0.125	1	2.96(14)
O	32*e*	0.4173(5)	0.4173(5)	0.4173(5)	0.25	2.9(4)

Space group $Fd\bar{3}m$. Cell parameters: $a = b = c = 10.49894(9)$ Å

Final fit parameters: $\chi^2 = 6.428$, $R_{wp} = 8.22$ %, $R_p = 6.53$ %

Table 4.2.2 – Important values providing an overview for the comparison of fit provided by the various models used for $KTaWO_6.nH_2O$ from PXRD data. E.S.D.'s are given in parenthesis.

Model	K *x* position	K U_{iso}	O of H_2O *x* position	O U_{iso}	R_{wp}	χ^2	Framework O, *x* position
K on 16*d* O on 16*d*	0.5	28.9(13)	0.5	-5.9(2)	18.31%	31.89	0.3184(7)
K on 16*d* O on 8*b*	0.5	3.33(10)	0.375	18.4(9)	8.45%	6.799	0.3147(4)
K on 16*d* O on 32*e*	0.5	3.44(10)	0.415557	2.9(4)	8.27%	6.508	0.3154(3)
K on 32*e* O on 8*b*	0.4820(3)	-0.34(16)	0.375	17.0(8)	8.22%	6.437	0.3135(4)
K on 32*e* O on 32*e*	0.4827(3)	0.00(16)	0.4157(5)	-2.0(4)	8.04%	6.210	0.3154(3)

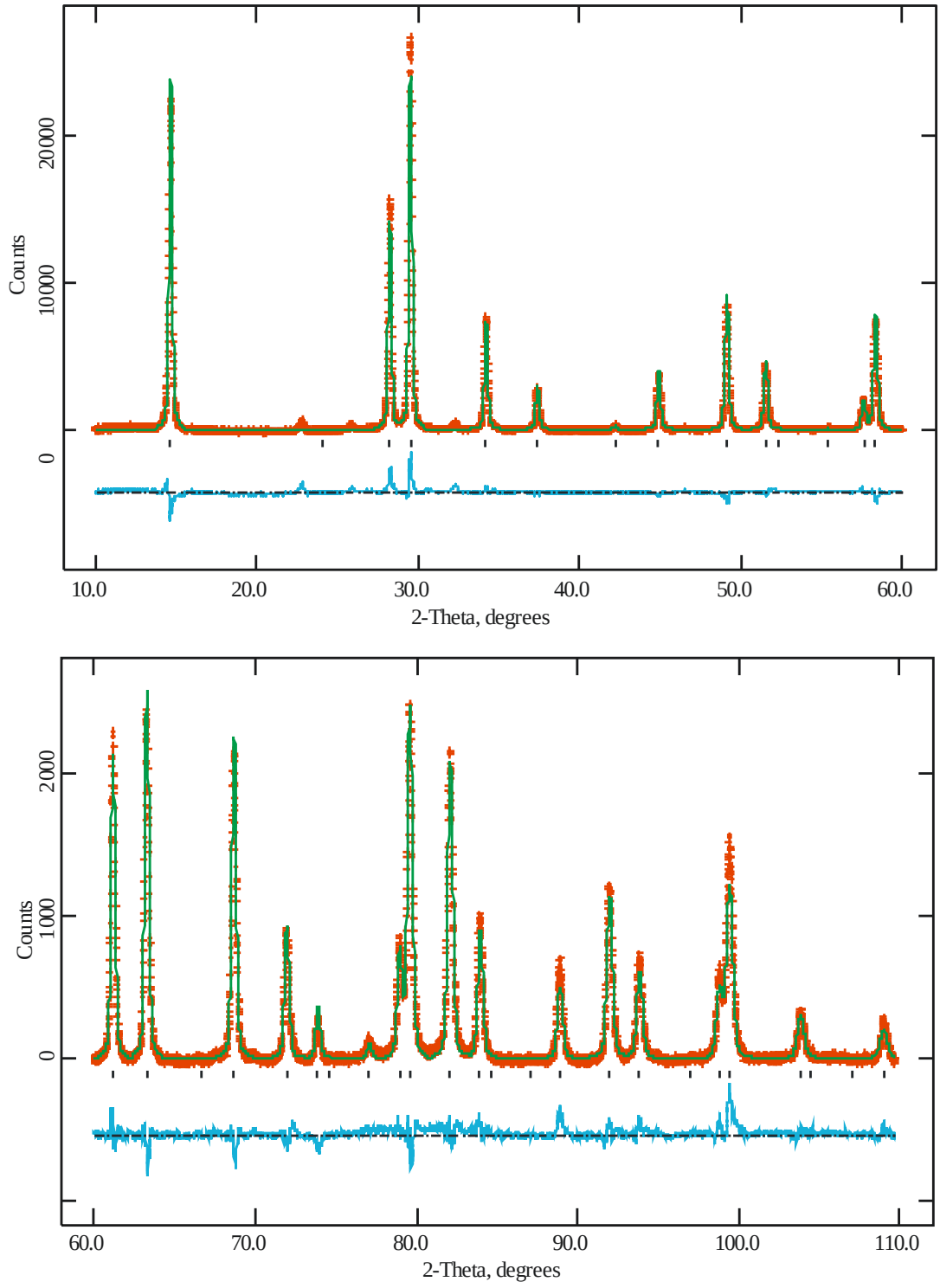

Figure 4.2.3 – Profile fit to PXRD data for $KTaWO_6.nH_2O$. Experimental data points are shown as red crosses, upper continuous green line the calculated profile and the lower continuous blue line the difference. Allowed reflections positions are indicated by tick marks. Un-indexed peaks at ~24, 26 and 32º were identified as a Ta_2O_5 phase which could not be stably refined.

4.2.4 Discussion

The final model selected provides a good degree of fit to the data with values for each refined parameter that prove consistent with those observed elsewhere. The refined thermal motions of the individual atoms proved reasonable with the degree of thermal motion roughly corresponding to the mass of the atoms being studied. The refined lattice parameters prove to be a reasonable fit to those from the study of Darriet *et al*[2] who suggested a value of 10.475 Å at room temperature compared to 10.49894(9) Å presented here, with their data being collected over a smaller range of 2θ.

A model different from those previously presented for this material has provided the best fit to the data collected. Whereas the two previous studies[2,28] carried out upon this hydrated phase have placed both the oxygen atoms of the water molecules and the potassium atoms on or near to the 16*d* site leaving the larger cavities of the phases empty, it can clearly be shown that significant electron density is present there, as shown in Figure 4.2.2.

Whilst the last model to be investigated, where both the potassium cations and oxygen atoms of the water molecules occupying 32*e* positions, proved inadequate it should not be disregarded. The model used for $KNbWO_6.nH_2O$ by Barnes *et al.* showed a small degree of displacement for the potassium ions on to the 32*e* site (x = 0.4838(6))[22] from high quality PND data, very close to that shown in the discarded model. It seems feasible that this displacement may be occurring at room temperature in this material, but that the data is of insufficient quality to separate this movement from the thermal parameters.

Attempts were also undertaken to ascertain the level of hydration directly by refinement of the occupancy of the 32*e* water position, variation of ~10 % was observed when allowed to freely refine with no significant improvement in the level of fit. It was therefore decided that the values calculated from TGA data, showing a full occupancy on this site, were reasonable, with no further refinement of the occupancies being undertaken.

4.3 PXRD studies of $KTaWO_6$

To study the effect of hydration upon this material the dehydrated analogue has also been characterised, a study that does not appear elsewhere in the literature. Of particular interest is the behaviour of the potassium cations within the cavities of this material. Low temperature studies of similar materials have seen the potassium occupying a fixed 32*e* site towards the side of the internal voids of the material at low temperature[35], these materials however have considerably smaller lattice parameters than $KTaWO_6$ and it may thus be reasonable to expect to see this displacement at a higher temperature than observed in other pyrochlore phases. In addition we aim to better understand the coordination environment of the potassium ions and how this in turn affected the lattice parameters and geometry of the BO_6 octahedra that compose the B_2O_6 network.

4.3.1 Data collection

Structural studies were undertaken on a dehydrated sample of $KTaWO_6.nH_2O$, with the dehydration being undertaken *in situ* to ensure that the sample remained dry throughout. Collected TGA data and previous studies[28] have shown that this material will rehydrate rapidly and thus extra care was taken throughout to ensure that this did not occur.

The material was initially prepared as detailed in Section 4.2.1 for the hydrated analogue of this phase. Dehydration was then undertaken using a Paar HTK1200 furnace unit attached to a Bruker D8 Advance diffractometer with the sample being heated to 130 °C and held there for 24 hours. The sample was then cooled under flowing, dry nitrogen, to room temperature and data collected for 40 hours between 10 and 100° 2θ and a step size of 0.02°. Initial inspection of the data clearly showed both a shift in peak positions, relating to a change in lattice parameter and a change in the relative intensities of the observed peaks when compared with the hydrated phase previously studied.

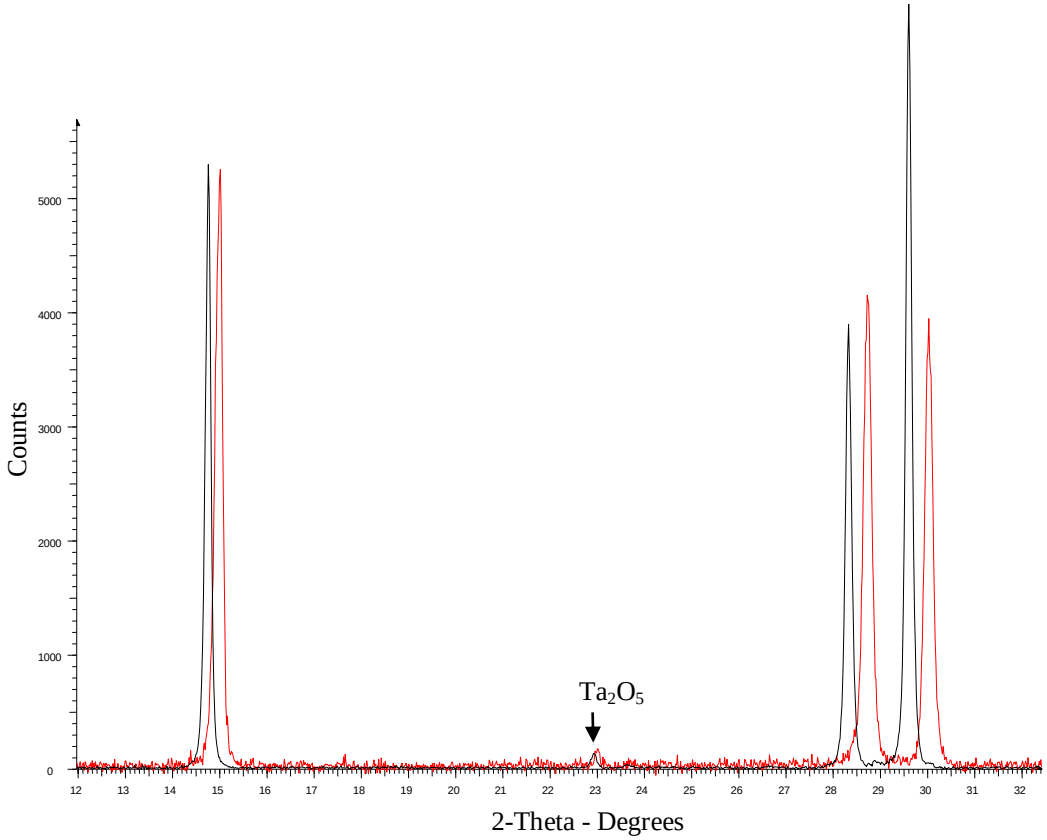

Figure 4.3.1 - Partial PXRD patterns for $KTaWO_6$ (Red) and $KTaWO_6.nH_2O$ (Black) showing the first three reflections of the pattern. The peak at ~26° 2Θ is attributed to a small Ta_2O_5 impurity. The background has been subtracted and peak intensity scaled to allow direct comparison between the two phases.

4.3.2 Structural analysis

The phase was refined initially in the ideal *beta*-pyrochlore structure with the potassium on the 8*b* site as used by Kar and Choudhary[36], a second phase of ~2 % of Ta_2O_5 was also shown to be present and was included in the refinement. This model however resulted in a poor fit to the data, producing a very large thermal parameter for the potassium atoms. An alternative model was therefore introduced with the potassium atoms displaced on to the adjacent 32*e* sites. This change improved the fit marginally and reduced the thermal parameter of the potassium significantly to a value in line with those displayed by the remaining atoms within the structure. Other models were also looked at for completeness; placing the potassium on the 16*d* position, as occupied in the hydrated phase, caused the refinement to diverge.

Placing the atom close to this point on the 32*e* site available was not possible as attempts to do so merely caused the site to converge with that used for the final model.

It is notable that the quality of the data set used in this refinement is lower than seen in the majority of other refinements presented in this work. This primarily occurred due to the instrument setup, with a large amount of beam intensity being lost through scattering off of the windows of the furnace stage coupled with a significant decrease in resolution. It is also characterised by a slight increase in peak width as a result of the same interaction.

Table 4.3.1 – Comparison of the fit provided by the two models used for $KTaWO_6$ from PXRD data. E.S.D's are given in parentheses.

K site	K *x* position	K U_{iso}	R_{wp}	χ^2	Framework O, *x* position
8*b*	0.375	16.7(11)	16.67%	1.378	0.3193(12)
32*e*	0.4092(12)	2.4(12)	16.62%	1.371	0.3202(12)

Table 4.3.2 – Final refined atomic parameters for a room temperature PXRD data set of $KTaWO_6$ E.S.D's are given in parentheses.

Atom	Site	*x*	*y*	*z*	Occupancy	U_{iso}
K	32*e*	0.4092(12)	0.4092(12)	0.4092(12)	0.25	2.4(12)
Ta	16*c*	0	0	0	0.5	1.91(9)
W	16*c*	0	0	0	0.5	1.91(9)
O	48*f*	0.3202(12)	0.125	0.125	1	0.9(5)

Space group $Fd\bar{3}m$. Cell parameters: $a = b = c = 10.3507$ (3) Å

Final fit parameters: $\chi^2 = 1.371$, $R_{wp} = 16.62$ % $R_p = 12.69$ %

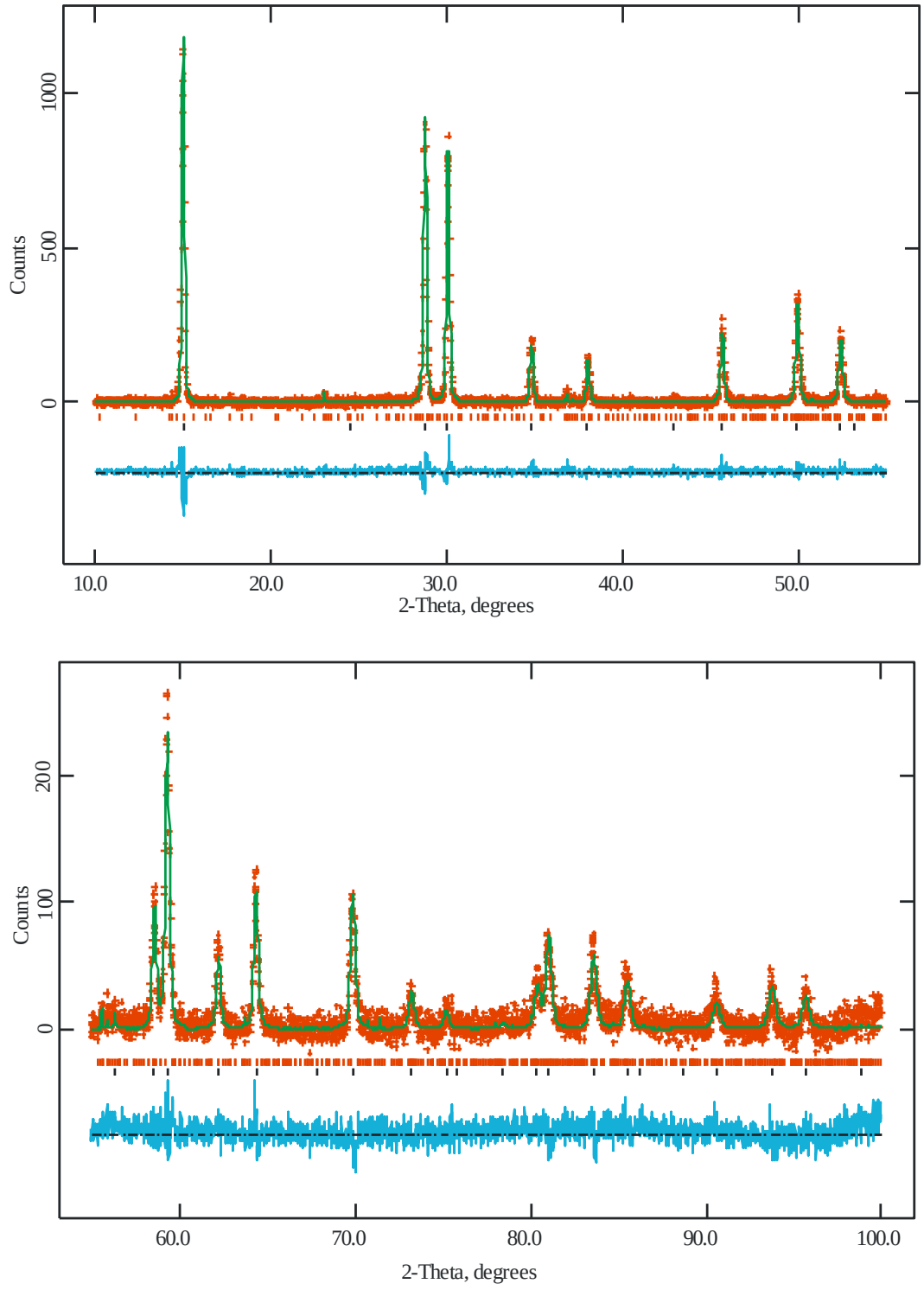

Figure 4.3.2 – Refined profile fit to PXRD data for $KTaWO_6$. Data points are shown as red crosses, the upper continuous green line is the calculated profile and the lower continuous blue line the difference. The upper red tick marks represent the reflections associated with the Ta_2O_5 impurity and the lower $KTaWO_6$.

4.3.3 Discussion

It can be seen that whilst the calculated fit does not change significantly between the two models presented in Table 4.3.1 there is a small improvement in fit with the introduction of a displaced potassium ion site which, coupled with the significant reduction in thermal motion of this atom, poses a strong argument that this is a better model to adopt. As would be expected the degree of displacement in this material is considerably larger than in other materials studied in this work. As presented in Chapter Three, $KNbTeO_6$ even at 2 K, never achieves this level of displacement of the potassium ions with the *x* coordinate shifting to 0.3947(6) compared to 0.4092(12) at room temperature in $KTaWO_6$. This behaviour is as predicted with the overall lattice being considerably larger at 10.3507(3) Å in $KTaWO_6$ as compared to 10.23973(14) Å in $KNbTeO_6$, this difference in lattice dimensions actually results in very similar coordination environments in both materials with the shortest potassium-oxygen bond lengths in each material being 2.9632(13) and 2.845(17) Å for $KNbTeO_6$ and $KTaWO_6$, respectively and the overall bond valance contributions being similar for each.

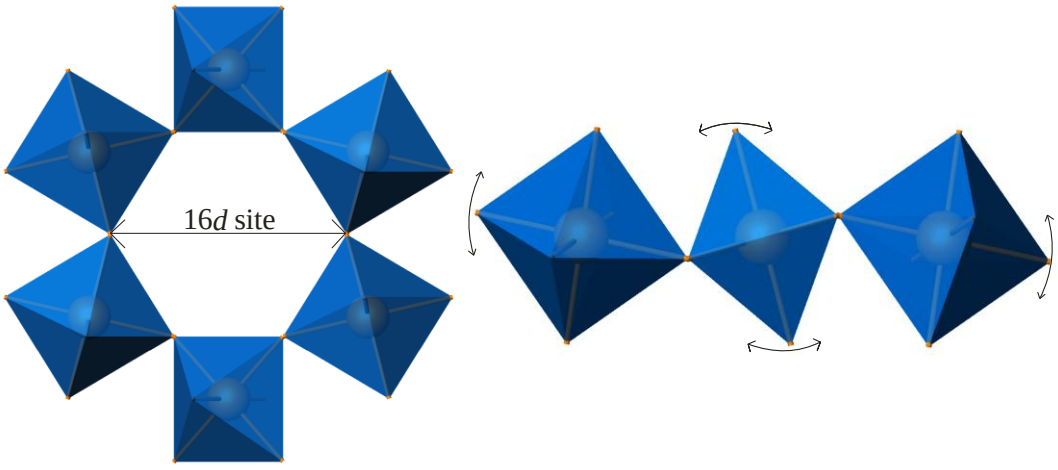

Figure 4.3.3 – The left hand image displays the six octahedra surrounding the 16d site. The right hand image shows a side on image of the same octahedra, as these polyhedra tilt they cause the total width of this unit to expand or contract which in turn cause the entire lattice dimensions to alter.

The removal of water from $KTaWO_6$ results in a contraction of the lattice constants from 10.49894(9) to 10.3507(3) Å, with the movement of a cation from the smaller 16*d* site to the larger cavities surrounding the 8*b* site. This contraction occurs

through a small shortening of the metal-oxygen bonds from 1.9781(12) Å in the hydrated phase to 1.969(5) Å in the dehydrated phase, coupled with a tilting of the octahedra. In both materials the polyhedra display a degree of distortion away from the perfect octahedra, with the internal bond angle changing from 91.08(13) ° to 93.0(5) °. The combination of these two actions cause the dimensions of the six-membered rings, composed of six octahedral units, to shrink from an internal width of 5.3701 to 5.2201 Å. Figure 4.3.3 shows these BO_6 units and the effects that these distortions have upon the local environment.

4.4 Variable temperature powder X-ray diffraction study of $KTaWO_6.nH_2O$

A variable temperature study was undertaken on $KTaWO_6.H_2O$ to attempt to better ascertain the structural changes occurring as water is lost from the structure. TGA data collected on the material implies that the water is lost gradual between room temperature and ~120 °C and thus data was collected at discreet intervals over a similar temperature range.

4.4.1 Data collection

Data were collected on a Bruker D8 Advance diffractometer with a Paar HTK1200 furnace stage using a standard scintillation counter over a temperature range of 30 to 140 °C at 10 °C intervals. A collection time of ~10 hrs was used for each data set over a 2θ range of 10 to 110° with 0.02° steps.

4.4.2 Data analysis

An initial refinement was carried out on the 30 °C data set using the GSAS software[33,34] and the model for the hydrated phase as used in Section 4.2.1. The data sets collected on this material were of low quality and whilst lattice parameters could be accurately extracted atom positions could not. Thus, only a comparison of lattice parameters against temperature was undertaken. Refinements of the remaining data sets were undertaken using the SEQGSAS program included within the GSAS software suite and allowed the rapid, systematic refinement of multiple data sets.

A simplified model was used allowing only the background, zero point, peak profile and lattice parameters to vary in the subsequent refinements. These refinements ran smoothly across the entire temperature range.

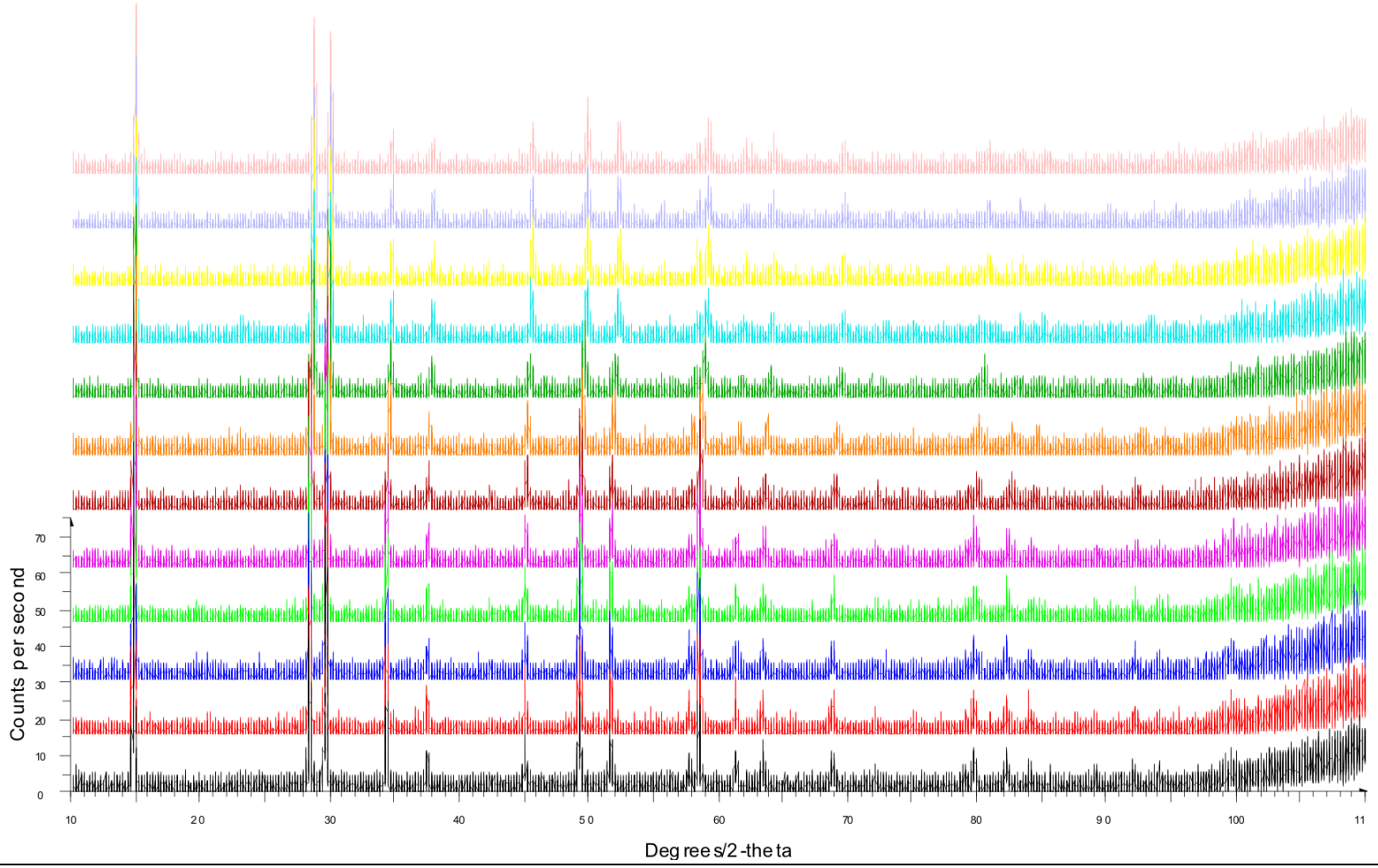

Figure 4.4.1 – PXRD patterns from a variable temperature data collection on $KTaWO_6.nH_2O$, data was collected at 10°C intervals from 30-110°C for 7hrs at each temperature. Plots are shown from high temperature (top) to low (bottom).

4.4.3 Discussion

Figure 4.4.2 shows the strong correlation between the lattice parameter of the materials and the calculated water content, as collected in Section 4.1. Whilst the water is loosely bound within the framework, as shown by the low temperature range at which it is lost, the process of dehydration still remains gradual with the majority of water being lost between 60 and 95 °C, relating to a period of ~40 hrs at elevated temperatures.

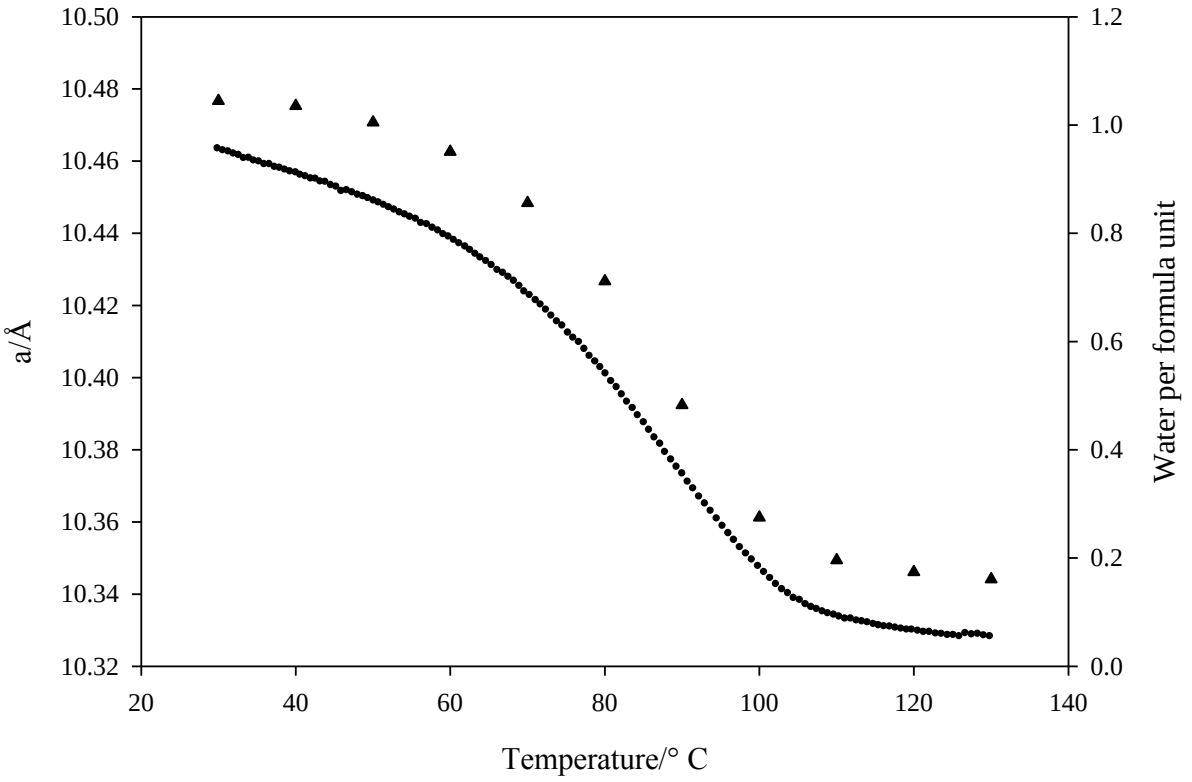

Figure 4.4.2 – Plot showing the changes in the refined lattice parameter (▲) and calculated water content (●) with respect to temperature for $KTaWO_6.nH_2O$.

Inspection of the data shows a small peak broadening across the temperature range studied followed by a return to something close to the original peak widths once the phase is fully dehydrated. This suggests behaviour similar to what we would intuitively predict; that although the average lattice parameter shrinks as water is lost this in fact corresponds to areas of local contraction as water is lost from that portion of the crystallites composing the sample, whilst other areas retain their original size allowing them to incorporate water. Behaviour other than this would be unusual as the cavities would no longer possess sufficient available volume to contain water.

4.5 Powder neutron diffraction studies of $KTaWO_6.nH_2O$

Powder neutron diffraction experiments were undertaken on samples of $KTaWO_6.nH_2O$ in order to more accurately determine the position of the lighter elements present within the framework. In particular we were keen to locate water molecules and if feasible their orientation with respect to the B_2O_6 network. Finally we wished to more accurately determine the precise shape of the BO_6 octahedra using a low temperature environment and thus determine the coordination of the remaining cations within the framework from this.

4.5.1 Data collection

Powder neutron diffraction data were collected on ~5g sample of $KTaWO_6.nH_2O$ using the high resolution instrument D1A at the ILL, Grenoble. Data were collected over a period of 4 hrs at 2 K for a 2θ range of 3 to 157°. For the final refinements only data above 12° 2 θ was used as no reflections were observed below this value.

Attempts were also undertaken to produce deuterated samples with the synthesis undertaken using dried $KTaWO_6$ which was then left exposed to a deuterated environment to form $KTaWO_6.D_2O$. Whilst PXRD clearly showed the expected shift in peak positions and intensities associated with the lattice expansion of a hydrated sample refinement of the powder neutron data indicated a lack of neutron density, with respect to the amount of oxygen present, in the positions where we would expect to observe the deuterium atoms of the D_2O. As hydrogen atom positions could be accurately determined in the hydrated material this data is not presented here. It does however imply that the hydration of the material is a fluid process as while exposure of the material to a hydrated environment was brief, ~2 minutes for sample preparation, the proportion of water molecules that had exchanged was significant. This implies that the water is loosely bound within the structure, that it can easily be lost/gained and that as predicted by the structural model presented here it is unlikely that all available 16*d* sites are occupied in the hydrated phase as if this was the case the movement of water molecules between the cavities would be inhibited by the potassium atoms.

4.5.2 Data analysis

Initially the refinement was carried out in the standard *beta*-pyrochlore model, but incorporating only the atomic positions of the B_2O_6 network. This refinement proceeded smoothly with the variation of global parameters, the positional parameter of the oxygen anions and the thermal motion of all atoms. Once this initial structural model had been established Fourier density maps were calculated to locate the remaining neutron density within the framework. Initial neutron density was located near to both the 16*d* and 8*b* sites as previously seen in the PXRD data and a second phase was identified within the material corresponding to a small impurity of Ta_2O_5 which was incorporated into the refinements using the model of Hummel *et al*[37].

A variety of models were tested, following the same general procedure as used for the PXRD data analysis in Section 4.2.3 with each model refined independently and presented in Table 4.6.1. Alternative models, with the potassium and oxygen atoms on opposing sites to those expected, were also tested. However, with their respective neutron scattering cross sections being significantly different, 4.232 and 1.96 barns' for oxygen and potassium atoms[38], it is possible to say that the potassium is not present within the main central cavities of the framework as even on a fully occupied 8*b* site the amount of neutron density present would be insufficient to match that which was observed.

The model placing the potassium ions on a 16*d* site and the oxygen anions of the water molecules on a 32*e* site was shown to be the preferred model, providing sensible values for all the refined parameters and the best level of overall fit. Attempts to move the potassium atoms away from this 16*d* site to nearby 32*e* sites led to a reduction in fit and a change in atomic position that was within the error boundaries. The oxygen atom positions were similar in behaviour, fixing them to an 8*b* site provided a reduction in fit and a greatly increased thermal parameter, up from 1.1(3) to 21.5(10) U_{iso}[38], implying that the model was trying to spread the density out to better compensate for the four separate sites no longer being allowed. As mentioned above, although tested, the model placing both atoms on to identical 16*d* sites with shared occupancies was discarded rapidly and provided an extremely low level of fit.

Table 4.6.1 – Comparison of the fit provided by the various models used for $KTaWO_6.nH_2O$ from neutron data. (*) *value proved unstable and tended to infinity.*

Model	K, *x* position	K U_{iso}	O of H_2O *x* position	O of H_2O U_{iso}	R_{wp}	χ^2	Framework O, *x* position
K on 16*d* O on 16*d*	0.5	-1.0(4)	0.5	80.00(*)	7.49%	42.10	0.3098(3)
K on 16*d* O on 8*b*	0.5	0.4(3)	0.375	21.5(10)	6.12%	28.08	0.3089(2)
K on 16*d* O on 32*e*	0.5	1.5(3)	0.4127(5)	1.1(3)	5.49%	22.56	0.3090(2)
K on 32*e* O on 8*b*	0.499(6)	1.1(5)	0.375	21.6(10)	6.15%	28.27	0.3090(2)
K on 32*e* O on 32*e*	0.5110(19)	2.1(6)	0.4127(5)	0.7(3)	5.76%	24.88	0.3090(2)

Once an initial model had been established attempts to ascertain proton positions were undertaken. Once again Fourier density maps were calculated for the phase with previously assigned density subtracted displaying only the remaining unassigned neutron density. The most significant area of negative density, as observed for protons due to their neutron scattering cross section being negative[38], was located around 0.375, 0.375, 0.51 a 48*f* position within the main cavity. This position is adjacent to those used in a model for $KNbWO_6.0.69D_2O$ by Murphy *et al* derived from PND data where the deuterium atoms were placed on to the 96*g* site at ~0.899, 0.899, 0.499[39]. This model was tested and proved stable, providing bond distances that were deemed reasonable for a water molecule and proving significantly superior to a model with the hydrogen atoms on the 48*f* position.

Table 4.6.2 – Final Refined atomic parameters for a low temperature PND data set of $KTaWO_6.H_2O$ E.S.D's are given in parentheses.

Atom	Site	*x*	*y*	*z*	Occupancy	Ui/Ue*100
K	16*d*	0.5	0.5	0.5	0.5	1.0(3)
Ta	16*c*	0	0	0	0.5	0.56(9)
W	16*c*	0	0	0	0.5	0.56(9)
O	48*f*	0.31005(14)	0.125	0.125	1	0.31(6)
O	32*e*	0.4169(5)	0.4169(5)	0.4169(5)	0.252(7)	1.60(32)
H	96*g*	0.9153(10)	0.9153(10)	0.5094(17)	0.169(9)	8.4(9)

Space group $Fd\bar{3}m$. Cell parameters: $a = b = c = 10.4658(3)$ Å

Final fit parameters: $\chi^2 = 9.405$, $R_{wp} = 3.52$ % $R_p = 2.61$ %

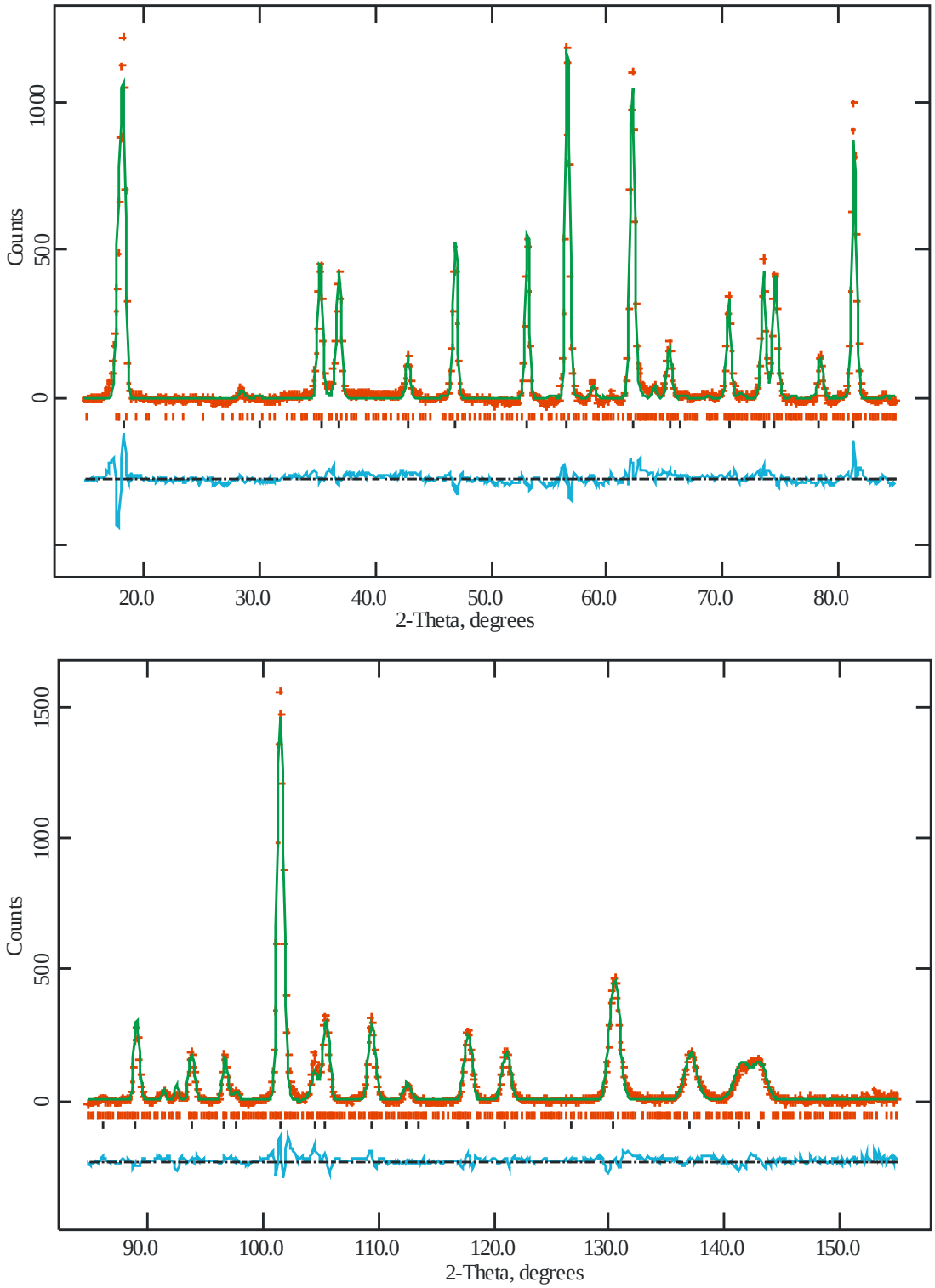

Figure 4.6.1 – Profile fit to PND data for $KTaWO_6.nH_2O$. Experimental data points are shown as red crosses, upper continuous green line the calculated profile and the lower continuous blue line the difference. Allowed reflections positions are indicated by tick marks, red for the Ta_2O_5 impurity and black for $KTaWO_6.nH_2O$.

4.5.3 Discussion

Comparison to the previously discussed PXRD data for this phase the material shows strong agreement with the oxygen of the water situated at 0.4173(5) and 0.4169(5) for the PXRD and PND data, respectively. As would be expected thermal parameters for all atoms are significantly lower for the PND data, a likely result of both the technique and the sample being cooled to 1.5 K. The lattice itself contracts marginally upon cooling, showing similar changes in lattice parameter to the dehydrated series, ANbTeO$_6$ (where A = Cs, Rb and K), studied in Chapter Three.

The main advantage of using PND has been the extraction of accurate positions for the hydrogen atoms, allowing us to better understand how the water molecules are accommodated in the structure. Two models were thoroughly tested; with the hydrogen atoms placed onto 48*f* or 96*g* positions, both models significantly improving the calculated fit but the model allowing the hydrogen to shift to the 96*g* positions providing values closer to those expected for a water molecule. Whilst the bond distances from this model for water prove reasonable, 0.97 Å as opposed to ~0.94 Å for 'free' water, the internal H-O-H bond angle is much narrower than would be expected at ~98 °, much tighter than the 104.5° expected. The primary reason for this would appear to be the improvement of coordination to the surrounding oxygen atoms of the B_2O_6 framework that this allows. The model using a 48*f* position results in a O(water)-H-O(framework) bond angle of 158.0° with the hydrogen atoms 2.1 Å from the surrounding framework, introducing the higher symmetry model allows this bond to become more linear, thus shortening this distance to 1.95 Å at 163.9°. This in turn provides more stability for this orientation of the water molecule. In reality it seems highly likely that these water molecules exhibit behaviour similar to that seen in the motion of the cations inhabiting this site in other *beta*-pyrochlores. On this site the water molecule is able to both rotate, with hydrogen atoms flipping between the three crystographically allowed sites surrounding each oxygen position, and 'rattle' with the oxygen atoms moving between the four allowed sites in each cavity. This is further evidenced by the higher than expected thermal parameters seen for all atoms of the water molecule, which whilst providing a stable model does imply that the atoms are not static on these positions even at 1.5 K.

4.6 Powder neutron diffraction studies of $NaTaWO_6.nH_2O$

To better understand the behaviour of water within the $KTaWO_6$ framework $NaTaWO_6.nH_2O$ has also been studied by PND. The presence of the smaller cation would lead us to expect a corresponding reduction in lattice parameter, as has previously been observed by Michel *et al*[40] where the phase was synthesised by an ion exchange route and characterized by PXRD. This study did not attempt to accurately ascertain the location of all atoms within the framework and this is therefore something we have undertaken.

4.6.1 Synthetic route

The $NaTaWO_6.nH_2O$ phase was synthesised by an ion exchange route using the previously discussed phase $KTaWO_6.nH_2O$ as a starting material. A sample, ~3g, of $KTaWO_6$ was suspended in a 5 M solution of NaCl and stirred constantly for 48 hours. After this time the suspension was allowed to settle and the solution decanted off and replaced. This process was repeated for two weeks after which time the remaining liquid was removed and the resulting white powder washed repeatedly with distilled water. The sample was then dried at ~60 °C overnight before further analysis was undertaken.

Phase purity was checked using EDX, which showed that potassium was no longer present in the sample, with only sodium peaks being observed. Short PXRD scans showed the retention of the pyrochlore phase and a reduction in lattice parameter from ~10.47 Å in the $KTaWO_6$ starting material to 10.36 Å in the ion exchanged product, this is in good agreement with those presented by Michel *et al*. TGA was also undertaken showing an almost identical dehydration curve to that observed in $KTaWO_6.nH_2O$ and corresponding to 1 water molecule per formula unit.

4.6.2 Data collection

Data were collected on the Super D2B high resolution powder neutron diffraction instrument at the ILL, Grenoble. The data were collected using a monochromated beam of neutrons at 1.594Å between 0.1 and 158.2° 2θ for 2 hours. The sample was housed in an 8 mm vanadium can and cooled using a standard Oxford instruments orange cryostat to 1.5 K before data were collected.

4.6.3 Data Analysis

Initial inspection of the data led to the exclusion of all data points below 10° 2θ, where no reflections would be observed for the pyrochlore structure and above 149.5° where a significant peak, arising from the sample environment, was observed to be overlapping the pyrochlore reflections. Although the level of incoherent scattering is relatively low, with only a small contribution to the pattern, the overall signal to noise ratio is poor with a background level of 2-300 counts per second on data that peaks at 600 counts per second. The subsequent refinement of this data was carried out using the GSAS suite of von Dreele and Larson[33,34] with all reflections being rapidly assigned to the pyrochlore structure using the model of Michel *et al*.[4] The refinement proceeded smoothly with the initial variation of lattice parameter, zero point and background coefficients. Peak shape parameters followed by individual atomic thermal motions and atomic positions were then introduced leading to reasonable values for all parameters. The model of Michel *et al* had not attempted to locate hydrogen positions within this framework and this was therefore undertaken, Fourier maps were calculated to locate areas of negative neutron scattering that may be associated to the presence of protons at that location. The strongest model identified assigned the same position to the protons as was previously used for $KTaWO_6.H_2O$, i.e. at the 48*f* site (3/8, 3/8 ,*x*).

Several other factors were also studied; variation of the water content by refinement of the levels of occupation on the 8*b* oxygen and the 48*f* hydrogen positions resulted in a very low level of variation, ~ ± 5 %, with an error of ~ 3% this was therefore retained as a fully occupied site as identified by the previously analysed TGA data. Similarly occupation of the sodium site was attempted, a stable variation of ~ 15 % above the nominal level arose from this, however no significant changes were observed in either the graphic or calculated fit parameters, with the chi squared values and R_{wp} values remaining the same regardless of whether this parameter was refined or not. This effect was attributed to the relatively low neutron scattering cross section of sodium with respect to the other materials in this framework and was therefore ignored with the retention of an occupation of 0.5 relating to one sodium per formula unit.

As the water molecule in $KTaWO_6.H_2O$ was refined to a position away from the centre of the 8*b* cavity a similar exercise was undertaken for this material. Altering the oxygen position from an 8*b* to an adjacent 32*e* site lead to no significant change in profile fit, the resulting refinement did however prove unstable, diverging to other positions and causing the level of thermal motion to increase significantly. Whilst the model with these cations of the 8*b* position results in larger than ideal levels of thermal motion it proved to be the most stable and was thus used for all subsequent analysis.

Table 4.7.1 – Final Refined atomic parameters for a 1.5K PND data set collected on the super D2B instrument for $NaTaWO_6.H_2O$. E.S.D's are given in parentheses.

Atom	Site	*x*	*y*	*z*	Occupancy	Ui/Ue*100
Na	16*d*	0.5	0.5	0.5	0.5	2.7(3)
Ta	16*c*	0	0	0	0.5	1.24(7)
W	16*c*	0	0	0	0.5	1.24(7)
O	48*f*	0.31161(16)	0.125	0.125	1	0.92(4)
O	8*b*	0.375	0.375	0.375	1	7.2(3)
H	48*f*	0.375	0.375	0.4899(18)	0.3333	10.5(9)

Space group $Fd\bar{3}m$. Cell parameters: $a = b = c = 10.36134(16)$ Å

Final fit parameters: $\chi^2 = 3.135$, $R_{wp} = 3.82$ % $R_p = 2.93$ %

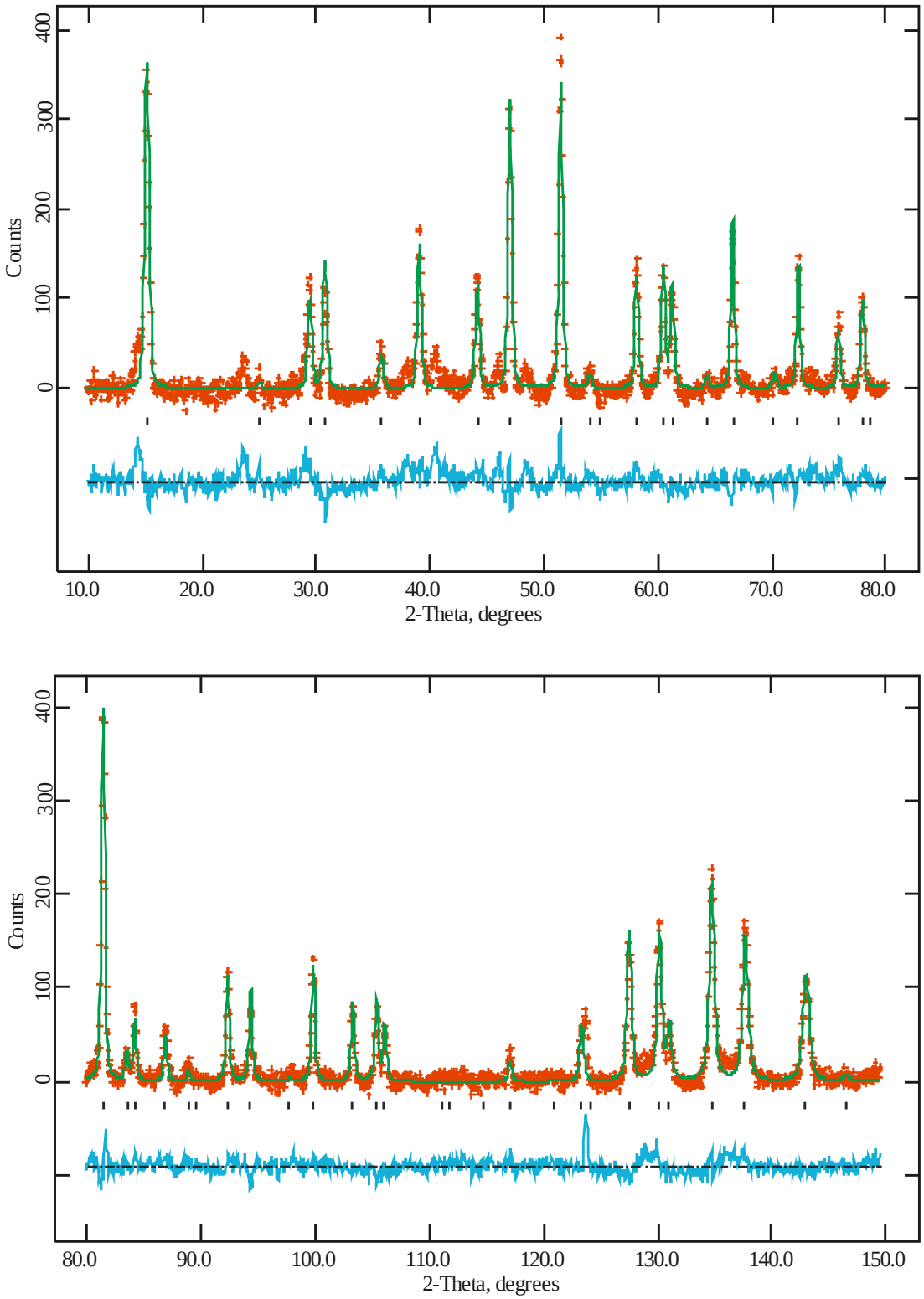

Figure 4.7.1. – Profile fit to PND data for $NaTaWO_6.nH_2O$. Experimental data points are shown as red crosses, upper continuous green line the calculated profile and the lower continuous blue line the difference. Allowed reflections positions are indicated by tick marks.

4.6.4 Discussion

The result of the poorly defined oxygen position in this refinement is an unsatisfactory model of the water with calculated bond lengths of 1.191(19) Å as opposed to a value of ~0.94 Å in an ideal water molecule. The nature of the relationship between the two positions for the component atoms, both on a position of 0.375,0.375,*x* site, means that the resulting internal bond angle for these water molecules is 90° clearly unsatisfactory. Inspection of calculated Fourier density maps show the neutron scattering density associated with the oxygen atoms to be well defined at the centre of the cavity, with no nodes as observed in $KTaWO_6.H_2O$ (Figure 4.2.2), although the density is spread over a larger area. It is probable that the oxygen atoms inhabit areas of this section depending upon where their corresponding hydrogen positions are, with displacements within this zone allowing both the contraction of bond lengths and the corresponding increase in bond angle.

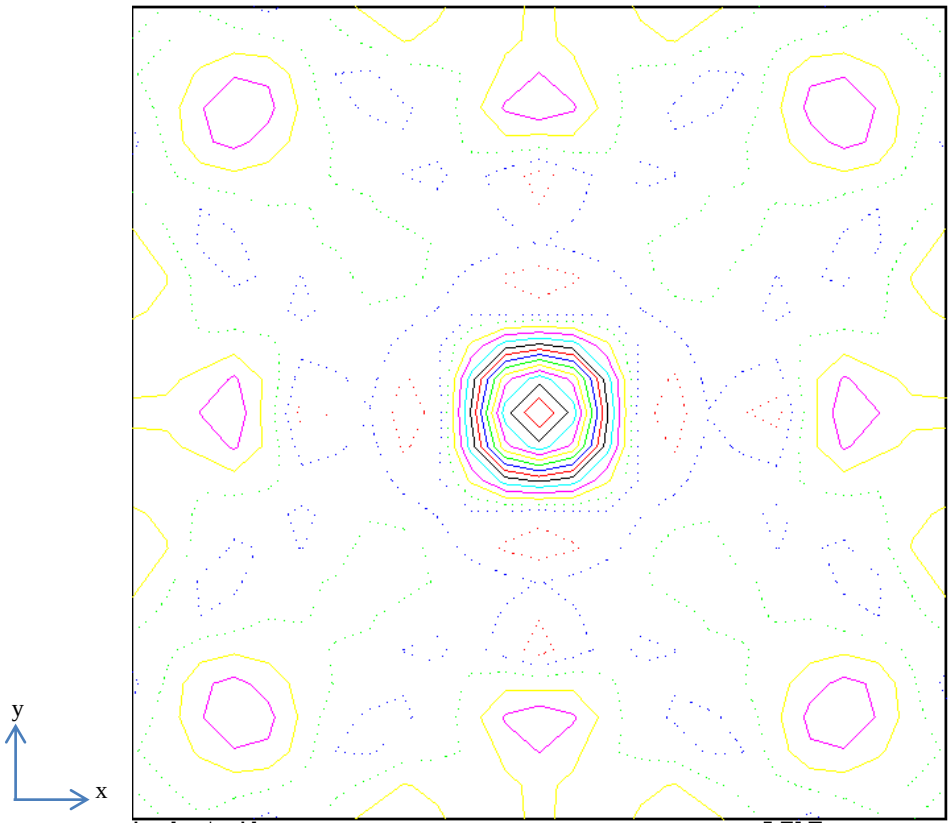

Figure 4.7.2 –A calculated Delta-F image for $NaTaWO_6$ clearly showing a defined area of neutron density. The image is centred on a 8b site, 0.375, 0.375, 0.375, looking along the x-axis. Solid contour lines represent areas of positive nuclear density whilst dotted lines areas of negative density.

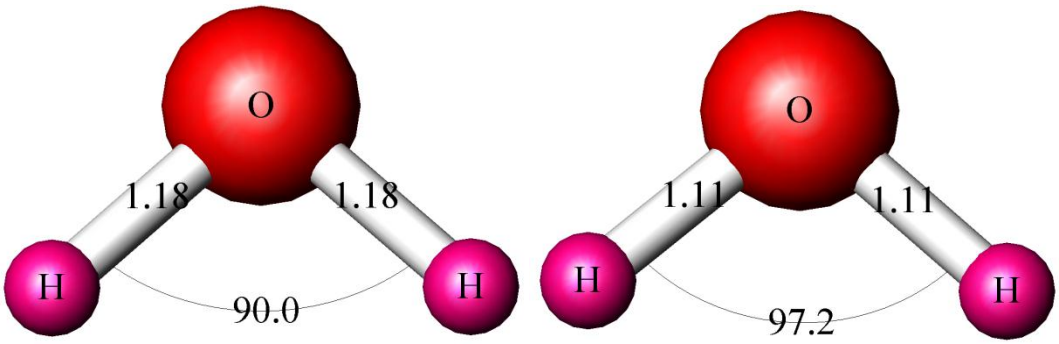

Figure 4.7.3 – The left hand image shows the orientation of the water molecules suggested by the model, the right hand image shows the effect of moving the oxygen atom to the a position at the limit of its allowed thermal model.

As Figure 4.7.3 shows a small change in the oxygen position, in this case moving that atom to the edge of the sphere allowed by its calculated thermal motion, improves the model significantly. Incorporation of the errors related to the hydrogen atoms would allow a significant shortening of the bond lengths to something closer to a reasonable value although still leaving an internal bond angle that is significantly shorter than is ideal. The effects of the surrounding lattice may also play an important role as the hydrogen atoms are also roughly aligned with the oxygen atoms of the framework and the contribution of these atoms may lead to a small increase in these bond lengths. It is also highly plausible that the model of Murphy *et al* as discussed in Section 4.6.3 where the hydrogen atoms are on 96*g* sites adjacent to the 48*f* position would provide a more favourable model, retaining almost identical bond lengths whilst increasing the bond angle to something closer to what we would expect for a water molecule. Whilst testing of this model proves stable there was no improvement in the fit parameters, the thermal motions of the atoms are reduced but this is an expected result as the two positions effectively overlap with this higher symmetry position.

In general the incorporation of sodium on to the 16*d* site can be seen as much more favourable in this material than for potassium in $KTaWO_6$. The BO_6 polyhedra display near perfect octahedral coordination with very low levels of distortion of the framework (values within three standard deviations of an 'ideal' octahedra) required to provide a stable sodium position. The B_2O_6 network can also be viewed as 'relaxed' and results in a material with lattice dimensions and a polyhedral framework with more in common with $KTaWO_6$ than $KTaWO_6.H_2O$.

4.7 Conclusions

$KTaWO_6.nH_2O$ phases

Both the hydrated and dehydrated phases of this material have been studied by PXRD. The main feature of this dehydration has been the contraction of the B_2O_6 network that caused a shift of the potassium ions from a 16*d* site to the larger cavities surrounding the 8*b* site. This movement has allowed the polyhedra to both compress and distort, the compression as the potassium ions no longer require coordination on a site that is nominally smaller than is ideal and the distortion allowing better coordination of these ions on their new site. The potassium cations remain highly delocalised on their new site, shifting to and probably between the 32*e* positions within each of the large cavities.

Study of the dehydration process undertaken by this phase has shown that this process is both gradual and predictable, with the water being lost over a broad temperature range, ~RT to 120 °C. It is likely that this arises as the water is structurally trapped rather than bonded to the structure and is therefore lost as the energy becomes available for it to escape from its individual cavity.

Finally the use of low temperature PND has allowed an accurate picture of the water molecules and their interactions with the surrounding framework to be built up. This has shown that the water distorts slightly to allow the protons to align with the oxygen atoms of the B_2O_6 framework and it has been assumed that this occurs as it in turn allows the water to be stabilised in a particular orientation. It has also been deemed likely that these water molecules rapidly shift between different alignments, indicated by high thermal parameters for both the oxygen atoms and protons, a process that seems probable in a framework like this where the water molecule is smaller than the space available to it and is not stabilised by any other form of bonding.

$NaNbWO_6.H_2O$

In relation to the B_2O_6 framework this material has been shown to be extremely structurally similar to $KTaWO_6$ with the material forming polyhedra that are near to the ideal octahedral geometry. This can be attributed in part to the smaller *A*-type cation present which is of a size more conducive to the orientation of polyhedra commonly seen surrounding the 16*d* position. Whilst the PND data on this phase has also allowed the locating of the protons associated with the intercalated water they have been assigned to the 48*f* positions rather than the nearby 96*g* as there was no meaningful change in the criteria of fit by placing them here. This may arise from one of two reasons; firstly it may be assigned to the relatively poor level of data, which has does not allow us to distinguish between what are effectively overlapping positions or secondly it may be due to the rapid movement of the water molecules in the cavities which restricts the degree to which we may accurately determine their location. This second option can be justified by the oxygen of the water being assigned to a 8*b* site with a particularly large thermal motion rather than the 32*e* sites more commonly seen in other hydrated *beta*-pyrochlores, possibly indicating that the molecule is shifting around this site.

4.8 References

(1) Babel, D.; Pausewang, G.; Viebahn, W. *Zeitschrift fuer Naturforschung, Teil B. Anorganische Chemie, Organische Chemie* **1967**, *22*, 1219.

(2) Darriet, B.; Rat, M.; Galy, J.; Hagenmuller, P. *Mat. Res. Bull.* **1971**, *6*, 1305.

(3) Goodenough, J. B.; Hong, H. Y. P.; Kafalas, J. A. *Mat. Res. Bull.* **1976**, *11*, 203.

(4) Michel, C.; Groult, D.; Deschanvres, A.; Raveau, A. *J. of Inorg. and Nuc. Chem.* **1975**, *37*, 251.

(5) Michel, C.; Groult, D.; Raveau, B. *Mat. Res. Bull.* **1973**, *8*, 201.

(6) Groult, D.; Michel, C.; Raveau, B. *J. of Inorg. and Nuc. Chem.* **1973**, *35*, 3095.

(7) Michel, C.; Groult, D.; Raveau, B. *J. of Inorg. and Nuc. Chem.* **1975**, *37*, 247.

(8) Groult, D.; Michel, C.; Raveau, B. *J. of Inorg. and Nuc. Chem.* **1974**, *36*, 61.

(9) Groult, D.; Pannetier, J.; Raveau, B. *J. of Sol. St. Chem.* **1982**, *41*, 277.

(10) Isasi, M. J.; Lopez, M. L.; Veiga, M. L.; Ruiz-Hitzky, E.; Pico, C. *J. of Sol. St. Chem.* **1995**, *116*, 290.

(11) Norby, T. *J. Mater. Chem.* **2001**, *11*, 11.

(12) Irvine, J. T. S.; Feighery, A. J.; Fagg, D. P.; Garcia-Martin, S. *Solid State Ionics* **2000**, *136*, 879.

(13) Wilde, P. J.; Catlow, C. R. A. *Solid State Ionics* **1998**, *112*, 173.

(14) Bhat, S. V.; Binesh, N.; Bhat, V. *Chem.Phys. Letters* **1994**, *231*, 487.

(15) Binesh, N.; Bhat, V.; Bhat, S. V. *Solid State Ionics* **1996**, *86-8*, 665.

(16) Groult, D.; Michel, C.; Raveau, B. *J. of Inorg. and Nuc. Chem.* **1974**, *36*, 61.

(17) Slade, R. C. T.; Hall, G. P.; Ramanan, A.; Prince, E. *Solid State Ionics* **1996**, *92*, 171.

(18) Chowdhry, U.; Barkley, J. R.; English, A. D.; Sleight, A. W.; du Pont de Nemours, E. I.; Inc, C. *Mat. Res. Bull.* **1982**, *17*, 917.

(19) Groult, D.; Pannetier, J.; Raveau, B. *J. of Sol. St. Chem* **1982**, *41*, 277.

(20) Butler, M. A.; Biefeld, R. M. *Phys. Rev. B* **1979**, *19*, 5455.

(21) Dickens, P. G.; Weller, M. T. *Solid State Commun.* **1986**, *59*, 569.

(22) Barnes, P. W.; Woodward, P. M.; Lee, Y.; Vogt, T.; Hriljac, J. A. *J. of the Amer. Chem. Soc.* **2003**, *125*, 4572.

(23) Galati, R.; Simon, C.; Knee, C. S.; Henry, P. F.; Rainford, B. D.; Weller, M. T. *Chem. Mat.* **2008**, *20*, 1652.

(24) Chernorukov, N. G.; Suleimanov, E. V.; Kortikov, V. E.; Suchkov, A. I. *Zhurnal Neorganicheskoi Khimii* **1998**, *43*, 1251.

(25) Groult, D.; Michel, C.; Raveau, B. *J. of Inorg. and Nuc. Chem.* **1975**, *37*, 2203.

(26) Hervieu, M.; Michel, C.; Raveau, B. *Bulletin de la Societe Chimique de France* **1971**, *1971*, 3939.

(27) Nagao, Y.; Yamaura, J. I.; Ogusu, H.; Okamoto, Y.; Hiroi, Z. *J. of the Phys. Soc. of Japan* **2009**, *78*, 21.

(28) Mari, C. M.; Catti, M.; Castelli, A.; Bonino, F. *Mat. Res. Bull.* **1986**, *21*, 773.

(29) Moller, T.; Clearfield, A.; Harjula, R. *Micro. and Meso. Mat.* **2002**, *54*, 187.

(30) Holcombe, C. E.; Smith, D. D. *J. Am. Ceram. Soc.* **1978**, *61*, 163.

(31) Roth, R. S.; Waring, J. L.; Parker, H. S. *J. of Sol. St. Chem.* **1970**, *2*, 445.

(32) Mertin, W.; Gruehn, R.; Schäfer, H. *J. of Sol. St. Chem* **1970**, *1*, 425.

(33) Larson, A. C.; Von Dreele, R. B. Los Alamos National Laboratory Report LAUR 86-748 (2000). 1990.

(34) Toby, B. H. *J. of Appl. Crys.* **2001**, *34*, 210.

(35) Galati, R.; Simon, C.; Henry, P. F.; Weller, M. T. *Phys. Rev. B* **2008**, *77*.

(36) Kar, T.; Choudhary, R. N. P. *Mat. Sc. and Eng. B* **2002**, *90*, 224.

(37) Hummel, H. U.; Fackler, R.; Remmert, P. *Chemische Berichte* **1992**, *125*, 551.

(38) Sears, V. F. *Neutron News* **1992**, *3*, 26

(39) Murphy, D. W.; Cava, R. J.; Rhyne, K.; Roth, R. S.; Santoro, A.; Zahurak, S. M.; Dye, J. L. *Solid State Ionics* **1986**, *18*, 799.

(40) Michel, C.; Groult, D.; Deschanvres, A.; Raveau, B. *J. of Inorg. and Nuc. Chem.* **1975**, *37*, 251.

Chapter Five

ION EXCHANGE PYROCHLORES

5.1 Introduction

In solid state chemistry the term ion exchange relates to any process by which ions are exchanged between a complex and an electrolyte. Common materials of this type are used in the fields of purification, separation and decontamination of aqueous solutions, and are generally split into two classes known as solid polymeric and mineralic ion exchangers. Examples of materials commonly used as ion exchangers include; resins[1], zeolites[2], montmorillonite[3], clay[4] and soil humus[5]. In general these materials are separated into two main categories either cation or anion exchangers, although amphoteric exchangers are known but are rarely used commercially as a mixture of other materials generally proves more efficient. The applications of materials of this type vary widely and include; in the food and beverage industry, in nuclear waste disposal, the pharmaceutical industry, as sugar and sweeteners, in batteries and fuel cells and in water purification.

Pyrochlores specifically have found uses in the separation of specific nuclei from radioactive nuclear waste[6,7] where their highly stable B_2O_6 network coupled with often loosely bound A_2O' networks provided the two main features required for this property, that is long-term stability in a radioactive environment and rapid initial ion exchange. An additional feature of these materials that proved interesting to scientists in the field is their ability to adopt significant levels of defects within the structure without structural collapse. This feature has been seen as being of particular importance in the storage of radioactive isotopes as the high levels of radiation present can cause a significant level of defects to form which in turn may lead to certain materials being amorphous and increases the mobility of the radioactive material.

Other work has shown the potential application of these phases, in particular the materials adopting the *beta*-pyrochlore structure type, in the disposal of heavy metal waste[8]. Once again the final stability of the product is key to this functionality as leeching of the stored heavy metals is highly undesirable. The high mobility of the -*A*-site cations in the starting materials favours the exchange of these ions suggesting great potential for ion exchange.

5.2 Synthesis and characterisation of the series $A^{2+}(B^{5+}WO_6)_2.2H_2O$ (A^{2+} = Cd, Pb ,Ca, Sr and Ba and B^{5+} = Nb or Ta)

Whilst a truly wide range of materials adopting the pyrochlore framework are known, the vast majority are still produced by conventional solid state routes. However some phases of this type can and have been synthesised by ion exchange methods. *Alpha*-pyrochlore phases do, in general, not lend themselves to this route as they are truly two interpenetrating networks, mutually supporting one another so the removal of one cation from the phase causes the collapse of the entire framework. In contrast *beta*-type phases are often somewhat different with the BO_6 framework effectively self supporting or only weakly supported by the *A*–site cations present in the framework. This is seen markedly in certain tantalum containing pyrochlores where the inclusion of protons alone within the cavities allows the retention of the structure[9] and in a wide range of other pyrochlores where lithium and sodium cations provide the required stability[10] even though they do not occupy the larger sites within the cavities. This property of these materials also allows for the presence of empty cavities, i.e. the space surrounding the 8*b* sites and some of these materials are studied here. A limited family of materials was synthesised by Chernorukov *et al*[11] who presented the first and only series of materials with *A*-site cations that have a charge higher than 1+ and retain a *beta*-type structure. This family adopts the general formula $A^{2+}(B^{5+}WO_6)_2.2H_2O$ where A^{2+} = Ca, Sr and Ba and B^{5+} = Nb or Ta and were produced by ion exchange routes. In this study the structure was determined by powder X-ray diffraction, completion of ion exchange by elemental analysis and water content by thermogravimetric analysis. The data presented was limited to confirmation of structure and composition with only lattice parameters presented and the remainder of the structural information extrapolated under the assumption that the structure is simple and analogous to other hydrated phases. The work presented in this section aims to better characterise and increase the range of known compounds of this type.

The nature of the synthesis of these materials also provides a source of interest. Ion exchange materials as a functional product are commonly used in several areas of industry with uses ranging from simple washing detergents to the disposal of heavy elements from toxic waste. Pyrochlores are excellent candidates for applications as

functional ion exchange materials, with a potentially high rate of ion exchange and a considerable degree of control over the pore sizes and thus cations that can be accommodated. Pyrochlore phases, particularly zirconates and titanates, have been used in the disposal of actinides produced by fission as the framework they provide is particularly stable to irradiation thus providing a medium for long term storage[12]. Several of the phases presented here are of particular interest as barium, strontium and caesium isotopes are all major products of fission with half lives ranging from months to years and are therefore important in the disposal of nuclear waste[13].

As well as considerably more in-depth studies of the known series $A^{2+}(B^{5+}WO_6)_2.2H_2O$ (A^{2+} = Ca, Sr and Ba and B^{5+} = Nb or Ta) studies of four new phases are also presented, $A^{2+}(BWO_6)_2.H_2O$ (A = Cd and Pb and B = Nb or Ta). Whilst similar phases of the general formula $A^{II}B_2O_6.H_2O$ (known for A = Cd and Pb, B = Nb and Ta)[14] these phases with mixed occupancy on the *B*-site and partial occupancy on the *alpha*-network have not previously been reported. This increases the range of materials formed with this structure type through ion exchange reactions and shows the potential of these systems for applications in heavy metal waste disposal.

5.2.1 Synthetic route

Initially work was attempted to establish whether a direct solid state route would enable the synthesis of phases of the types discussed later in this chapter, in each case no pyrochlore type phase was observed and this route was rapidly abandoned. The lack of success with this route can readily be explained by the need for a stabilising cation for the framework to form around, with only a theoretical average of half a cation per formula unit there is insufficient stability available for the cavities to form and be retained at the high temperatures required for synthesis.

Successful synthesis of these phases appears to rely upon a starting material which has an extremely stable B_2O_6 framework with, ideally, a smaller than optimum *A*-site cation which enables ion exchange to occur more readily. For this reason $KNbWO_6$ and $KTaWO_6$ were used as starting materials, as discussed in Chapter Four these materials have both of the characteristics mentioned above and are also readily synthesised in bulk quantities.

These two phases, $KNbWO_6$ and $KTaWO_6$, were initially synthesised by direct solid state routes using stoichiometric quantities of K_2CO_3 (Hogg, 99 %), WO_3 (Alfa Aesar, 99.7 %) and Nb_2O_5 (Sigma Aldrich, 99.9 %) or Ta_2O_5 (Sigma Aldrich, 99 %) as the starting materials. The starting materials were ground together and calcined at 600°C for 16 hrs. The resulting phase was then reground, pelletised at 15 tons/cm^2 and annealed again at 800 and 900 °C for $KNbWO_6$ and $KTaWO_6$ respectively for a further 16 hrs. These phases were then checked for purity using PXRD and shown to be phase pure.

Ion exchange using molten solutions of certain metal chlorides along with the appropriate starting materials was studied briefly at this point. Lead chloride (m.p. 501 °C) and cadmium chloride (m.p. 568 °C) were initially used due to their melting points being considerably lower than the remaining chlorides of interest. The method allowed a small degree of ion exchange, confirmed by elemental analysis but did not go to completion. For this reason along with the lack of applicability in industry for a molten system and the considerably higher temperatures that would be required for several of the other metal chlorides required this route was rapidly abandoned.

The final, successful, synthetic route was a simple ion exchange one as used by Chernorukov *et al*[11]. The previously synthesised pyrochlores (~5g) were placed in a standard set of reflux apparatus along with ~50ml of a 5M solution of the appropriate metal chloride or metal nitrate. The choice between whether to use a solution of nitrate or chloride was made based upon what was readily available and both proved to be adequate for what was required. The solution was then stirred under reflux for two weeks, with the solution allowed to settle, drained off and replaced with fresh solution every 48 hours to ensure a maximum concentration gradient was maintained throughout. Upon completion of this method the resulting powders were repeatedly washed with distilled water before being dried at ~60 °C. At the end of this period phase purity was confirmed through PXRD with each material showing the retention of the pyrochlore framework. The tantalum containing frameworks also showed a small amount of tantalum oxide as an impurity. The samples retained a total mass within 10% of the starting material used in each case, which was deemed as acceptable as a small amount of powder was lost with each ion exchange cycle and subsequent washing. Where elemental analysis showed incomplete ion exchange the samples were refluxed for further periods of time until EDX showed no further ion-exchange or full ion-exchange had been reached. The starting materials and total period of ion exchange are summarised in Table 5.2.1.

Table 5.2.1 – Total time under reflux, along with ion exchange source material for the series $A^{2+}(B^{5+}WO_6)_2$ where A = Ca, Sr, Ba, Pb and Cd, and B = Nb and Ta.

Target phase	Metal ion source	Total time in solution/days
$Ca(NbWO_6)_2.nH_2O$	$CaCl_2$	18
$Ca(TaWO_6)_2.nH_2O$	$CaCl_2$	14
$Sr(NbWO_6)_2.nH_2O$	$Sr(NO_3)_2$	14
$Sr(TaWO_6)_2.nH_2O$	$Sr(NO_3)_2$	22
$Ba(NbWO_6)_2.nH_2O$	$BaCl_2$	14
$Ba(TaWO_6)_2.nH_2O$	$BaCl_2$	14
$Pb(NbWO_6)_2.nH_2O$	$Pb(NO_3)_2$	18
$Pb(TaWO_6)_2.nH_2O$	$Pb(NO_3)_2$	14
$Cd(NbWO_6)_2.nH_2O$	$Cd(NO_3)_2$	14
$Cd(TaWO_6)_2.nH_2O$	$Cd(NO_3)_2$	22

5.2.2 Elemental analysis of $A^{2+}(B^{5+}WO_6)_2.nH_2O$

Elemental analysis was routinely carried out on each phase to confirm the level of ion exchange that had occurred within the materials using a JEOL JSM 5910 scanning electron microscope, fitted with an Oxford Instruments Inca Energy 300 energy-dispersive X-ray spectrometry analysis system. When the sample was seen to have undergone complete ion exchange or there was no noticeable change in the ratio of A^{2+}: K synthesis was halted. The elemental composition for each phase was averaged over several data collections and a mean value calculated. The results of these analyses are tabulated below in Table 5.2.2 with the proportion of oxygen excluded due to the poor ratios provided by this method in the presence of heavy atoms. As tungsten is the common element across the series all values are given with respect to proportion of tungsten present.

During this work the oxygen content was ignored as it was deemed unreliable and only the ratio of metal atoms was used for analysis.

Table 5.2.2 – Calculated mean compositional values from EDX data for the series $A^{2+}(B^{5+}WO_6)_2.nH_2O$, in the ideal structure values for B^{5+} = 1 , K = 0 and A^{2+} = 0.5

Target phase	Elemental ratio with respect to tungsten			
	K	A^{2+}	B^{5+}	W
$Ca(NbWO_6)_2.nH_2O$	0.04	0.46	0.85	1.00
$Ca(TaWO_6)_2.nH_2O$	0.00	0.69	0.88	1.00
$Sr(NbWO_6)_2.nH_2O$	0.00	0.69	1.05	1.00
$Sr(TaWO_6)_2.nH_2O$	0.07	0.36	0.84	1.00
$Ba(NbWO_6)_2.nH_2O$	0.00	0.61	0.98	1.00
$Ba(TaWO_6)_2.nH_2O$	0.00	0.63	0.71	1.00
$Pb(NbWO_6)_2.nH_2O$	0.04	0.49	1.05	1.00
$Pb(TaWO_6)_2.nH_2O$	0.00	0.76	0.85	1.00
$Cd(NbWO_6)_2.nH_2O$	0.00	0.36	1.05	1.00
$Cd(TaWO_6)_2.nH_2O$	0.02	0.47	0.89	1.00

Data from EDX must be viewed carefully and is not readily used as a quantitative tool, this is particularly true for these families of materials where the energy bands observed are often overlapping, this effect can be viewed in Figure 5.2.2 where it can readily be seen that the peaks along with their intensities cannot be easily separated from one another. The niobium, tungsten and tantalum peaks overlap across the energy range, particularly at lower energies where the more intense peaks provide the most accurate information for quantitative analysis. It is also worth mentioning that several peaks overlap with those of the divalent cations being looked at and thus this information must be carefully used. The only reliable information that can be taken from this data is that of the presence of the elements labelled and very rough ratios to one another.

It is worth noting at this juncture that whilst some potassium is still present in these materials attempts to locate it, on positions separate from those of the divalent cations, when refining the various data sets did not succeed. As the levels of occupation, when present at all, are extremely low this has not been discussed further, it is however worth noting that this element is still present in several of the phases even after the ion exchange process has been completed.

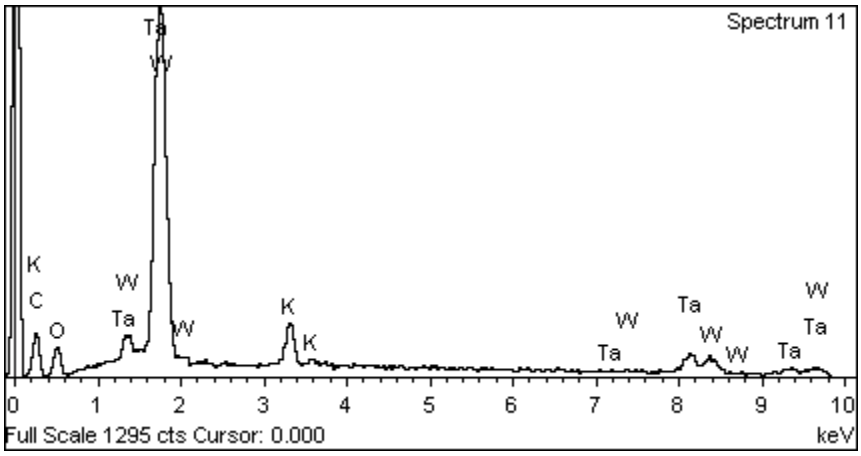

Figure 5.2.1 – Counts vs KeV for the ion exchange starting material $KTaWO_6$, peak assignments are labelled and the carbon at low KeV is assigned to the coating used in sample preparation.

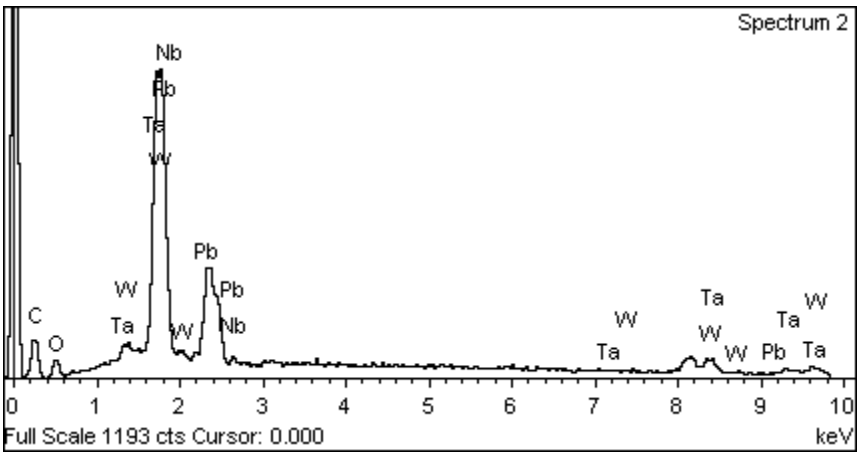

Figure 5.2.2– Counts vs KeV for the ion exchange material $Pb(TaWO_6)_2$, peak assignments are labelled and the carbon at low KeV is assigned to the coating used in sample preparation.

For comparison data for the starting materials $KTaWO_6$ and $KNbWO_6$ are also included in Table 5.2.3 where we can view the discrepancies between the phase composition arising from the data and that which we would expect. It is reasonable to assume that within experimental limits these materials will follow the ideal stoichiometry, it can thus be seen that the experimental limits of assigned composition vary widely. Once again the presented data is the result of multiple summed data sets, which were in themselves even more widely spread.

Table 5.2.3 – Elemental composition for the starting materials used for the ion exchange reactions discussed in this section.

Target phase	Elemental ratio with respect to tungsten		
	K	B^{5+}	W
$KTaWO_6$	0.84	0.93	1
$KNbWO_6$	0.95	1.04	1

5.2.3 Thermogravimetric data analysis for the series $A^{2+}(B^{5+}WO_6)_2.nH_2O$

Data was collected for each member of the series to identify the level of hydration for each phase. For a fully exchanged material a water content of two water molecules per unit would be expected, giving a standard formula of $A^{2+}(B^{5+}WO_6)_2.2H_2O$. However if complete ion exchange has not occurred then we will expect a value of less than one as the potassium ions remaining in the structure will occupy the cavity surrounding the 8*b* site leaving insufficient room within for a water molecule to be present. Data was collected for each phase over a temperature range of 25 to 600 °C with mass change and DSC recorded, typically each data set was collected over a period of 1 to 2 hours.

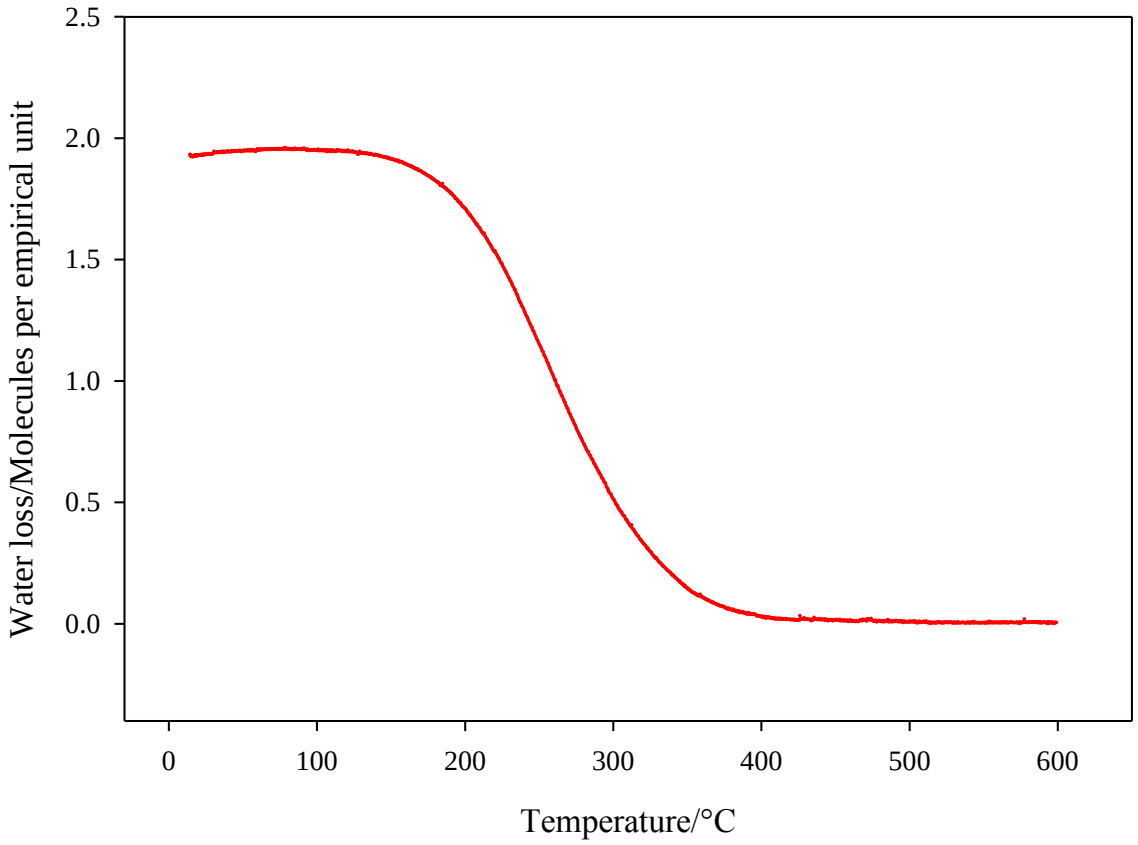

Figure 5.2.3– A plot of calculated water content against temperature for $Ba(NbWO_6)_2.xH_2O$ showing the broad temperature range over which water is lost.

The majority of phases studied displayed the relatively simple behaviour as characterised by $Ba(NbWO_6)_2.xH_2O$ (Figure 5.2.3) with a consistent loss of mass over a wide range of temperatures. The one phase showing significantly different behaviour is $Cd(NbWO_6)_2.xH_2O$, unlike the remaining materials in the series this phase does not display the characteristic smooth dehydration with a 2-3 % mass loss but instead loses a much more significant 29 % of the sample's mass. If we were to assume that only Nb_2O_5 and WO_3 remain at 600 °C, as both are thermally stable to considerably higher temperatures than this, then we would expect to observe an even higher mass loss than is seen, in the region of 35 %. Inspection of the accompanying DSC plot shows a series of thermal events occurring over the full range of temperatures implying a complex process of decay is occurring. PXRD data collected on the sample after heating showed a total loss of the pyrochlore structure, with only amorphous scattering observed from the resulting product. In contrast the second cadmium containing phase studied, $Cd(TaWO_6)_2.nH_2O$, whilst displaying a much broader dehydration curve with water being lost up to approximately 500°C, retained the pyrochlore structure throughout.

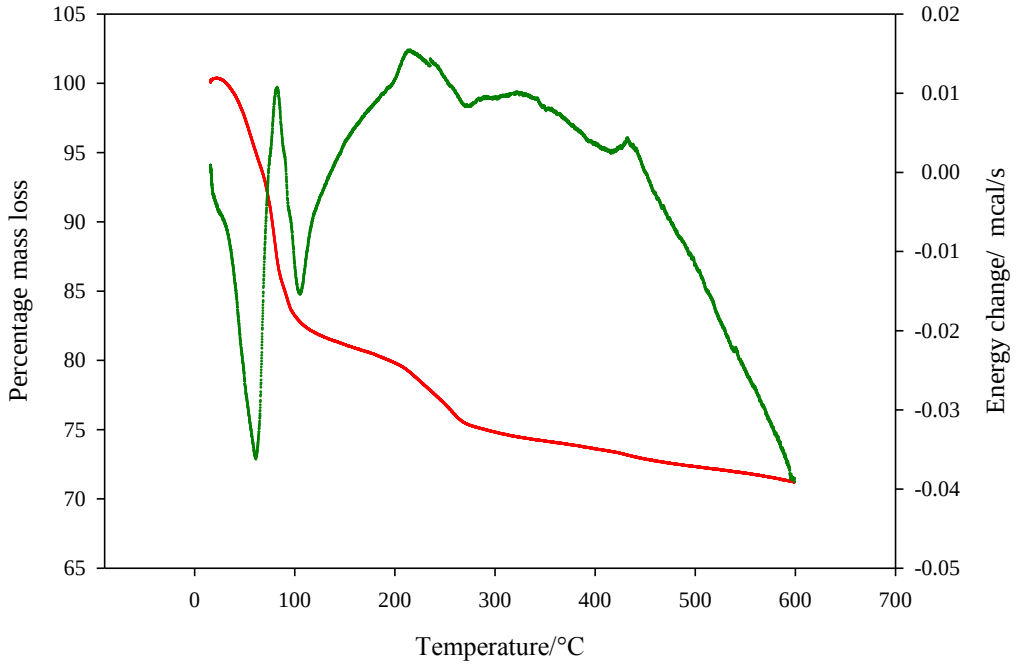

Figure 5.2.4 – TGA (red) and DSC (green) plots for $Cd(NbWO_6)_2.xH_2O$ collected over a temperature range of 25 to 600 °C.

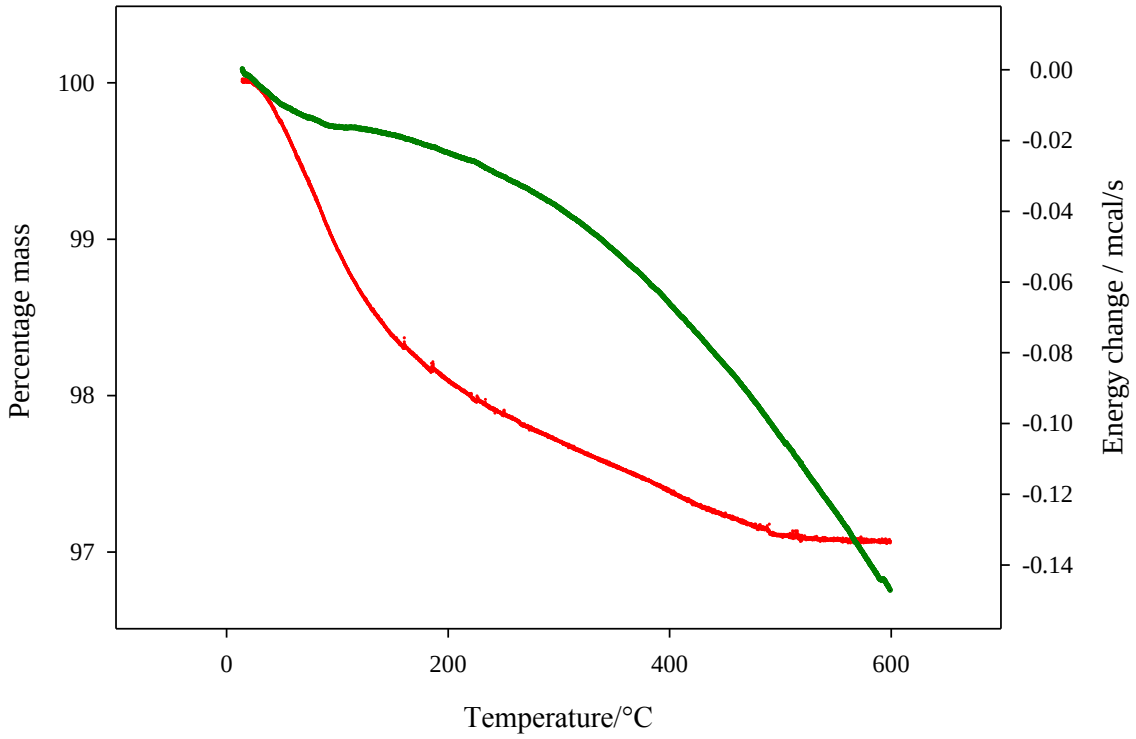

Figure 5.2.5 - TGA (red) and DSC (green) plots for $Cd(TaWO_6)_2.xH_2O$.

A sample of $Sr(NbWO_6)_2$ was also studied over a temperature range of 25 to 900 °C to observe the thermal stability over a wider range, no unusual behaviour was observed over this extended range with just a slight further mass loss at the higher temperatures which was attributed to the loss of some of the *A*-site. This behaviour showed a thermal stability similar to that displayed by the starting materials, a feature we would not readily predict as it would be expected that losing a significant proportion of the A^{2+} cations would lead to some reduction in overall structural stability.

Brief collections of powder X-ray diffraction data were also carried out on completion of the thermal gravimetric studies; these showed that the pyrochlore structure was retained after heating of the samples to 600 °C for all phases except for $Cd(NbWO_6).xH_2O$. A sample of $Sr(NbWO_6)_2.xH_2O$ was dried at 600 °C for 6 hours to remove all water, the sample was the allowed to cool and left in air for 48 hours. A further TGA was then run on the same $Sr(NbWO_6)_2.xH_2O$ sample with the resulting mass change being within 0.2% of that observed for the untreated sample

suggesting that the dehydration of these samples is at least partially, if not completely reversible.

Table 5.2.4- Calculated waters per formula unit for the series $A^{2+}(B^{5+}WO_6)_2.nH_2O$ calculated from TGA data

Material	*n* for $A^{2+}(B^{5+}WO_6)_2.nH_2O$
$Ca(NbWO_6)_2.nH_2O$	1.74
$Ca(TaWO_6)_2.nH_2O$	2.16
$Sr(NbWO_6)_2.nH_2O$	2.21
$Sr(TaWO_6)_2.nH_2O$	1.60
$Ba(NbWO_6)_2.nH_2O$	1.96
$Ba(TaWO_6)_2.nH_2O$	1.97
$Pb(NbWO_6)_2.nH_2O$	1.86
$Pb(TaWO_6)_2.nH_2O$	2.05
$Cd(NbWO_6)_2.nH_2O$	Decomposes
$Cd(TaWO_6)_2.nH_2O$	1.75

5.2.4 IR spectra of $A^{2+}(B^{5+}WO_6)_2.2H_2O$

Infrared spectra were collected on the hydrated samples presented to confirm the presence of water within the structure. Figure 5.2.6 shows a plot of $Sr(TaWO_6)_2.2H_2O$ where the peaks associated with water molecules can clearly be observed. The typical stretches of water molecules in solid state spectra are observed as a broad stretch between 3600-3200 cm^{-1} and a weaker band at 1640-1615 cm^{-1}, both of which are seen in these spectra.

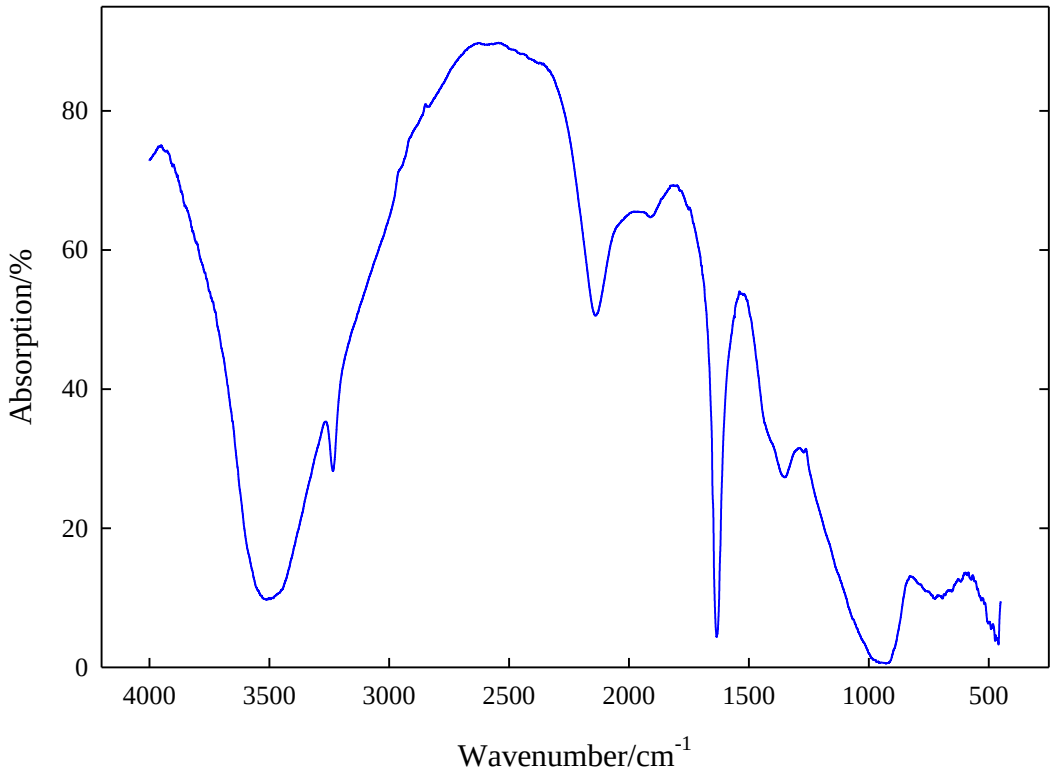

Figure 5.2.6 – Collected IR absorption spectra for $Sr(TaWO_6)_2.2H_2O$.

5.3 PXRD study of the series $A^{2+}(B^{5+}WO_6)_2.2H_2O$ where A^{2+}= Cd, Pb, Sr, Ba and Ca and B^{5+}= Nb and Ta

Data in the 2θ range 10 to 110° 2θ with a step size of 0.02° were collected over 16 hours for all the phases being studied using a Siemens D5000 diffractometer in a standard θ/2θ setup. All data was collected at room temperature in air.

5.3.1 Structural refinements

Initial refinements placed all atoms on the sites of the standard model as used by Chernorukov *et al*[11] and proceeded with the variation of global parameters; background, zero point, peak profile coefficients and the lattice constants. The isotropic temperature factors were then introduced for the individual atoms, along with the allowed atomic positions being refined; this provided a solid indication of whether the position was viable within the structure. For the majority of phases the oxygen atoms of the water molecules initially occupying the 8*b* site produced considerably larger than expected temperature factors. These oxygen atoms were therefore shifted to a 32*e* site placing them on the (110) plane that runs between adjacent 8*b* and 16*d* sites. A small displacement to 0.38,0.38,0.38 was initially used along with the necessary reduction in occupancy to 0.25 to retain the same overall stoichiometry. Refinement in this model whilst providing an improvement in fit proved unstable for several of the phases even with significant degrees of dampening, the oxygen atomic position was therefore left refining on the initial 8*b* site for the strontium and calcium containing phases.

For the remainder of this chapter all oxygen positions relating to the framework will be noted as O1 and those of the water molecules O2 when presenting structural data.

Table 5.3.1– Starting structural model used in the refinements of the series $A^{2+}(B^{5+}WO_6)_2.2H_2O$ (where A^{2+} = Ca, Ba, Sr, Pb and Cd, B^{5+} = Nb and Ta)

Atom	Site	*x*	*y*	*z*	Occupancy
A^{2+}	16*d*	0.5	0.5	0.5	0.25
B^{5+}	16*c*	0	0	0	0.5
W	16*c*	0	0	0	0.5
O1	48*f*	0.312	0.125	0.125	1
O2	8*b*	0.375	0.375	0.375	1

Table 5.3.2 - Structural model used in the refinements of the series $A^{2+}(B^{5+}WO_6)_2.2H_2O$ (where A= Ca, Ba, Sr, Pb and Cd, B = Nb and Ta) where a significant improvement in fit was observed with inclusion of a variable O2 position relating to the oxygen of the intercalated water.

Atom	Site	*x*	*y*	*z*	Occupancy
A^{2+}	16*d*	0.5	0.5	0.5	0.25
B^{5+}	16*c*	0	0	0	0.5
W	16*c*	0	0	0	0.5
O1	48*f*	0.312	0.125	0.125	1
O2	32*e*	*x*	*x*	*x*	0.25

Several of the tantalum containing phases included small impurities of tantalum oxide which was thus refined using the model of Stevens and Roth[15] for an orthorhombic tantalum oxide phase, providing a suitable fit. $Ca(TaWO_6)_2.2H_2O$ also included a small, ~1%, impurity phase of orthorhombic $CaTa_2O_6$[16] along with a corresponding amount of the triclinic phase WO_3[17], and Ta_2O_5 as with the other tantalum containing materials. This phase is included in Figure 5.3.1 displaying the most complex data set, in terms of overall refined parameters relating to the multiple phases from the available data. Finally the $Pb(TaWO_6)_2.2H_2O$ phase contained a significant impurity, ~15%, of $PbWO_4$. This was added to the refinement using the model of Moreau *et al*[18], the addition of this phase resulted in negative thermal motion being observed in the oxygen atom of the water molecule, likely resulting from overlapping reflections and a poorly refined second phase contribution. This variable oxygen position was however retained as it provided a significant improvement in fit to the data with this shift in atomic position. Refinements using

the 8*b* site for this material had the reverse effect producing a degree of thermal motion far in excess of what would be deemed acceptable in comparison to the other phases being studied here.

Models for all phases being studied were refined satisfactorily in this way and all impurities identified. The niobium phases were selected for further study using powder neutron diffraction primarily due to the large absorption cross section for tantalum and secondarily due to their slightly superior phase purity. All subsequent refinements on these materials, using PND on both the hydrated and dehydrated materials, included these impurity phases as required.

Table 5.3.3 – Calculated refined parameters for the series $A^{2+}(B^{5+}WO_6)_2.2H_2O$ (where A= Ca, Ba, Sr, Pb and Cd, B = Nb and Ta) from PXRD data at room temperature using the model presented in Tables 5.3.1 and 5.3.2. E.S.D. are included in parenthesis.

Target phase	Lattice parameter/Å	Oxygen 1 *x* position	Oxygen 1 U_{ISO}	Oxygen 2 *x* position	Oxygen 2 U_{ISO}
$Ba(NbWO_6)_2.nH_2O$	10.47446(12)	0.3102(9)	1.32(30)	0.4102(17)	3.01(203)
$Ba(TaWO_6)_2.nH_2O$	10.45320(19)	0.3140(10)	1.6(4)	0.4012(18)	0.2(12)
$Pb(NbWO_6)_2.nH_2O$	10.42647(10)	0.3126(9)	1.48(30)	0.4033(25)	1.29(223)
$Pb(TaWO_6)_2.nH_2O$	10.40226(27)	0.3236(16)	3.0(7)	0.4047(20)	-3.9(18)
$Sr(NbWO_6)_2.nH_2O$	10.41004(13)	0.3108(9)	2.20(30)	0.375	8.88(120)
$Sr(TaWO_6)_2.nH_2O$	10.39151(16)	0.3163(10)	0.63(35)	0.375	7.87(148)
$Ca(NbWO_6)_2.nH_2O$	10.37248(17)	0.3157(10)	1.1(4)	0.375	7.3(13)
$Ca(TaWO_6)_2.nH_2O$	10.34667(14)	0.3168(8)	1.89(31)	0.375	3.77(73)
$Cd(NbWO_6)_2.nH_2O$	10.44809(9)	0.3116(7)	1.83(24)	0.3955(22)	5.26(11)
$Cd(TaWO_6)_2.nH_2O$	10.42740(25)	0.3164(14)	1.1(5)	0.3989(20)	4.6(17)

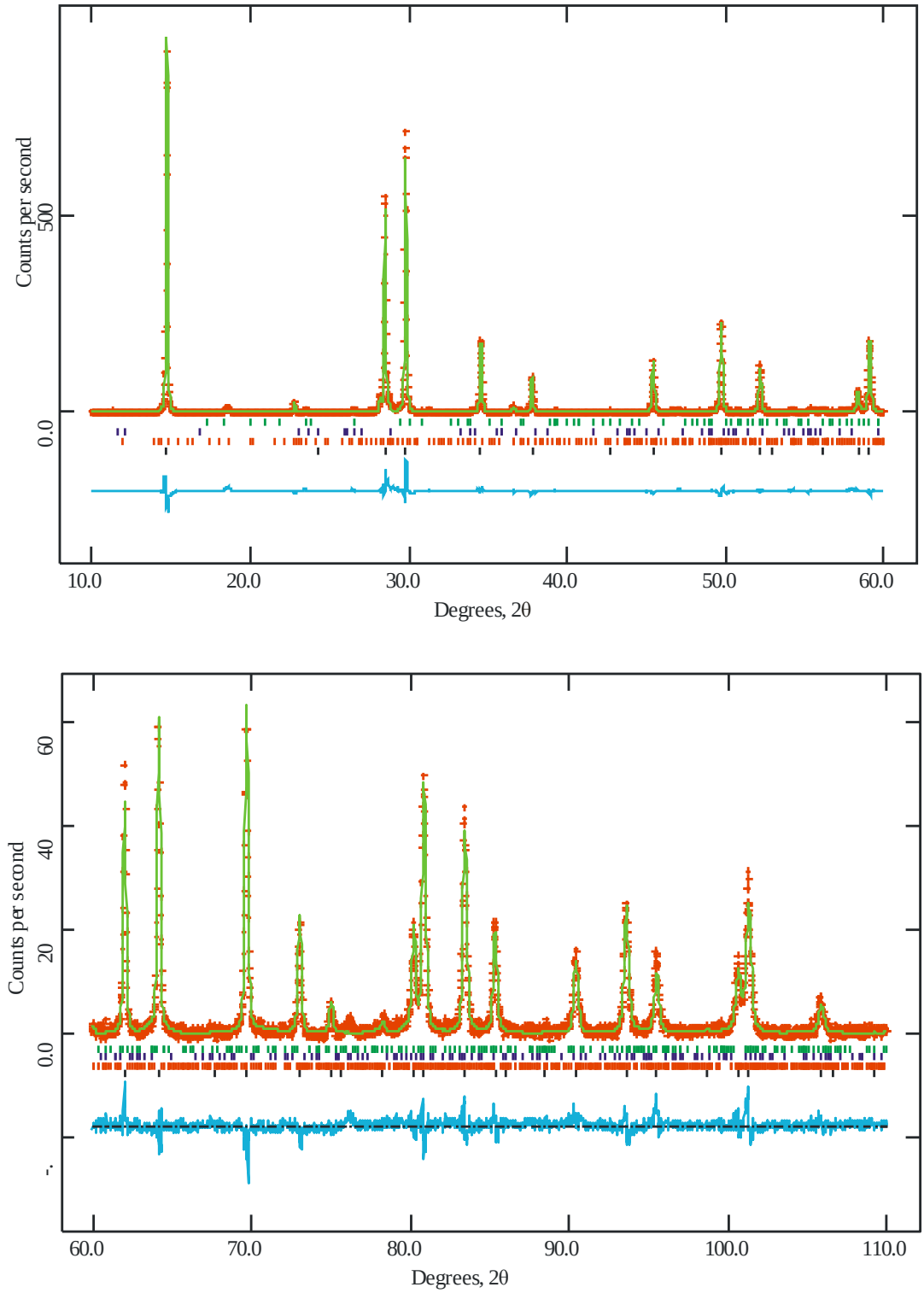

Figure 5.3.1 – Profile fit to PXRD data for $Ca(TaWO_6)_2.H_2O$. Experimental data points are shown as red crosses, the upper continuous green line is the calculated profile, lower continuous blue line the difference and allowed reflections indicated by tick marks. From top to bottom the tick marks represent $CaTa_2O_6$, WO_3, Ta_2O_5 and $Ca(TaWO_6)_2.nH_2O$ respectively.

Finally it was noted that for several of the phases values for the thermal parameters of divalent cations were considerably higher than those of the framework. This effect was particularly notable with the calcium and cadmium containing phases, the two smallest cations being studied. Further refinements were therefore carried out displacing the divalent cations away from the 16*d* site along the (110) plane, whilst providing no significant improvement in fit for the calcium phases a noticeable change was observed in the cadmium phases. The final calculated positional parameters used for the cadmium containing phases are displayed in Table 5.3.4.

T*able 5.3.4 - The final structural model used in the refinements of* $Cd^{2+}(B^{5+}WO_6)_2.2H_2O$ *(where B = Nb and Ta) with the addition of a variable position for the position of the* Cd^{2+}.

Atom	$Cd(NbWO_6)_2.2H_2O$	$Cd(TaWO_6)_2.2H_2O$
$Cd^{2+}(1)$: (*x*)	0.4828(7)	0.4767(8)
U_{ISO}	3.38(35)	1.2(8)
O1: (*x*)	0.3101(7)	0.3157(15)
U_{ISO}	2.20(25)	1.8(5)
O2: (*x*)	0.3626(217)	0.3559(12)
U_{ISO}	7.61(62)	5.5(22)
a	10.44811(9)	10.42737(25)

The refinement of $Pb(TaWO_6)_2.2H_2O$ also provided some minor discrepancies with a negative thermal parameter for the oxygen atom of the water molecule and a higher than expected value of *x* for the O1 oxygen of the framework, which would correspond to a significant increase in the level of distortion in the BO_6 octahedra. This is probably explained by the presence of the $PbWO_4$ impurity, although the phase is readily modelled there are significant overlaps particularly on the 311 and 440 reflections at ~29.8 and 49.5 2θ respectively. The data for this phase was therefore treated with a reasonable degree of caution.

5.3.2 Discussion

Looking at the lattice parameter changes across the series, Figure 5.3.2, we can see a clear trend in the reduction of lattice size corresponding well to the reduction in the *A*-site cation size. The two cadmium phases in contrast do not fit this pattern with a significantly larger than expected lattice constant. This can likely be explained by the size of the cadmium ions, as discussed previously the smaller cadmium atoms (~0.95Å) are best modelled on a 32*e* site allowing a change in coordination. Not only does this change the environment in which the cadmium atoms reside it also allows the lattice to relax. Similar behaviour is seen in $NaNbWO_6.nH_2O$ where the hydrated phase is in fact smaller than the dehydrated analogue, an effect that relates to the varying stabilising effects of both the water and *A*-site cations[19]. It appears that the expansion and subsequent displacement of the cadmium ions is the dominant force in this material.

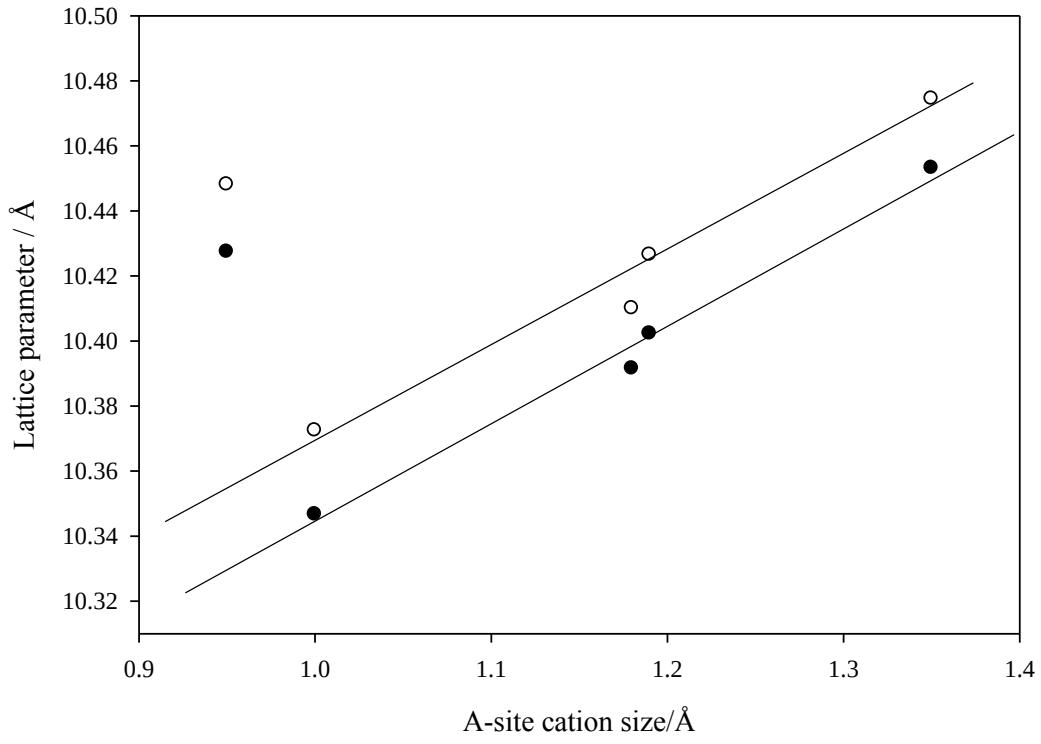

Figure 5.3.2 – A plot of lattice parameter against A-site cation size for the series $A^{2+}(B^{5+}WO_6)_2.2H_2O$ (where A^{2+} = Cd, Ca, Pb and Sr and B^{5+} = Ta (●) and Nb(○))

This material can then be viewed as possessing a framework in a state approaching total relaxation; it is therefore possible to interpret the shift in cadmium position as also allowing the lattice to relax and providing a solid thermodynamic rationale for this structural change with the corresponding increase in lattice parameter being seen in both phases studied.

As a general trend we can see that the niobium phases are consistently larger than the tantalum containing ones. Shannon[20] implies that both of these cations should have identical ionic radii, however we can interpret this difference partly from the fact that Shannon's radii are taken as averages across different structure types and thus have a margin of error and from the chemistry of the niobium itself which tends to not occupy the centre of octahedra but rather sits to one side leading to larger than expected polyhedra.

Positions for the oxygen atoms of the water molecules require the use of two models with either the oxygen of hydration fixed on the 8*b* site or placed on a 32*e* site slightly displaced from here. This behaviour can once again be explained by accounting for the change in lattice parameter. Whilst the lattice parameter in general reduces in line with a reduction in *A*-site cation size the water will continue to require the same volume for an ideal coordination. As the cavity surrounding the 8*b* site increases in volume the water molecule can no longer achieve sufficient coordination by remaining at the centre, it thus moves towards the side of the cavity retaining a similar distance from the framework and requires a shift in crystallographic position. Smaller shifts may occur in the strontium and calcium phases but are unobservable in the PXRD data available as until the oxygen atom has moved a reasonable distance from this site it is not possible to distinguish between oxygen atoms with a larger thermal parameter and cations occupying a different position. This is something particular prevalent in PXRD data where the proportional contribution of the oxygen to the reflections is relatively low.

The observed shift in position of the cadmium ions allowed by the adopted model leads to a significant change in the coordination environment of the atoms compared to the other cations studied here. In the initial model studied the cadmium atom was located out of the centre of the puckered ring of six oxygen atoms centred around the 16*d* site with two oxygen atoms also potentially contributing electron density from

the waters of hydration. The new site ~0.25Å along the (110) plane changes this significantly. The cadmium ion moves further into one of the surrounding cavities, moving closer to one of the possible oxygen, of the water, atom positions. This movement shortens the Cd-O bond length to this atom as well as shortening three of the oxygen bonds to the surrounding framework. It seems likely that the stabilisation gained from the shortening of these four bonds is greater than the reverse effect from the lengthening of three of the other bonds to the framework (an ideal Cd-O bond length for an eightfold environment is 2.45Å or 2.30Å for a six fold site, still nominally shorter than those observed here). Figure 5.2.3 shows the oxygen atoms surrounding the cadmium ions, it is likely that only the longer O5 atom sites are occupied as these sites allow the hydrogen's of the water to point away from the cadmium whereas the shorter distance should require at least one hydrogen to be pointing in the direction of the cadmium, negatively effecting the available stabilising charge.

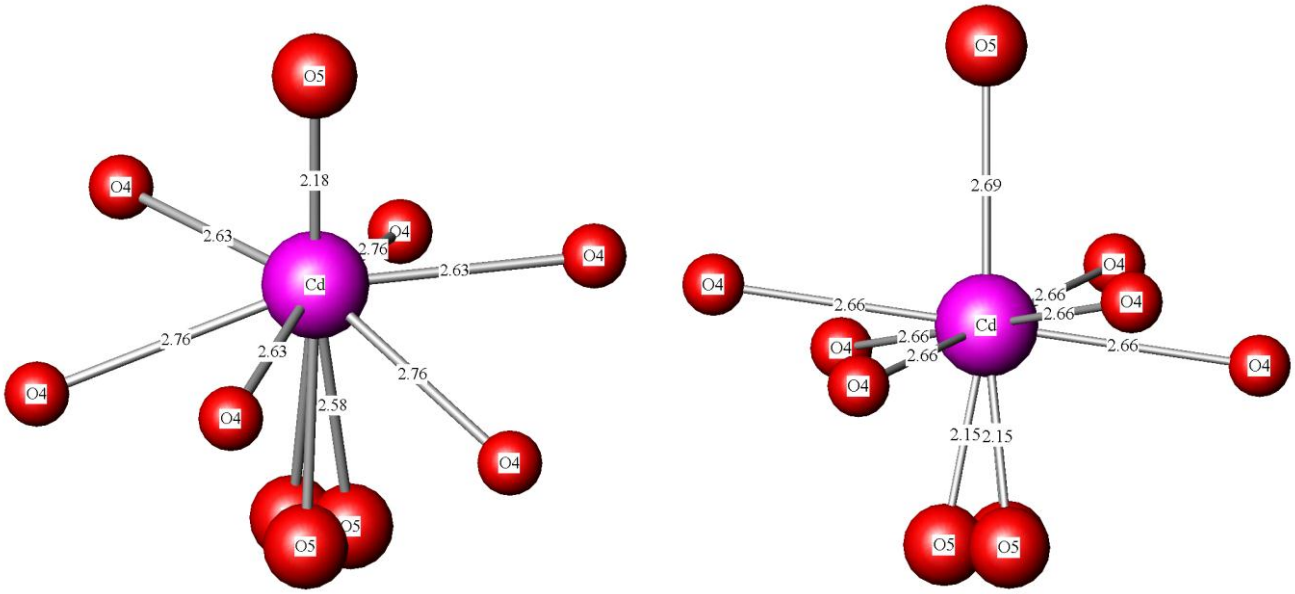

Figure 5.3.3 – The left hand image shows the calculated coordination environment for cadmium atoms and the right hand image the environment if the cation is placed on the ideal 16d site. O4 represents the oxygens of the BO_6 lattice and O5 the waters of hydration, of which only one of the four positions would normally be occupied.

5.4 PND study of the series $A^{2+}(B^{5+}WO_6)_2.nH_2O$

Data were collected on the powder neutron diffraction instrument Super D2B at the ILL, Grenoble at a wavelength of 1.594Å. Individual data sets were collected at 1.5K using a standard Oxford instruments orange cryostat with a collection time of 4 hours on four of the five niobium containing materials discussed earlier in this chapter. Data was not collected for the cadmium containing phase $Cd(NbWO_6)_2.H_2O$ due to the large neutron absorption cross section exhibited by this phase causing data quality to be below a reasonable threshold[21]. The PND data proved to be of a high enough quality that proton positions could also be extracted.

5.4.1 Structure refinements

To allow a stronger picture of the process of ion exchange to be built up we wished to fully characterise the structure of the hydrated phases particularly the positions of both the oxygen atoms of the framework and the water molecules. Thus powder neutron diffraction data were collected to allow more accurate determination of the atomic positions, most particularly those of the lighter elements.

An initial model based upon that calculated in Section 5.3 from PXRD was used as a starting point for the structural refinement of each phase. These refinements produced a much higher than expected thermal parameter for the oxygen atoms of the water molecules for all phases studied, the overall fit was improved by the displacement of this oxygen to a nearby 32*e* site significantly improving the fit. Unlike the previously collected PXRD data, the higher quality of the PND data also allowed refinement of hydrogen atom positions. To accurately determine these positions the structure was fully refined without the hydrogen atoms being incorporated, difference Fourier maps were then calculated and possible sites located within the framework. Several reasonable sites were studied with the site which provided by far the most significant improvement in fit being located on a further 48*f* site aligned directly between the ideal oxygen atom position at 8*b* and the nearest framework oxygen atom at the previously discussed 48*f* site. The extracted bond lengths in each case were deemed reasonable, with molecular alignment of the water molecules proving logical, thus the model was adopted and used in the final refinements. This model is presented in Table 5.4.1 along with the extracted data for each phase in Table 5.4.2.

Table 5.4.1 – Initial structural model used in the refinements of the series $A^{2+}(NbWO_6)_2.2H_2O$ (where A= Ca, Ba, Sr and Pb)

Atom	Site	*x*	*y*	*z*	Occupancy
$\boldsymbol{A^{2+}}$	16*d*	0.5	0.5	0.5	0.25
$\boldsymbol{B^{5+}}$	16*c*	0	0	0	0.5
W	16*c*	0	0	0	0.5
O1	48*f*	*x*	0.125	0.125	1
O2	32*e*	*x*	*x*	*x*	0.25
H	48*f*	0.375	0.375	*z*	0.33˙

The positions of the *A*-site cations was also investigated, displacement away from the 16*d* site was attempted but produced no improvement in fit and the cations continued to be placed on sites identical to the 16*d* site once calculated errors had been taken into account. The refined occupancies loosely agreed with those provided by EDX. It may also be worth noting that whilst we are not willing to use the results of EDX as a truly quantitative tool the proportion of strontium present in $Sr(NbWO_6)_2.nH_2O$ was highlighted as being slightly higher than would be expected and that this is reflected well in the occupancies calculated from the refinement, it is also noticeable to a lesser degree in the barium containing phase presented here. An occupancy of >0.25 on this site relates to more than one divalent cation per formula unit and would also suggest a further source of negative charge within the framework possibly arising from a reduction in charge on the *B*-site cations or from the presence of HO^- anions on the water sites.

Table 5.4.2 – Extracted phase information from the refinement of data collected on the Super D2B instrument at the ILL for the series $A^{2+}(NbWO_6)_2.H_2O$ where A^{2+} = Pb, Ca, Sr and Ba.

Atom	$Ca(NbWO_6)_2$ $2H_2O$	$Sr(NbWO_6)_2$ $2H_2O$	$Pb(NbWO_6)_2$ $2H_2O$	$Ba(NbWO_6)_2$ $2H_2O$
A^{2+} size for a VIII co-ordinated environment/Å	1.12	1.26	1.29	1.42
A^{2+}: (*x*)	0.5	0.5	0.5	0.5
Occupancy	0.2509(11)	0.297(4)	0.2591(10)	0.271(7)
UISO	2.29(5)	2.09(2)	1.53(4)	1.09(20)
Nb/W: UISO	2.06(4)	2.16(4)	1.88(1)	2.12(4)
O(1): (*x*)	0.311283(17)	0.31078(8)	0.309879(21)	0.30880(9)
UISO	1.18(4)	1.036(18)	0.82(3)	0.904(21)
O(2): (*x*)	0.390417(28)	0.39582(27)	0.3964(6)	0.39901(68)
UISO	3.11(4)	1.33(19)	7.1(5)	8.7(7)
H(2): (*z*)	0.4815(7)	0.4898(5)	0.4874(11)	0.4927(10)
UISO	3.67(24)	2.44(20)	7.2(4)	4.8(6)
a	10.37339(13)	10.40060(13)	10.41570(7)	10.46640(8)
χ^2	12.37	6.516	10.09	17.51
R_{wp} (%)	3.35	2.88	2.79	4.00
R_p (%)	2.42	2.05	2.04	2.78

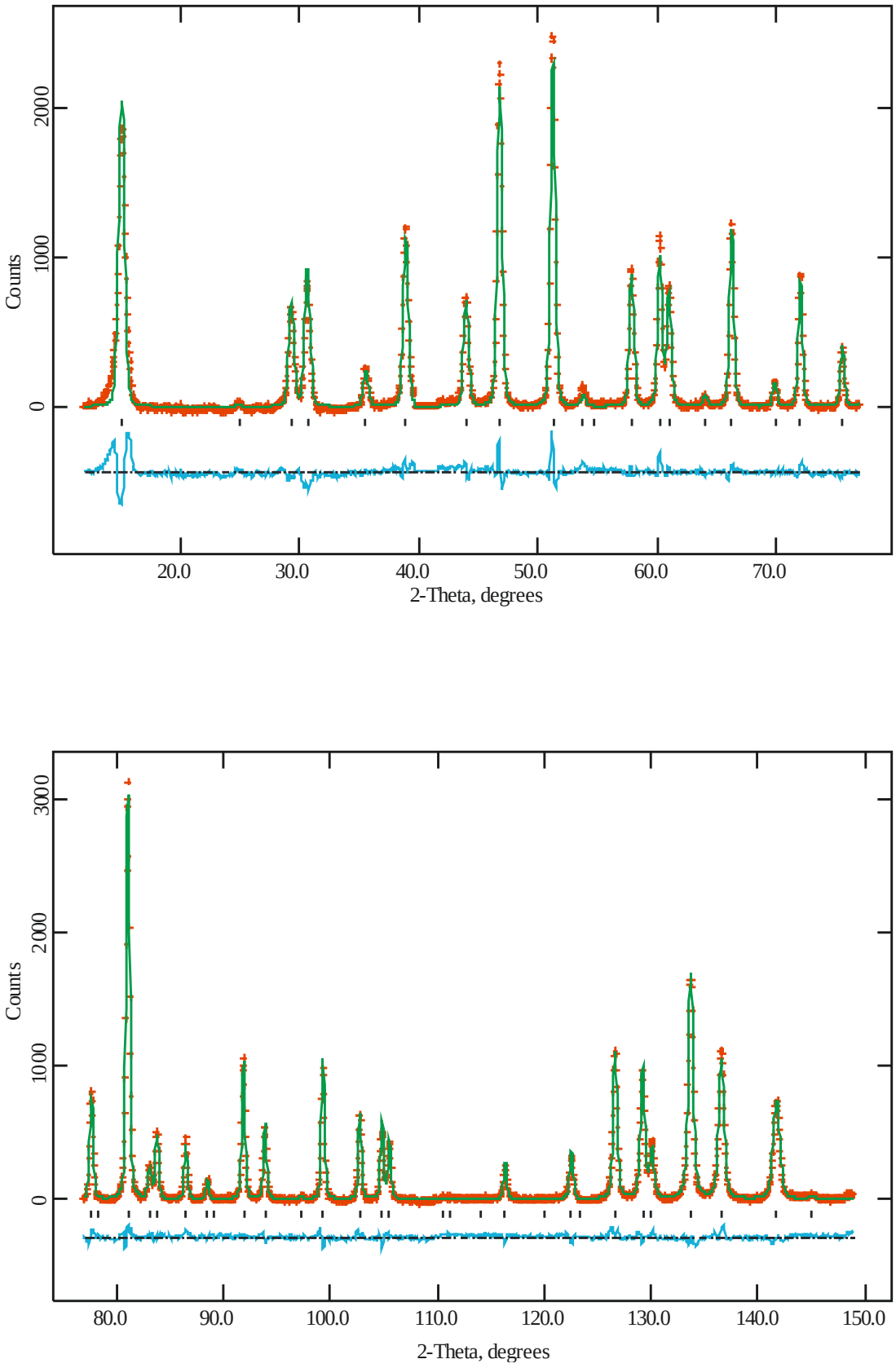

Figure 5.4.1 - Profile fit to PND data for $Sr(NbWO_6)_2.H_2O$. Experimental data points are shown as red crosses, upper continuous green line is the calculated profile, lower continuous blue line the difference and allowed reflections indicated by tick marks.

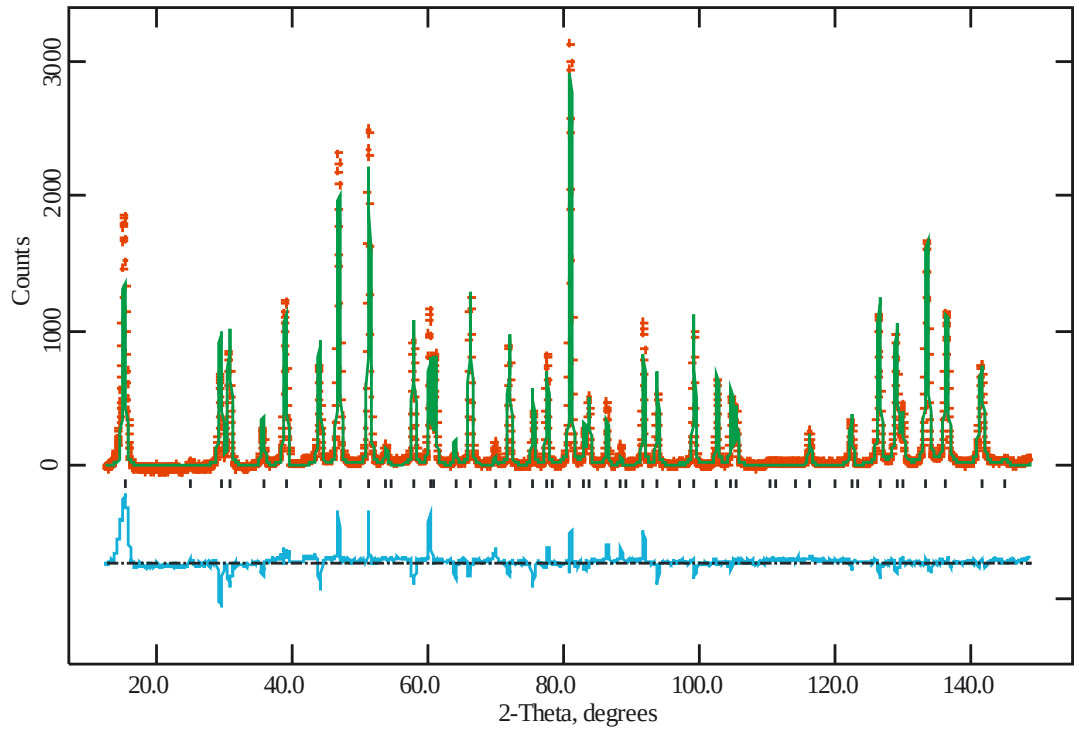

Figure 5.4.2 – Profile fit for the same data plotted in Figure 5.3.2but with the hydrogen positions removed from the refinement, it can be clearly seen that the addition of hydrogen atoms to the refinement significantly improves the profile fit.

5.4.2 Discussion

As with the PXRD data presented earlier in this chapter the lattice parameter shows a direct correlation with the ionic radii of the divalent cations exchanged into the structure, with both increasing at a similar rate. Comparison of the lattice constants extracted from both PND and PXRD shows the lattice parameters to be extremely similar to one another; this is not entirely expected as the PND data was collected at 1.5 K whilst the PXRD was collected at room temperature. For each material a small contraction is observed of approximately ~0.01 Å, in the case of $Ba(NbWO_6)_2.nH_2O$ from 10.47446(12) Å at room temperature to 10.46640(8) Å at 1.5K. This change is smaller than that observed in other materials of this type, for example the series $ANbTeO_6$ (where A = Cs, Rb and K) investigated in Section 3.5.3 shows a lattice contraction of >0.1 Å for each material over this temperature range.

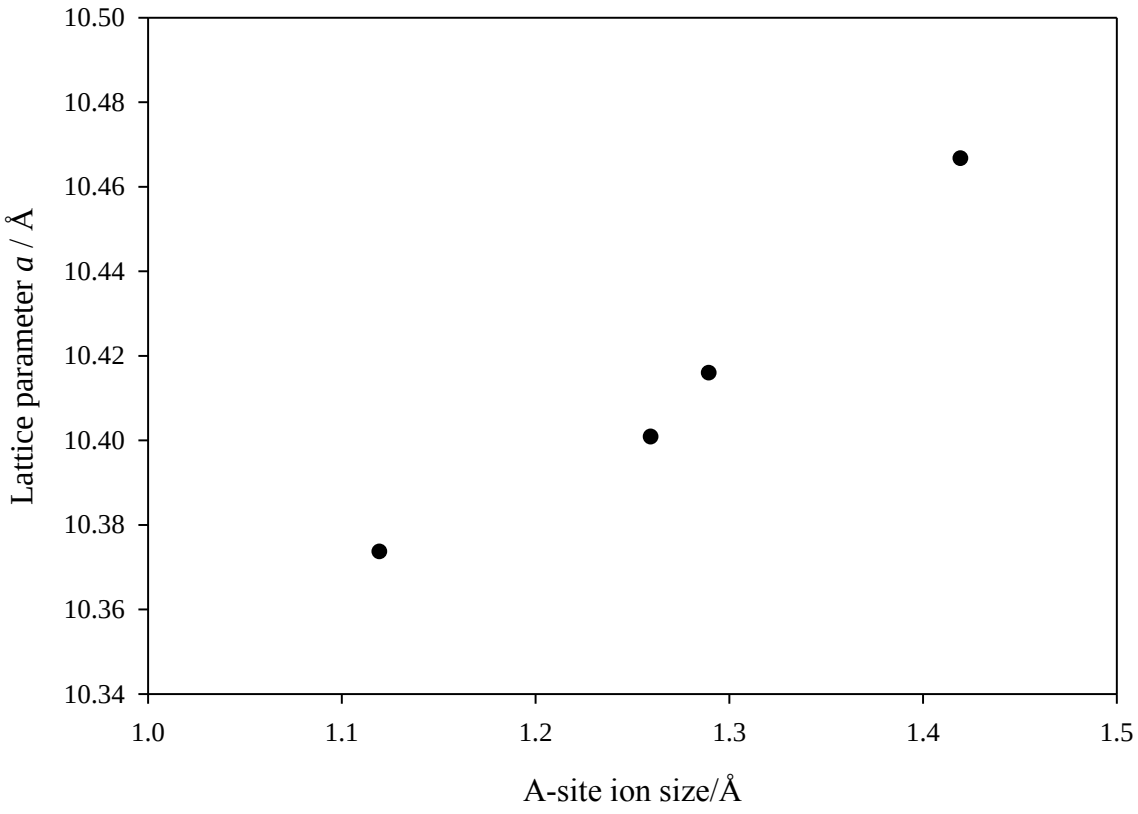

Figure 5.4.2 – Plot of the lattice parameter against ionic radii of the A^{2+} cation for the series $A^{2+}(NbWO_6)_2.nH_2O$ where A^{2+} = Sr, Pb, Ca and Ba.

This smaller than expected contraction may be explained by the occupation of the 16*d* site, in the other materials studied as a function of temperature this site has not been occupied. It seems likely that where as in other *beta* pyrochlores the lattice contraction is driven by a reduction in metal-oxygen bond length and a slight change in the oxygen-metal-oxygen bond angles that compose the polyhedra, the occupation of the 16*d* site inhibits this as its effective ionic radii does not change significantly upon cooling.

In contrast to the pure *beta*-pyrochlore materials studied in Chapter Three these hydrated materials display elongation of the BO_6 octahedra in the [111] direction. This concerted elongation allows the 16*d* site to be larger than it would be in a material with the same lattice parameter but without this characteristic, and therefore provides a site that may be better suited to the coordination of the large divalent cations now occupying this position. As the site is unoccupied in the true *beta*-phases this is not required and instead the framework 'relaxes' to some degree causing the polyhedra to compress. In all cases this effect is weak with a displacement of 2-4°

away from the ideal 90° internal bond angles of the polyhedra. Figure 5.4.3 clearly shows that the level of displacement, arising from increasing values for the *x* coordinate , are correlated to the increasing ion size, a trend which allows the larger ions to be accommodated whilst reducing the proportional increase in lattice parameter required.

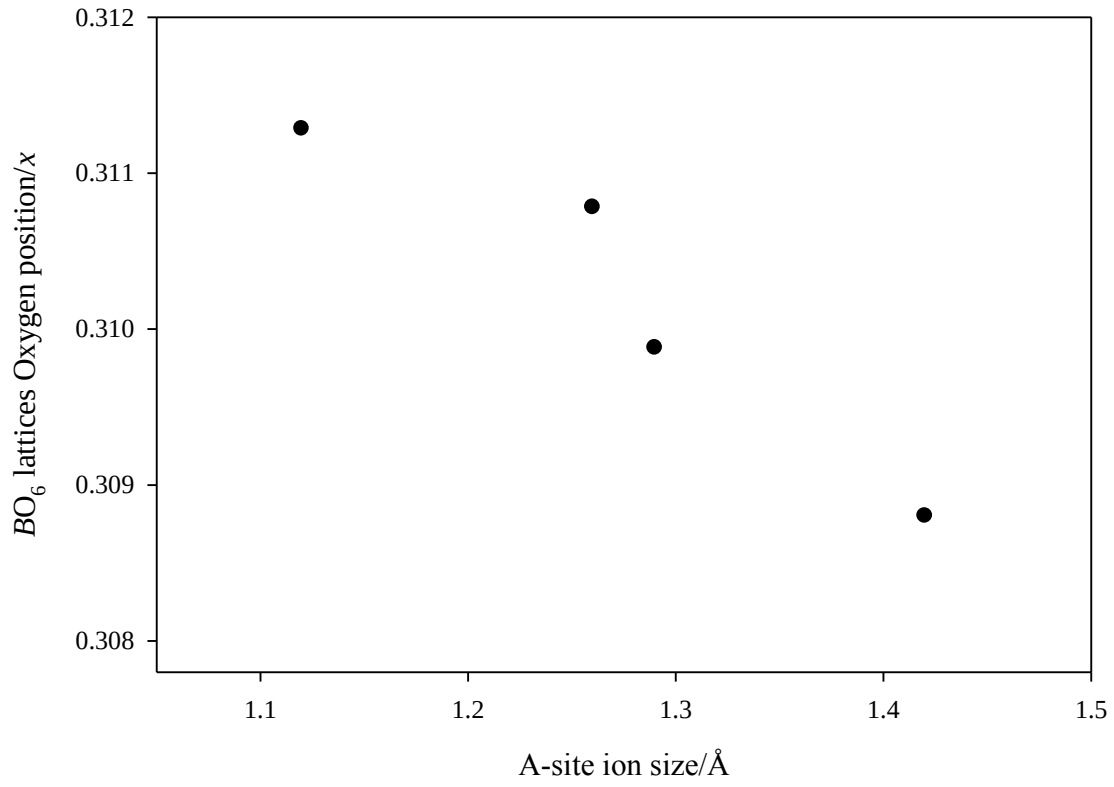

Figure 5.4.3 - Calculated oxygen position for the B_2O_6 network against cation size for the series $A^{2+}(B_2O_6)_2.nH_2O$ where A^{2+} = Pb, Ca, Ba and Sr

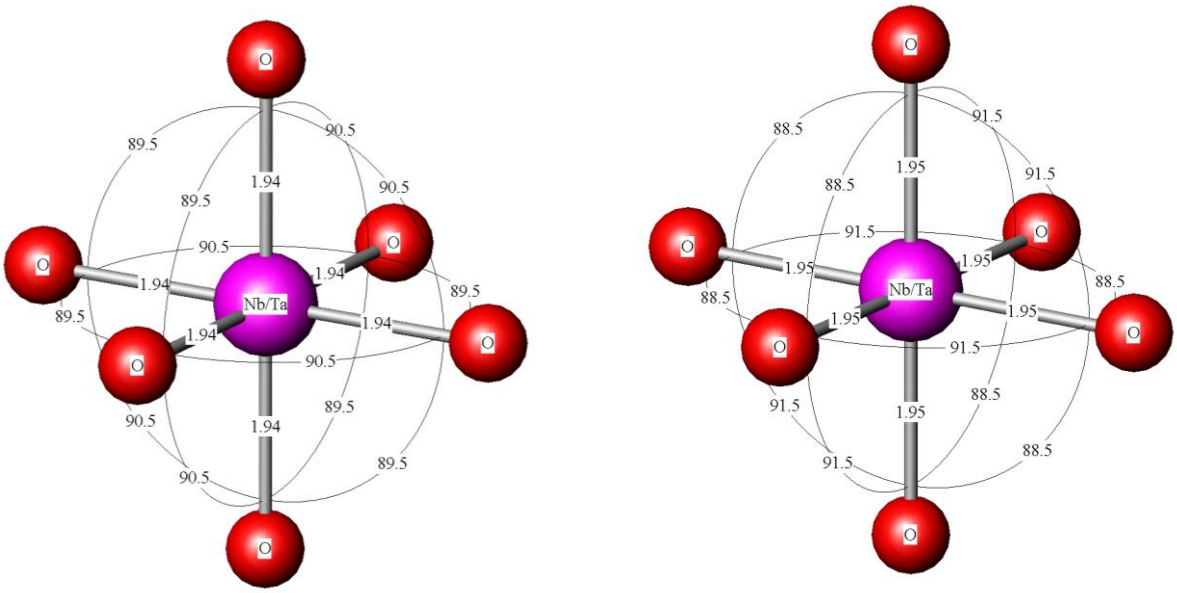

Figure 5.4.4 – Showing the two extremes of the BO_6 octahedral distortions at 0.5 and 1.5° for $Ca(NbWO_6)_2.2H_2O$ (Left) and $Ba(NbWO_6)_2.2H_2O$ (Right) respectively.

The level of displacement displayed by the water molecules appears to correlate well to the changes in lattice parameter. As expected as the lattice parameter, and thus cavity size, increase the degree of displacement also increases proportionally. This proves logical and allows an almost constant distance to be maintained between the oxygen atoms of the framework and those of the water molecule.

Table 5.4.3 – Refined positions and associated data for the waters of hydration for the phases $A^{2+}(NbWO_6)_2.H_2O$ where A^{2+} = Pb, Ca, Sr and Ba

Phase	Hydrogen atom position , *z*	Oxygen atom position, *x,y,z*	Hydrogen-Oxygen bond length	H-O-H bond angle
$Ca(NbWO_6)_2.2H_2O$	0.4815(7)	0.390417(28)	0.972(7)	107.04(11)
$Sr(NbWO_6)_2.2H_2O$	0.4898(5)	0.39582(27)	1.024(5)	111.03(9)
$Pb(NbWO_6)_2.2H_2O$	0.4874(11)	0.3964(6)	0.999(12)	112.0(6)
$Ba(NbWO_6)_2.2H_2O$	0.4927(10)	0.39901(68)	1.015(8)	117.8(4)

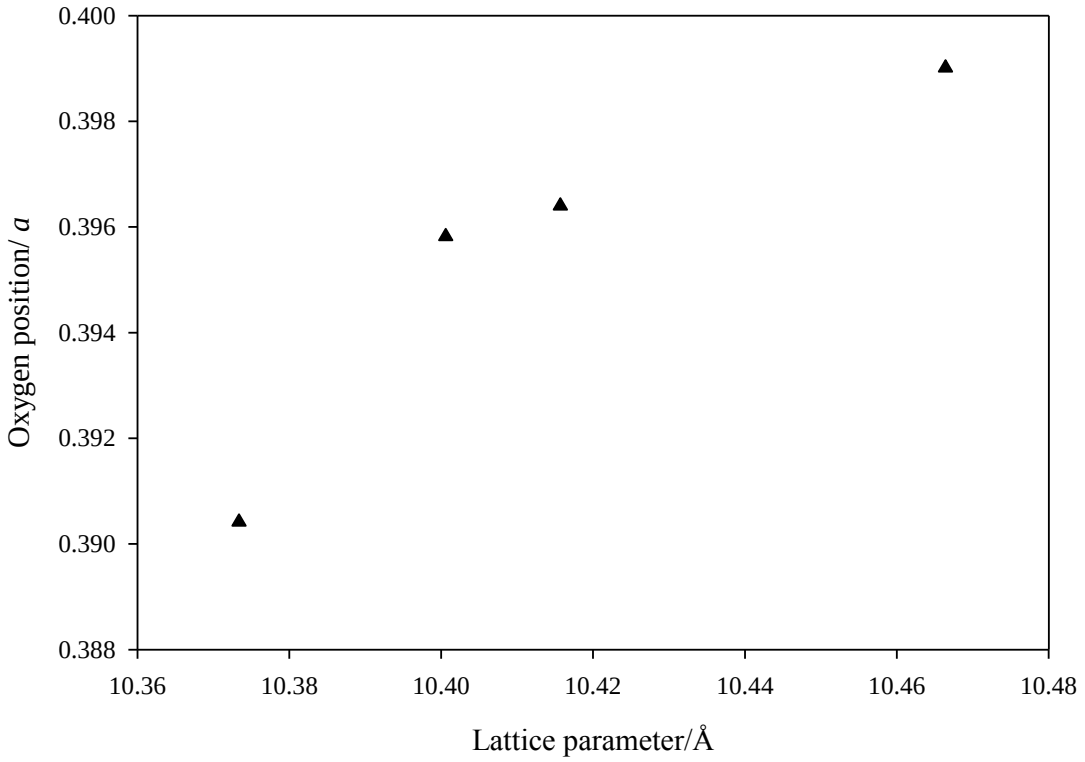

Figure 5.4.5 – Plot of Lattice parameter against the position of the oxygen atoms belonging to the water molecules.

Extraction of the water molecules structure and orientation from this model in general shows a good level of agreement with that expected. The possible exception are those of $Ba(NbWO_6)_2.2H_2O$ where the resulting positions imply a more obtuse angle than would normally be expected within a water molecule.

Refinement of the levels of occupation for the *A*-type cation site led in all cases to slightly higher than expected values, relating to 1.0036 to 1.188 cations per formula unit. Whilst these values are all higher than would necessarily be expected, as stated previously it is not entirely unreasonable to observe higher occupancies on these positions. Such phenomena have been observed in mono-valent analogues, most notably in the series A_2NbWO_6, a series of materials examined more closely later in this chapter[22].

5.5 PND study of the series $A^{2+}(NbWO_6)_2$ where *A* = Ca, Sr, Pb and Ba

In an attempt to better understand the structure within these phases' data has been collected on the dehydrated analogues of those studied earlier in this chapter. By looking at the dehydrated materials it was hoped that we could establish a better understanding of the environment present within them and thus improve our understanding of what phases can form and will be stable in this structure type. Ideally a study of this type should also provide a better picture of the relationship between cation size and site occupation.

5.5.1 Sample preparation

The samples were initially prepared by an identical ion exchange route as used for the hydrated phases. The materials were then dehydrated overnight at 500 °C under nitrogen to remove the structural and surface bound water; this temperature was selected through testing via TGA above which all samples showed the mass loss expected from the loss of these waters. To confirm dehydration was complete the dehydration process was replicated on the TGA apparatus, with additional heating and cooling cycles carried out under a nitrogen atmosphere showing no further mass loss.

5.5.2 Data collection

Data was collected on the medium resolution time-of-flight powder neutron diffraction instrument POLARIS at ISIS, Oxfordshire with a collection time of ~1 hour at 30 K. Samples of ~4 g were sealed in 8 mm, thin walled vanadium cans prepared under a nitrogen environment to ensure water was not reabsorbed. The powder pattern was collected simultaneously on all four detector banks with information from the backscattering, 90° and low-angle detector banks used in the final refinements. The very low angle bank was excluded as no extra information was provided by this bank and provided no overall improvement to the fit due to the lower peak intensity to background ratio.

5.5.3 Structural refinement

An initial structural model was built up based upon that used for the hydrated phases in Section 5.4. The water molecules were initially removed and structural refinements carried out. In all cases this model proved inadequate with significantly larger than expected thermal motions on the *A*-site cations. Concurrently the occupancies of these atoms were also varied, with density being shown to be present at this location for the strontium, barium and lead phases, however in the case of the calcium containing material no density could be located at this site with the occupancy tending to zero. Movement of the strontium, barium and lead atoms to a 32*e* site close to the 16*d* site provided significant improvements in the fit profile and a lowering of the thermal parameters of these atoms to much more reasonable levels. Inspection of calculated Fourier density maps from the $Ca(NbWO_6)_2$ data showed significant neutron density near to, but displaced from, the 8*b* site with this site therefore being used instead.

Table 5.5.1- Starting structural model for the dehydrated series $A^{2+}(NbWO_6)_2$ where A = Sr, Ba and Pb.

Atom	Site	x	y	z	Occupancy
$\boldsymbol{A^{2+}}$	32*e*	*x* (~0.46)	*x* (~0.46)	*x* (~0.46)	~0.18
Nb	16*c*	0	0	0	0.5
W	16*c*	0	0	0	0.5
O	48*f*	0.311	0.125	0.125	1

Once a suitable starting model was established a complete refinement was carried out for each phase. The final TOF data range selected for each refinement was chosen to ensure the maximum amount of reflections were included whilst retaining a high level of resolution, thus for each data set the final refined data range differs to some degree.

Final refined phase data for all four materials, along with profile fit parameters, are presented in Table 5.5.2. The corresponding graphical fit for $Ba(NbWO_6)_2$ corresponding to the 145° backscattering detector bank is shown in Figure 5.5.1 as a typical example of the degree of fit observed in all four of the refinements undertaken.

Table 5.5.2 - Extracted data from the refinement of data collected on the Super D2B data at the ILL for the series $A^{2+}(NbWO_6)_2.H_2O$ where A^{2+} = Pb, Ca, Sr and Ba.

Atom	$Ca(NbWO_6)_2$	$Sr(NbWO_6)_2$	$Pb(NbWO_6)_2$	$Ba(NbWO_6)_2$
A^{2+}: (*x*)	0.3888(3)	0.4886(3)	0.4921(3)	0.4608(3)
Occupancy	0.182(2)	0.170(2)	0.139(1)	0.189(3)
Ui/Ue*100	0.32(12)	0.64(9)	1.75(7)	2.24(16)
Nb/W: Ui/Ue*100	1.58(3)	1.50(3)	1.573(15)	1.54(2)
O: (*x*)	0.31174(5)	0.31146(6)	0.31061(3)	0.31077(5)
Ui/Ue*100	0.540(8)	0.490(9)	0.547(5)	0.713(9)
a	10.36901(16)	10.4040(2)	10.41626(11)	10.4280(3)
χ^2	8.183	6.663	6.139	6.344
R_{wp} (%)	2.79	2.21	2.62	2.77
R_p (%)	3.65	3.45	6.29	5.57

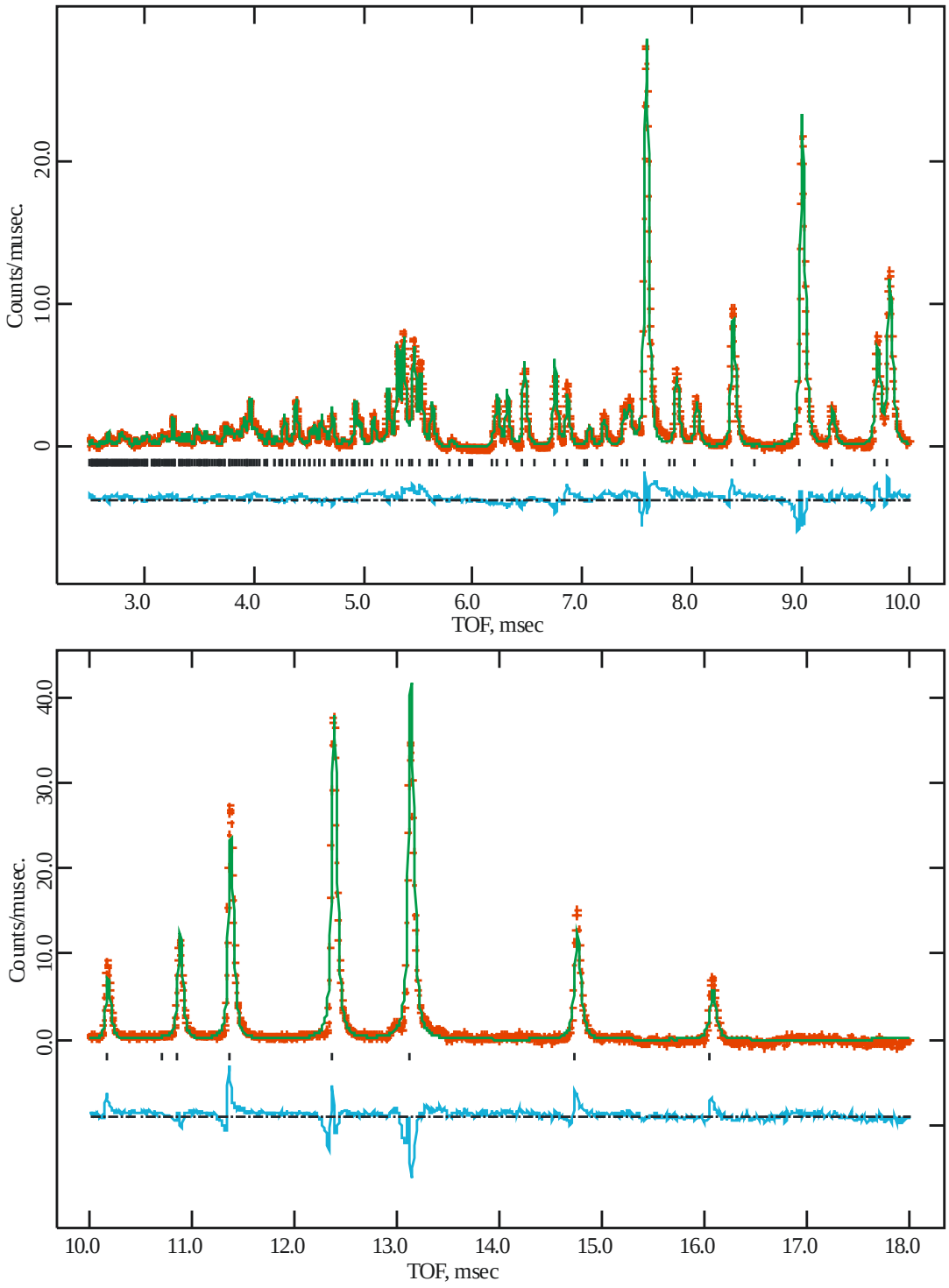

Figure 5.5.1 – Graphical profile fit from the PND data obtained for $Ba(NbWO_6)_2$ from the backscattering detector (145°) on the POLARIS instrument. Red crosses mark observed intensities, upper continuous blue line the calculated profile, lower green line the difference and allowed reflections with tickmarks.

5.5.4 Discussion

As with the majority of pyrochlores studied in this work the lattice size appears to be very closely linked to the size of the *A*-site cation, increasing as the effective ionic radii increase. An interesting feature of note is that the difference in lattice dimensions between the hydrated and dehydrated materials, with the exception of $Ba(NbWO_6)_2.nH_2O$, is minimal for all phases. This results in the barium, strontium and lead phases displaying more similar lattice dimensions to one another than seen in the hydrated phases.

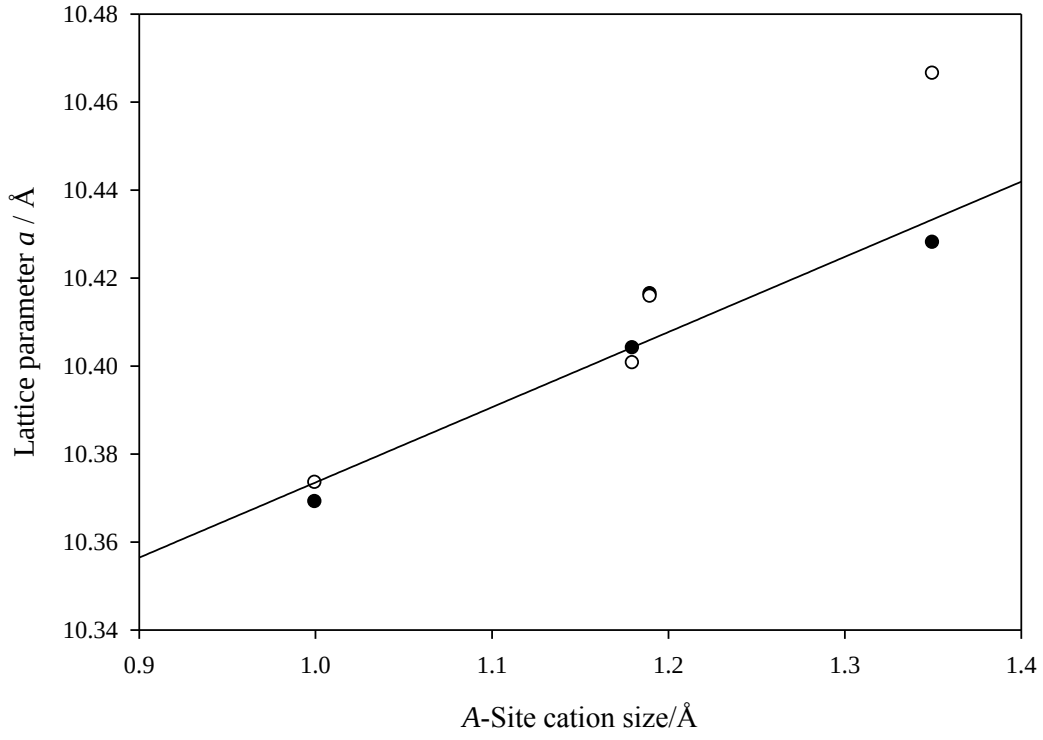

Figure 5.5.2 – Plot of the lattice parameter against ionic radii of the A-site cation size for the series $A^{2+}(NbWO_6)_2.nH_2O$, Hydrated phases are shown as(○)and the dehydrated phases(●).

The interesting feature of note in these phases is the location of the *A*-site cations within the framework. Initial inspection of the barium atom position shows it to be significantly displaced from the 16*d* site; this is probably explained by the barium being larger than is ideal for this site with this movement allowing both more space for the cation and the framework to contract. This displacement coupled with a larger than expected thermal parameter suggests that the nuclear density is spread over a range of sites around, but not on, the 16*d* position. A similar effect is observed in the lead phase with the atomic position moving closer to the 16*d* site but

still displaying a larger than expected degree of thermal motion suggesting the cation is closer to but still not the 'ideal' size for this site. The behaviour of the strontium phase differs once again; the cation is further displaced from the 16*d* site but the position is much better defined displaying a degree of thermal motion in line with the other atoms of the material, this effect is not entirely expected as the change in effective ionic radii between lead and strontium is minimal yet the change in position and behaviour of the cation seems to be significant. It seems likely that the lead atoms are in reality displaced to a similar degree but that the large thermal parameters causes the nuclear density to be spread over a wider range and thus appear closer to the 16*d* sites. Finally the calcium containing phase refines with the cation on a very different coordination site close to the 8*b* site near to the centre of the large cavities, although this is coupled with a reduction in lattice dimensions, assumedly to provide better overall coordination for these cations, it is not entirely expected. The movement of the smaller cation to a larger site appears to be counter intuitive but can possibly be explained by the effects of the contracting lattice being more significant than the stabilising contribution of the calcium ion position.

Refinement of the occupancies of the *A*-site shows levels of occupation that are in general considerably higher than those expected. To provide the ideal stoichiometry of $A(NbWO_6)_2$ the degree of occupation for the *A*-site should be ~0.125, however a higher level of occupation is observed in every phase. A part of this in discrepancy may be explained by the presence of small amounts of potassium within the network resulting from incomplete ion exchange. Unlike the majority of the *beta*-pyrochlores presented in Chapter three which were all white, these materials are varying degrees of beige/brown suggesting that not all the elemental components may be present in maximum oxidation states, something that would be required for an excess of *A*-type cation to be present. It is notable that whilst small increases above the ideal stoichiometry were observed in Section 5.3 for the hydrated phases they were not as significant as those observed here. This suggests that the refined degrees of occupation may be inaccurate, it is possible that this can be explained by the cations themselves being displaced over several sites which the model adopted fails to allow for. Finally it is interesting to note that whilst the occupancies show poor levels of agreement with those achieved through the various other diffraction methods utilised

they do appear to agree to a higher degree with those indicated by elemental analysis shown in Section 5.2.3.

5.6 Variable Temperature Study of $Pb(NbWO_6)_2$ by PND

In order to better understand the structural changes occurring with respect to temperature a sample was selected for further study. The $Pb(NbWO_6)_2$ sample was chosen primarily due the presence of the lone pair on the ion which may potentially lead to more interesting behaviour than in the other *A*-type cations being studied which are all present in d^0 ground states. Lone pairs of this sort on the lead atoms have previously been shown to cause a displacement of the ions away from the site normally occupied and we were keen study if similar effects were occurring in this material[23,24].

5.6.1 Data collection

The series was studied on the POLARIS instrument at ISIS, Oxford. Various collection times were used at a range of temperatures from 5 to 250K, these are displayed in Table 5.6.1. Longer collection times were used at lower temperature allowing the extraction of more precise structural data, study of the data for the two different collection times provided a marginal improvement of the statistics, in the region of a 5% improvement and thus minimal difference to the overall fitting

Table 5.6.1 – Table showing the collection times used for the variable temperature data collection on $Pb(NbWO_6)_2$

Temperature/ Kelvin	Collection times µA/hrs
5	200
20	200
50	150
100	150
150	150
200	150
250	155

5.6.2 Structural refinement

All collected data was refined using the GSAS structural refinement suite and a standard model for a dehydrated *beta*-pyrochlore phase. The lead atom was initially refined on the 16*d* site (0.5,0.5,0.5) but an significant improvement in fit was achieved by a displacement of this atom to the nearby 32*e* site (~0.49,~0.49,~0.49). As with all similar phases the two *B*-site cations are randomly assigned to the 16*c* sites and therefore are constrained for all variable parameters to one another. The final refined parameters for $Pb(NbWO_6)_2$ at 5 K are presented in Table 5.6.2 along with the profile fit in Figure 5.6.1.

Table 5.6.2 – Refined atomic parameters for $Pb(NbWO_6)_2$ at 5K from PND: E.S.D's are given in parentheses.

Atom	Site	x	y	z	UISO	Occupancy
Pb	32*e*	0.4924(3)	0.4924(3)	0.4924(3)	1.79(7)	0.139(1)
Nb	16*c*	0	0	0	1.587(15)	0.5
W	16*c*	0	0	0	1.587(15)	0.5
O	48*f*	0.31056(3)	0.125	0.125	0.588(17)	1

Space group $F\,d\,\bar{3}m$. Cell parameters: a = 10.41612(11) Å, $a = b = c$

Final fit parameters: χ^2 = 6.288, R_{wp} = 3.17%, R_p = 6.30%

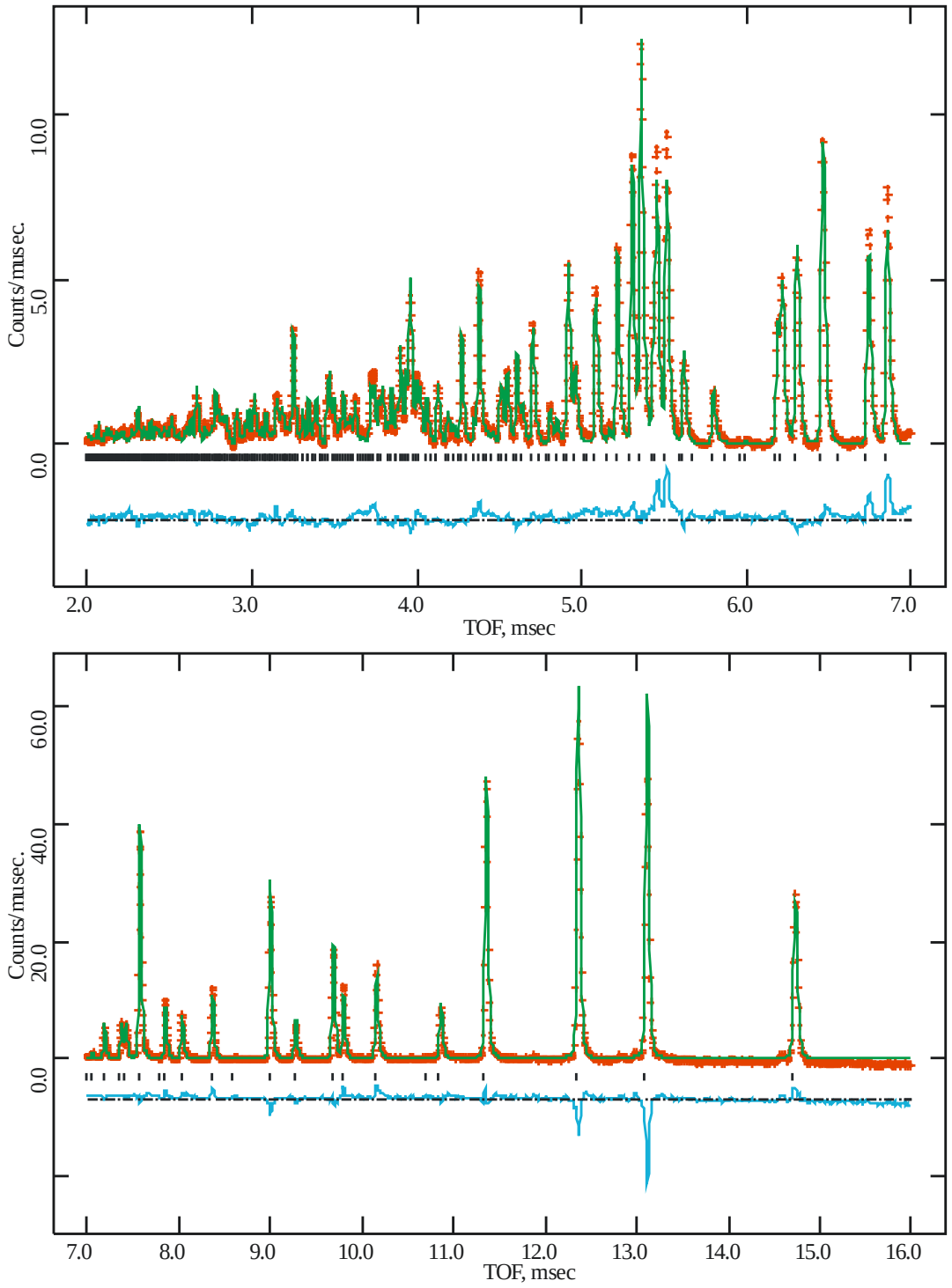

Figure 5.6.1 – Profile fit to 1.5K TOF neutron data for $Pb(NbWO_6)_2$ refined from the data collected on the backscattering bank of the POLARIS instrument. Experimental data points are shown as crosses, upper continuous line is the calculated profile, lower continuous line the difference and allowed reflections indicated by tickmarks. The top plot displays longer d-spacing whilst the bottom plot shows the shorter d-spacing reflections observed.

5.6.3 Discussion

The materials were studied over a temperature range of 5-250 K with data collected at discrete temperatures. The pyrochlore structure is retained in this range and no extra peaks relating to a lowering in symmetry as a consequence of ion ordering are observed. The material displays a standard thermal expansion profile with the expected corresponding changes in lattice parameter with respect to temperature (Figure 5.6.2). There is a slight downward trend at 5 K possibly corresponding to the movement of the lead ion to a more fixed position; however attempts at refining the data in other models, allowing for ordering of the cation or displacement to a site closer to the larger 8*b* site provided a worse fit to the data available. To establish whether this is an artefact of the data acquisition or a genuine effect we would require further low temperature data.

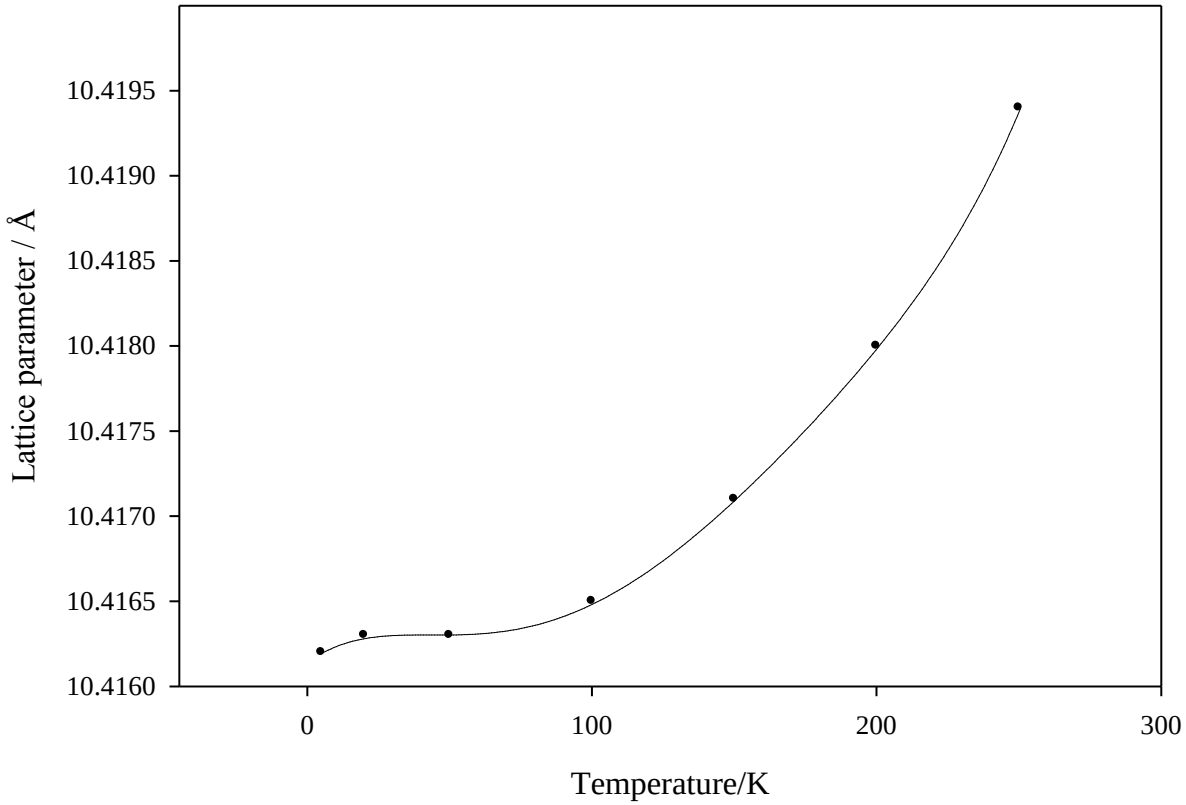

Figure 5.6.2 – A plot of calculated lattice parameters against temperature for $Pb(NbWO_6)_2$ from data collected on the POLARIS instrument.

The expected changes in the refined thermal energy are also observed for all the atoms of the structure (Figure 5.6.3) with a steady decrease and then levelling out of thermal motion as the temperature is reduced. As would be expected both the lead and niobium/tungsten site exhibit larger degrees of thermal motion than the corresponding lattice oxygen atoms. For the lead this can be attributed to the occupation of a site that provides what is far from an ideal coordination environment with six bonds, three + three, that are longer than would be expected from the sum of the ionic radii. The high thermal parameters for the *B*-site cations may be explained by the property of niobium to occupy a site away from the centre of its octahedron, as explained by Jahn-Teller effects as discussed in Section 3.4 leading to the spreading of the nuclear density, observed as an increase in thermal motion due to the limitations of the model.

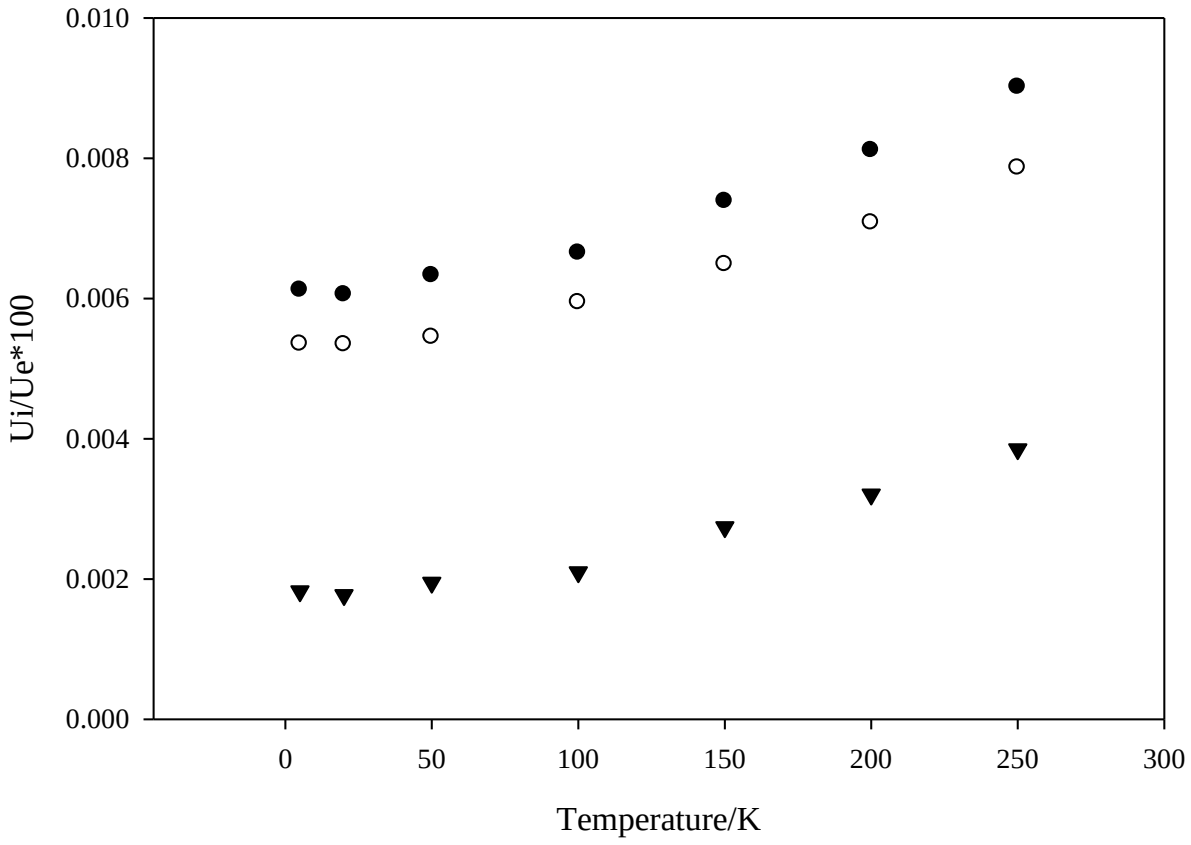

Figure 5.6.3 – A plot of the refined thermal parameters for the niobium/tungsten(○) , lead (●) and oxygen (▼) atoms against temperature for the phase $Pb(NbWO_6)_2$ from data collected on the POLARIS instrument.

This effect may be further enhanced in this material by the possibility of the metal cations being present in ground states other than d^0 leading to further Jahn-Teller distortions.

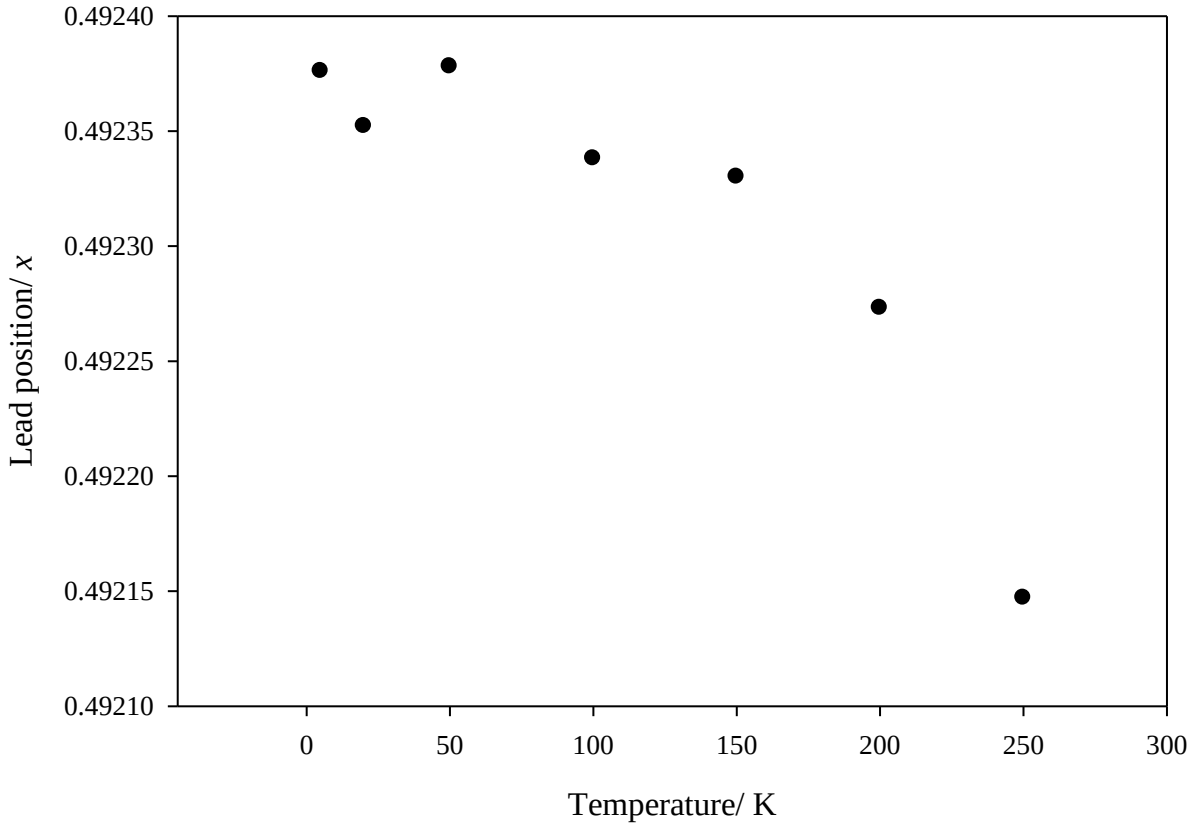

Figure 5.6.4 - Plot of the refined lead position against temperature for $Pb(NbWO_6)_2$ from data collected on the POLARIS instrument

Looking at the position of the lead within the framework, shown in Figure 5.6.4, a gradual movement of the lead atoms away from the 16*d* site as temperature increases is observed. This corresponds well to the increase in thermal motion displayed above; as the effective ion size increases it is unable to remain as close to this position and thus is forced away from the surrounding lattice.

The movement of the lead away from the ideal 16*d* position can be explained in terms of relative ionic radii. For lead in an ideal six fold coordination site we would expect to observe an atomic radius of 1.19 Å. Nominally the oxygen atoms are on a twofold site bound to the framework metals with a smaller coordination contribution from the lead, for two and three fold sites this leads to an ionic radius of 1.35 and 1.36 Å respectively, thus 1.35 Å will be used as a reference value from here

on. The sum of these values leads to an ideal lead-oxygen distance of 2.54 Å. The movement of the lead away from the 16*d* site causes the elongation of three of the nearest oxygen bonds and the shortening of the remaining three, this provides a coordination environment which is still far from ideal but allows a better overall degree of coordination than that provided otherwise. It should be noted however that this is a marginal effect as the site, whilst being too large for an idealised Pb^{2+}, is considerably closer to this ideal than any other site available within the framework.

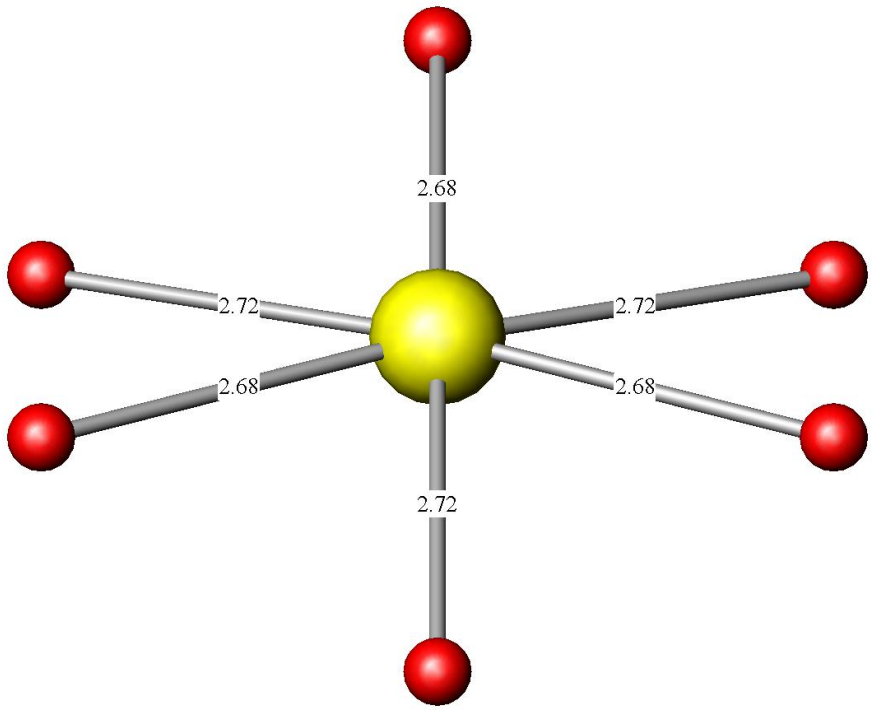

Figure 5.6.5 – Showing the coordination environment of the lead atoms in $Pb(NbWO_6)_2$ to the surrounding oxygen atoms of the BO_6 framework. The red atoms represent the oxygen atoms and the yellow the lead atom.

5.7 Incorporation of trivalent *A*-site cations into the *beta*-pyrochlore framework

As phases of the general stoichiometry $A^{2+}(BB'O_6)_2$ had been successfully synthesised and characterised further work was undertaken to establish whether other *A*-site cations, ideally with higher charges, could be exchanged into the B_2O_6 network. As with the studies carried out earlier in this chapter $(NbWO_6)^-$ and $(TaWO_6)^-$ were selected as the potential acceptor networks, primarily due to their stability both at elevated temperatures and within acidic environments.

5.7.1 Initial studies $A^{3+}(M^{5+}WO_6)_3$ frameworks

The study of the series $A^{2+}(BWO_6)_2$, both here and in other works[11], has shown that ion exchange can readily be used to produce dehydrated pyrochlore phases which are significantly ion deficient on the A_2O' network. The main effect that would be predicted is a reduction in stability of the B_2O_6 network as the contribution from the cationic *A*-site species is reduced. It is therefore expected in turn that there should be a limit to the degree of ion deficiency which these structures can accommodate before structural collapse occurs. Whilst it has been shown that only very weak interactions are required to stabilise the framework, as seen in $HTaWO_6$ where only displaced protons are present outside of the B_2O_6 lattice[25,26], there have been no examples of these frameworks existing without any stabilising cations present.

Work was therefore undertaken to further expand the range of cations that can be accepted onto these sites. This was done with the aim of exchanging trivalent cations into the structure; initially bismuth was studied but limited work was also undertaken with several lanthanide compounds. Whilst the bismuth phases have been shown to form these are the only pyrochlore phases of the general stoichiometry $A^{3+}(BWO_6)_3$ that have been identified, with no phases forming lanthanides retaining the pyrochlore network.

5.7.2 Synthetic route

Synthetic conditions employed were based on the same principle as used to produce the series $A^{2+}(B\mathrm{WO_6})_2$ in Section 5.2.2, however due to the nature of the bismuth sources available adjustments were made as required. Initially both $\mathrm{KNbWO_6}$ and $\mathrm{KTaWO_6}$ were synthesised by conventional high temperature routes, also discussed in Section 5.2.1. to be used as the starting materials. As both of these phases rapidly hydrate in air to $\mathrm{KNbWO_6.H_2O}$ and $\mathrm{KTaWO_6.H_2O}$ the samples were heated to 300 °C under a nitrogen atmosphere for 3 hours to ensure that the starting materials were fully dehydrated before ion exchange was begun. From this point on all samples were handled under a nitrogen atmosphere to minimise the exposure to water.

The ion exchange solution was produced by dissolving $\mathrm{BiNO_3}$ in dried acetone (Sigma Aldrich), minimising the exposure of this solution to water proved particularly important as not doing so resulted in the rapid formation of insoluble $\mathrm{Bi_2O_3}$. A sample, ~ 5 g, of the $K\mathrm{BWO_6}$ starting material was placed into a sealed flask and covered in ~50 ml of the ion exchange solution. This solution was then allowed to stir for 48 hours, after which time it was removed and replaced with fresh $\mathrm{BiNO_3}$ solution. This process was repeated for 21 days after which PXRD patterns were collected to ensure the pyrochlore framework was retained. As well as a pyrochlore framework being observed significant amounts of $\mathrm{Bi_2O_3}$ were also present, ~50 %, which were removed before final analysis. This was done by repeated washings in dilute Oxalic acid, ~2 M, which successfully removed all of the bismuth oxide whilst appearing to have no effect on the pyrochlore framework. Once a pure sample had been obtained the composition of the material was studied using EDX analysis.

In addition a final mass calculation was undertaken to determine whether material had been lost through the process. For both phases complete ion exchange would be expected to lead to a mass increase of 7-8 % however the reverse was in fact observed with both phases losing approximately 15 % of the starting mass during the synthetic process. Several possible explanations can be offered for this loss, with two rationales being that a small amount of material was lost each time the ion exchanged solution was changed as the particle size was extremely small and thus

the material highly mobile or that although weak an acid was used as a washing agent this may have attacked the structurally weakened framework.

5.7.3 Compositional analysis

To ascertain whether ion exchange had occurred within these materials, and if so the level of this ion exchange, compositional data was collected on a JEOL JSM 5910 Scanning Electron Microscope, fitted with an Oxford Instruments Inca Energy 300 Energy-Dispersive X-ray Spectrometry analysis system. For each material multiple data sets were collected to provide better statistics.

Both materials showed a significant amount of bismuth was present, whilst also retaining potassium in the framework. These quantities are very close to one another, by atomic percentages, suggesting general formulae of something similar to $(KBi)(NbWO_6)_2$ and $(KBi)(TaWO_6)_2$. Both formulas would prove reasonable and allow a fully charge balanced structure with an identical overall composition as for the $A^{2+}(BWO_6)_2$ also studied in this work where half of the available cavities within the BO_6 network are occupied.

5.7.4 PXRD structural studies

An initial data set was collected on both samples using a Siemens D5000 diffractometer over a 2 θ range of 10-80° and a total collection time of 3 hours. Both samples were shown to have a pyrochlore framework as their primary phase with multiple small impurities in each material; both contained ~4-6% of WO_3[27] along with a corresponding quantity of B_2WO_6 (B = Nb or Ta)[28,29].

Attempts to collect further data sets did not prove possible as the pyrochlore sample degraded rapidly over time, after ~4 weeks both samples no longer displayed the reflections characteristic of the pyrochlore framework, collapsing instead to a variety of other identifiable phases. These included further quantities of the impurities seen in the initial PXRD data collections along with $BiTaO_4$[30] and $BiNbO_4$[31].

As only a relatively short data set was available for each materials being studied care must be taken with the extracted information. Refinements for both phases proceeded smoothly and provided stable models in both cases for the BWO_6 frameworks. Further study of the data allowed potential positions to be refined for the Bi/K present suggesting the most significant area of electron density, once the contribution of the BWO_6 frameworks had been removed, to be on 32*e* positions roughly half way between the 8*b* and 16*d* sites. In both cases assigning an atom to these positions proved stable but separate positions for the bismuth and potassium cations, potentially achievable due to their significantly different levels of electron density, was not possible.

Table 5.7.1- Refined lattice parameters for $(KBi)(NbWO_6)_2$ and $(KBi)(TaWO_6)_2$ along with the lattice parameters of the pure potassium phases for comparison.

Phase	Lattice parameter/Å	Lattice parameter of potassium only phase
$(BiK)(NbWO_6)_2$	10.4569(2)	10.4747(2)
$(BiK)(TaWO_6)_2$	10.4253(5)	10.49859(16)

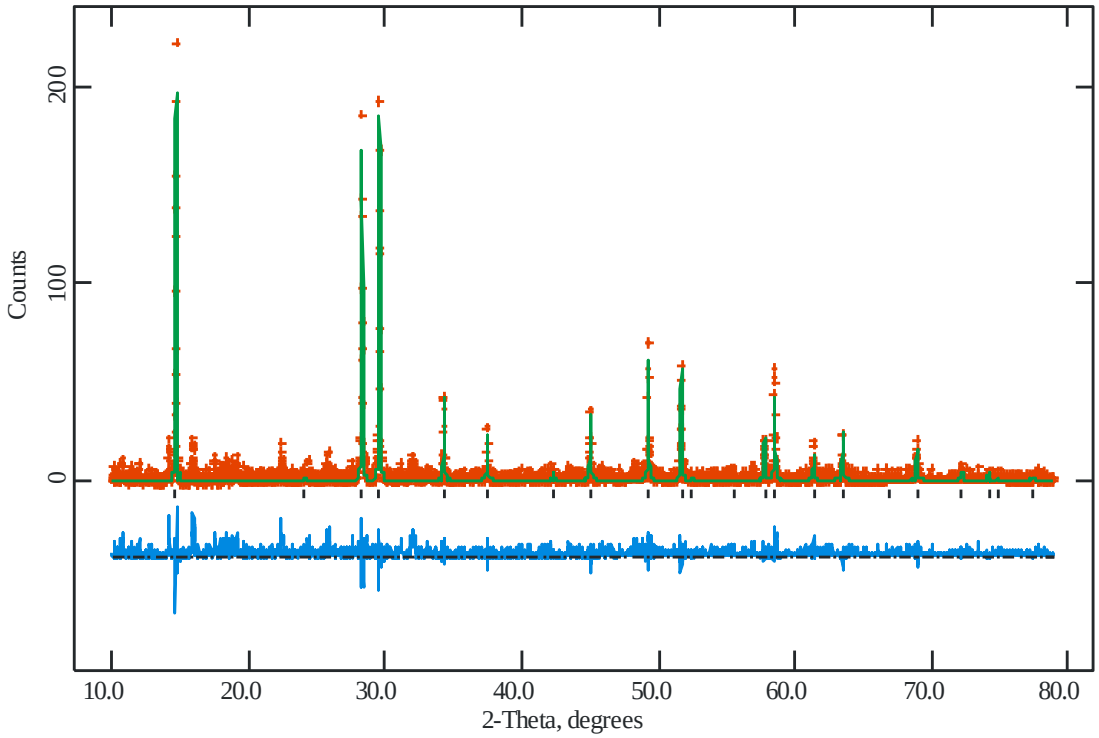

Figure 5.7.1 – Profile fit to PXRD data for (BiK)(NbWO$_6$)$_2$. Experimental data points are shown as crosses, upper continuous line is the calculated profile, lower continuous line the difference and allowed reflections indicated by tickmarks.

5.7.5 Discussion

The primary focus of this section of work was to determine whether defect pyrochlore phases could be synthesised with the inclusions of 3+ cations on the A_2O' network. Whilst this has not proved possible by direct methods, ion exchange has allowed cations of this type to be incorporated. Complete ion exchange was not achieved; instead approximately 75% of the potassium cations appear to have been exchanged for bismuth ions, with one bismuth atom replacing every three potassium atoms removed. Both frameworks synthesised have proved to be highly unstable, breaking down to denser phases when exposed to air for several days.

In the case of both materials the level of extracted phase information has proved limited due to the poor stability of the bismuth containing phases synthesised. Whilst in each case a precise model was built up only the lattice parameters may be relied upon to provide an accurate value. Table 5.7.1 clearly shows that both samples display shorter lattice parameters with the inclusion of bismuth into the

framework; this corresponds well with what has been seen in the materials studied earlier in this chapter. The inclusion of smaller cations leads to the occupation of the 16*d* site as opposed to the larger 8*b* positions; this in turn allows the framework to relax to smaller overall lattice dimensions.

Taking the general formula of these materials as (KBi)(BWO$_6$)$_2$, where B = Nb or Ta, it can be seen that, in common with the series A(BWO$_6$)$_2$, half of the available cavities are occupied within the material whilst the other half are entirely vacant. That ion exchange only occurs to this degree strongly suggests that this level of ion occupation is the limit of what is achievable whilst retaining the pyrochlore structure, with insufficient stabilisation being provided by a level of occupation lower than this. Whilst care must be taken with the interpretation of the refined PXRD data, as the quality is poor compared to the other data being studied in this work, calculated Fourier density maps imply that neither the 16*d* site nor the 8*b* sites are occupied to a significant degree. Instead all cation density on this network is assigned to sites between these two positions, with the apparent level of displacement being more significant than seen in the potassium only analogues.

5.8 Structural studies of K_xNbWO_6

5.8.1 Introduction

The K_2NbWO_6 phase is unusual in both its empirical make up and the apparent charge of the transition metals that compose the B_2O_6 framework. The vast majority of the *beta*-pyrochlores discussed in this work have involved transition metals in their maximum oxidation states, the series A_2NbWO_6 (where *A*= Na, K and Rb) however does not meet this criteria. The addition of a second alkali metal on to the available A_2O' network positions moves the framework away from that of a standard *beta*-pyrochlore framework, with insufficient 8*b* sites available within the structure to accommodate the cations.

This series, with both the sodium, rubidium and potassium analogues, was first presented by Murphy *et al*[22] as part of a wider study of intercalation reactions. The phase $KNbWO_6$ was used as a starting material with an insertion reaction being carried out at low temperature to achieve the desired phase. The series was originally studied by PXRD and no quantitative methods were used to ascertain the level of insertion. Complete insertion appears to have been assumed and exact structural data was not available. Murphy *et al* presented their results with an assumed full occupation on the hexagonal 16*d* site as this best explained the significant lattice expansion in comparison to the $ANbWO_6$ analogues previously presented within the literature[32,33], however PXRD data itself was insufficient to conclusively prove this assumption. Only one other series of materials have previously been observed that display a directly comparable stoichiometry, these being A_2GeTeO_6 (*A*= K, Rb and Cs)[34], which differs in nature in that both germanium and terbium are present at their highest oxidation states.

A further study of this material has therefore been undertaken, using PND as the primary tool of characterisation.

5.8.2 Synthetic Route

To produce a suitable starting material for the insertion stage of this reaction process $KNbWO_6$ was initially synthesised as specified in Section 3.2.1. The purity of the resulting phase was then checked by powder X-ray diffraction which confirmed a single phase sample.

From this point onwards preparation of the sample was carried out entirely under nitrogen replicating the method specified by Murphy *et al*; initially the starting material was heated to 500 °C for 4 hours to ensure the materials were fully dehydrated. The sample (~5g) was then placed in to a Schlenk tube along with the appropriate alkali metal (2-3g), and ammonia (~50ml) condensed onto the sample at -79 °C. The reaction vessel was then left for 2 hours at this temperature before being allowed to warm to -20°C over a further 2 hour period. The remaining ammonia was then allowed to boil off until the sample was dry. Excess alkali metal was then removed by reaction with dry ethanol, followed by repeated washing with further dried ethanol. Finally the sample was left under vacuum for ~1 hr to ensure all solvent had been removed. Throughout the subsequent characterisation process care was taken to minimise the exposure of the sample to air, this was primarily undertaken to reduce the chance of water being incorporated into the structure.

5.8.3 Additional samples

Further work was also undertaken to attempt to synthesise and study Rb_2NbWO_6 and Na_2NbWO_6 as presented by Murphy *et al*. A similar method of insertion was attempted as described above using $NaNbWO_6$ and $RbNbWO_6$ as the respective starting materials. Whilst the rubidium phase was synthesised as previously described the sodium phase was itself made by an ion-exchange route from $KNbWO_6$.

Approximately 5 g of $KNbWO_6$ was placed under a saturated NaCl solution and heated to 95 °C for several days, with the solution drained off and replaced daily. The new stoichiometry, $NaNbWO_6$, was confirmed by elemental analysis and a clear shift in lattice parameter seen, confirming an increase in lattice parameter expected. The insertion reaction was then repeated as for the potassium phase using sodium metal in place of potassium metal.

However of the three phases where synthesis was attempted only the potassium phase proved fully successful on completion of the reaction scheme. Whilst the sodium phase also formed readily and was initially identified as phase pure by PXRD it deteriorated over the course of several weeks, with an amorphous element becoming increasingly more significant. On the collection of PND data an extremely high hydrogen background was observed, far higher than for other hydrated *beta*-pyrochlore phases. It was therefore postulated that the structure may have incorporated NH_4^+ into the structure as part of the synthetic process, something previously observed in NH_4NbWO_6[35,36] where the ammonium ions occupy the cavity around the 8*b* site.

Theoretically it would be possible for both NH_4^+ and Na^+ ions to be present within the framework however the collected neutron diffraction data was of insufficient quality to accurately provide information on the location of both atom types with such a degree of hydrogen present within the sample. It is possible that the basicity of the ammonia is sufficient that it causes the structure to collapse over time. We can be relatively certain that ammonia was incorporated into the structure as care was taken throughout the synthetic procedure to ensure that the material was kept dry by constant handling under nitrogen, thus the ammonia should be the only potential hydrogen source. Future attempts to characterise this phase should therefore take this into account and it is possible that an additional heating step after the current synthetic steps identified would prove sufficient to remove the ammonia from the framework.

5.8.4 Structural Studies of K_xNbWO_6

After the completion of synthesis the retention of the pyrochlore structure was confirmed using PXRD which showed the expected reflections for the cubic pyrochlore structure. It was however clearly visible that whilst the same reflections were retained the relative intensities of these reflections had altered significantly from the starting materials.

PND data was subsequently collected on the K_xNbWO_6 phase using the high resolution D1A instrument at the ILL, France. Data sets were collected between 14 and 157.9° 2θ over a period of 6 hours at 5 and 150 K using a neutron wavelength of 1.909 Å, with the resulting data sets subsequently refined using the GSAS refinement suite[37]. An initial model was established using the atomic positions and lattice constants extracted for $KNbWO_6.H_2O$ in Chapter Three, with the oxygen position of the water molecule as the second potential potassium site. The refinement proceeded with the variation of background parameters, histogram scale factor, peak shape, lattice parameter and zero point displacement. This was followed by a more in-depth investigation of the variables relating to the individually refineable atomic parameters, including; thermal motion, degree of site occupation and atomic positions.

The structural model initially used for refinement allowed for two independent potassium positions, initially on the 8*b* and 16*d* sites assigned to K and O2 respectively in the $KNbWO_6.H_2O$ model. Testing of the 32*e* site (~0.4,~0.4,~0.4) as opposed to this 8*b* position provided a significantly improved fit with the potassium position remaining stable, whilst still not matching the values expected the thermal parameters of the potassium ions were also significantly improved with this change.

Presented in Tables 5.8.1 and 5.8.2 are the final refined values for the 5 K and 150 K data sets respectively whilst Figure 5.8.1 shows the fit profile for the 5 K data set.

Table 5.8.1 – Refined atomic parameters for K_xNbWO_6 at 5K from PND: E.S.D's are given in parentheses.

Atom	Site	x	y	z	UISO	Occupancy
K	32*e*	0.4155(9)	0.4155(9)	0.4155(9)	-1.0(4)	0.258(10)
Nb	16*c*	0	0	0	1.21(3)	0.5
W	16*c*	0	0	0	1.21(3)	0.5
O	48*f*	0.30891(7)	0.125	0.125	0.65(5)	1
K	16*d*	0.5	0.5	0.5	-0.89(14)	0.425(17)

Space group $F\,d\,\bar{3}m$. Cell parameters: a = 10.5070(9) Å, $a = b = c$

Final fit parameters: χ^2 = 1.923, R_{wp} = 3.33%, R_p = 2.74%

Table 5.8.2 – Refined atomic parameters for K_xNbWO_6 at 150 K from PND: E.S.D's are given in parentheses.

Atom	Site	x	y	z	UISO	Occupancy
K	32*e*	0.40977(7)	0.40977(7)	0.40977(7)	-1.1(4)	0.264(8)
Nb	16*c*	0	0	0	1.61(7)	0.5
W	16*c*	0	0	0	1.61(7)	0.5
O	48*f*	0.30939(3)	0.125	0.125	0.89(3)	1
K	16*d*	0.5	0.5	0.5	-0.7(3)	0.400(14)

Space group $F\,d\,\bar{3}m$. Cell parameters: a = 10.5087(7) Å, $a = b = c$

Final fit parameters: χ^2 = 1.092, R_{wp} = 3.93%, R_p = 2.97%

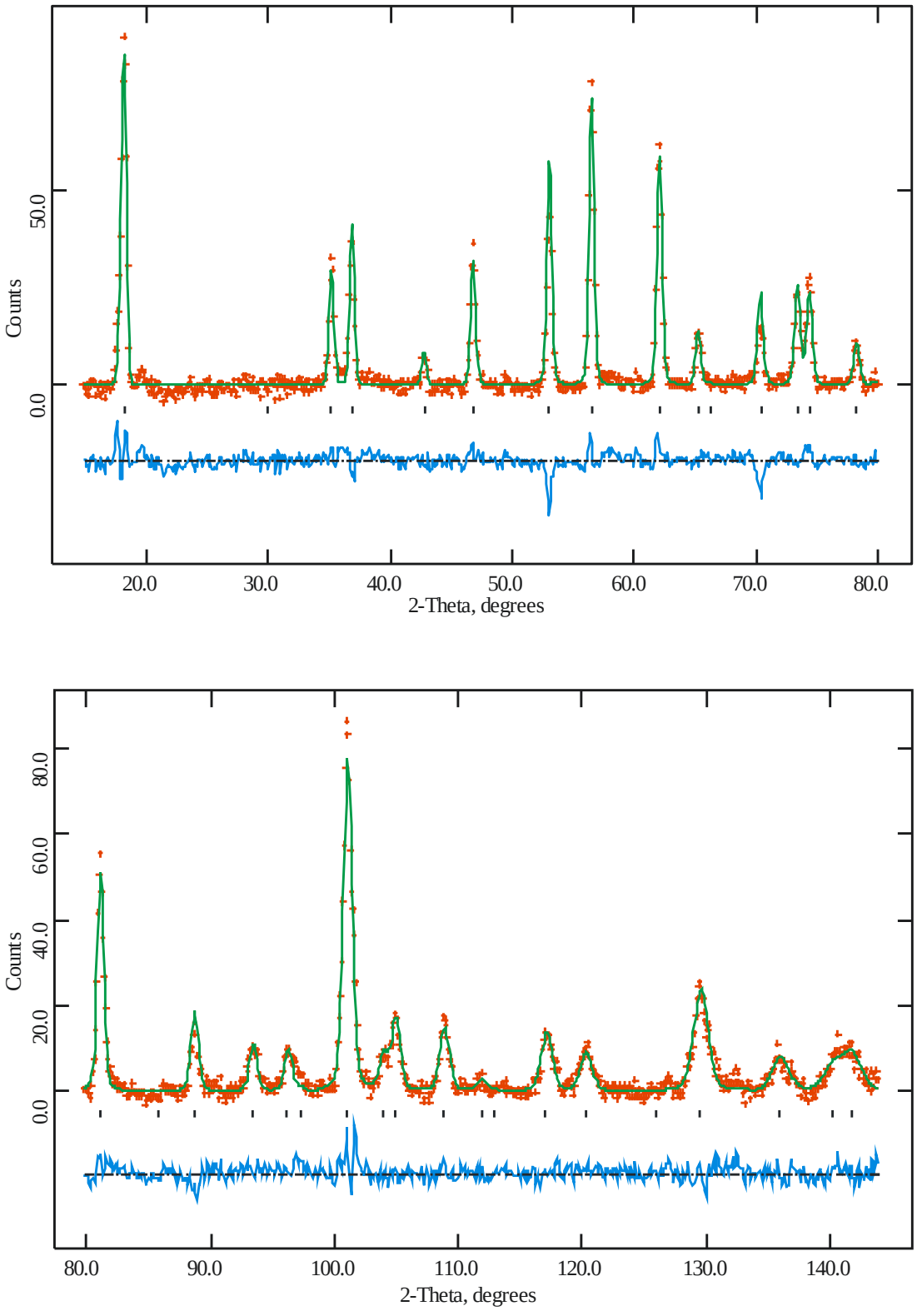

Figure 5.8.1 – Profile fit to PND data for K_xNbWO_6 collected at 5K. Experimental data points are shown as red crosses, the upper continuous green line is the calculated profile, lower continuous blue line the difference and allowed reflections indicated by tick marks.

5.8.5 Discussion

Figure 5.8.1 shows a relatively poor fit to the data for the refined 5 K data set collected for K_xNbWO_6. In a large part this appears to be a result of the relatively poor quality of the data with insufficient counts to provide a smooth background and high quality peak shapes. With this in mind all data should be analysed with care and further analysis may be required to provide suitable validation of the discussion presented here.

The two refinements undertaken present broadly similar findings to one another, locating neutron density on the same positions. Lattice parameters are consistent, showing only a small contraction on cooling and at values of ~10.5 Å are in good agreement with those observed for $KNbWO_6.H_2O$ (10.4747(2) Å) where the 16*d* site is also occupied and considerably larger than those for $KNbWO_6$ (10.3566(2) Å) where this site is unoccupied. In addition the relatively low level of diffuse scattering strongly suggests that no hydrogen has been incorporated into the structure as significantly more noise would be expected if this had occurred.

Refinements of the degree of occupation for the 32*e* and 16*d* sites proved stable for both models, whilst the individual levels of occupation differed slightly between the two data sets the total calculated potassium per formula unit was refined as 1.856 and 1.882 for the 150 and 5 K data sets respectively. Both refined structures did however provide negative thermal parameters for all potassium sites, along with slightly greater than complete occupancy on the collective 32*e* positions (~1.1). Whilst these proved stable they must be taken as unreasonable, fixing these parameters to small positive values provided no statistically significant change to the fit. It is believed that this effect can be assigned to the poor level of data and should thus be taken as representative rather than conclusive. What both data sets clearly show is that neutron density is present on both the 32*e* and 16*d* positions; this coupled with the lack of water within the sample strongly suggests that a significant degree of insertion has occurred.

The identification of this material as a viable phase and the approximate locations of the potassium ions within the structure is significant in that it present a chemical unusual material; very few *beta*-pyrochlores are known where the transition metals

composing the framework are in oxidation states other than a d^0 configuration. In all other ways this material behaves and appears similar to that of a hydrated *beta* phase with an expanded lattice parameter and the 16*d* site occupied.

The one remaining feature of this material that appears to differ from the other *beta*-pyrochlores discussed in Chapter Three is the value of the one variable positional coordinate of the B_2O_6 framework; that of the x position of the oxygen. Both refinements present values where $x < 0.3125$ suggesting a compression of the BO_6 octahedra as opposed to the elongation more commonly observed. It is postulated that this may be as a result of the extra charge now housed within this framework causing a reconfiguration of these building units; it is also plausible that this effect is a result of the data quality.

5.8 Conclusions

Presented in this chapter are a series of materials synthesised by ion exchange methods from other structurally similar pyrochlore frameworks. Broadly these materials undergo ion exchange on the *A*-cation site only, with the exchange of more highly charged ions causing the level of occupation of these sites to fall.

It has been shown that whilst the divalent cations occupy the 16*d* site it is the size of these ions that provides the dominant effect in determination of the lattice parameters, Figure 5.2.2. However once the cations begin to move away from this position, as is seen in both of the cadmium containing hydrated phases, this effect changes and providing an optimum coordination environment for the cadmium ions forces an enlargement of the lattice allowing the adoption of a site with one short, two medium and three long bonds to the surrounding oxygen atoms. The water molecules captured within the framework provide a stabilising effect, rapidly being reabsorbed into the structure on exposure to air. The position of these molecules within the framework shifts depending upon the lattice parameter of the material, which in turn determines the volume of the internal cavities available. The removal of this water causes only small shifts in the lattice dimensions and can therefore be interpreted as being desirable but not required for these materials to remain stable.

A correlation has been observed between the oxygen positions of the BO_6 octahedra and the *A*-site cation size. This shift in oxygen position suggests a concerted change to the structure to better allow the coordination of the cations through an elongation or contraction of the octahedra as required. Low temperature PND data for the series $A(NbWO_6)_2$. (*A* = Sr, Ca, Pb and Ba) has provided compelling evidence for the adaptability of this structure type , showing the significant changes in coordination of the *A*-site cations that can be adopted by these structure types in order to incorporate unusual levels of occupation and anion types.

In addition $Pb(NBWO_6)_2$ was studied by variable temperature TOF powder neutron diffraction and displayed conventional thermal expansion, with the lead ions shifting towards the 16*d* site on cooling. This suggests that when available, i.e. not sterically constrained, this site is preferable in terms of coordination.

The synthesis of $K_{\sim 1.8}NbWO_6$, $(KBi)(NbWO_6)_2$ and $(KBi)(TaWO_6)_2$ has shown the wider potential of *beta*-pyrochlore frameworks to adopt unusual stoichiometries and the capacity of these phase to accommodate levels of occupation both above and below those normally observed in theses phases when appropriate conditions are adopted. All of these phases would however benefit significantly from further characterisation so more specific conclusions regarding the level of occupation and the location of the individual atoms can be undertaken.

5.9 References

(1) Merrifield, R. B.; Vizioli, L. D.; Boman, H. G. *Biochemistry* **1982**, *21*, 5020-5031.

(2) Iwamoto, M.; Yahiro, H.; Tanda, K.; Mizuno, N.; Mine, Y.; Kagawa, S. *J. of Phys. Chem.* **1991**, *95*, 3727-3730.

(3) Fornes, T. D.; Yoon, P. J.; Hunter, D. L.; Keskkula, H.; Paul, D. R. *Polymer* **2002**, *43*, 5915-5933.

(4) Beckett, P. H. T. *J. of Soil Science* **1964**, *15*, 9-&.

(5) Abdelfattah, A.; Wada, K. *J. of Soil Science* **1981**, *32*, 271-283.

(6) Moller, T.; Clearfield, A.; Harjula, R. *Micro. and Meso. Mats.* **2002**, *54*, 187-199.

(7) Luca, V.; Griffith, C. S.; Chronis, H.; Widjaja, J.; Li, H. J.; Scales, N. In *27th Symposium on Scientific Basis for Nuclear Waste Management*; Oversby, V. M., Werme, L. O., Eds.; Materials Research Society: Kalmar, SWEDEN, 2003, p 309-314.

(8) Babel, S.; Kurniawan, T. A. *J. of Hazardous Mats.* **2003**, *97*, 219-243.

(9) Groult, D.; Pannetier, J.; Raveau, B. *J. of Sol. State Chem.* **1982**, *41*, 277-285.

(10) Michel, C.; Groult, D.; Deschanvres, A.; Raveau, B. *J. of Inorg. and Nuc. Chem.* **1975**, *37*, 251-255.

(11) Chernorukov, N. G.; Suleimanov, E. V.; Kortikov, V. E.; Suchkov, A. I. *Zhurnal Neorganicheskoi Khimii* **1998**, *43*, 1251-1253.

(12) Ringwood, A. E.; Kesson, S. E.; Ware, N. G.; Hibberson, W.; Major, A. *Nature* **1979**, *278*, 219-223.

(13) Kondev, F. G. *Nuclear Data Sheets* **2008**, *109*, 1527-1654.

(14) Groult, D.; Michel, C.; Raveau, B. *J. of Inorg. and Nucl. Chem.* **1975**, *37*, 2203-2205.

(15) Stephens.Nc; Roth, R. S. *J. of Sol. St. Chem.* **1971**, *3*, 145-&.

(16) Foord, E. E.; Mrose, M. E. *Amer. Mineralogist* **1978**, *63*, 709-714.

(17) Woodward, P. M.; Sleight, A. W.; Vogt, T. *J. of Phys. and Chem. of Solids* **1995**, *56*, 1305-1315.

(18) Moreau, J. M.; Galez, P.; Peigneux, J. P.; Korzhik, M. V. *J. of Alloys and Compounds* **1996**, *238*, 46-48.

(19) Michel, C.; Groult, D.; Deschanvres, A.; Raveau, A. *J. of Inorg. and Nuc. Chem.* **1975**, *37*, 251-255.

(20) Shannon, R. D. *Acta Crystallographica Section A* **1976**, *32*, 751-767.

(21) Sears, V. F. *Neutron News* **1992**, *3*, 26 - 37.

(22) Murphy, D. W.; Dye, J. L.; Zahurak, S. M. *Inorg. Chem.* **1983**, *22*, 3679-3681.

(23) Shpanchenko, R. V.; Chernaya, V. V.; Tsirlin, A. A.; Chizhov, P. S.; Sklovsky, D. E.; Antipov, E. V.; Khlybov, E. P.; Pomjakushin, V.; Balagurov, A. M.; Medvedeva, J. E.; Kaul, E. E.; Geibel, C. *Chemistry of Materials* **2004**, *16*, 3267-3273.

(24) Mentre, O.; Dhaussy, A. C.; Abraham, F.; Suard, E.; Steinfink, H. *Chemistry of Materials* **1999**, *11*, 2408-2416.

(25) Groult, D.; Pannetier, J.; Raveau, B. *J. of Sol. St. Chem.* **1982**, *41*, 277-285.

(26) Butler, M. A.; Biefeld, R. M. *Phys. Rev. B* **1979**, *19*, 5455-5462.

(27) Locherer, K. R.; Salje, E. K. H. *Phase Transitions* **1999**, *69*, 85-93.

(28) Lundberg, M. *Acta Chemica Scandinavica* **1972**, *26*, 2932-&.

(29) Santoro, A.; Roth, R. S.; Minor, D. *Acta Crystallographica Section B-Structural Science* **1979**, *35*, 1202-1205.

(30) Ivanova, L. A.; Venevtsev, Y. N.; Noskova, E. A. *Kristallografiya* **1977**, *22*, 1098-1100.

(31) Popolitov, V. I.; Lobachev, A. N.; Ivanova, L. A.; Stefanovich, S. Y.; Golder, G. A.; Chechkin, V. V.; Venevtsev, Y. N.; Pakhulskaya, E. I. *Kristallografiya* **1975**, *20*, 783-787.

(32) Babel, D. *Zeitschrift fuer Anorganische und Allgemeine Chemie* **1972**, *387*, 161-178.

(33) Pannetier, J. *Sol. St. Comms.* **1980**, *34*, 405-408.

(34) Amarilla, M.; Veiga, M. L.; Pico, C.; Gaitan, M.; Jerez, A. *Inorg. Chem.* **1989**, *28*, 1701-1703.

(35) Groult, D.; Michel, C.; Raveau, B. *J. of Inorg. and Nuc. Chem.* **1974**, *36*, 61-66.

(36) Perottoni, C. A.; Haines, J.; da Jornada, J. A. H. *J. of Sol. St. Chem.* **1998**, *141*, 537-545.

(37) Larson, A. C.; Von Dreele, R. B. 1990.

(38) *Physical Review* **1922**, *20*, 113.

Chapter Six

OSMATE PYROCHLORE PHASES

6.1 Introduction

In 2001 the first superconducting pyrochlore phase was reported, $Cd_2Re_2O_7$ with T_c = 1.4 K[1,2] displaying conventional Type II superconduction. Shortly after a further family of superconducting *beta* pyrochlores were also discovered, AOs_2O_6 (*A*= K, Rb and Cs) with reported T_c's of 3.6 K, 6.3 K and 9.6 K respectively[3-5] since this point scientific interest in this area has been intense with a significant number of articles appearing in print each year. This entire osmate series was reported as adopting the conventional pyrochlore model for *beta*-phases in the cubic $Fd\bar{3}m$ space group. The nature of the superconduction in these materials has recently been shown to alter between the phases, with $CsOs_2O_6$ displaying weak coupling, $RbOs_2O_6$ strong coupling and KOs_2O_6 extremely strong coupling with BCS-type superconductivity[6]. The enhancement of T_c in these phases, from caesium to potassium, has been shown to be linked to the level of thermal motion of the alkali metal cation[7], with the value of T_c increasing as the degree of thermal motion also does so.

Recent structural work on these osmate oxides has focused on KOs_2O_6 with various structural models being presented from single crystal X-ray data, with particular attention being paid to the changes occurring with respect to temperature and the effects this has upon ionic motion. Schuck *et al.*[8] suggested that between 100 and 400 K extra reflections were observed that violate $Fd\bar{3}m$ symmetry and proposed a reduction in symmetry to a crystal system in the $F\bar{4}3m$ space group. This was contradicted by Yamaura *et al.*[9] who found no evidence for these extra reflections in data collected between 5 and 300 K and thus concluded that the material was best described in $Fd\bar{3}m$. All models in these and other works show that the potassium ions, sited on the 8*b* position, exhibit an abnormally large degree of thermal motion. This observation is in good agreement with the work of Kunes and Pickett[10] who undertook band structure calculations which showed an instability in the optic mode of the potassium ion resulting in 'rattling' type behaviour. Larger than expected thermal motions of the *A*-site cation have also been observed in the rubidium and caesium analogues, although the degree of this increase is significantly lower than for the potassium phase[9]. More recent work by Hiroi has suggested a different phase transition occurs, a first order transition at T_p = 7.5 K whilst the material is in the superconducting state in zero magnetic field[11]. This study suggested that the transition is associated with the rattling of potassium ions located in an anharmonic potential created

by the Os-O units. It was assumed that this transition can have a structural origin, however no evidence was observed for this phenomena with neither a symmetry change nor cell doubling[12]. The structure of both $RbOs_2O_6$ and $CsOs_2O_6$ have also been studied extensively with both phases retaining the expected symmetry elements across a broad range of temperatures[12]. Studies undertaken on $RbOs_2O_6$ by variable temperature powder neutron diffraction[13] have shown unusual behaviour relating to the atomic displacement parameter of the rubidium but with no change in overall cell symmetry.

Work carried out within this research group has studied all three of these phases by variable temperature powder neutron diffraction[14]. Whilst both the rubidium and caesium phases were shown to display standard thermal expansion across the temperature range studied, 200 to 500 K, the potassium analogue did not. At ~80 K the potassium anion was shown to be delocalized away from the 8*b* site to the 32*e* sites within the same cavity, the degree of this displacement continues as the temperature is reduced and is complete before T_c. It was therefore suggested that any discussion of the structure and derived properties of the superconducting pyrochlore osmate phases must employ a structural model with locally delocalised alkali metal cations.

Work in this chapter looks at the effects of water, both structural and surface bound, upon the superconducting transitions of $RbOs_2O_6$ and KOs_2O_6. Work carried out within the research group has shown that KOs_2O_6 can incorporate a small amount of water into the framework[15], causing a increase in the lattice dimensions and we wished to study the effects that this change has upon the superconducting nature of this material.

6.2 The effects of hydration on T_c for KOs_2O_6

The series AOs_2O_6 has been extensively studied in recent years due to the non-conventional superconduction that has been observed in these phases. KOs_2O_6 phases both partially hydrated and dehydrated are presented here along with a detailed discussion and interpretation of the effects of hydration upon the superconducting state. Much of this work was published by ourselves in 2008[15] as a part of a wider study on the low temperature behaviour of KOs_2O_6. We also look at different methods of sample preparation presented in the literature and comment upon the effects we have observed in relation to the temperature at which superconduction occurs.

6.2.1 Sample preparation

A range of samples of $AOs_2O_6.nH_2O$ (A = K and Rb) were prepared by Miss R. Galati. These samples were each prepared under different conditions to enable the investigation of the effects the synthetic routes has upon the final composition of the sample and what consequent influence this has upon the onset of superconduction.

In general each sample was synthesised by the reaction of stoichiometric quantities of high purity OsO_2 and KO_2. These materials were ground together, pelletised inside of a nitrogen glove box (as KO_2 rapidly hydrates in air) and sealed under vacuum in a silica ampoule along with a small gold tube containing Ag_2O (<0.1g), used to create an oxidising atmosphere. The samples were then heated to 450 °C at a rate of 100 °C/h and held there for 16 hours.

The samples produced contained KOs_2O_6 as their primary product with OsO_2 (~5 %) and $KOsO_4$ (~20 %) as secondary products. A further product OsO_4 was also present as small crystals coating the inside of the tube wall; however this was easily removed by passing a stream of dry nitrogen across the surface. To enable a degree of control over the level of hydration the samples were treated differently when removed from the sealed tube. Samples A and B were handled in air then washed in distilled water for 1 hour and 30 minutes respectively. Sample A was then allowed to dry in air whilst sample B was dried under nitrogen at 350 K for 3 hours. Sample C was washed in DMF followed by a rapid washing in distilled water and dried at 598 K also for 3 hours under nitrogen. Finally two

further samples were produced, neither of which was washed. The first of these, sample D, was dried under flowing nitrogen at 598 K for 3 hours whilst the final sample, sample E, was studied as synthesised. All samples were then stored under nitrogen once preparation was completed.

Table 6.1 – Summary of the synthetic conditions used in the preparation of the various $KOs_2O_6.nH_2O$ samples presented here.

Sample	Sample description	Washing agent	Drying Temperature and conditions
A	Hydrated 1	Stirred with water. 1 hour	298 K air
B	Hydrated 2	Stirred with water. 30 minutes	350 K in air
C	Partially hydrated	Stirred with DMF, quick water washing on filtering	298 K air 598 K/N_2
D	Dried. Exposed to air and dried at 573 K	Not washed	598 K/N_2
E	Handled under dry $N_{2(g)}$ only	Not washed	-

In each case phase composition was studied using a Siemens D5000 diffractometer operating at λ = 1.54056 Å over a 2θ range of 10 to 110 ° with a step size of 0.02 ° and a total data collection time of 15 hours. All data was collected under a dry nitrogen atmosphere. The collected profiles showed that for the washed phases (A-C) the primary peaks could all be assigned to a cubic cell with $a \sim 10$ Å with the *Fd-3m* space group. A few very weak peaks ($I/I_o < 0.04$) could also be assigned to OsO_2. For the unwashed samples (D and E) as well as the peaks observed in the washed samples additional peaks from $KOsO_4$ were also observed and fitted well to the standard model for this phase type[16].

6.2.2 Magnetic data collection

Magnetic and superconductivity data were collected using an Oxford Instruments 3001 Vibrating Sample Magnometer (VSM) with a 12 T superconducting magnet. Data were collected through the superconducting transition of the material over a temperature range of 14 K to ~2 K using a cooling rate of ~1 K/minute under an applied field of 100 gauss. Data was collected every 2 seconds and stored for later analysis.

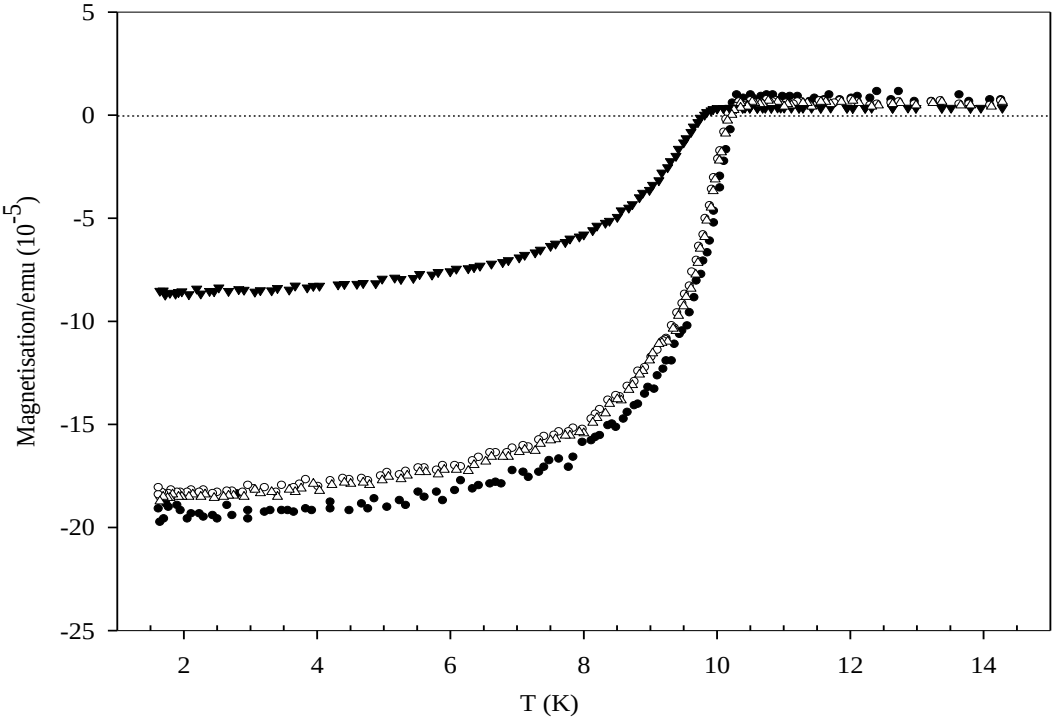

Figure 6.1 - Overall Magnetisation of the materials for D (dried,●), C (never washed but exposed to air,○), B (washed in water then dried,Δ) and A (fully hydrated, ▼) samples.

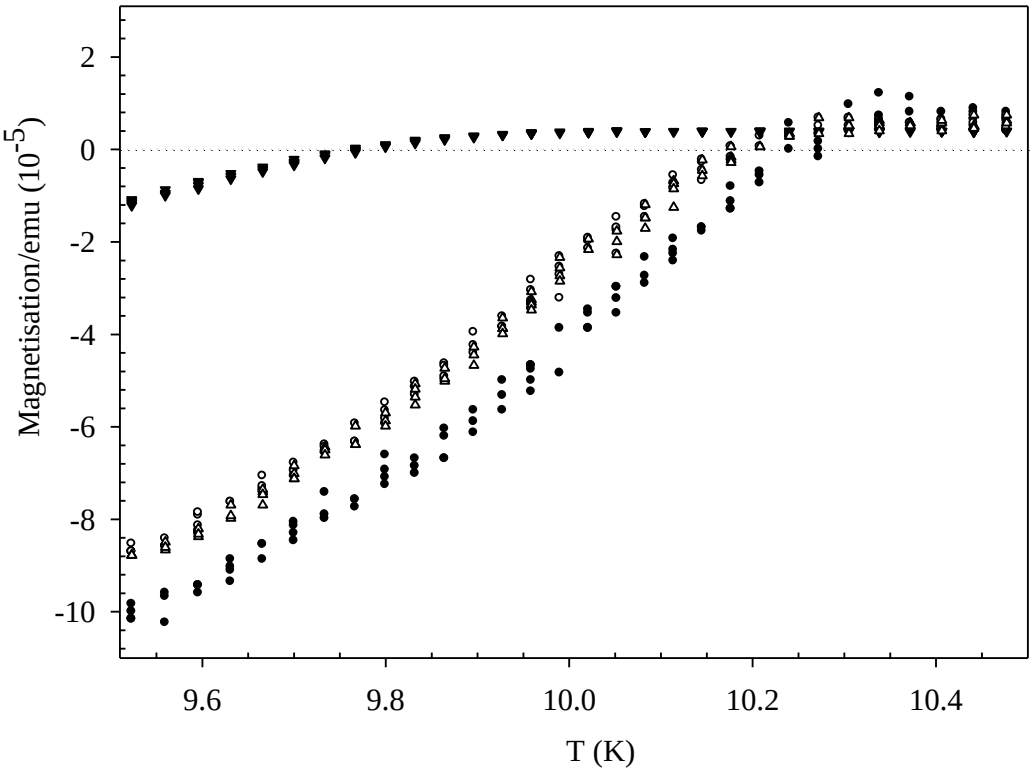

Figure 6.2 – Showing the transition region of the magnetic data collected, clearly showing the change of the material to a superconducting state. Key is as for Figure 7.1

The data appears to show a correlation between the level of hydration and the superconducting transition of the material, with T_c lowering as more water is incorporated into the structure. This leads to T_cs for A, B, C, D and E of 9.8 K, 10.1 K, 10.1 K, 10.2 K and 10.2 K respectively.

Table 6.2 – Observed temperatures at which the samples studied undergo a transition to the superconducting state. Estimated errors are given in parenthesis.

Sample	Sample description	Drying Temperature and conditions	T_c (K)
A	Hydrated 1	298 K air	9.8(1)
B	Hydrated 2	350 K in air	10.1(1)
C	Part hydrated	298 K air 598K/N_2	10.1(1)
D	Dried. Exposed to air and dried at 573 K	598K/N_2	10.2(1)
E	Dry box	-	10.2(1)

6.2.3 Discussion

To better understand and try to explain what is occurring it is important that we take into account other factors such as the level of dehydration as it is altered within these materials. Alongside the collection of magnetic susceptibility work presented here other methods of characterisation were undertaken. Diffraction data, both PXRD and low temperature PND, were collected by Miss R Galati to better display the structural effects of the incorporation of water into the structure. Comparison of lattice parameters with room temperature PXRD data showed a strong correlation with the observed T_c (Table 6.3) with the lattice parameter decreasing as the T_c increases. Refinements of PND data collected between 2 and 500 K on the D20 instrument at the ILL, Grenoble, on the B, hydrated, sample showed a steady increase in lattice parameter as expected with increasing temperature until ~350 K after which a lattice contraction occurs. This lattice contraction was assigned to the loss of water and once complete provides unit cell dimensions similar to those of the dried samples at the same temperature.

TGA data was also collected on our behalf on samples A and C by Dr Chris Knee at the University of Gothenburg (Figure 6.3). This data showed that the mass loss upon heating between 323 K and 523 K are 0.42 % and 0.17 % for the A and C samples respectively. The fully hydrated sample, A, then shows a further substantial mass loss above 530 K while for C a similar loss appears to occur >573 K. These larger mass losses were attributed to the evolution of the residual impurity phases present, $KOsO_4$ and OsO_4, followed by the decomposition of the pyrochlore framework itself. Allowing for only the mass loss between 323 and 530 K, a temperature range that corresponds to the temperature region in which observable lattice parameter changes occur to these phases upon heating, leads to a calculated water content of 0.11 mol, $KOs_2O_6.0.11H_2O$ for the fully hydrated sample and approximately half this value for the partially hydrated sample. These values also proved to be consistent with the refined occupancies determined from PND data.

Table 6.3 – Refined lattice parameters for the various $KOs_2O_6.nH_2O$ samples and their corresponding T_cs.

Sample	Lattice parameter, *a*/Å (PXRD (* PND) at 298 K)	T_c (K)
A	10.1202(12)	9.8(1)
B	10.1106(3)	10.0(1)
C	10.08825(17)	10.1(1)
D	10.0828(12)	10.2(1)
E	10.0795(2)	10.2(1)

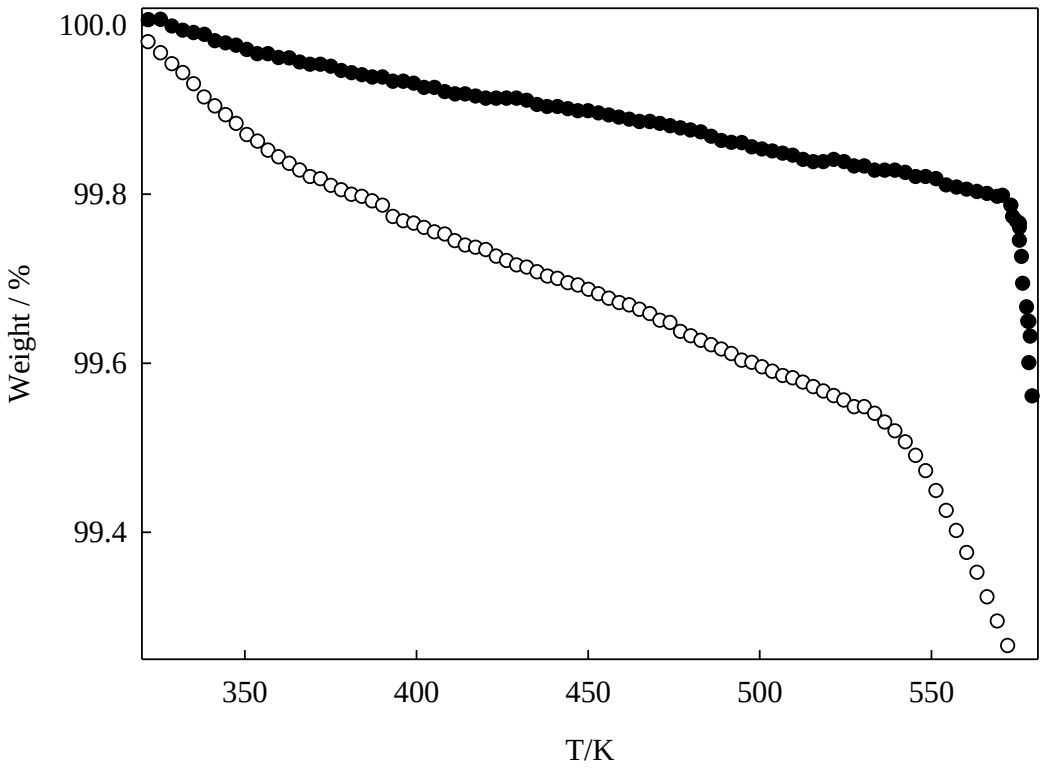

Figure 6.3 – TGA data collected on the fully hydrated sample, A, and the partially hydrated sample, C. All data was collected by Dr Chris Knee

The final model used to describe $KOs_2O_6 0.11H_2O$ allowed for the incorporation of water as seen in other, structurally similar, pyrochlores *ie* $KNbWO_6.H_2O$[17] where the water occupies a 32*e* site near to the 8*b* site. Unlike many other materials this osmate phase only contains a small amount of water per unit cell, therefore the majority of cavities are still inhabited by potassium ions with ~11% filled with water displacing the potassium towards the adjacent 16*d* sites. Two possible explanations for the low level of water incorporation are proposed; that the water undergoes slow redox reactions with the material causing further reduction of the $Os^{+5.5}$, this was seen when it was attempted to further increase the water content leading to sample degradation or that the water content is limited purely by steric constraints. The similar hydrated phase, $KTaWO_6.H_2O$ discussed earlier in this work, has a lattice parameter of ~10.3 Å compared to the smaller KOs_2O_6 at ~10.1 Å, thus impeding the diffusion of the potassium cations and water molecules within the framework. This effect can be clearly seen in many of the *beta*-pyrochlore phases in Chapter Three where from all of the phases studied only the two largest studied, $KTaWO_6$ and $KNbWO_6$, are able to incorporate water into the structure. Several non-oxide pyrochlores have also been shown to be hydrated, but once again they are characterised by their large lattice parameters, one example being $KNiCrF_6.H_2O$[18] where a = 10.24 Å.

The nature of superconduction in these materials has repeatedly been assigned to the rattling[8,9] of the potassium ions in a cavity that is larger than ideal for a cation of this size providing a non-ideal coordination environment. The effect of this cation displacement upon the superconducting properties seems to be a slight degradation in both T_c and superconducting volume. Therefore a fall in T_c is observed from 10.2 to 9.8 K between the dry and hydrated materials. Most interesting is that the values of T_c presented here for the dry phases are higher than those previously reported for KOs_2O_6, strongly suggesting that the generally accepted method of preparation, involving a step where the sample is washed in water leads to suppression of the onset of the superconducting state. There are likely to be two primary factors that may lead to this change in T_c. Firstly the incorporation of water into the structure leads to a small increase in the lattice parameter, if we look at the remainder of the osmate series, AOs_2O_6 (*A*= Cs, Rb and K), there is a strong correlation between the decreasing lattice parameter and an increasing T_c thus this effect may also be weakly seen in these materials. A second consideration requires an understanding of the effect that the 'rattling' of the alkali metal ions in these materials has

upon the onset of T_c. This effect has been explained by the presence of low lying phonons, associated with the rattling potassium ions located in a highly anharmonic potential, which give rise to anomalous electron scattering and strong coupling superconductivity[19]. Incorporation of water into the framework affect the rattling of the potassium ions and thus the nature of the low lying phonons as a result of both the displacement of the potassium ions by the water molecules and the partial occupation of the sites normally solely occupied by potassium. This quenching of a number of the low-energy phonons would be expected to lead to a suppression of T_c in what is a very strongly coupled superconducting material[12].

It seems likely that the change in properties and structure of this material arises solely from the choice of preparation methods and therefore care must be taken to establish the exact stoichiometry of these highly studied materials. It is also likely that these effects are observable in both poly crystalline and single crystal samples, which would be expected to rapidly take up water into their surface layers even in moist air. This effect may affect the measured properties and be a contributing factor to the variety of structures proposed for KOs_2O_6 by various groups where the preparation methods have not scrupulously avoided water. It is also worth noting that the degree of hydration and the effects this in turn may have upon the structure may be dependent upon the nature of the material, i.e. whether it is a single crystal or a powder, with the possibility of localised hydration in single crystals leading to a change in structure not observed in powders where the surface area to volume ratio differs significantly.

6.3 Comparison to $RbOs_2O_6$

To provide a comparison for analysis of KOs_2O_6 VSM data was also collected for samples of $RbOs_2O_6$, on both 'wet' and dry samples, shown in Figure 6.4. Although no evidence exists that this phases absorbs water we wished to firmly establish that it was not surface water causing the variations in T_c observed in the potassium phases. $RbOs_2O_6$ has also been extensively studied, with a similar mechanism proposed for the onset of superconduction[7] and the suggestion that the cation may also be delocalised at low temperatures[13].

Samples were prepared by a similar method as used for KOs_2O_6 but with the reaction temperature altered to 400 °C and duration to 14 hours. A small level of $RbOsO_4$ was present after this reaction process which was removed by washing with 20 % HCl solution followed by a further washing in water. Both samples were then dried in air at 60 °C. One sample, sample A, was then left in air for 48 hours before being studied, whilst the second sample, sample B, was heated to 300 °C for 3 hours under nitrogen then stored under a nitrogen atmosphere before data was collected as for the KOs_2O_6 samples in Section 6.2.2.

TGA data was also collected on this sample and whilst showing a small mass loss between RT and 300 °C the variation was within potential errors of the instrument and therefore must be handled with care and cannot be used as conclusive evidence that water was present within the structure.

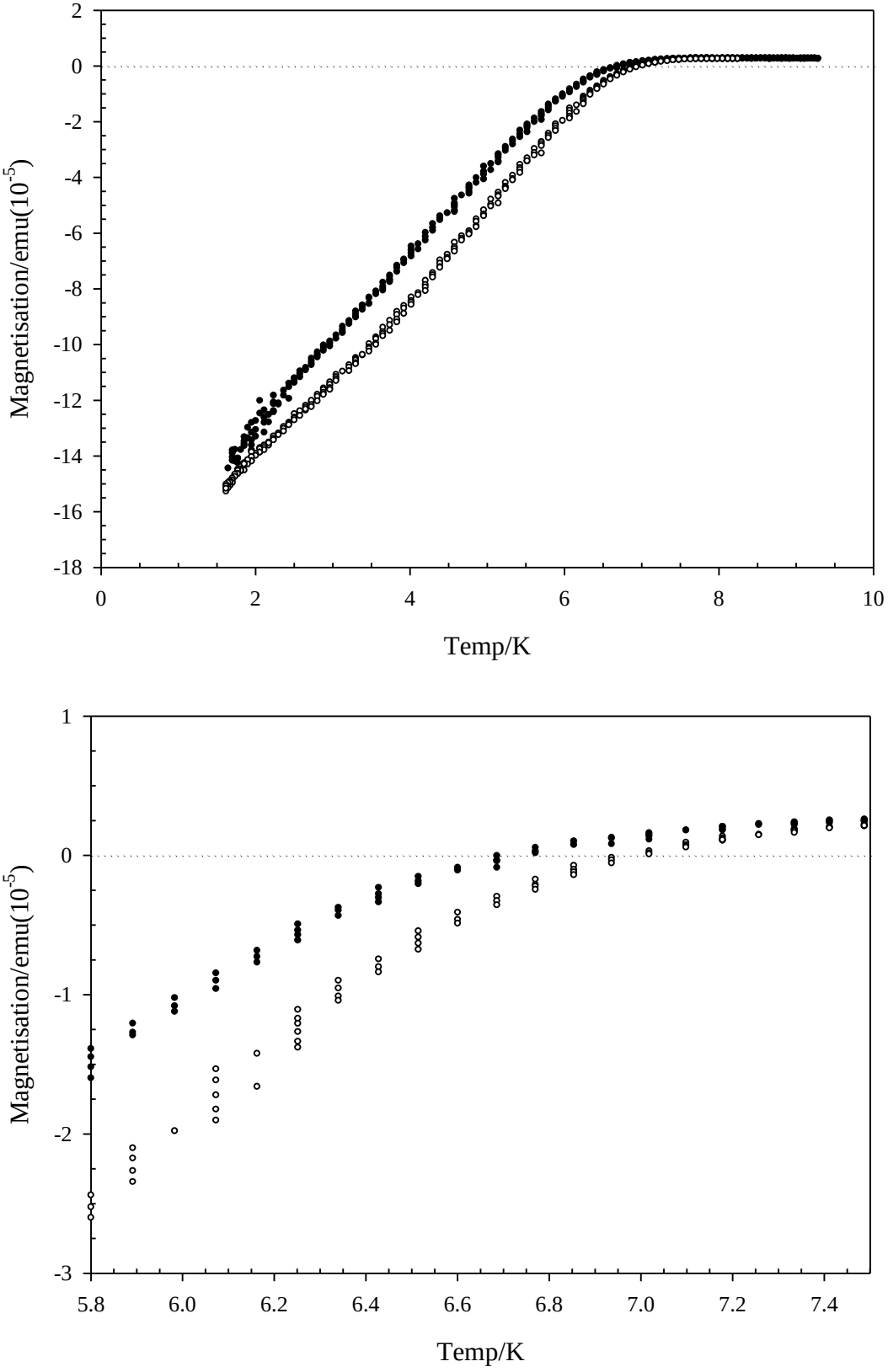

Figure 6.4 – Plots of temperature against magnetisation for $RbOs_2O_6$, Sample A (●) was measured as synthesised whilst Sample B (○) was dried at 300 °C. The upper image shows the full temperature range studied whilst the lower plot displays the superconducting transition.

6.3.1 Discussion

Initial inspection of the data clearly suggests that drying the sample has an effect upon the onset of the superconducting state, with similar behaviour seen in this material as observed in KOs_2O_6. The level of change in T_c is however less marked in this material, with a variation of ~0.2 K as opposed to ~0.4 K in the potassium osmate. The principle difference between these two materials is that KOs_2O_6 has been shown to have structural water present within the framework whereas $RbOs_2O_6$ only appears to have surface water. These measurements can therefore be interpreted as showing that surface water appears to play some part in the suppression of T_c in these alkali metal osmates, but that it is not solely responsible for the changes, with the remaining suppression being assigned to the water found within the cavities of the KOs_2O_6.

It is also worth noting that whilst the presence of water in the KOs_2O_6 causes a shift in lattice parameter no corresponding change is observed in $RbOs_2O_6$ strongly suggesting that water is not being incorporated into the structure. This presents a second option, that it is the increasing lattice parameter of KOs_2O_6 rather than the direct incorporation of water that is the primary effect in the lowering of T_c.

6.4 Conclusions

Work presented within this chapter has sought to understand the effects on the transition to a superconducting state of KOs_2O_6 and $RbOs_2O_6$ when water is present within the pyrochlore structure. Structural study of $KOs_2O_6.nH_2O$ has shown a clear link between the lattice parameter of the material and the temperature at which the material becomes superconducting; with the T_c increasing as the lattice parameter decreases.

The observed contraction of the lattice parameter is assigned to the loss of water with a maximum hydration of $KOs_2O_6.0.11H_2O$ leading to a lattice parameter of 10.1202(12) Å and a T_c of 9.8(1) K in agreement with those previously published in the literature[9]. Complete loss of this water leads to a contraction to 10.0795(2) Å and a rise in the T_c to 10.2(1) K. This water content, of ~0.11 H_2O per unit cell, was established by both TGA and PND. Two possible explanations have been postulated for the low level of water incorporation in this phase, differing from the fully occupied state more commonly observed; the first is that the water undergoes a slow redox reaction with the material causing a further reduction of the osmium from +5.5 or the second that the water content is limited by purely steric constraints.

The elevated observed value for the T_c of $KOs_2O_6.nH_2O$ after the removal of water from the structure at 10.2(1) K differs from the commonly reported value of 9.8K strongly suggesting that the presence of water has a marked influence upon this property and that care should therefore be taken throughout the synthetic process to ensure the sample remains dry. The investigation of the effects of drying upon $RbOs_2O_6$, where no evidence of water intercalation has been observed, suggest whilst surface water alone may suppress the onset of the superconducting state the effect is not as marked with a decrease of ~0.2 K as opposed to the 0.4 K change seen in $KOs_2O_6.nH_2O$.

6.5 References

(1) Sakai, H.; Yoshimura, K.; Ohno, H.; Kato, H.; Kambe, S.; Walstedt, R. E.; Matsuda, T. D.; Haga, Y. *J. of Physics-Condensed Matter* **2001**, *13*, L785-L790.

(2) Hanawa, M.; Muraoka, Y.; Tayama, T.; Sakakibara, T.; Yamaura, J.; Hiroi, Z. *Phys. Rev. Letters* **2001**, *8718*.

(3) Hiroi, Z.; Yonezawa, S.; Muraoka, Y. *J. of the Phys. Soc. of Japan* **2004**, *73*, 1651-1654.

(4) Yonezawa, S.; Muraoka, Y.; Hiroi, Z. *J. of the Phys. Soc. of Japan* **2004**, *73*, 1655-1656.

(5) Yonezawa, S.; Muraoka, Y.; Matsushita, Y.; Hiroi, Z. *J. of the Phys. Soc. of Japan* **2004**, *73*, 819-821.

(6) Wang, W.; Sun, J. F.; Liu, M.; Liu, S. *Acta Physica Sinica* **2009**, *58*, 5632-5639.

(7) Nagao, Y.; Yamaura, J. I.; Ogusu, H.; Okamoto, Y.; Hiroi, Z. *J. of the Phys. Soc. of Japan* **2009**, *78*, 21.

(8) Schuck, G.; Kazakov, S. M.; Rogacki, K.; Zhigadlo, N. D.; Karpinski, J. *Phys. Rev. B* **2006**, *73*.

(9) Yamaura, J. I.; Yonezawa, S.; Muraoka, Y.; Hiroi, Z. *J. of Sol. St. Chem.* **2006**, *179*, 336-340.

(10) Kunes, J.; Pickett, W. E. *Physica B-Condensed Matter* **2006**, *378-80*, 898-899.

(11) Hiroi, Z.; Yonezawa, S.; Yamaura, J. In *International Conference on Highly Frustrated Magnetism*; Iop Publishing Ltd: Osaka, JAPAN, 2006.

(12) Sasai, K.; Hirota, K.; Nagao, Y.; Yonezawa, S.; Hiroi, Z. *J. of the Phys. Soc. of Japan* **2007**, *76*, 5.

(13) Galati, R.; Hughes, R.; Knee, C.; Henry, P. F.; Weller, M. T. *J. Mat. Chem.* **2007**, *17*, 160-163.

(14) Galati, R.; Simon, C.; Henry, P. F.; Weller, M. T. *Phys. Rev. B* **2008**, *77*.

(15) Galati, R.; Simon, C.; Knee, C. S.; Henry, P. F.; Rainford, B. D.; Weller, M. T. *Chem. of Mats.* **2008**, *20*, 1652-1659.

(16) Levason, W.; Tajik, M.; Webster, M. *J. of the Chem. Society-Dalton Transactions* **1985**, 1735-1736.

(17) Barnes, P. W.; Woodward, P. M.; Lee, Y.; Vogt, T.; Hriljac, J. A. *J. of the Amer. Chem. Soc.* **2003**, *125*, 4572-4579.

(18) Babel, D.; Pausewang, G.; Viebahn, W. *Zeitschrift fuer Naturforschung, Teil B. Anorganische Chemie, Organische Chemie* **1967**, *22*, 1219-1220.

(19) Hiroi, Z.; Yonezawa, S.; Nagao, Y.; Yamaura, J. *Phys. Rev. B* **2007**, *76*, 19.

Chapter Seven

CONCLUSIONS

7.1 Conclusions

This work has sought to investigate a wide range of defect pyrochlore structures, looking to improve upon previous characterisation and expand the known family of materials in order to allow a more complete understanding of the factors that affect their structure and formation. Whilst extensive work was carried out seeking to incorporate, by direct high temperature methods, ions other than the mono valent species typically seen on the *A*-site this was not achieved. It seems likely that the main force behind this is the continued presence of transition metals with d^0 configurations of the *B*-cation sites, with alternative products, typically with more complex crystallographic structures, when these more highly charged species were present. A strong example of this preference for retaining a d^0 configuration is observed in $(BiK)(NbWO_6)_2$ and $(BiK)(TaWO_6)_2$; synthesised under driving conditions the materials readily replace ¾ of the potassium of the starting material, $KBWO_6$, with a third as much of bismuth. The substitution however appears to progress no further than this point. It seems plausible that this occurs as at higher levels of bismuth substitution one of two things may occur; the level of occupation becomes too low reducing the structural stability and therefore making this undesirable or that the B_2O_6 framework is unable to retain the d^0 electronic configuration beyond this degree of substitution.

One example is presented where the level of perceived A_2O' framework occupation must lead to a non d^0 state, in $K_{\sim 1.8}NbWO_6$. This was however undertaken in highly reducing conditions which may be a key factor in the formation. Taking this into account further work could potentially be undertaken looking at the plausibility of inserting additional metal ions into the framework using this reaction scheme. Other electropositive metals such as calcium, strontium, barium and ytterbium are possible alternatives to the alkali metals and it may be interesting to see if the ion exchange reactions utilising the alkali earth metals maybe pushed into insertion schemes under these conditions. Whilst this electronic state is unusual in defect pyrochlores is has been observed and commented upon previously, in the family A_2GeTeO_6 (*A* = K, Rb and Cs)[1].

Evidence has been presented across the sample set for the factors that appear to determine lattice volume. These materials broadly follow two trends, with the trend being followed being dependent upon the relative ion radii of the *A* and *B* site cations present. For the smaller *A*-site cations the determining factor is the ionic radii of the *B*-site cation which in turn determines the size of the BO_6 polyhedra that make up the B_2O_6 framework.

However beyond a certain point, nominally when the *A*-site cation becomes too large for the inter cavity spaces allowed by a relaxed B_2O_6 framework; it is the size of these ions that begins to determine the lattice volume. This expansion is accommodated through a reorientation of the BO_6 polyhedra and an elongation of the *B*-O bonds that they are composed of. In materials where it is the *B*-site cation that determines the lattice parameter it has also been shown that it is the larger of the two cations that proves the dominant factor; as opposed to the average size of the ion occupying this site.

Overall lattice parameters in these materials have should only a small degree of variability, ranging loosely between 10.0 and 10.5 Å, a ~5% by length, ~10% by volume variability. This suggests only a small range of steric conditions in which these materials will preferentially form, something endorsed by the reasonably narrow range of elements that can be incorporated into *beta* phase in comparison to the much wider range that are observed in the pyrochlore family as a whole.

Low temperature studies of the $ANbTeO_6$ (*A* = K, Rb or Cs) family has shown a generally conventional behaviour across a wide range of temperatures. In particular study of this series has provided significant insight when compared to the superconducting AOs_2O_6 (*A* = K, Rb or Cs) family[2] with similar levels of *A*- site ion displacement, and negative thermal expansion, being observed in the two potassium containing frameworks at the lowest temperatures studied. These structural studies have also been combined with the investigation of the onset of superconductivity and the effects of hydration upon this that are seen in KOs_2O_6 and $RbOs_2O_6$. It has been shown that when prepared by the standard method presented in the literature[3] KOs_2O_6 incorporates a measurable quantity of water, ~0.1 H_2O per formula unit, and that the inclusion of this water causes a suppression of the superconducting state to ~9.8 K (that generally reported), removal of this water causes T_c to increase to ~10.2 K. The study of $RbOs_2O_6$ alongside this material, a phase that no evidence could be found for the inclusion of water, has shown that the presence of water, even on the surface of the material alone as opposed to incorporated into the structure, causes a small degree of suppression to the onset of the superconducting state . This is however to a smaller degree than the total reduction observed in KOs_2O_6 and appears to be insufficient to attribute the entire observed effect to.

In depth investigation of both this and other hydrated phases, notably $KTaWO_6.H_2O$ and the series $A(NbWO_6)_2.H_2O$ (*A* = Sr, Ca, Pb and Ba), has allowed the accurate location of

both the oxygens and hydrogen atoms of the water molecules. Broadly these waters are located within the cavities of the B_2O_6 framework, near to the 8*b* positions. The exact positioning of the molecules appears to be determined by the space available within this cavity with the degree of displacement increasing as the cavity size increases. The hydrogen atoms were located at nearby 96*f* positions, allowing them to be aligned with the nearest oxygen atoms of the surrounding framework. This in turn had significant effects upon the internal bond angles of the water molecules causing them to shift significantly away from the 104.5° angle observed in 'free' water molecules.

The study of $KTaWO_6.H_2O$ has provided some evidence that the water is structurally trapped as opposed to structurally bound, with the water being lost both gradually and at low temperatures upon heating, complete dehydration having occurred by 120 °C. The effect is less defined in $A(BWO_6)_2.H_2O$ (*A* = Sr, Ca, Pb, Cd and Ba, *B* = Nb or Ta), where the dehydration occurs over a much wider range of temperatures. This may indicate that the water is more significant in the structural makeup of these phases providing a more stabilising effect to the framework; this seems likely as these materials otherwise have a very low level of occupation on the A_2O' network which generally appears unfavourable in these materials.

The synthesis of several phases including $K_{\sim 1.8}NbWO_6$, $CsTa_2O_{5.5}$, $(KBi)(NbWO_6)_2$ and $(KBi)(TaWO_6)_2$ has shown the wider potential of *beta*-pyrochlore frameworks to adopt unusual stoichiometries and the capacity of these phase to accommodate levels of occupation both above and below those normally observed in theses phases when appropriate conditions are adopted. All of these phases would however benefit significantly from further characterisation so more specific conclusions regarding the level of occupation and the location of the individual atoms can be undertaken.

Overall study has shown that the boundaries of what may successfully be synthesised by conventional high temperature methods have been fairly well established; however it has also been shown that there may be great potential in expanding the range of known phases through other methods such as ion exchange and insertion reactions.

7.2 References

(1) Amarilla, M.; Veiga, M. L.; Pico, C.; Gaitan, M.; Jerez, A. *Inorg. Chem.* **1989**, *28*, 1701-1703.

(2) Galati, R.; Simon, C.; Henry, P. F.; Weller, M. T. *Phys. Rev. B* **2008**, *77*.

(3) Hiroi, Z.; Yonezawa, S.; Muraoka, Y. *J. of the Phys. Soc. of Japan* **2004**, *73*, 1651-1654.

(4) Yamaura, J. I.; Yonezawa, S.; Muraoka, Y.; Hiroi, Z. *J. of Solid State Chem.* **2006**, *179*, 336-340.